ACOUSTIC SCATTERING FROM COMPACT BUBBLE CLOUDS

A Report to the ONR AASERT Program Under

the Support of Grant N00014-93-1-0749

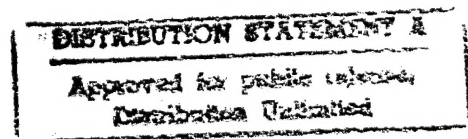Ronald A. Roy

The Applied Physics Laboratory
University of Washington
1013 NE 40th St.
Seattle, WA   98105

Jeffrey A. Schindall*

Department of Physics
University of Mississippi
Oxford, MS   38677

January 22, 1996

19960801 184

* Current Address: Code 7121 , Naval Research Laboratory
4555 Overlook Avenue SW
Washington D.C. 20375-5350

DISCLAIMER NOTICE

THIS DOCUMENT IS BEST
QUALITY AVAILABLE. THE COPY
FURNISHED TO DTIC CONTAINED
A SIGNIFICANT NUMBER OF
COLOR PAGES WHICH DO NOT
REPRODUCE LEGIBLY ON BLACK
AND WHITE MICROFICHE.

ACOUSTIC SCATTERING FROM COMPACT BUBBLE CLOUDS

Ronald A. Roy

The Applied Physics Laboratory
University of Washington
1013 NE 40th St.
Seattle, WA   98105

Jeffrey A. Schindall*

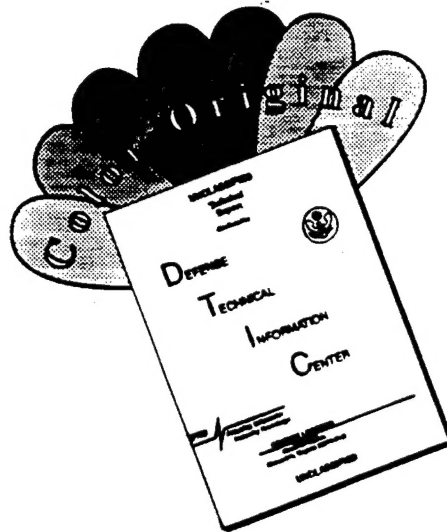Department of Physics
University of Mississippi
Oxford, MS   38677

January 22, 1996

* Current Address: Code 7121 , Naval Research Laboratory
4555 Overlook Avenue SW
Washington D.C. 20375-5350

Acoustic Scattering from Compact Bubble Clouds

Jeffrey A. Schindall, Ph.D.

The University of Mississippi, 1995

Supervisor: Ronald A. Roy

In this study, a simple model describing the low–frequency scattering properties of high void fraction bubble clouds in both the free field and near the ocean surface is developed. This model, which is based on an effective medium approximation and acoustically compact scatters, successfully predicts the results of the bubble cloud scattering experiment carried out at Lake Seneca in New York state for frequencies consistent with the model assumptions (Roy et al., 1992). The introduction of the surface is facilitated by the method of images and is subject to the same constraint of low–acoustic frequency imposed by the compact scatterer assumption. This model is not intended to serve as an exact replicate of oceanic bubble cloud scattering. The model herein was kept simple by design, for only then can the complex physical behavior be expressed in a simple analytical form. Simple, analytic theories facilitate the exploration of parameter space, and more importantly serve to illuminate the underlying physics.

Contents

List of Tables

vii

List of Figures

xi

xiii

Chapter 1

Introduction

Until 1985, the primary source mechanism for the wind dependent ambient noise[1] spectrum after the appearance of breaking waves on the sea surface in the frequency range 20 to 2000 Hz was not well understood. Below 2000 Hz, it has proven difficult to explain the ambient noise spectrum primarily since the localization of the source mechanisms is difficult without the use of a large directional receiver. Carey and Wagstaff (1986) and Carey and Bradly (1985) summarized experimental evidence which strongly suggests that low frequency noise is wind dependent and locally generated. Although it had been suggested for many years that bubbles play a significant role in the creation of ambient noise at the higher frequencies (Wenz, 1962; Kerman, 1984), the problem of ambient noise generation at the lower frequencies was unclear.

Carey and Bradly (1985) and Prosperetti (1985) first suggested that collective oscillations of bubble plumes or clouds near the ocean surface con-

---

[1] An informal definition of ambient sound or ambient noise is the background sound that is unwanted by anyone performing an acoustic measurement.

tributed to low–frequency wind–dependent ambient noise as a natural source mechanism. Collective oscillations is a phenomenon in which individual bubbles in a mixture pulsate in unison at frequencies well below the natural resonance frequencies of the bubbles, resulting in a significant reduction in the sound velocity. Needless to say, this phenomenon and the candidate source mechanisms were met with less than universal enthusiasm. However, in the past decade, many laboratory and field experimental efforts have established that bubble cloud production is a viable source of low frequency sound in the ocean (Roy *et al.*, 1992; Carey *et al.*, 1993; Kolaini *et al.*, 1994; Yoon *et al.*, 1991; Nicholas *et al.*, to be submitted; Hollet, 1994; Farmer & Vagle, 1989).

As early as 1946, it was established that the scattering of sound from ship wakes was highly dependent on the population or density of bubbles entrained by turbulence or formed by propeller cavitation (NDRC, 1946). The fundamental question to be answered is: what role, if any, do bubble clouds play in sea surface scatter? Given that bubble clouds radiate sound at low frequencies, it seems plausible that such clouds might be efficient scatterers of sound as well. This hypothesis was recently tested and verified in a well controlled field experiment in a freshwater lake in New York state. The experimental design, analysis, and associated modeling effort is the topic of this dissertation.

2

1.1 Ambient noise in the ocean

Prior to World War II, literally nothing was known about oceanic ambient sound in a scientific context. Since that time, a prolific effort devoted to the experimental characterization and theory of ambient noise production has generated hundreds of publications. The first to make an effort at measuring the noise spectrum was Knudsen *et al.* (1948). Early in the war, his group performed a series of ambient noise measurements in a number of bays, harbors, and near off–shore areas. For obvious reasons, this data was not obtained in the open sea. His results are known as the "Knudsen Curves" and display an increasing source level with wind speed. The slopes of the curves are not wind speed dependent and average -5 dB per octave in the frequency range 2–20 kHz. At the time, the source mechanisms were unknown. He commented that the near–surface noise contributions can be attributed to individual waves and whitecaps, but that these momentary variations are not important at depth (in his case 20 to 300 ft). These curves were regularly used in the years following the war to estimate the noise levels in deep water.

In the years after the war, many experimental efforts were performed in deeper water which confirmed the spectral slope of the Knudsen spectra, but also encompassed a much broader frequency range both above and below Knudsen's experimental capabilities. Following Urick (1984), the noise spectrum is divided into five distinct bands as follows: Ultra–Low Band (< 2 Hz); Infrasonic Band (2 to 20 Hz); Low Sonic Band (20 to 200 Hz); the High Sonic Band (200 Hz to 20 kHz); and the Ultrasonic Band (> 20 kHz). A summary of the noise contributions and the sources encompassing these bands is illus-

trated in Figure 1.1 (Wenz, 1962). It is clear that the noise spectrum slopes primarily in a negative direction, but some regions possess a flat or positive slope. The wind speed dependence in the figure is denoted by the Beaufort wind force presented in Table 1.1.

Beaufort Force	Sea State	Mean Wind Speed (m/s)	Appearance	Probable Wave Height (m)
0	0	0	Sea like a mirror	0
1	1/2	1	Ripples w/out foam crests	0.08
2	1	2.5	Small wavelets; no breaking	0.15
3	2	4.5	Large wavelets; crests begin to break	0.6
4	3	6.5	Small waves, becoming longer; common breaking	1.1
5	4	9.5	Moderate waves, long form; maybe some spray	1.8
6	5	12.5	Large waves begin to form. The white foam crests are more extensive everywhere	2.9
7	6	15	Sea heaps up and white foam from breaking waves begins to blow in streaks along the direction of the wind.	4.1

Table 1.1: Beaufort scale of wind force and sea state.

The focus of this work is in the frequency range 20 to 2000 Hz for which ambient noise displays a dominant dependence on shipping traffic and wind speed. In remote areas where shipping noise is not prevalent (mostly in the southern hemisphere), the noise spectrum is clearly dominated by wind speed alone at the upper and lower frequencies (Kibblewhite *et al.*, 1976). Furthermore, Whittenborn (1976), Bannister *et al.* (1981), and Kewley *et al.* (1990) recognized that there are at least two wind dependent mechanisms responsible for ambient noise; one occurs before the onset of wave breaking, and one after. Kennedy and Goodnow (1990) also reported a wind speed dependence
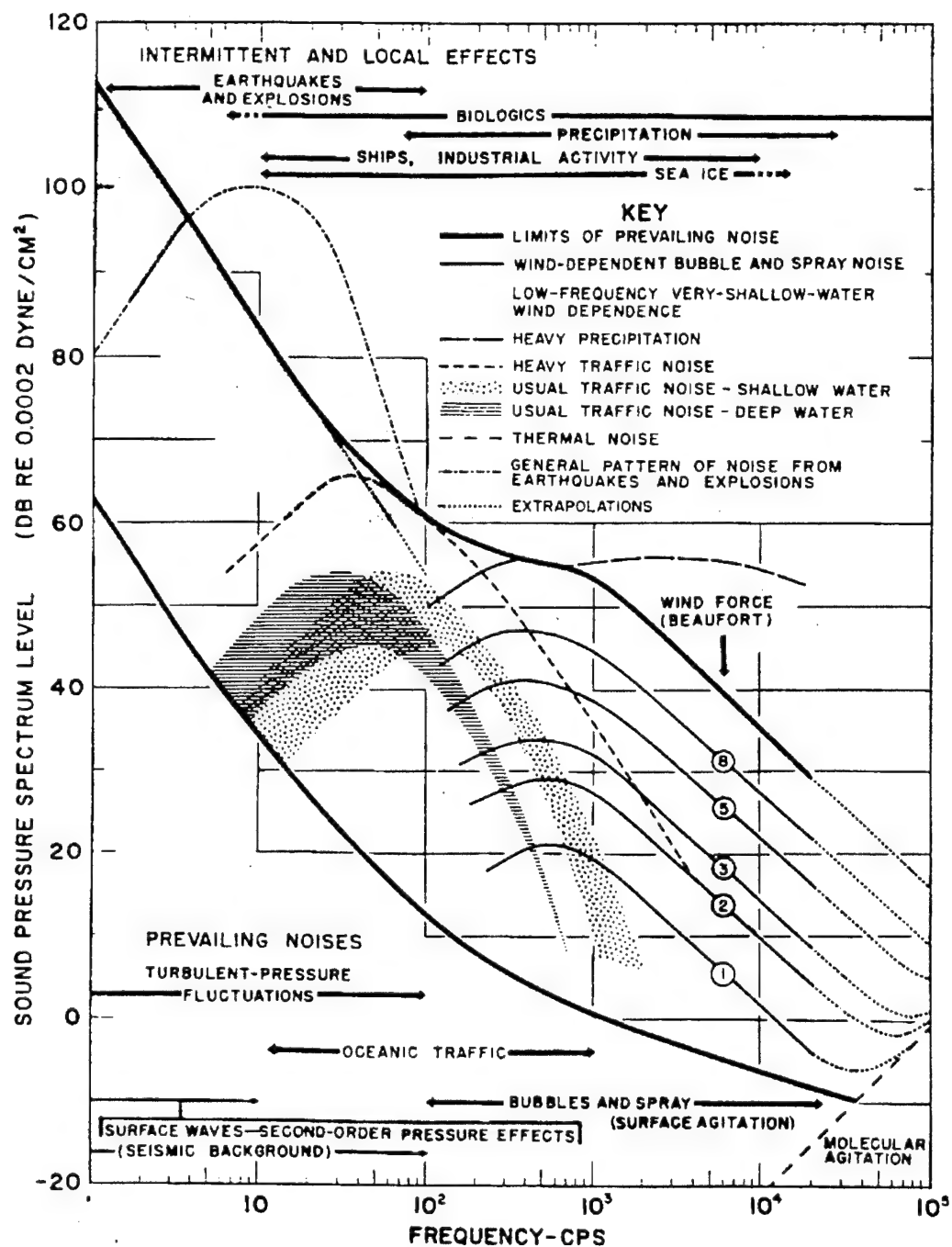
Figure 1.1: Ambient noise spectrum and source mechanisms. From Wenz (1962). The levels in this figure should be increased by 66 dB to conform to the current standard (dB re $1\,\mu$Pa).

5

on the vertical directionality of ambient noise. For wind speeds exceeding the wave breaking threshold, the noise field exhibits a vertical directional spectra consistent with a distribution of dipole sources (40–4000 Hz) near the sea surface.

In Urick's review of ambient noise in the ocean (1984), the wind–dependent processes hypothesized to contribute to surface noise generation after wave breaking includes wind turbulence coupled into surface waves, pressure deviations due to surface motion, nonlinear wave–wave interactions, and spray and cavitation. Furduev (1966) suggested that noise emissions from cavitating bubbles might be a key source near the sea surface. The driving mechanism for cavitation is theorized to be the changing pressure under surface waves which results in bubble growth by 'rectified diffusion' and a subsequent violent collapse. Bubbles entrained by impacting spray from whitecaps are also thought to contribute to the noise spectrum (Wilson, 1980); this view is supported by the experimental data reported by Morris (1978).

Kerman (1984) correctly surmised that densely populated bubble formations created by breaking waves played a significant role in ambient noise production for frequencies above 50 Hz. Furthermore, he speculated that there are two regions of low frequency wind dependence, one preceding to and one following wave breaking, indicating the existence of separate source mechanisms. He recognized that the popular forcing mechanisms of the day (cavitation, spray, large amplitude non linear forcing at frequencies below the bubble resonance, and simple volume pulsations) were inadequately formulated. Nevertheless, he chose to model 'weak cavitation'—the below resonance forcing due

6

to large amplitude turbulent flow in transient bubble populations—as a candidate mechanism. Recently, however, Prosperetti and Lu (1988) discounted the likelihood that cavitation is a natural source mechanism since the extreme pressure fluctuations required are unrealistic.

For frequencies above 10 kHz, the wind dependent noise is due, in part, to single bubble resonant (volume) pulsations driven by the bubble formation process and by turbulent flow[2]. However, in the frequency range 200 to 2000 Hz the oscillation of single bubbles is not thought to significantly contribute to the ambient noise spectrum since such bubbles would have to approach diameters greater than 3 mm. Although bubbles of this size do appear beneath breaking waves, they are extremely buoyant and rise to the surface quickly (Lamarre & Melville, 1992). Furthermore, the bubble distribution is thought by some to peak near 80 μ m (Wu, 1981), which would seem to suggest that the role played by single bubbles below 2000 Hz is minimal. During the period following Knudsen's initial measurements during WW–II until Urick's review of ambient noise in the sea in 1984 the structure of the noise spectrum (20 to 2000 Hz) was well documented, but not well understood.

---

[2]The resonance frequency, in Hz, of an air bubble in water at atmospheric pressure is given approximately by $f_o = 3.2/R_o$, where R_o is the bubble radius in m.

1.2 The Theory of Low Frequency Ocean Ambient Noise: A Paradigm Shift

The understanding of natural source mechanisms of ambient noise recently became a subject of renewed interest in the ocean acoustics community. This began at the Fall 1985 meeting of the Acoustical Society of America (ASA), at which point the current base of knowledge was reviewed. Since then, no less than 12 sessions devoted to ambient noise processes have been convened at the ASA. In addition, a trio of international symposiums entitled Sea Surface Sound were conducted in 1987, 1990, and 1994. These were multi–disciplinary efforts attended primarily by hydrodynamicists and acousticians who had a common interest in addressing the unresolved issues related to natural source mechanisms of surface generated noise in the ocean. By far, the most controversial topic of discussion at these meetings was the role played by bubbles and the collective oscillations of bubble ensembles in wind dependent ambient noise generation at frequencies below 2000 Hz.

Collective oscillations is not a new idea. In fact, Wood (1941) was among the first to develop a model describing this behavior at frequencies well below the bubble resonance. Over the years, many laboratory studies were conducted which confirm its utility (Silberman, 1957; Fox *et al.*, 1955; Karplus, 1958; Gouse & Brown, 1964; Ruggles, 1987; Lamarre & Melville, 1994; Cheyne *et al.*, 1995). In a two–phase mixture of air bubbles in water, and for frequencies well below individual bubble resonance, the effective mixture

density and compressibility are described by

$$\rho_e \;=\; (1-\beta)\rho + \beta\rho_g, \tag{1.1a}$$

$$\kappa_e \;=\; (1-\beta)\kappa + \beta\kappa_g, \tag{1.1b}$$

respectively. Here, β is the void fraction or ratio of gas volume to total volume (often expressed as a percentage); ρ, κ, ρ_g, and κ_g are the densities and compressibilities of the liquid and gas, respectively. The sound velocity in the mixture is given approximately by

$$c_e \approx (\rho_e\kappa_e)^{-1/2} \approx \sqrt{\gamma P_\infty/\beta(1-\beta)\rho}, \tag{1.2}$$

which follows directly from the equation of state (Wood, 1941). Thus, for a mixture having void fraction $\beta = 10^{-2}$, the effective sound speed is $c_e \approx 100\,\mathrm{m/s}$; significantly lower than the speed of sound in the gas! In Chapter 2, the interesting subject of sound propagation in bubbly mixtures will be discussed more formally, including the dispersive characteristics.

The question that remains is: how might an isolated, densely populated bubble–water mixture (*i.e.*, a bubble cloud) contribute to the low frequency noise spectrum? For the purposes of this study a bubble cloud is defined as a mixture of air bubbles and water where $\beta \approx 10^{-2}$ to 10^{-5}, is assumed to be spherical and has a radius $a < 1\,\mathrm{m}$. It is entrained beneath the surface via a breaking wave and persists for a period of only a few seconds (Monahan & Lu, 1990). Is it plausible that such a spherical cloud, characterized by an effective density and sound speed as given by the collective oscillations model,

9

will radiate sound and resonate at its fundamental eigenfrequency given by the simple approximate expression (Carey & Fitzgerald, 1993; Carey & Roy, 1993; Roy *et al.*, in press)

$$\Omega_0 \approx \frac{1}{2\pi a}\sqrt{\frac{3\gamma P_\infty}{\beta(1-\beta)\rho}} \quad ? \qquad (1.3)$$

For example, a spherical cloud of radius $a = 0.1\,\text{m}$, possessing void fraction $\beta = 10^{-2}$, will resonate at approximately $274\,\text{Hz}$. This will be shown explicitly in Chapter 3, and is true regardless of the bubble size distribution, provided that the resonance frequency of the largest bubbles is much greater than the acoustic (driving) frequency.

The acoustic forcing which excites the low frequency modes of a bubble cloud is thought to be individual bubble formation and turbulent flow (Oğuz, 1994). As stated by Longuet–Higgens (1993):

> "Each bubble, when it is formed, emits a short acoustical pulse
> lasting for a few milliseconds only–a kind of birth yell. In listening
> to underwater sound at these frequencies we are, it appears, hearing
> a chorus of such birth yells."

The so called 'birth yell' is in fact a damped–resonant volume oscillation. Since no sound of finite duration can be a pure tone, a short duration pulse is composed of a broad spectrum of frequencies which in turn excite the low frequency eigenmodes of the cloud.

1.2.1 Experimental evidence of low–frequency noise production by bubble clouds

Several laboratory measurements of the sound produced by bubble clouds have been performed in recent years. Some were conducted using continuously rising bubble columns with the goal of confirming that the collective oscillations model could be used to explain the low–frequency sonic emissions. Others were conceived with the notion that breaking wave occurances are discrete, transient events that entrain large amounts of air, and therefore might explain the low–frequency bursts of sound observed in the ocean.

Yoon *et al.* (1991) conducted a laboratory experiment in which a cylindrical bubble column was generated by an array of hypodermic needles located at the bottom of a fresh water tank. The peak low frequency acoustic signature from the bubble column (260 to 550 Hz) matched very well the theoretical frequencies predicted by the bubble cloud model of Lu *et al.* (1990). Similar modeling and measurements by Koller and Shankar (1993; 1994) have shown that the pressure field outside the bubble mixture was, however, evanescent rather than oscillatory.

Nicholas *et al.* (1994) conducted an experiment with an artificial cylindrical bubble cloud bounded at the top and bottom by pressure release surfaces. In this study, a well controlled, continuously rising cylindrical column of bubbles was produced in a freshwater tank and the higher order radiation modes were found to be in good agreement with the collectively oscillating bubble column model presented in of Lu *et al.* (1990) and in Commander and Prosperetti (1989). This was followed by an experiment involving bubble

11

columns created in salt and fresh water (Roy *et al.*, 1991), with special care taken to insure that the column dimension and void fraction was constant in the two experiments. Although the relative bubble size distributions differed significantly, the peaks in the noise spectrum generated by fresh and salt water columns were virtually identical provided the void fraction and column dimensions were held fixed. This confirms the notion that it is the effective sound speed (*i.e.*, void fraction), not bubble size that dictates the low–frequency response of a bubbly assemblage.

Kolaini *et al.* (1993) measured the low frequency acoustic resonance signature of bubble plumes generated by dropping masses of water from cylindrical containers into a large tank and a pool. They observed that low frequency sound was generated the instant that a large "substructure" detached from the plume. Their observations showed that the substructures were *spherical* regions of very high void fraction and they demonstrated that the lowest resonance frequency would match the measurements if the mean void fraction was assumed to be approximately 40%.

Kolaini followed the laboratory experiments with a series of well controlled field experiments in which a cylindrical container of water was released into a freshwater lake and the sea water of Puget Sound (Kolaini *et al.*, 1994). Again they observed a damped resonant oscillation as spherical region 'pinched–off' from the cloud. Unlike Roy *et al.* (1991), they found that the resonance frequency of the newly formed plumes was slightly increased in the marine environment compared to the fresh water of the lake. This, in part, was due to a 10–15 % smaller plume radius in the Puget Sound experi-

ment, but also likely due to slight differences in the void fraction, which was not accurately measured. In addition, the salt water emissions were typically 3–4 dB lower, which was attributed to the presence of significantly smaller radius bubbles. The radiation pattern was dipole, which is consistent with the notion that the source is a compact monopole in the vicinity of a pressure release surface.

Finally, recent measurements by Carey *et al.* (1993) on the sound generated by a tipping trough in both fresh and salt water have shown that the bubble plumes radiate sound at low frequencies in a manner that was consistent with theory and that the resonance frequency was in agreement with a *modified* Minneart expression (Eq. 1.3) first derived by Carey and Fitzgerald (1993). While the aforementioned experimental measurements were conducted in the near field, this experiment has the distinction of being the first in which the sound radiated by a controlled bubble plume was measured in the far field, with known volume fractions and salinity concentrations. In reverberant tanks, they found that the frequency of oscillation did not change between fresh and salt water. This was determined to be due to the fact that the plume had similar dimensions and void fractions in both cases. It was clear from their measurements that the bubble population was different in fresh and salt water, thus once again it is concluded that the low frequency acoustic characteristics of a bubble cloud are dictated by the void fraction, and *not* the individual bubble dynamics. The main difference observed between fresh and salt water was in the level of the acoustic radiation. It was found that the salt water case had lower levels due to the higher proportions of small bubbles, resulting in

13

greater surface area and correspondingly greater attenuation.

Taken as a whole, these studies conclude that reasonably densely populated bubble assemblages radiate sound at frequencies much too low to be described by the resonance of individual bubbles. Furthermore, the theoretical models achieve good agreement with the laboratory studies using a well established collective oscillations model. In such a case, the sound speed at low frequencies is reduced (primarily depending on the void fraction) and the fundamental frequencies of the cloud or plume are determined by the eigenmodes of the system—that is, the resonance frequency is based on the effective sound speed (*i.e.*, β) and length scales of the cloud. At the fundamental resonance frequency, these assemblages possess a characteristic dimension which is less than the acoustic wavelength and can thus be regarded as acoustically compact. In such a case, the source is well approximated in the far field as a monopole source. When placed near a pressure release surface, the radiation from a monopole source takes on a dipole characteristics (*i.e.*, using the method of images). The most important parameter in describing these phenomena is the void fraction. Unfortunately, there is little quantitative data reported on the void fraction of clouds and plumes near the sea surface.

14

1.3 Breaking Waves, Bubble Clouds and Low–Frequency Ambient Noise

In the deep ocean, it is well known that the propagation of surface waves obeys the following dispersion relation (Lighthill, 1975):

$$\Omega^2 = gK(1 + \tau K^2), \tag{1.4}$$

where Ω is the radian ocean wave frequency, K is the wave number of the traveling wave, g is the acceleration of gravity, and τ is the ratio of the surface tension to the product of g and the water density.

After sufficient periods of high winds, the sea reaches an equilibrium state. The wave height and frequency spectrum can then be predicted by one of several wind–speed based empirical models (Pierson & Moskowitz, 1964; Donelan *et al.*, 1985; Hasselman *et al.*, 1976). Waves of this nature are wind driven, and build up momentum until at some point they break, forming white–caps and entraining air beneath the surface. The onset of this wave breaking process typically begins at wind speeds exceeding $U > 6\,\mathrm{m/s}$.

It is not the instantaneous wind speed, but rather the significant wave height that characterizes the sea state. The Beaufort scale of wind force (Table 1.1) describes the sea state in terms of significant wave height and characteristic appearance (Allen, 1983). The first column lists the Beaufort number, the second the sea state, the third column lists the wind speed required to build up the sea (over a period many hours), and the last column lists the

15

mean probabilistic wave height. A wind of a given Beaufort force will produce a characteristic appearance of the sea surface provided that it has been blowing for a sufficient length of time, and over a sufficiently long fetch. The term fetch refers to the length of the stretch of water over which the wind acts on the sea surface from the same direction (the longer the fetch, the greater the disturbance for a given wind speed). Small breaking waves (or breakers) begin to appear on the surface of a fully developed sea at the critical windspeed ($U \approx 6\,\mathrm{m/s}$). At this point, the Beaufort wind force is 3 and sea state is 2. As the wind speed increases, the disturbances at the sea surface become more frequent and more violent. For sea states between 3–5 a significant number of white caps appear, followed by sea spray.

According to a model proposed by Monahan and Lu (1990), bubble assemblages created by breaking waves fall into three distinct categories determined by their lifetimes, volume fractions, and penetration depths. The bubble ensembles are known as Type–A, Type–B, and Type–γ, and are summarized in Table 1.2 and described below. First, as a wave breaks, a white–cap appears on the surface marking the birth of a Type–A *plume*. Bubbles in this densely populated formation penetrate to depths near 0.25 m, maintaining contact with the surface in an area of approximately $0.5\,\mathrm{m}^2$. Typical void fractions for these plumes are on the order of a 10^{-2}, but values exceeding this by an order of magnitude have been observed (Lamarre & Melville, 1994; Farmer, 1992).

The Type–A plume quickly decays into a Type–B white–cap in roughly 0.5 s and is indicated by the presence of a white foamy patch on the sea surface.

Type	depth (m)	Area (m^2)	Void Fraction	Life time
A	0.25	0.5	< 0.10	0.5 s
B	0.5	up to 1	10^{-4} 10^{-3}	4.0 s
γ	10	10	$O(10^{-6})$	10-100 min

Table 1.2: Characteristics of bubble ensembles following a breaking wave event.

Continued momentum transfer forces the bubbles beneath the whitecap to depths on the order of 0.5 m, as the now detached *cloud* continues to grow in size. In the next 4 s, the void fraction of this densely populated cloud decreases to the order of 10^{-4}, occupying on the average a cross sectional area of $1\,m^2$. The decrease in void fraction is due to the increase in cloud volume and the loss of larger bubbles rising to the surface.

The larger bubbles in the cloud continuously rise to the surface, leaving behind smaller bubbles which can be stabilized by surfactants (chemical pollutants) and convected to depths on the order of 10 m by a mechanism known as Langmuir circulation[3]. This formation is known as Type–γ, or *tenuous* assemblage, and is noted for void fractions less than 10^{-6} and lifetimes of minutes to hours at a time. Eventually, the 'stabilized' bubbles dissolve into solution.

The distinction between clouds and plumes is clearly demarcated by their respective lifespans, penetration depths, void fractions, and attachment to the surface. That is, plumes are relatively small, densely populated ensembles attached to the surface and lasting only for brief periods of time. While clouds, on the other hand, are detached from the surface, have lifetimes on the order of 4 s, void fractions in the range 10^{-5} to 10^{-2}, volumes less than $1\,m^3$,

---

[3]Langmuir circulation is a down welling turbulent current aligned with the wind which convects micro–bubbles to depth (Thorpe, 1984).

and penetration depths on the order of 1 m. The tenuous assemblage has a length scale on the order of 10 m, an extremely low void fraction ($\beta < 10^{-5}$), and can persist for hours at a time. In this work, the primary concern is with the relatively densely populated, short–lived bubble clouds, and *not* the surface–attached plumes or tenuous assemblages.

In the introduction of Lamarre's dissertation (1993) is a compilation of experimental efforts aimed at obtaining the bubble size and spatial distributions in the laboratory and in the sea. From his review, it is clear that the typical bubble size in the ocean is less than $100\,\mu$m, and that the distributions obey an exponential depth dependence. While, bubbles larger 1 mm radius have been observed in the ocean (Lamarre & Melville, 1992), buoyancy forces cause them to rise to the surface quickly and thus their contribution to the noise spectrum ($< 2000\,$Hz) is limited.

As previously noted, the speed of and attenuation of sound are affected in a dispersive manner by the presence of bubbles. This is due to the increased compressibility of the mixture while the density of the mixture remains near that of water. In such a mixture, a phenomenon known as collective oscillations can occur in which the sound speed can be lowered dramatically, even to values below that of air, depending on the void fraction. For example, for a void fraction of 10^{-5}, the speed of sound is reduced to about 170 m/s. Also, increased attenuation due to the presence of bubbles in the mixture is observed.

In Lamarre's (1994) recent research effort, the speed and attenuation of sound were measured beneath breaking waves using a pulse propagation delay technique. The sound speed was estimated by dividing the propagation

distance by the transit time of the pulse. The distance between the source and receiver was 1.2 m and the measurements were performed at four depths (0.25 m vertically spaced stations just below the surface). They typically observed decrements in the sound speed on the order of 100 m/s and a maximum deviation of 800 m/s, all attributed to the presence of bubbles. The sound speed decrements were found to decrease with depth in accordance with the bubble population density. Although this effort reported decrements in the sound speed in excess of 800 m/s, it is likely that a closer spacing between the source/receiver pairs would provide a more highly localized result. That is, when the distribution of bubbles is not uniform across the 1.2 m separation (suppose one had a smaller densely populated bubble cloud of dimension 0.25 m) the measurement would likely be biased to sound speeds closer to the liquid and therefore would not yield an accurate result for the maximum sound speed decrement in the bubbly region under a breaker. The difficulty in performing this type of acoustic measurement is apparent since it must be conducted at frequencies well below the bubble resonance frequency, which limits one to relatively distant separations.

In a previous experiment, Lamarre and Mellville (1992) used a conductivity probe to measure the void fraction, not the sound speed, beneath breaking waves in the ocean and the laboratory. In their field experiment the reported void fractions at six depths (equally spaced by 0.15 m beginning at the surface) on the order of 10^{-2}, but at times exceeding 10^{-1}. In the laboratory, surface waves were propagated down the length of a narrow flume and made to break above a single fixed–depth void fraction probe. Thus as the plume

19

beneath the breaking wave travelled past the sensor a temporal image of the localized void fraction was obtained at a particular depth. The probe depth was varied and the measurement repeated for several more breaking events which allowed them to construct a spatial and temporal image of the void fraction beneath a wave. These images suggested that the laboratory plumes were nominally hemi–cylindrically shaped. When the sensors were deployed on a buoy in the ocean, void fractions in the range 10^{-2} to 10^{-1} were typically observed directly beneath an actively breaking wave—in good agreement with the sound speed decrements they later measured using acoustic techniques.

That the Type–A/B bubble assemblages described above are responsible for the discrete bursts of low frequency (LF) sound has recently been established by Hollet (1994) (see also Carey and Monahan (1990)). In this experiment, an end–fired 32 element vertical array (3 nested subelements of 375, 750, and 1500 Hz) was deployed and pointed toward the surface and a land–based video camera focussed on the same patch of the surface were used to correlate visually observed white–cap breaking events with broad band sound emissions below 1500 Hz. These sound bursts typically persisted for a few seconds and then died out, presumably since no more bubbles were being formed.

Simultaneous acoustic and video measurements of breaking wave events were reported by Farmer and Vagle (Farmer & Vagle, 1989). Using an omni–directional hydrophone deployed 14 m below the surface, and a sub–surface video camera, they correlated sonic emissions as low as 50 Hz occurring simultaneously with visual observation of bubble cloud production beneath a breaking wave. In order to produce sound at a frequency of 50 Hz, a bubble

20

radius of 6.4 mm is required. These low frequencies are similar to those observed radiating from the bubble clouds produced by the 'tipping–trough' of Carey *et al.* (1993) and the bucket drops by Kolaini *et al.* (1994). A subsequent experiment by Vagle and Farmer (1992) made use of the ambient sound radiated by a bubble cloud to precisely track single breaking wave events in both space and time. Here, they utilized a self–contained freely drifting instrument platform deployed to a depth of 50 m and consisting of six receiving hydrophone elements.

In a recent model proposed by Oğuz (1994), the sound radiated by the formation of bubble plumes beneath the sea surface is discussed. In this study, Oğuz presents an idealized geometry where the sea surface is taken as planar and the bubble plumes are hemispherical. A fundamental feature of his model is that the plumes were allowed to grow with time as the air entrainment takes place, and thus the void fraction evolves as well. The acoustic forcing in the mixture is achieved by broadband emissions from newly 'birthed' bubbles in the vicinity of the perfectly reflecting surface (Pumphrey & Ffowcs-Williams, 1990). This modeling effort results in noise levels that are comparable with the reported field measurements of Hollet (1988; 1994) while using a minimal amount of experimental input (*i.e.*, only the bubble size distribution, mean void fraction, and wind speed need to be known), further evidence that the collective oscillations model is on a strong footing.

Currently, the notion that bubble clouds contribute to the production of low frequency ambient noise is widely accepted. The recent field measurements of Hollet and of Farmer and Vagle, when considered along with the good

theoretical agreement of the laboratory results of Carey's tipping–trough and Kolaini's bucket–drop experiments suggest that the bubble clouds generated beneath breaking waves are a fundamental contributing source of natural low frequency noise in the ocean. It is interesting to note that there was no mention of low frequency noise production by bubble clouds in Urick's review of ambient noise in 1984. That this paradigm shift in perception occurred within a ten year span and continues to this day[4] is remarkable and forms a good part of the motivation for the work described in this thesis.

1.4   Sea–surface scatter

A related field which has also gained renewed interest in the last decade is that of low–frequency sea surface scattering and reverberation. Scattering can be regarded as radiation from a 'source' which is driven by an incident wave rather than by a local external generator. The scattering sources near the ocean surface include the surface itself, fish, resonant bubbles, and perhaps bubble assemblages beneath breaking waves. Reverberation is the totality of sound energy scattered from a myriad of inhomogeneities present in the sound beam as well as boundaries along its path. Examples of reverberation include volume and surface reverberation. Volume reverberation is defined as the sound returned by scattering centers in a volume of the sea, whereas surface reverberation is the sound returned by scattering centers at or near the sea

---

[4]The author in the spring of 1995 participated in an experiment (SWELLEX–4) with participants from the U.S. Naval Research Laboratory (NRL) and the Scripps Institute of Oceanography designed to measure the sound produced by breaking waves at frequencies below 400 Hz.

surface. The strength, or efficiency, of these scatterers would be expected to be a function of environmental parameters: wind velocity, sea state, whitecap coverage, temperature, fish populations, etc. The primary distinction between volume and surface reverberation is that surface reverberation is regarded as that part which is dependent on the sea state.

Many fundamental research programs in sea surface scattering and reverberation were carried out in the years since WW–II. One should keep in mind these so called fundamental efforts were not fundamental in the usual scientific context. For the most part, they were designed to accumulate information useful in the fields of anti–submarine or pro–submarine warfare rather than aimed at locating and understanding the physical factors which result in the observed spectrum of sea surface scatter. Regardless, much of the work was both seminal and pioneering (NDRC, 1946).

Among the first efforts at understanding the theory of sea surface scatter were undertaken by Eckart (1953). He considered the scattering of sound from a rough pressure release surface using the Helmholtz–Kirchoff integral (borrowed from the optics community), while neglecting the contribution of point scatterers located near the sea surface (*i.e.*, bubbles and biologics). The quantity $\mu = \exp(-2kh\sin\phi_g)$, is the amplitude reflection coefficient of a rough surface; the expression $2kh\sin\phi_g$ is known as the Rayleigh parameter, where k is the sonic wave number in water, h is the rms wave height for a gaussian distributed sea surface, and ϕ_g is the surface grazing angle. Thus, for acoustic wavelengths greater than the scale of roughness, the scattering strength of the sea surface is predicted to decrease with decreasing frequency.

23

For short wavelengths, the surface scattering strength is relatively independent of frequency (incoherent scattering dominates). This work was an extension of the problem first discussed by Lord Rayleigh (1877) in which the scattering of sound from a sinusoidal corrugated surface was theoretically investigated.

Urick and Hoover (1956) discussed the backscattering of sound from the sea surface, its measurement, causes, and application to the prediction of reverberation levels. Smooth curves representing their measurements are depicted in Figure 1.2. Their experiments, performed at 60 kHz, indicated that for grazing angles below 30°, the scattering strength was relatively flat (independent of grazing angle), but increased with increasing wind speed. Above about 50°, all wind speed cases showed an increasing scattering strength with grazing angle, and at normal incidence the scattering strength decreased with increasing wind speed. They contend that at low grazing angles and for wind speeds sufficient to cause wave breaking, the flatness of backscattering curves suggests that the roughness of the sea surface alone is not the cause of the scattering. They further speculated that the natural formation of bubbles or bubble layers play a role in the scattering of sound from the near surface layer, but at the time evidence of such a mixture layer had not been established.

Chapman and Harris (1962) used explosive charges to illuminate the sea surface and measured the surface backscatter at grazing angles between 15° to 40° in the frequency range 400 to 6400 Hz. The measurements were made over a 52 hour period in which the wind speed varied from 0 to 15 m/s; the sea state varied from 0 to 6. For wind speeds less than 7.5 m/s they observed general agreement with Eckart's predictions; that is, the backscattering strength was
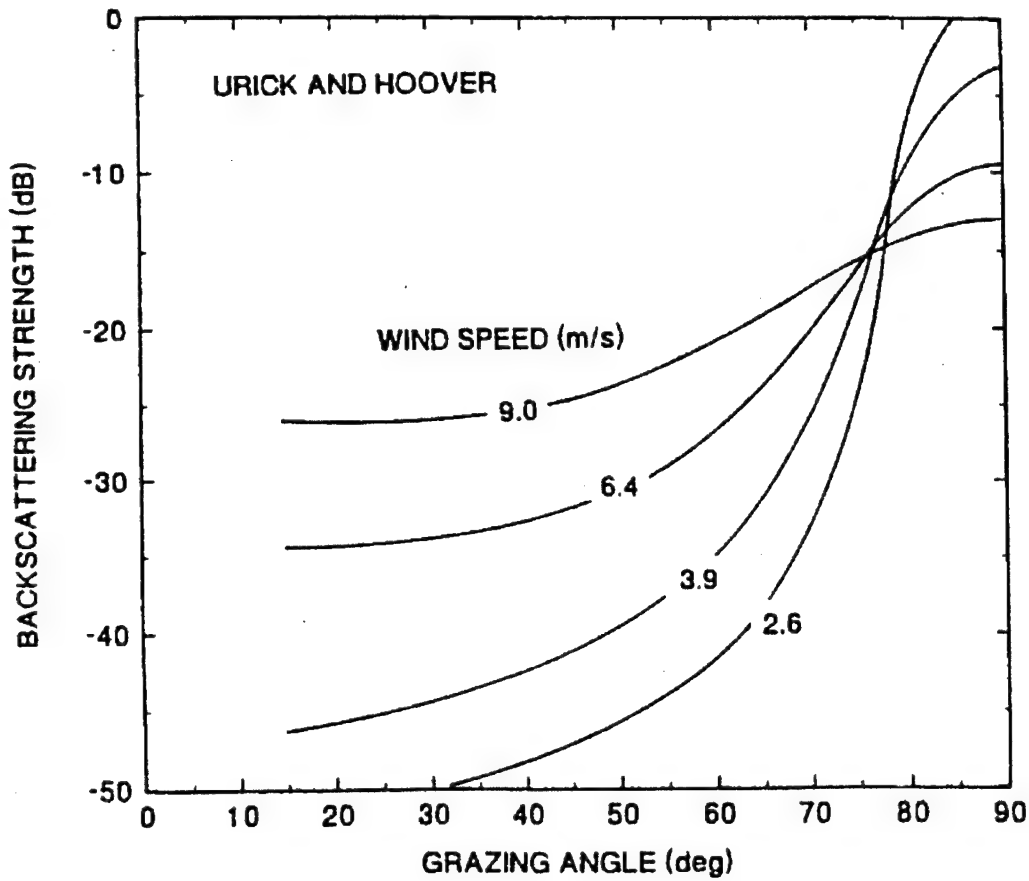
Figure 1.2: Smooth curves of the backscatter from the sea surface as a function of windspeed and grazing angle at 60 kHz (Urick & Hoover, 1956). They speculated that bubbles, or a bubble layer, were responsible for the increase in the scattering for increasing wind speed curves at the lower grazing angles. From McDaniel (1993).

relatively independent of frequency for low wind speeds. However, as the wind speed increased, high backscattering strengths were measured. The data were fitted to an empirical relation based on the Eckart model and referenced to a surface grazing angle of 30°:

$$SS = 3.3\eta \log \frac{\phi_g}{30} - 4.24 \log \eta + 2.6, \tag{1.5}$$

25

where $\eta = 158 \left(v f^{\frac{1}{3}} \right)^{-0.58}$; v is the wind speed in knots; f is the frequency in Hz; and ϕ_g is the grazing angle. They conjectured that the anomalously high returns were due to a subsurface layer of scatterers, probably of biological origin.

Because of the possible biological contamination, a follow up experiment was performed by Chapman and Scott (1964) in order to measure the sea surface backscatter over an extended range of frequencies (100 to 6400 Hz) and grazing angles ($\phi_g < 80°$). In this experiment, the wind speed ranged from 1 to 13 m/s with a mean sea swell of 1.8 m. For the lower wind speeds, the scattering returns were consistent with sea surface scatter—that is, the scattering of acoustic radiation from a surface whose scale of roughness is appreciably greater than the wavelength of the incident sound. At the lower wind speeds (*i.e.*, smaller significant wave heights), the data was not found to be dependent on frequency, consistent with Eckart's surface scattering model. Again, however, the higher wind speed cases showed general disagreement with the surface scattering theory.

The results predicted by Eq. (1.5) cannot be explained by the conventional perturbation or composite roughness models for surface backscatter, especially at shallow grazing angles and low frequencies where the measured scattering strengths are 10 to 100 times stronger (McDaniel, 1993), and it is not likely that advances in the rough surface scattering theories will bridge the gap. Evidently, an unaccounted source mechanism for sea surface backscatter exists, and it appears that this mechanism is present only for wind speeds high enough to cause waves to break. Thus, bubble clouds, layers, and plumes are

26

likely candidates.

1.5 Sea surface scattering: selected field experiments

In the late 1980s and early 1990s a series of tests of low frequency sonar experiments were performed (Critical Sea Tests, CST) in which one of the objectives was to measure boundary scattering strengths at frequencies below 1000 Hz and to investigate the dependence on various acoustical and environmental properties. One of the motivations to perform these tests was to address the observations made by Chapman and Harris (1962), hereafter CH. Ogden and Erskine (1994), like CH, used SUS (explosive) charge sources to insonify the sea surface during periods in which the sea state varied from 0 to 4.5. They performed direct path surface scattering measurements and found general disagreement with the CH empirical model for grazing angles between 10° to 30° and for wind speeds varying between 1.5 and 14 m/s at a center frequency of 70 Hz. However, for a frequency of 930 Hz, a wind speed dependence similar to the CH model was observed—particularly for the higher wind speeds.

Their results, illustrated in Figure 1.3, can be summarized as follows: For relatively calm seas at all frequencies and for rougher seas at the lower frequencies, the scattering strengths are reasonably well characterized by perturbation theory in which air–sea interface scattering is the dominant mechanism (Thorsos, 1990). In the transition region, in which the whitecap coverage of the sea changes from a few to commonly visible, the scattering levels are

27

difficult to predict with any accuracy. Presumably, a competition between interface scattering and the onset of scattering from bubble assemblages occurs. At higher wind speeds and higher frequencies, the CH empirical formula is found to be consistent with the field data. In this region, the frequency/wind speed/grazing angle dependence given by Eq. (1.5) and calculated using perturbation methods are radically different, strongly suggesting that some other mechanism plays a role.
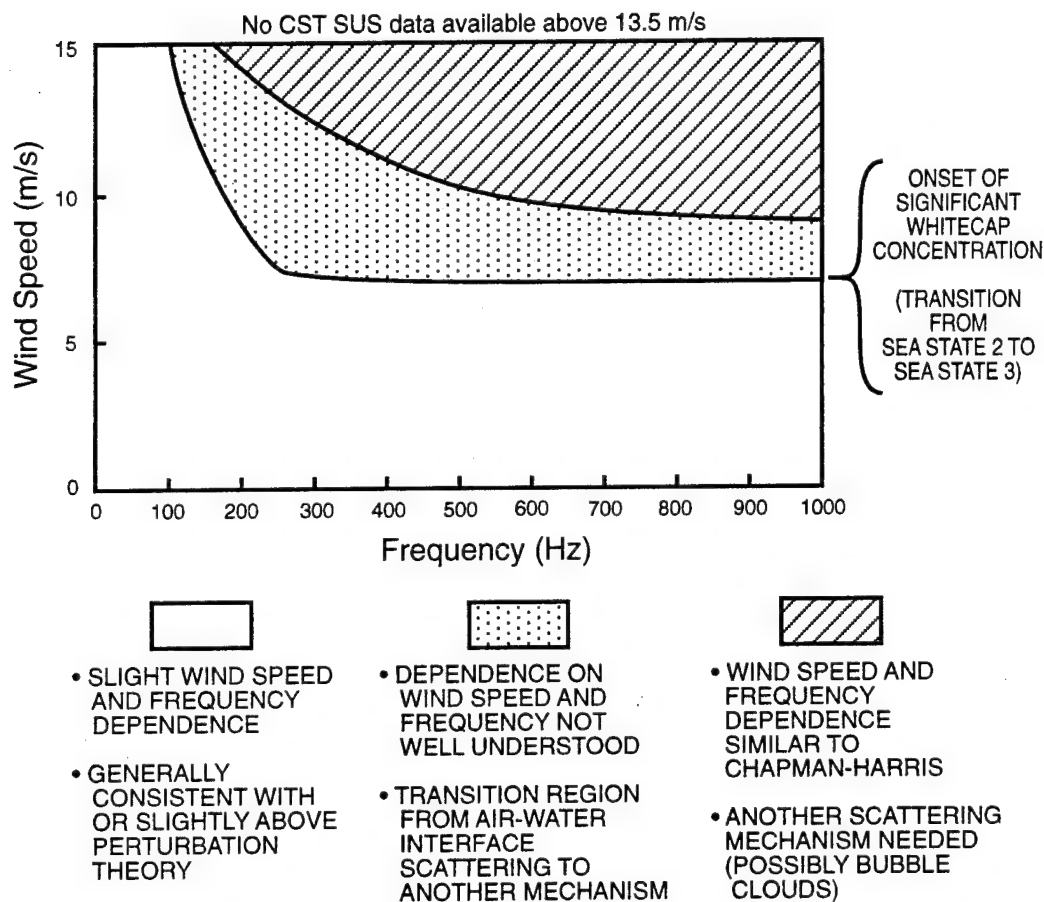
Figure 1.3: Summary of SUS surface scatter results. From Ogden and Erskine (1994).

In the Gulf of Alaska, Gauss *et al.* (1993) measured surface scattering for a range of significant wave heights (1.5 to 5 m) and very low grazing angles (between 1.5 to 3.5°) using a high resolution receiving array limited to frequencies below 1000 Hz. A vertical array consisting of 10 low frequency and 10 high frequency sources designed to emit 80 Hz bandwidth tones centered at 250 Hz, and 170 Hz bandwidth tones centered at 915 Hz, respectively was deployed at a depth of 150 m. They reported strong evidence of volume scattering (believed to be salmon) in the lower frequency band, and surface scattering for the upper frequencies. However, in the upper band, they also observed prominent, temporally discrete backscatter returns from the surface lasting less than 45 s (the scan repetition rate). The spatial character of these signals revealed strong, isolated features less than 10 m in size. Given the sea state, these transient scattering results are consistent with the spatial and temporal properties of newly formed bubble clouds such as those observed by Farmer and Vagle (1989) and Lamarre and Mellville (1992), and with the notion that such clouds might contribute to the scattering.

Adair and Huster (1992; 1993) managed to image the scattering strength of the upper 5 m of a large patch ($\sim 1\,\text{km}^2$) of the ocean surface using a long towed horizontal line array and conventional wideband processing techniques in an effort to characterize near–surface reverberation at wind speeds exceeding 7 m/s and for a grazing angles near 10°. Two types of sources were used: SUS charges, which yield high signal–to–noise images with 5 m^2 spatial resolution; and conventional projectors with higher repetition rates (6.7 and 20.1 s). Conventional sources were employed to achieve intermediate range resolution

29

on the order of $50\,\mathrm{m}^2$. The SUS experiment should be able to resolve and track the scattering from tenuous bubble *plumes*, which should be extended in space and persist for periods up to tens of minutes.

During periods of no breaking wave activity, they observed isolated bright targets consistent with the scattering strength, frequency response, and migration patterns expected from salmon (see Figure 1.4). Similar bright spots, although more numerous and more broadband, appeared during the high sea state tests. These are believed to be due to scattering from subsurface bubble ensembles since the images showed no ping–to–ping correlation (their lifetimes were less than $10\,\mathrm{s}$). The short lifetimes of the bright echoes are consistent with scattering caused by relatively short lived bubble clouds having void fractions on the order 10^{-4} to 10^{-3} and sizes on the order of $1\,\mathrm{m}$ or less. Although features greater than $100\,\mathrm{m}$ are shown on the image in Figure 1.4, they reported no long lived, high target strength events.

In a high frequency (3 to $80\,\mathrm{kHz}$) monostatic scattering experiment conducted during wave breaking activity in the North Sea, Nützel and Herwig (1993) and Nützel *et al.* (1994) observed normal incidence backscatter returning from the sea surface arriving in temporally and spatially discrete 'clumps.' The data was corrected for arrival time differences of the individual echoes due to the varying wave heights, strongly suggesting that bubble clouds were the dominant scattering targets. At $40\,\mathrm{kHz}$, and for a wind speed of $8.5\,\mathrm{m/s}$, the backscatter measurements indicated the presence of transient bubble clouds penetrating to depths of $2\,\mathrm{m}$; at $10\,\mathrm{m/s}$, the clouds penetrated to $5\,\mathrm{m}$; and at $14\,\mathrm{m/s}$, scattering from a continuous layer of bubbles was observed down to
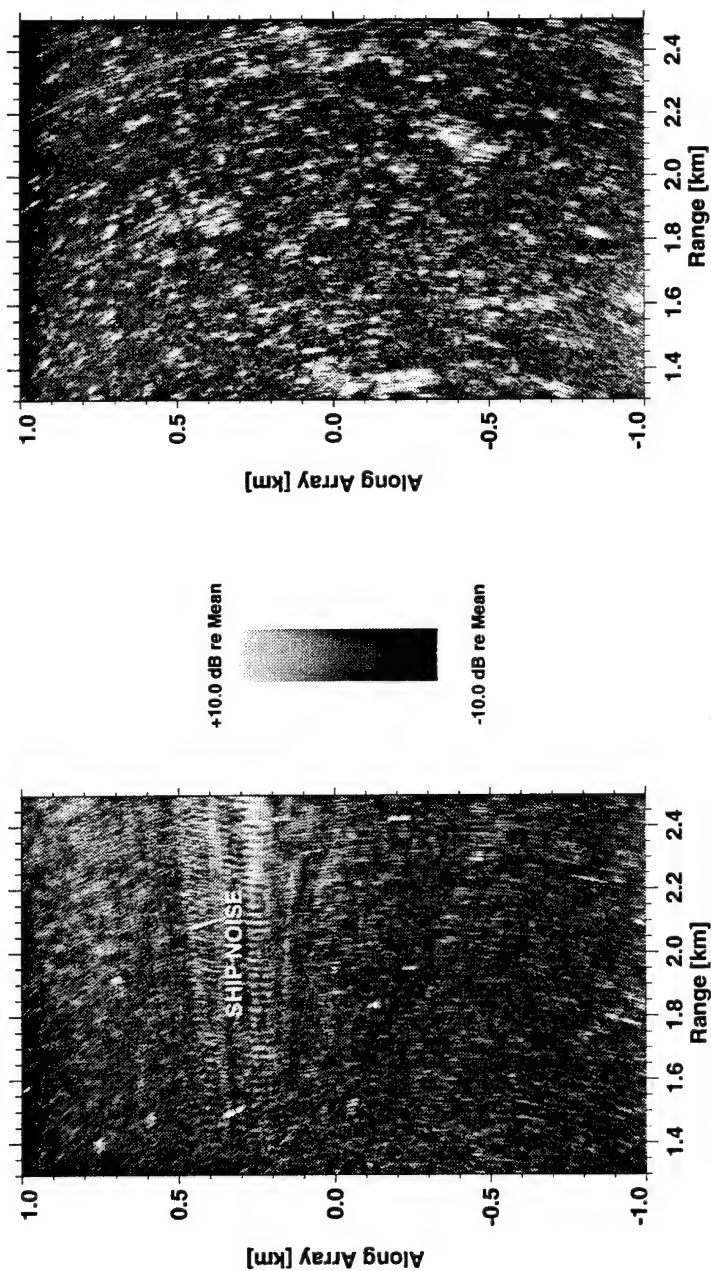
Figure 1.4: Sea surface scattering measurements in the upper 5 m of the ocean surface during CST-7. In the figure to the left, the wind speed was $U = 4.1$ m/s (significant wave height 2.2 m, no breaking waves). The average scattering strength in this image is -53 dB. Only a few events, believed to be salmon, exceed the average by +10 dB. In contrast, in the figure on the right, the wind speed is $U = 16.8$ m/s (wave height 5.0 m) and a great number of high target strength scattering events exceeding the average (-30 dB) by +10 dB are prevalent. The image resolution is 1 m in range and 0.005 radians in azimuth (120–1430 Hz). This figure was graciously provided by Aretè Associates (Miklovic *et al.*, 1995).

31

6 m and transient plumes at depths of 10 m. Although the acoustic frequencies used during this experiment are beyond the scope of the present study, the reported observations are, nevertheless, enlightening.

1.6   Sea surface scattering: modeling efforts

Prosperetti *et al.* (1993) and Sarkar and Prosperetti (1993) have modeled sub–kilohertz acoustic backscatter at shallow grazing angles ($< 20°$) from hemispherical, hemicylindrical, and hemispheroidal bubble plumes attached to a idealized plane sea surface. In their calculations, they obtain quantitative agreement with the CH curves using a wind speed dependent white–cap coverage ratio to populate the surface with a density of plumes. The plumes they examined had a radial footprint on the sea surface of 0.5 m, and void fraction in the range 10^{-3} to 10^{-1}; in the hemispheroidal case the extent of the cloud depth was made to vary by 1–5 radii. Both of these studies were based on a relatively simple acoustic propagation model for a bubbly liquid; a model that has been found to be in excellent agreement with the available data (Commander & Prosperetti, 1989; Lu *et al.*, 1990; Yoon *et al.*, 1991; Silberman, 1957; Cheyne *et al.*, 1995).

In Henyey's (1991) recent study, the well known Born approximation (a weak scattering theory) was used to estimate the acoustic backscatter from the larger tenuous bubble plumes ($\beta < 10^{-5}$, depths and lengthscales on the order of 10 m, and lifetimes of tens of minutes to hours) beneath the sea surface. In another study by McDonald (1991), vertically oriented low–void fraction

bubble plume cylinders with rigid boundary conditions were modeled. While both of these efforts were able to show general agreement with the CH empirical equation, they failed to obtain the precise grazing angle dependence obtained by CH. Furthermore, it is not clear, given the available evidence, that any of the models which demonstrate agreement with the Chapman–Harris curves are accurate.

Many investigators currently believe that the global features of the frequency and grazing angle dependence of sea surface backscatter are more closely influenced by the tenuous (low–void fraction) clouds, which occupy a greater fraction of the surface for longer periods of time. This position is not disputed here, for it is to a large extent based on the result of assumptions regarding the statistics and anatomy of oceanic bubble clouds. However, observations of long term, isolated scatterers have not been measured acoustically as would be expected from a tenuous bubble distribution. It seems clear that the high–sea state surface scattering observations that are correlated with spatially and temporally discrete high target strength scatterers (*i.e.*, "spiky returns") are best modeled using short–lived, near surface bubble clouds. Such clouds might possess length scales ranging from 0.1 to 2 m, and void fractions ranging from 10^{-5} to 10^{-2}. They would exist on the order of 10 seconds at depths ranging from just below the surface to 8 m. Is it possible for such small, shallow clouds to generate sub–kilohertz target strengths[5] in excess of -5 dB?

---

[5]By definition, a 1 m–diameter perfectly reflecting sphere has a target strength of -12 dB.

1.7 Resonance scattering from bubble clouds

Substantial laboratory and field evidence suggests that acoustically compact ($ka < 1$), high void fraction bubble clouds oscillate collectively. When excited, these clouds radiate low–frequency sound that possesses spectral features dictated by the normal modes of the cloud; they scale with the cloud dimensions and the mixture sound velocity. It therefore seems reasonable to assume that such a cloud would scatter sound in a similar fashion. This notion was vigorously promoted in the works of Carey *et al.* (1985; 1988; 1993) and Prosperetti *et al.* (1985; 1988b; 1988a; 1990; 1993). However, until recently this view had not been experimentally verified for sub–kilohertz frequencies. This dissertation discusses an experiment, and the associated modeling effort, which demonstrates that acoustically compact bubble clouds are effective scatters of sound.

The so called "Lake Seneca Experiment" took place in the summers of 1989 and 1990 at the NUWC fresh–water sonar test facility at Lake Seneca, NY. It was a multi–institutional effort, with contributions from researchers at NUWC, NCPA, BB&N, and the University of Connecticut[6]. The purpose of this experiment was to measure the frequency–dependent backscatter from a well–characterized bubble cloud in the absence of boundaries and for known propagation conditions. This experiment was not designed to duplicate the oceanic environment. Rather the effort was designed to obtain data to test and validate the collective oscillation model hypothesis. The bubble cloud

---

[6]NUWC = Naval Underwater Warfare Center; NCPA = the National Center for Physical Acoustics at the University of Mississippi; and BB&N = Bolt Berenek and Newman

was generated using a transiently–vented compressed air source submerged to 91 m. The rising bubble cloud was insonified using a highly–directional parametric array sound source. Although data was obtained for frequencies ranging from 250 Hz to over 10 kHz, the interest in this effort is primarily in the scattering response of bubble clouds at sub–kilohertz frequencies, where low–frequency sonar systems operate, and much of the existing field data has been obtained. The estimated cloud *in situ* properties were known accurately enough to effectively model the scattering response for frequencies near the lowest–order (monopole) resonance. At these low frequencies, the cloud is acoustically compact, and the details of its shape are unimportant. In essence, the cloud behaves like a volume scatterer and the resonance response is that of a monopole or equivalent pulsating sphere. In this limit, the monopole resonance frequency and target strength are described by simple analytical expressions that effectively highlight the underlying physics and facilitate experimental confirmation.

For the sake of clarity, this dissertation is subdivided into the three parts. Part–I offers a development of the collective oscillations model and the scattering from a high volume fraction bubble cloud in the low–frequency limit, where the resonance of the individual bubbles are much higher than the driving frequency and the effective medium approximation is valid. Following this development, which is derived from the classical literature, theoretical expressions for the frequency–dependent acoustic backscatter from a spherical bubble cloud in the free field are presented. It is important to note that Part I of this dissertation is devoted solely to the modeling of bubble cloud scattering

in the free field. In Part II, the Lake Seneca bubble cloud scattering experiment and associated analysis is described and compared with the model. Finally in Part III, a model of the low–frequency monopole scattering from a bubble cloud near the sea surface is presented. Using the method of images, the predicted low–frequency backscatter target strength is computed as a function of grazing angle, frequency, and wind speed. Once again, the low–frequency, acoustically compact (monopole) scatterer assumption results in expression for which the underlying physics becomes evident. Trends in the calculations are described and comparison is made with field measurements of Adair and Huster (1992; 1993).

Several tacit assumptions will be made in the development of the models herein. First, the bubble cloud is spherical and consists of a mean void fraction mixture. That is, the boundaries of the cloud are well defined, and the distribution of bubbles within the sphere is uniform. Furthermore, the cloud is embedded in a fluid free of other inhomogeneities (i.e., the presence of a bubble layer or other clouds will not be considered). The bubbles, and the cloud, are fixed both temporally and spatially. Although these assumptions are nonphysical from an oceanographic standpoint, the goal here is to consider the scattering response from a single cloud beneath the sea surface, and thus the 'ideal' case will be entertained.

The goal of this dissertation is not to resolve the discrepancies between the sea surface scattering models and the field measurements. Rather, the interest is in the physics of scattering of sound from an acoustically compact bubble cloud both in the proximity and in the absence of the sea surface. The

contribution due to scattering from an ensemble of bubble clouds will not be considered. It is a fact that bubble clouds and plumes are produced at the sea surface during wave breaking activity. It is also well established that the generation of these clouds releases a significant amount of acoustic energy into the ocean concentrated in the frequency range 20 to 2000 Hz. Is it plausible then that the presence of these clouds near the sea surface contributes to the overall backscatter observed during wave breaking?

Part I

Acoustic scattering from bubble clouds in the absence of boundaries: Theory

Chapter 2

Propagation of sound in a bubbly mixture

2.1 Introduction

The propagation of acoustic waves in fluids is highly influenced by properties such as absorption and scattering. In fact, for a two–phase fluid consisting of water mixed with a sufficiently dense concentration of air bubbles, the sound velocity is frequency dependent. This dependence is a consequence of the marked change of the fluid's natural compressibility when mixed with bubbles (Brekhovskikh & Lysanov, 1991). It will be shown that for frequencies below the fundamental resonance of the individual bubbles, the sound speed can be lowered dramatically. This dependence is solely on the fractional volume or void fraction of bubbles in the fluid (Wood, 1941). The physics behind the lowering of the sound speed is that the bubbly region possesses a density

39

close to that of the liquid, but a much greater compressibility. The free gas establishes the compressibility, while the water provides inertia. If one recalls that the sound speed in a fluid medium is proportional to the square–root of the inverse product of these quantities, the physical basis for the sound speed defect becomes obvious.

Two models will be considered. First, in the low frequency quasi–static limit a model for the sound propagation in a bubbly fluid similar to that originally proposed by Wood (1941) will be presented. He derived the mixture sound speed based on the assumption that bubbles pulsate isothermally; a good approximation for extremely small bubbles driven at low frequencies. In addition, Wood neglected attenuation.

A second, dispersive model will be presented which spans a much greater frequency range (above and below the bubble resonance frequency) and accounts for energy losses through viscous, thermal, and acoustic damping (Commander & Prosperetti, 1989; Lu *et al.*, 1990). The basis of the dispersion model can be traced back to Spitzer's early work outlined in the classic text *Physics of Sound in the Sea* (1943). In his study, the bubbles oscillations were considered in the adiabatic limit. In the present work, the methodology presented in Commander and Prosperetti (1989) will be followed. The bubble dynamics are treated rigorously so that both the damping 'constant' and the polytropic exponent of the gas in the interior of the bubble are frequency dependent. In both cases the *effective* (*i.e.*, mixture) properties of the medium will be denoted by the subscript e.

2.2 Sound speed in bubbly liquids — Low Frequencies

In the quasi–static limit, the effective medium approximation is obtained by applying an 'order of magnitude' analysis. Let ρ and ρ_g be the liquid and gas densities in a fixed *suspension* of gas bubbles in liquid; by *suspension*, it is meant that there is no relative motion between bubbles and liquid. The bubbles are assumed small and sparsely distributed, but sufficiently densely populated on some macroscopic scale that they can be regarded as determining the properties of a single phase *continuum* of density ρ_e.

Let β be the void fraction (or concentration) of bubbles (*i.e.*, the ratio of the total gas volume to the total mixture volume). The effective density is defined by

$$\rho_e \equiv (1 - \beta)\rho + \beta\rho_g. \qquad (2.1)$$

Because of the assumption of no relative motion, the mass of the gas in a unit mass of mixture must be constant. The volume of unit mass of mixture is $1/\rho_e$, the fraction of this volume occupied by bubbles is β/ρ_e, and the mass of gas in this fraction is $\beta\rho_g/\rho_e$ (Crighton *et al.*, 1992). Hence,

$$\frac{\beta\rho_g}{\rho_e} \equiv \text{Constant}. \qquad (2.2)$$

Furthermore, suppose a *quasi*-uniform pressure exists everywhere within the mixture. This assumption is valid only at very low frequencies—frequencies

41

far below the bubbles' resonance frequency, ω_0, as will be shown in Section 2.3. As usual, the inverse square of the sound speed is given by the derivative of the density with respect to pressure (Pierce, 1989),

$$
\begin{aligned}
c_e^{-2} &= (1-\beta)\frac{d\rho}{dp} + \beta\frac{d\rho_\mathrm{g}}{dp} + (\rho_\mathrm{g} - \rho)\frac{d\beta}{dp} \tag{2.3} \\
&= \frac{1-\beta}{c^2} + \frac{\beta}{c_\mathrm{g}^2} + (\rho_\mathrm{g} - \rho)\frac{d\beta}{dp}. \tag{2.4}
\end{aligned}
$$

Now consider the following expression:

$$
\beta\rho_\mathrm{g} = \left(\frac{\beta\rho_\mathrm{g}}{\rho_e}\right)\rho_e, \tag{2.5}
$$

which, upon taking the derivative with respect to pressure and using the definition given by Eq. (2.2) yields,

$$
\rho_\mathrm{g}\frac{d\beta}{dp} + \frac{\beta}{c_\mathrm{g}^2} = \left(\frac{\beta\rho_\mathrm{g}}{\rho_e}\right)\frac{d\rho_e}{dp}, \tag{2.6}
$$

and finally,

$$
\frac{d\beta}{dp} = \left(\frac{\beta}{(1-\beta)\rho + \beta\rho_\mathrm{g}}\right)\frac{d\rho_e}{dp} - \frac{\beta}{\rho_\mathrm{g}c_\mathrm{g}^2}. \tag{2.7}
$$

Substitution of the preceding equation into Eq. (2.4) gives, after some algebraic manipulation,

$$
\frac{1}{c_e^2} = \frac{d\rho_e}{dp} = \frac{(1-\beta)^2}{c^2} + \frac{\beta^2}{c_\mathrm{g}^2} + \beta(1-\beta)\left\{\frac{\rho^2 c^2 + \rho_\mathrm{g}^2 c_\mathrm{g}^2}{\rho\rho_\mathrm{g}c^2 c_\mathrm{g}^2}\right\}. \tag{2.8}
$$

For the case where β is not too large, or too small, the first two terms

42

in Eq. (2.8) can be neglected, and the final term is approximated yielding the effective sound speed

$$c_e^2 \approx \frac{\rho_g c_g^2}{\beta(1-\beta)\rho},$$ (2.9)

since $\rho_g c_g^2 \ll \rho c^2$.

The sound speed in the gas is $c_g^2 = \kappa P_\infty/\rho_g$ (Kinsler *et al.*, 1982), where κ is the polytropic exponent of the gas, and P_∞ is the ambient static pressure in the fluid far from the mixture. For isothermal conditions, $\kappa = 1$ and for adiabatic conditions $\kappa = \gamma$, where γ is the ratio of specific heats. A more rigorous model is presented in the next section which describes the the frequency dependence of the polytropic exponent explicitly. Substitute the gaseous sound speed into Eq. (2.9) to arrive at the well known Wood expression (1941) for the speed of sound in a bubbly mixture in the isothermal and adiabatic limits, respectively:

$$c_e \approx \sqrt{\frac{P_\infty}{\beta(1-\beta)\rho}},$$ (2.10a)

$$c_e \approx \sqrt{\frac{\gamma P_\infty}{\beta(1-\beta)\rho}}.$$ (2.10b)

It will be shown in Section 2.3, that these expressions are valid only for frequencies well below the bubble resonance frequency. It should also be noted that for extremely small β, this approximation exceeds the sound speed in the host liquid—a limitation not imposed by Eq. (2.8). For example, in seawater the Wood's equation is valid for $\beta > 3 \times 10^{-4}$; for smaller values it rapidly

43

exceeds the liquid sound speed.

Figure 2.1 clearly illustrates one of the most remarkable features of sound propagation through bubbly fluids. It is clear that the sound speed in such a mixture of water and air can be much lower than either of the constituents over a large range of β—as low as $20\,\text{m/s}$. The calculation is shown for both isothermal ($\kappa = 1$) and adiabatic ($\kappa = 1.4$) bubble behavior using Eq. (2.10a) and Eq. (2.10b). The experimental data is from Karplus (1958) and Gouse and Brown (1964) and obtained at frequencies of $0.5\,\text{kHz}$ and $1.0\,\text{kHz}$. Notice that these measurements correspond to the isothermal model, indicating that the heat transfer from the liquid to the bubbles is enough to maintain constant temperature inside the bubbles.

2.3 Sound speed in a bubbly medium — dispersion

The concern here is with the frequency dependence, or dispersion, of sound waves propagating in a two–phase mixture of air bubbles in water. Bubbles are relatively high–Q simple harmonic oscillators and when driven at their fundamental resonance are both strong scatters and absorbers of sound. Actually, sound is attenuated at all frequencies, but at resonance the attenuation reaches a maximum. This indicates that the effective speed of sound has a significant imaginary component which was not addressed in the previous section. Furthermore, the response of the bubble is not uniform over the range of frequencies spanning the bubble resonance frequency. When the acoustic forcing

44
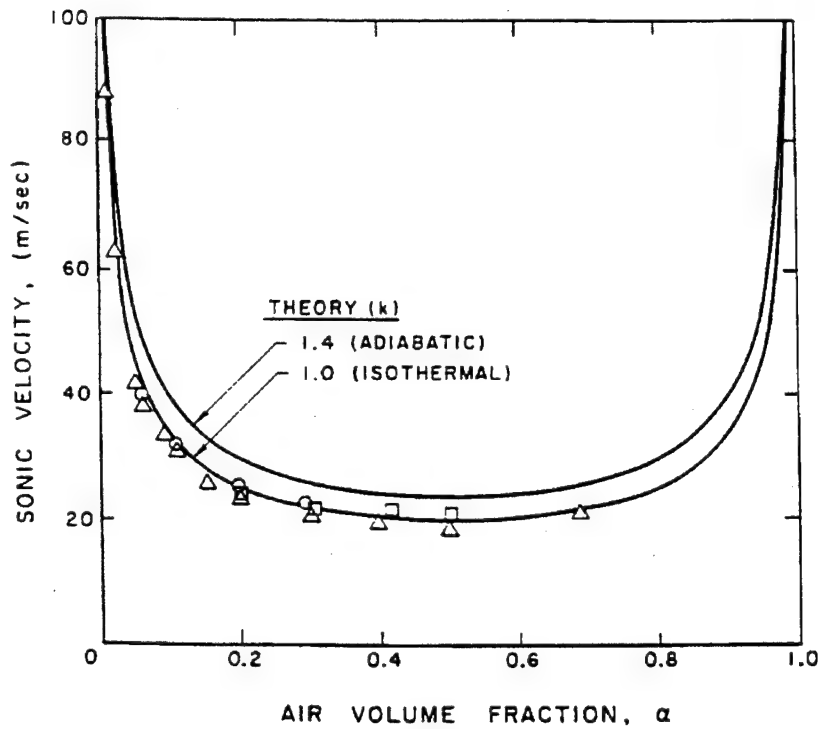
Figure 2.1: Sound speed in a bubbly liquid at atmospheric pressure for $\kappa =$ 1.0 and 1.4 as a function of the void fraction α. Experimental data from Karplus (1958) and Gouse and Brown (1964) for frequencies of 1 kHz ($\circ$), 0.5 kHz ($\square$), and extrapolated to zero frequency ($\triangle$). From Brennen (1995).

frequency is lower than the resonance frequency, the a bubble will pulsate in phase with the driving force. However, for frequencies exceeding the resonance frequency, the oscillations occur out of phase, and thus the bubble 'appears' stiffer, leading to a corresponding increase in the mixture sound speed.

2.3.1 Theory

In order to understand how harmonic waves of any type propagate, one commonly solves a set of linearized conservation equations which ultimately lead

45

to the Helmholtz or 'wave' equation. To follow in suit, first the conservation equations for a bubbly mixture will be defined. To begin, consider a bubbly mixture as an effective medium with density given by Eq. (2.1). Formally, the void fraction is described by

$$\beta(\mathbf{x}, t) \;\; = \;\; \frac{4\pi}{3} \int_0^\infty R^3(a; \mathbf{x}, t) f(a; \mathbf{x}) da. \tag{2.11}$$

Here, R is the instantaneous bubble radius at position $\mathbf{x}$ and time t having equilibrium radius a. The quantity $f(a; \mathbf{x}) da$ is the distribution function of the number of bubbles per unit volume with equilibrium radius between a and $a + da$. Note: for a monodispersed bubble population of radius R_o, $f(a; \mathbf{x}) = \eta \delta(a - R_o)$, where δ is the Dirac delta function, and η is the number of bubbles per unit volume. For simplicity, the spatial dependence of the bubble distribution is assumed to be fixed, but random in spacing. Furthermore, the bubble distribution is assumed monodispersed so that

$$\beta = \frac{4}{3} \pi R_o^3 \eta. \tag{2.12}$$

The averaged continuity and momentum equations applied to bubbly fluids having small β are (Commander & Prosperetti, 1989)

$$\frac{1}{\rho c^2} \frac{\partial P}{\partial t} + \nabla \cdot \mathbf{u} \;\; = \;\; \frac{\partial \beta}{\partial t}, \tag{2.13a}$$

$$\rho \frac{\partial \mathbf{u}}{\partial t} + \nabla P \;\; = \;\; 0, \tag{2.13b}$$

where $\mathbf{u}$ and P denote the averaged center–of–mass velocity and pressure fields

in the mixture. In order to consider the averaged quantities of the mixture, the nature of the interaction of sound waves with individual bubbles must be determined.

2.3.2 Linearized single–bubble dynamics

Bubble dynamics is a robust field both in terms of theory and experiment. Its origins can be traced to original works by Lord Rayleigh (1877). The individual bubble is well known to be a simple harmonic oscillator for which the time dependent radial oscillations can be described by the Keller equation (Keller & Kolodner, 1956)

$$(1 - \frac{\dot{R}}{c})R\ddot{R} + \frac{3}{2}(1 - \frac{\dot{R}}{3c})\dot{R}^2 = \frac{1}{\rho}(1 + \frac{\dot{R}}{c} + \frac{R}{c}\frac{d}{dt})(p_B - P), \qquad (2.14)$$

where $R(t)$ is the instantaneous radius of the bubble; P is the pressure at the bubble location in its absence; and p_B is the pressure at the bubble interface. Here, the bubble response is assumed to be linear and after making suitable approximations to Eq. (2.14) it can be shown that the radius of, and internal pressure in, the bubble are given by

$$R = R_o(1 + X), \quad p = p_e(1 - \Phi X), \qquad (2.15)$$

where R_o and p_e are the equilibrium values (Prosperetti *et al.*, 1988).

$$p_e = P_\infty + \frac{2\sigma}{R_o} \qquad (2.16)$$

47

where σ is the surface tension, and

$$\Phi = \frac{3\gamma}{1 - 3(\gamma - 1)i\chi\left\{(i/\chi)^{1/2}\coth[(i/\chi)^{1/2}] - 1\right\}}. \qquad (2.17)$$

The preceding equation arises from a solution of the thermomechanical behavior of spherical gas bubbles with the additional assumption of small amplitude oscillations (Prosperetti *et al.*, 1988), with γ denoting the ratio of specific heats in the gas. The thermal penetration length is given by

$$\chi = \frac{D}{\omega R_o^2}, \qquad (2.18)$$

in which D is the thermal diffusivity of the gas (Lu *et al.*, 1990; Commander & Prosperetti, 1989; Prosperetti, 1991). It is possible to show that the response of the bubbles to the harmonically oscillating averaged pressure field is given by

$$X = -\frac{(P - P_\infty)/\rho R_o^2}{\omega_0^2 - \omega^2 + 2ib\omega}, \qquad (2.19)$$

where ω_0 is the natural frequency of the bubble, and b is the effective damping 'constant' given by

$$\omega_0^2 = \frac{p_e}{\rho R_o^2}\left(3\kappa - \frac{2\sigma}{R_o p_e}\right) \qquad (2.20a)$$

$$b = \frac{2\mu}{\rho R_o^2} + \frac{p_e}{2\rho\omega R_o^2}\Im(\Phi) + \frac{\omega^2 R_o}{2c}. \qquad (2.20b)$$

Here, μ is the liquid viscosity, and $\Im(\Phi)$ returns the imaginary portion of Φ.

Neglecting the effects of surface tension in Eq. (2.20a), the well known Minneart (angular) resonance frequency is readily obtained for the bubble (Minneart, 1933)

$$\omega_0 \cong \frac{1}{R_o} \left(\frac{3\kappa P_\infty}{\rho} \right)^{\frac{1}{2}}. \tag{2.21}$$

Thus the resonance frequency is proportional to the inverse of the radius and in water at atmospheric pressure (*i.e.*, near the surface) is well approximated by the simple expression $f_o \approx 3.2/R_o$ in Hz.

In Eq. (2.20b) the damping term, b, is a frequency dependent complex quantity which accounts for viscous, thermodynamic, and acoustic losses; κ again is the frequency dependent polytropic exponent (Prosperetti, 1991),

$$\kappa = \Re(\Phi)/3. \tag{2.22}$$

A graph of its values for a bubble of radius $R_o = 500\,\mu$ m is shown in Figure 2.2. It is interesting to note that the polytropic exponent approaches unity (*i.e.*, the isothermal limit) well below the bubble resonance frequency ($f_0 \approx 6.4\,$kHz), and its adiabatic value of $\gamma = 1.4$, the ratio of specific heats for a diatomic gas, at higher frequencies. It seems that only in the extreme limits does the gas in the bubble portray purely isothermal or adiabatic thermodynamical behavior. Table 2.1 lists values of the physical constants and environmental parameters used in the calculations presented in this section.
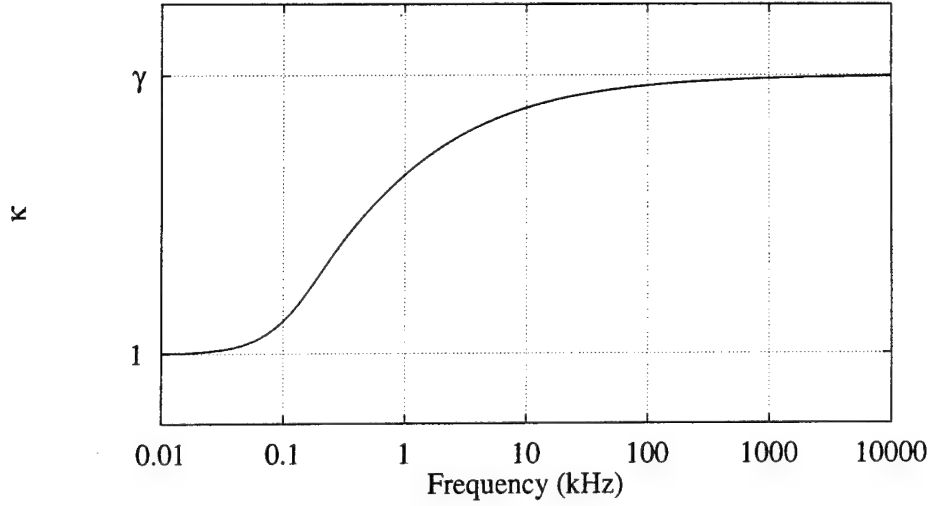
Figure 2.2: Polytropic index versus frequency for a $500\,\mu$ m radius bubble.

2.3.3 Effective wave equation

The effective wave equation in the bubbly fluid is obtained by eliminating the velocity field from Eq. (2.13a) and (2.13b), using Eq. (2.12) and (2.19). After linearizing (d'Agostino & Brennen, 1983; Commander & Prosperetti, 1989), the wave equation takes the following form:

$$\nabla^2 P + k_e^2(P - P_\infty) = 0, \tag{2.23}$$

ρ	1024	kg/m^3	c	1500	m/s
ρ_g	1.2	kg/m^3	c_g	330	m/s
P_∞	10^5	Pa	T	18	°C
γ	1.4		σ	7.2	N/m
μ	0.001	Pa·s			

Table 2.1: Physical parameters used in this section.

where $k_e = \omega/c_e$ is the effective wave number in bubbly mixture, and c_e is the effective sound velocity. The dispersion relation obtained is

$$k_e^2 = \frac{\omega^2}{c^2} + \frac{4\pi\eta R_o \omega^2}{\omega_0^2 - \omega^2 + 2ib\omega}. \qquad (2.24)$$

This wave equation (Eq. 2.23) describes the interesting phenomena alluded to earlier. Clearly the effective wave number in the mixture is frequency dependent and complex. Thus one can expect a maximum in the attenuation at the bubble resonance frequency. For frequencies below bubble resonance, the ω_0 term in the denominator of Eq. (2.24) dominates yielding a wave number proportional to the driving frequency, and hence an effective sound speed relatively independent of frequency.

The ratio of the sound speed in the liquid to the speed of sound in the mixture is obtained by dividing Eq. (2.24) by $k^2 = \omega^2/c^2$ yielding,

$$\frac{c^2}{c_e^2} = 1 + \frac{4\pi c^2 \eta R_o}{\omega_0^2 - \omega^2 + 2ib\omega}. \qquad (2.25)$$

Then for frequencies well below the bubble resonance frequency, the mixture sound velocity can be approximated by

$$c_e^{-2} \approx \frac{4\pi\eta R_o}{\omega_0^2} = \frac{3\beta}{\omega_0^2 R_o^2}, \qquad (2.26)$$

neglecting the damping term. Substitution of Eq. (2.12) and (2.21) into the preceding approximation yields $c_e = \sqrt{\kappa P_\infty/\beta\rho}$, which resembles our previous approximation Eq. (2.9) to within a factor of $(1-\beta)^{-1/2}$, reinforcing our earlier

51

assumption that below the bubble resonance frequency the mixture sound speed in dependent only on the void fraction.

Let the ratio of liquid sound speed to effective sound speed in the mixture be $c/c_e = u + iv$. Then the phase velocity in the mixture is $V = c/u$ rather than $\Re(c_e)$, because the time and spatial dependence of the harmonic waves in Eq. (2.23) are described by

$$\exp(ik_e x - i\omega t) = \exp(-\omega\frac{v}{c}x)\exp(i\omega(\frac{u}{c}x - t)). \qquad (2.27)$$

In the low frequency limit, the square of the phase velocity V is essentially equivalent to the previously derived expression (Eq. 2.9) and (2.26). The fact that the effective medium expressions, k_e and c_e, are complex indicates that sound propagation in the mixture is exponentially attenuated. The attenuation coefficient, $\mathcal{A} = 20(\log_{10} e)(\omega v/c)$, is attributable to the viscous, thermal, and acoustic energy loss mechanisms which affect the bubble as given in Eq. (2.20b).

2.3.4 Calculations and experimental results

To perform the calculations, codes based on the equations in (Commander & Prosperetti, 1989) and (Lu *et al.*, 1990) were originally written in *Mathematica* and tested using the data sets from these papers and compared to the figures in their papers. To improve the performance vastly, the codes were later cast in the C and C++ programming languages and executed on both Sun workstations and Apple Macintosh computers. Special attention was paid to

any calculation involving complex arithmetic. To evaluate these expressions ($e.g.$, $\sqrt{(z)}$, z^{-1}, etc.), standard techniques were used (Abramowitz & Stegun, 1972).

In Figure 2.3, the frequency dependent phase velocity and attenuation are plotted for a monodispersed bubble distribution of radii $500\,\mu$m, and for $\beta = 10^{-5}, 10^{-4}$, and 10^{-3}. The upper set of curves represent the phase speed in the mixture. For the majority of frequencies below the bubble resonance ($i.e.$, the sharp dip), the sound velocity asymptotes as predicted by the Wood's equation (Eq. 2.9) and is nearly flat. The bubble resonance frequency predicted by the Minneart expression (Eq. 2.21) for a $500\,\mu$m bubble is approximately 6.4 kHz. In Table 2.2, a comparison of the limiting forms for the sound speed is given. This reinforces the statement made earlier that for frequencies well below the bubble resonance the sound speed in the mixture is dependent only on the void fraction, and not the individual bubbles $per\ se.$

β	Wood's Eq.	Eq. (2.8)	Eq. (2.26)
10^{-5}	—	1363 m/s	1359 m/s
10^{-4}	988 m/s	850 m/s	841 m/s
10^{-3}	313 m/s	319 m/s	314 m/s

Table 2.2: Comparison of sound speed as given by Wood's equation (Eq. 2.9), Eq. (2.8) and the dispersive phase speed model (Eq. 2.26) evaluated at 100 Hz.

The 'supersonic' region following the bubble resonance broadens with increasing void fraction and is due to the bubbles pulsating out of phase with the pressure disturbance. This causes the mixture to appear stiffer, and hence the corresponding increase in the mixture sound velocity is observed. Well above the bubble resonance frequency, the phase speed asymptotes to its bub-
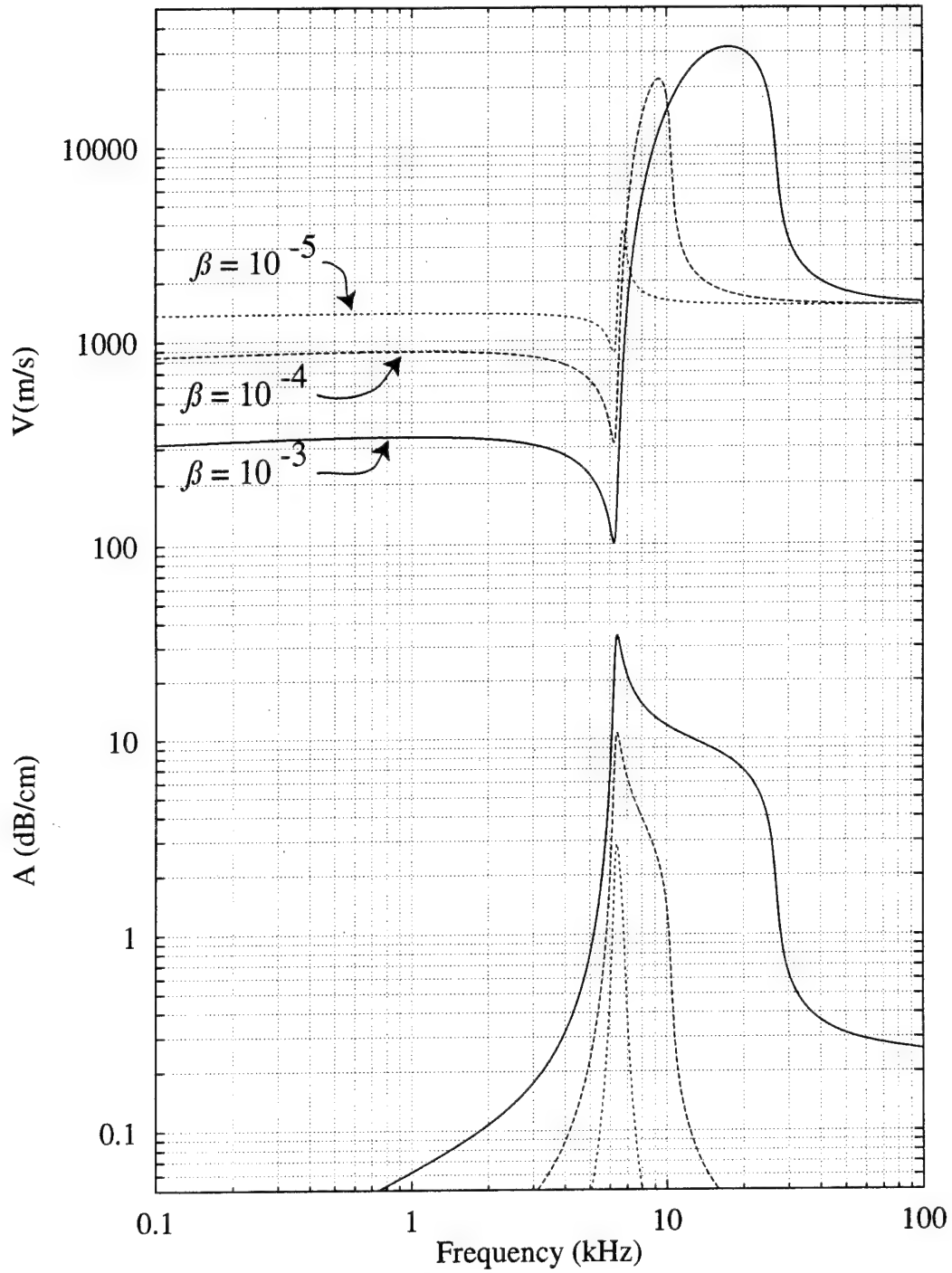
Figure 2.3: Phase speed (upper) and attenuation (lower) versus frequency for $\beta = 10^{-5}$, 10^{-4}, and 10^{-3}, and bubbles of radius $R_o = 500\,\mu\,\mathrm{m}$.

54

ble free value of c in the liquid. The attenuation is shown in the lower trio of curves, the peak in these curves occurs at the fundamental bubble resonance frequency. It is clear that the attenuation increases as the number density of bubbles increases, as one would expect.

For a given void fraction, increasing or decreasing the bubble radius has the affect of shifting the sharp dip at resonance in the phase speed and the peak in the attenuation curve to the left or right, respectively, as illustrated in Figure 2.4 for $\beta = 10^{-3}$ and bubble radii of 1.1 mm and 0.1 mm.
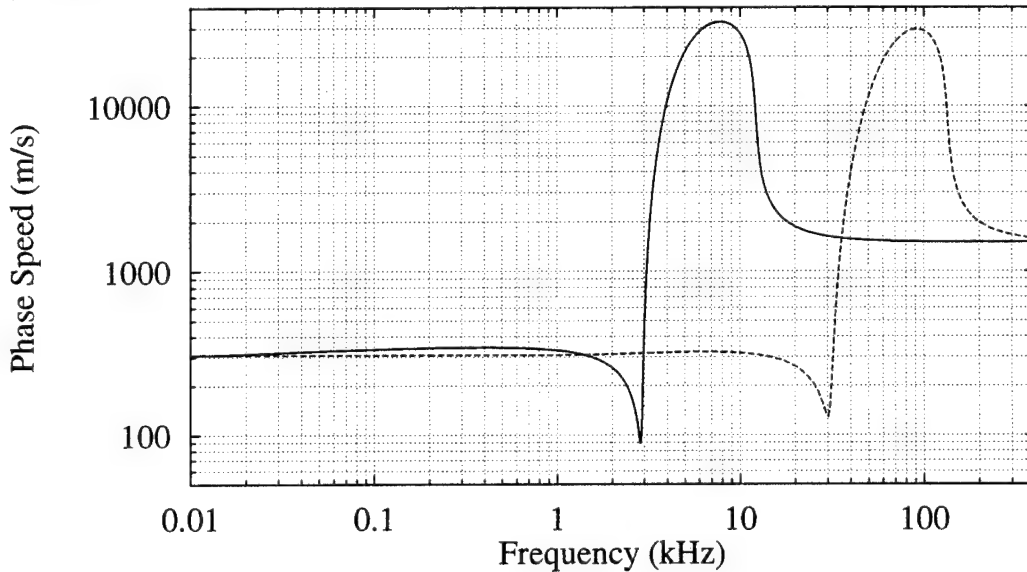
Figure 2.4: Phase speed versus frequency for $\beta = 10^{-3}$, and bubbles of radius $R_o = 1.11$ mm and $R_o = 0.1$ mm.

Silberman (1957) was one of the first to measure the sound speed and attenuation in bubbly mixtures. He filled a rigid cylinder with fresh water and created bubbles by forcing air through hypodermic needles being careful to maintain the water height and void fraction in the tube. Assuming the top and bottom of the tubes were pressure release, standing waves could be

set up in the cylinder well below the tube cut–off frequency. For a given driving frequency, the nodes (or pressure minima) were measured by lowering a hydrophone down the axis of the tube at the following positions $0, \lambda_e/2, \lambda_e$, etc., where λ_e is the sonic wavelength in the mixture. Using this information he calculated the mixture sound speed in the tube by multiplying the measured wavelength by the driving frequency. Below the bubble resonance frequency, his measurements were found in good agreement with the models proposed by Wood (Wood, 1941) and Spitzer (1943).

The attenuation due to the mixture was deduced by taking the ratio of the pressure amplitude measurements made at the anti–nodes near the driving transducer (*i.e.*, $\mathcal{A} = log_{10}(P_1/P_2)/(x_2 - x_1)$). Silberman's data compares favorably with Spitzer's classic effective sound speed model outlined in *Physics of Sound in the Sea* (NDRC, 1946). Spitzer's dispersion model assumes that bubbles behave adiabatically, which is reasonable for the relatively large bubbles sizes ($R_o > 1\,\mathrm{mm}$) in Silberman's experiment. For smaller bubbles, however, this approach cannot be expected to be accurate, especially since the radial pulsations are closer to isothermal at low frequencies. Also, the advantage of the model outlined in this chapter over Spitzer's is that both the damping constant for the bubble and the polytropic exponent of the gas are dependent on the bubble radius and driving frequency.

Fox *et al.* (1955) measured the phase velocity in a bubbly mixture by comparing the phase of a received signal in a tank containing pure water and finally a bubbly mixture. Thus, the attenuation measurements were easy to obtain. The agreement with the model is only semi-quantitive due to noise

from standing waves in the tank. This reverberation was likely driven by bubble formation noise.

In comparison with other experimental efforts, Silberman's measurements were unsurpassed in accuracy and control. However, a recent paper by Cheyne *et al.* (1995) rivals that of Silberman. They adopted the Silberman's standing wave in a tube approach, but developed a non–intrusive measurement technique utilizing a form of Laser Doppler Vibrometer (LDV). Measurements were also performed by lowering a hydrophone into the tube as indicated in the comparison with theory in Figure 2.5. A lightweight shaker was used to drive a piston at frequencies swept from 100 Hz to 20 kHz located at the bottom of the tube. The LDV data were acquired by placing the sensor at the vertical mid–point of the tube and the output recorded using a sweep spectrum analyzer. This resulted in a series of peaks in the frequency spectrum which corresponded to the tube resonances for a given water level and void fraction, and thus the sound speed was easily obtained. Strong attenuation and the extremely low phase speed at the bubble resonance (2.9 kHz) limited the data to values above and below the resonance frequency of the bubbles. Due to the extremely low sound speed at resonance, the tube would have to be less than only a few bubble radii in diameter to satisfy the planewave cutoff criteria. The close agreement with the theory evident in Figure 2.5 was achieved without resorting to fitting parameters. Note, in particular the exceedingly high sound speed measured in the 'supersonic' region around 10 kHz and overall excellent agreement with the model of Commander and Prosperetti.

In Lamarre's (1994) recent research effort, the speed of sound and atten-
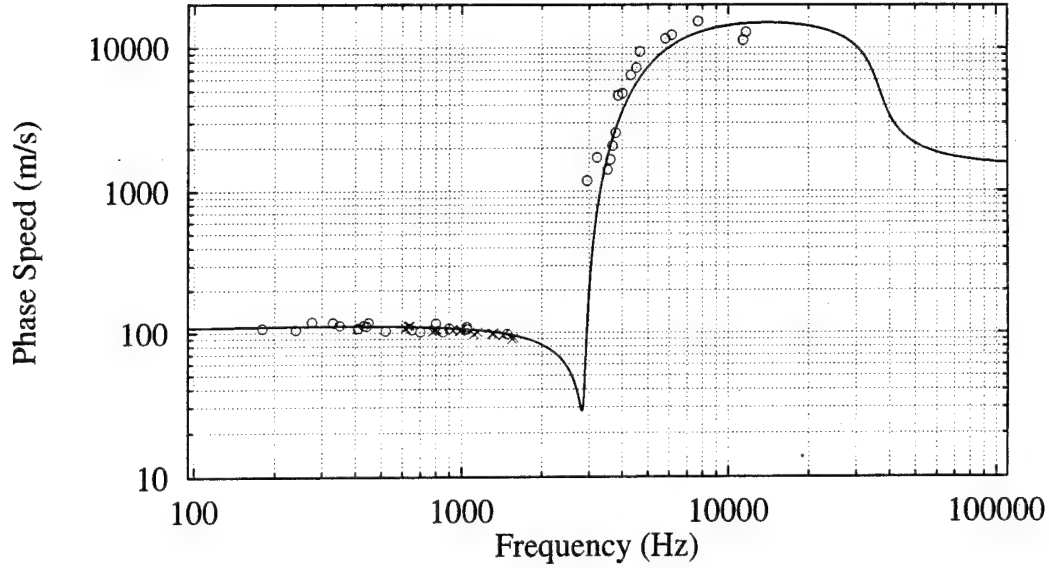
Figure 2.5: Frequency dependent phase speed. The bubble radius was 1.11 mm, and the void fraction $\beta = 10^{-2}$. The crosses represent the data measured by lowering a hydrophone down the length of the standing wave tube, and the circles using the LDV. Data courtesy of Cheyne *et al.* (1995)

uation were measured beneath breaking waves using a pulse propagation–delay technique. The sound speed was estimated by dividing the propagation distance by the transit time of the pulse. The distance between the source and receiver was 1.2 m and the measurements were performed at four depths (0.25 m vertically spaced stations just below the surface). They typically observed decrements in the sound speed on the order of 100 m/s and a maximum deviation of 800 m/s, which corresponds to void fractions of approximately 0.008 and 0.017 respectively. The sound speed decrements were found to decrease with depth in accordance with the lowered the bubble population. Although this effort reported decrements in the sound speed in excess of 800 m/s, it is likely that a closer spacing between the source/receiver pairs would provide a more highly localized result. That is, when the distribution of bubbles is

not uniform across the 1.2 m separation, say a smaller densely populated region of dimension 0.25 m, the measurement would likely be skewed to sound speeds closer to the liquid and therefore would not yield and accurate result for the minimum sound speed encountered in the bubbly region. The difficulty in performing this type of acoustic measurement is apparent since it must be conducted at frequencies well below the bubble resonance frequency, which limits one to relatively large separations.

In a previous experiment, Lamarre and Mellville (1992) used a conductivity probe to measure the void fraction, rather than the sound speed, beneath breaking waves in the ocean and the laboratory. Each sensor consisted of trio of nichrome wire electrodes spaced 1.6 cm apart and 20 cm in length arranged in a parallel fashion. As bubbles passed between the wires, the conductivity changed depending on the fraction of air occupied by the bubbles. The system was calibrated in a cylindrical tube in which the bubble size distribution, air flow rate, and void fraction were controlled. This method provided a substantially higher localization of measured void fraction, but is limited to larger void fractions in the range 10^{-3} to 0.3—the acoustic technique described above is capable of measuring void fractions down to 10^{-5}. In their field experiment, they reported instantaneous void fractions at six depths (equally spaced by 15 cm, beginning at the surface) on the order of 10^{-2}, but at times exceeding 10^{-1}. In the laboratory, surface waves were propagated down the length of a narrow flume and made to break above a single fixed–depth void fraction probe. Thus as the plume beneath breaking wave travelled past the sensor a temporal image of the localized void fraction was obtained at a particular

59

depth. The probe depth was varied and the measurement repeated for several more breaking events which allowed them to construct a spatial and temporal image of the void fraction beneath a wave. These images suggested that the laboratory plumes were nominally hemi–cylindrically shaped. When the sensors were deployed on a buoy in the ocean, void fractions in the range 10^{-2} to 10^{-1} were typically observed directly beneath an actively breaking wave—in good agreement with the sound speed decrements they later measured using acoustic techniques.

2.3.5 Bubble size distributions

In order to simplify the analysis, the model presented prior to this point is valid only for a monodispersed bubble radius distribution. However, in the sea, or even in well controlled laboratory experiments, this assumption is likely to break down. The definition of the void fraction (Eq. 2.11) provides a mechanism to include a wide range of bubble radius distributions through the distribution function $f(a)$. The limiting case of a monodispersed distribution is obtained by setting $f(a) = \eta\delta(a - R_o)$. A more realistic population would consist of range of radii, not a single radius. Examples might include a discrete bubble radius population for which

$$f(a) = \sum_{m=1}^{M} \eta_m \delta(a - R_{o,m}), \quad m = 1, 2, \ldots, M, \tag{2.28}$$

where η_m is the 'partial' number of bubbles per unit volume having radius $R_{o,m}$. Alternatively, a continuous radius distribution corresponding to the measured

populations at sea is given by

$$f(a) = \begin{cases} \eta_o\, a^{-H}; & a_1 < a < a_2, \\ \\ 0; & \text{otherwise,} \end{cases} \qquad (2.29)$$

where the coefficient H ranges from 3.5 to 5 as indicated in (Lamarre, 1993). Another common continuous distribution is the truncated Gaussian distribution

$$f(a) = \begin{cases} \eta_o e^{-\left(\frac{(a-R_o)}{2\sigma}\right)^2}; & a_1 < a < a_2, \\ \\ 0; & \text{otherwise,} \end{cases} \qquad (2.30)$$

Here, R_o is the mean radius; σ^2 is the mean square variance about the mean; η_o is the amplitude of the distribution; and the values a_1 and a_2 are the limits of the minimum and maximum bubble radii in the continuous distribution. For any of the above considerations, the integral relation $(4\pi/3)\int_0^\infty f(a)a^3\, da$ must yield the void fraction (Eq. 2.11).

An extension of the collective oscillations model to the more complex bubble distributions is outlined in (Commander & Prosperetti, 1989) and will not be presented in detail here. Instead, the results are given for the effective wave number in the mixture (Eq. 2.24),

$$k_e^2 = \frac{\omega^2}{c^2} + 4\pi \int_0^\infty \frac{f(a)a\omega^2}{\omega_0^2 - \omega^2 + 2ib\omega}\, da, \qquad (2.31)$$

and thus the sound speed ratio squared for a multi–dispersed radial distribu-

61

tion of bubbles is

$$\left(\frac{c}{c_e}\right)^2 = 1 + 4\pi c^2 \int_0^\infty \frac{f(a)a}{\omega_0^2 - \omega^2 + 2ib\omega} \, da. \qquad (2.32)$$

Generally, the distribution functions are truncated over some range of bubble radii as indicated in Eq. (2.29) and (2.30). Thus, it is trivial to demonstrate that for driving frequencies well below the lowest resonance frequency (*i.e.*, maximum radius bubble), that Eq. (2.32) approaches the Wood's expression and is therefore dependent only on β—the effect of the bubble distribution is small for frequencies below bubble resonance. However, in the frequency range near the bubble resonance, the multi–radial distributions tend to spread the resonance minimum and the broad peak of the phase speed curve over a wider range of frequencies. This is clearly illustrated in Figures 2.6, 2.7, and 2.8 for which the phase speed for the bubble radius distributions above are depicted.

$\eta_m(\%)$	$R_{o,m}(\mu\mathrm{m})$
10	100
20	200
30	300
25	400
15	500
5	600
2	700
1	800

Table 2.3: Discrete bubble size distribution used in Figure 2.6. The total volume fraction is $\beta = 10^{-3}$. The percentage of bubbles (by count) at each radius are listed in columns η_m and $R_{o,m}$, respectively.
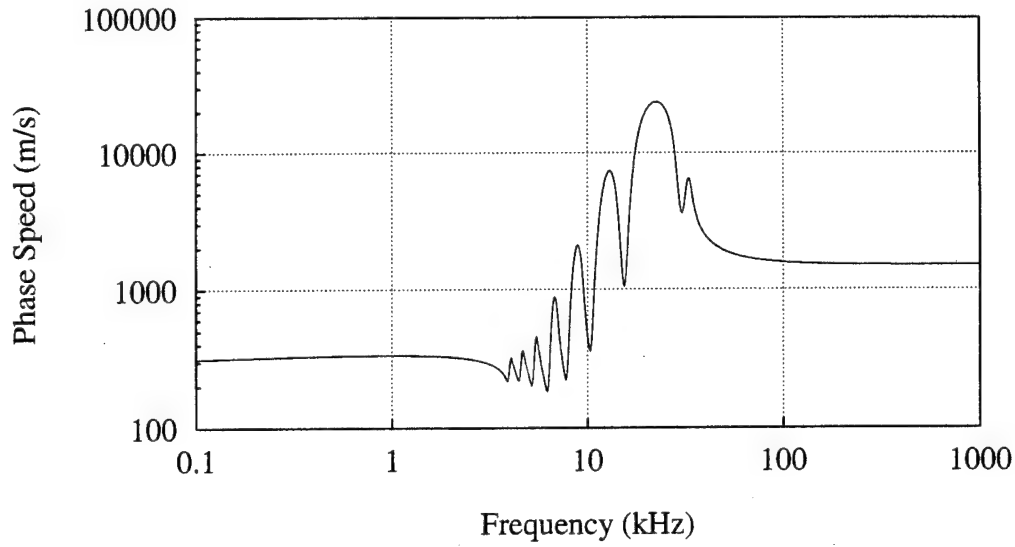
Figure 2.6: Phase speed as a function of frequency for a discrete bubble radius distribution. The average void fraction is $\beta = 10^{-3}$, and the bubble distribution is listed in Table 2.3.
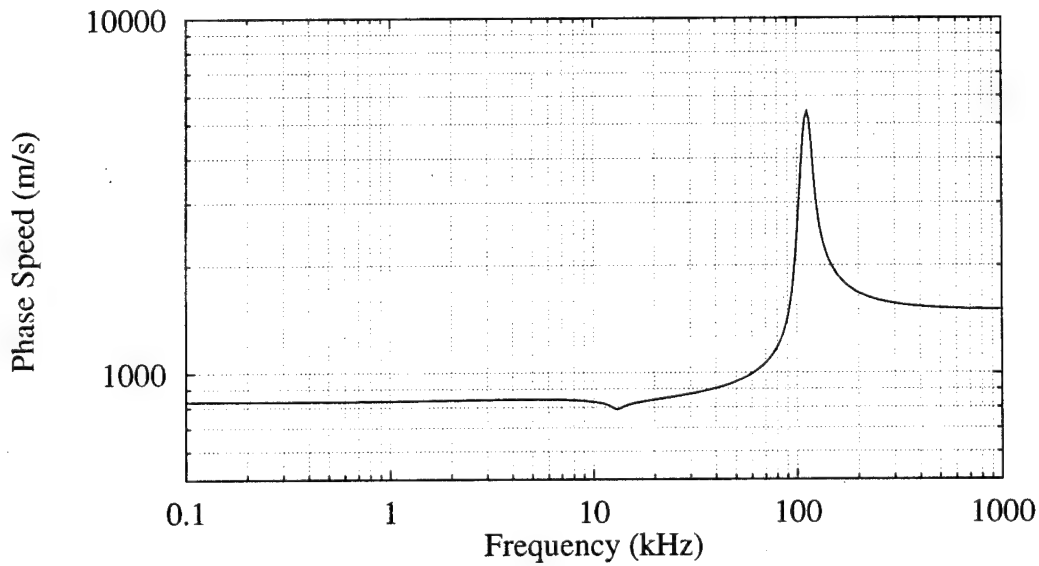
Figure 2.7: Phase speed as a function of frequency for a bubble radius distribution having $f(a) = \eta_o a^{-4.8}$. The void fraction is $\beta = 10^{-4}$; and the limits of the distribution is $30\,\mu\mathrm{m} \le a \le 240\,\mu\mathrm{m}$.

63
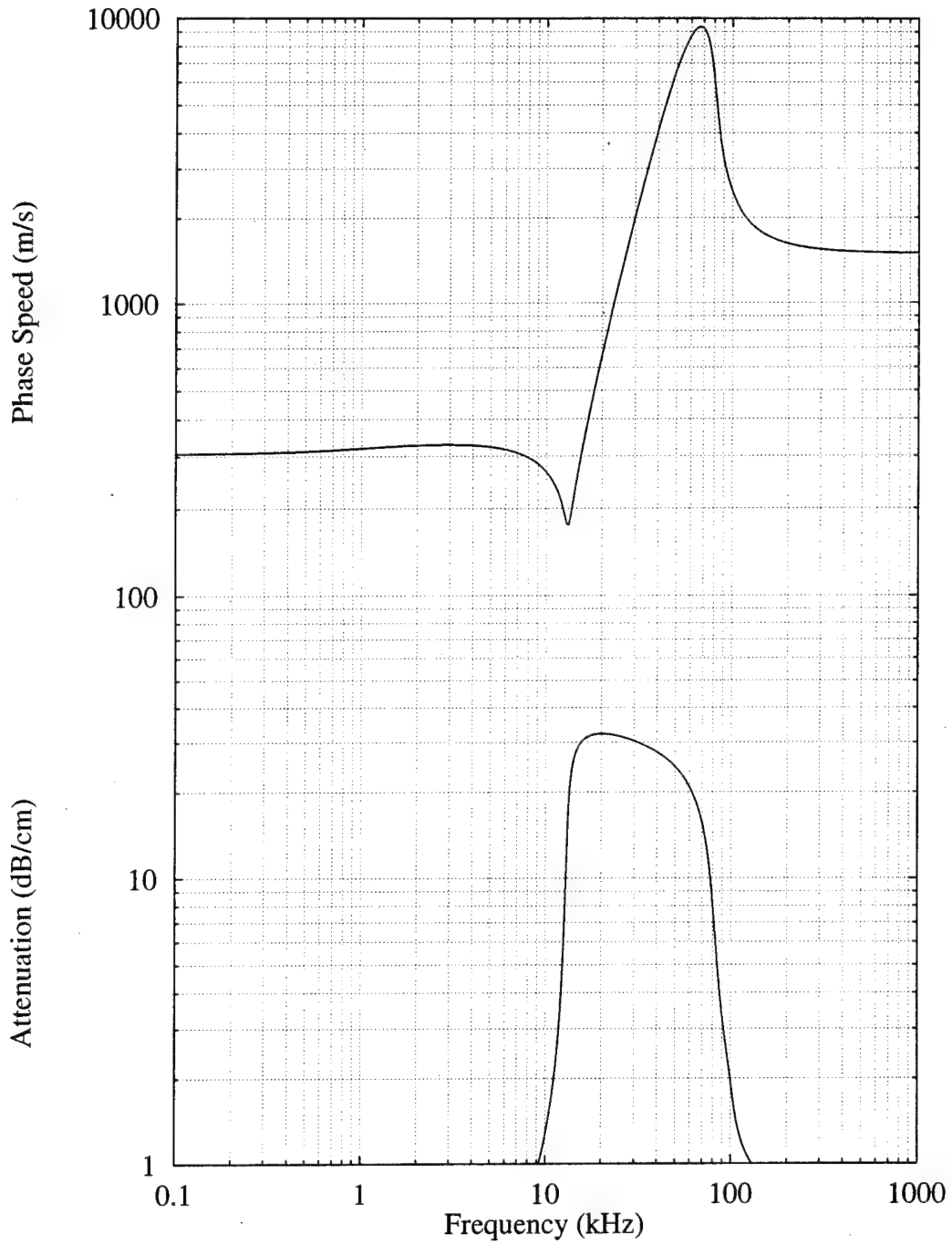
Figure 2.8: Attenuation and phase speed as a function of frequency for a truncated Gaussian bubble radius distribution. The void fraction is $\beta = 10^{-4}$; the mean bubble size is $R_o = 60\,\mu\,\mathrm{m}$; the standard deviation is $\sigma_{R_o} = 60\,\mu\,\mathrm{m}$; and the range of the distribution are $30\,\mu\,\mathrm{m} \le a \le 240\,\mu\,\mathrm{m}$.

2.4 Discussion and Summary

In this chapter the collective oscillations model for sound propagation in bubbly mixture was discussed. Three approaches were presented (the first in the introduction) which led to a good approximation for the speed of sound in the two–phase mixture at frequencies below the bubble resonance frequency. For this limiting case, the speed of sound in the mixture is primarily governed by the void fraction β. In the first two models, the sound speed in the quasi–static limit for collective bubble oscillations was derived—recall Eq. (2.8). It is clear then, that for the extremes of the void fraction ($\beta \rightarrow 1$ or $\beta \rightarrow 0$) that the speed of sound in the mixture approaches the values of the sound speed in the gas c_g or the speed of sound in the liquid c, respectively. However, for β in between these limits, the mixture sound speed can be lowered to values that fall well below the sound speed in the liquid, and even to values below the speed of sound in the gas. This indeed is remarkable! Since the wavelength of the sound at these frequencies is much greater than the bubble radii and their respective spacing, the mixture can be treated as an effective fluid having a density near that of water and a sound speed that is dependent only on the void fraction and not on the details of the bubble population statistics.

In the first two models, the dispersive effects of the bubbles in the mixture was not considered. However, it is well known that bubbles are simple harmonic oscillators which resonate at a frequency given by the Minneart expression (Eq. 2.21). In addition to resonance phenomena, the bubbles also attenuate sound significantly. The original model for a dispersive mixture sound speed was presented by Spitzer in *Physics of Sound in the Sea* (NDRC,

1946). A more mathematical approach was taken by Commander and Prosperetti (1989), in which they derived the frequency dependence of the sound speed in the mixture which includes attenuation due to acoustic, thermal, and viscous damping. Their model builds on previous work by considering the thermomechanical properties of bubbly fluids more rigorously than before.

There are three primary frequency regimes of interest in the collective oscillations theory: below resonance, near resonance, and above resonance. Below the fundamental resonance frequency of the bubbles the mixture sound speed asymptotes to the Wood's expression (Eq. 2.9), which is dependent only on the void fraction. In this limit the mixture can be considered an effective medium with density ρ_e and sound speed c_e given by the Wood's expression (Eq. 2.9). The imaginary part (attenuation) is small in this region and is generally neglected in most studies. As the driving frequency approaches the fundamental resonance frequency of the constituent bubbles, the sound velocity in the mixture drops sharply and then rebounds to values well above the speed of sound in the host fluid. A corresponding increase in attenuation is also observed. Following the bubble resonance, the sound speed approaches its bubble free value in the liquid. The roll–off into this regime displays a marked dependence on the void fraction (*i.e.*, for larger β the peak in the phase speed curve broadens). Phenomenologically, the collective oscillations model can be explained by considering the bubble as a simple resonance oscillator. The bubble oscillates in phase with the driving force below resonance, and out of phase with the driving force above resonance. In the higher frequency regime, the driving force 'sees' a much stiffer fluid medium, and hence a higher sound

66

speed.

In the effort described in this dissertation, the ultimate goal is to consider the scatter from spherical clouds of bubbles, primarily at frequencies below the bubble resonance. Hence, the asymptotic speed of sound given by the Wood's expression is of particular importance. This corresponds to the 'flat' region below the resonance frequencies of the largest bubbles. In this limit, the bubbly mixture can be modeled as a homogeneous fluid (Eq. 2.23) in which the effective sound speed is governed by β alone (Eq. 2.9) and not the individual bubbles. It is clear that this is not exactly true if one were to consider attenuation and the slight dispersive effects below bubble resonance—recall Figures 2.3, 2.4. However, the Wood's expression (Eq. 2.9) is often used since the difference in sound velocity between this approximation and that given by Eq. (2.23) is generally only a few meters per second and the attenuation is generally of negligible concern below the bubble resonance.

Several experimental efforts aimed at measuring the phase speed of sound and attenuation in a bubbly mixture have been conducted over the past fifty years. Most notable are those by Silberman (1957), and more recently by Cheyne et al. (1995). The excellent agreement with the model suggests that the bubbly bubbly fluid behaves as a homogeneous medium, especially well below the resonance frequencies of the individual bubbles. In the past decade, these ideas were independently (and vigorously) promoted by Carey (1985) and Prosperetti (1985) as a possible mechanism to explain low–frequency ambient noise emissions during wave breaking at sea. When a bubble cloud is created by a breaking wave or in a laboratory by a bubble plume generator, a

'self–induced' damped resonant oscillation results in which the eigenfrequency is determined by the phase speed within the effective medium and the characteristic length scale of the cloud (Oğuz, 1994; Yoon *et al.*, 1991; Nicholas *et al.*, 1994; Roy *et al.*, 1991; Carey *et al.*, 1993; Kolaini *et al.*, 1994). The low–frequency noise associated with bubble cloud formation is driven in part by the broad–band 'pinch–off' noise generated by a newly formed bubbles as they attempt to reach equilibrium shape and size, and in part by hydrodynamic flow associated with the air entrainment and cloud formation process (Oğuz *et al.*, 1995).

Chapter 3

Acoustic scattering from a spherical bubble cloud: Theoretical model

3.1 Introduction

Scattering can be regarded as radiation from a 'source' which is driven by an incident wave rather than by a local external generator. As an example, consider a plane wave traveling in the z–direction through a uniform fluid. A volume element of the fluid will be set into oscillatory motion in the direction of wave propagation, and it will be subject to periodic compression and rarefaction. The response of the fluid to the incident wave will involve both the inertial mass and the compressibility of the fluid. The volume element in the fluid responds by pulsating and oscillating, giving rise to both monopole and

69

dipole radiation.

For a uniform fluid, all volume elements represent sources of equal strength but different phases, where the phase is determined by the position of the element along the propagation path. A wave front is defined by all volume elements oscillating in equal phase. Ahead of the wave front sound is propagated by each volume element which radiates sound in phase (the so called Huygens' 'wavelets'), and behind it the radiation is 180° out of phase resulting in zero backwards propagation.

Now consider an inhomogeneous volume embedded within the previously uniform fluid. The foreign body possesses a different inertial mass and/or compressibility than that of the host fluid. The plane wave, as before, travels in the z–direction giving rise to Huygens' wavelets, but when the wavefront reaches the boundary of the inhomogeneous region the differing material properties create virtual sources having different strength and phase compared to their neighbors in the wavefront. This results in an excess or scattered wave contribution radiating from the foreign body. For non–uniformities within the wave front that are small in comparison to the wavelength ($ka < 1$), the monopole field will be proportional to the difference in compressibility and the dipole field proportional to the density contrast.

In this section a theoretical model for acoustical scattering from a penetrable sphere (target) in the free–field will be considered. Free–field implies that the host fluid is free of inhomogeneities or reflecting surfaces, with the exception of a single embedded target. Although the amplitude, periodicity, and phase of the incident plane waves are known, the exact driving force

causing the sphere to radiate sound is not, and therefore must be calculated exactly. For wavelengths much larger than the target radius ($\lambda \gg 2\pi a$), the scatterer is considered 'compact' and the driving pressure on the boundary is often assumed to be the incident field (*i.e.*, the Born approximation). This results primarily in monopole and dipole scattered contributions. However, for shorter wavelengths, the driving pressure on the surface of the sphere will not be uniform and the boundary value problem must be solved directly. In special cases, the sound waves penetrating the scatterer or traversing its boundary coincide with the eigenvibrations of the sphere and interfere constructively by setting up self–sustaining standing waves in the object or on its surface. It is intuitively clear that when the incident wave oscillates at one of the target's eigenfrequencies that the corresponding eigenvibration in the sphere will be excited and strongly affect the scattered wave.

Our interest is in scattering from bubble clouds in the ocean. Although it has long been known that a two–phase mixture of air bubbles in water pulsates in a collective fashion and that the sound speed in the mixture below the bubble resonance frequency is determined by the void fraction alone and therefore the region containing the mixture can be treated as an effective medium, it was not proposed until 1985 that such a mixture could serve as a simple radiation source and a scatterer of sound. When a bubble cloud is created by a breaking wave, a damped resonant oscillation results in which the eigenfrequency is determined by the phase speed within the effective medium and the characteristic length scale of the cloud (Carey & Browning, 1988; Oğuz, 1994). Several examples of 'self–induced' sub–kilohertz radiation from

71

bubbly mixtures were given in Chapter 1 and Chapter 2 (Yoon *et al.*, 1991; Carey *et al.*, 1993; Nicholas *et al.*, 1994; Roy *et al.*, 1991; Nicholas *et al.*, to be submitted). It seems plausible then that if a bubbly mixture is an efficient radiator of sub–kilohertz sound, that it might also serve as effective scattering target. This idea was explored in a recent experiment performed in a fresh water at Lake Seneca in New York state (Roy *et al.*, 1992) and is the impetus for the scattering model presented in this chapter.

3.2   Formalism

In this model, a continuous stream of monochromatic plane waves incident on a compressible sphere of radius a surrounded by an infinite fluid as indicated in Figure 3.1 is assumed. The density and sound speed within the sphere are denoted by ρ_e and c_e, respectively. In the surrounding fluid, these quantities are given by ρ and c. This solution is not limited to bubble clouds, but for the purposes of this work the effective medium approximations derived in Section 2 will ultimately be applied.

The solution for scattering from a sphere is straightforward. Anderson (1950) and Rshevkin (1963) treat the case for scattering from a fluid sphere. Morse and Ingard (1968) arrive at the solution after an extremely mathematical analysis using an integral Green's function technique. Morse and Feschbach (1953) used an elegant phase shift analysis which is better suited to spheres having an acoustic coating of known impedance or more complex geometries. A comprehensive survey of acoustic and electromagnetic scattering from sim-

72

ple shapes (*i.e.*, separable geometries) such as spheres, cylinders, spheroids, cones, plates, etc., can be found in (Bowman *et al.*, 1987)—much of this work is based on the previous solutions by (Morse & Feshbach, 1953). Flax *et al.* (1981) discuss resonance scattering theory and its application to solid spherical inclusions, air bubbles, and various fluid loaded shells. Their work departs from the previous in that they apply broad band (short pulse lengths) techniques, rather than the usual monochromatic (steady state or CW) assumptions, using Fourier analysis. All the works cited above, however, arrive at identical scattering solutions for the fluid sphere case[1]. However, Anderson's approach is preferred due to its inherent simplicity (one should note that his scattering angle is shifted 180° from the presently accepted notation).

An alternative approach taken by Gragg and Wurmser (1993) was to numerically solve for the backscattered wave from a bubble filled sphere or other shape. They implemented a Boundary Value Integral (BVI) technique to computationally solve for the scattered wave contribution from a bubble cloud (both spherical and spheroidal) by applying the appropriate boundary conditions on a boundary 'mesh' enclosing an arbitrarily shaped scatterer. This technique is shown to result in the exact scattering solution for the sphere and spheroid given an appropriate tiling, but is better suited to scattering from more complex geometries since the numerical method is computationally expensive. The advantage to the method presented in this chapter, on the other hand, is that it is simple and straightforward, and therefore can be used to efficiently predict the scattering spectrum from a spherical bubble cloud.

---

[1]This can be shown in particular for the solutions by Anderson, Rschevkin, and Morse and Ingard after much algebraic work.

It will be shown that the solution for acoustic scattering from a fluid sphere has a marked dependence on the internal sound speed and density. Thus, in order to consider the case of scattering from bubble clouds the collective oscillations model will be applied as presented in Chapter 2. Scattering from a spherical bubble cloud will be considered explicitly following a review of sound scattering from a 'hard' impenetrable sphere and an idealized (lossless) bubble. These cases are well known and they are discussed only for comparison and completeness. Furthermore, a simple analytic expression for the scattering response in the low frequency limit (*i.e.*, small ka) will be derived as it proves to be a fundamentally useful tool and yields considerable physical insight. In addition, this expression provides a good approximation for the monopole, or 'breathing mode,' resonance frequency of the sphere.

In this modeling effort, the sphere is chosen as the scattering target *not* because spherical bubble clouds are created beneath the ocean surface, but rather because the length scales of the clouds created are small in comparison to the wavelength of sound over the frequency range of interest (*i.e.*, the sub–kilohertz frequencies where long range sonar systems operate). The natural creation of bubble clouds results in a densely populated region of bubbly fluid having a characteristic size of $0.5\,\mathrm{m}$ or less in length scale. For low acoustic frequencies, such a target is termed acoustically compact, that is $ka < 1$. For most acoustic wavelengths encountered in this study, the cloud can be considered 'compact' since $\lambda \geq 2\pi a$, and the response of the cloud will be dictated by the monopole mode which is primarily dependent on the volume and compressibility of the target, and more or less independent of shape pro-

74

vided that the aspect ratio is close to unity. For example, consider an acoustic frequency of 300 Hz. The sonic wavelength in seawater is $\lambda \approx 5$ m, greater than the characteristic dimensions of the target $(a = 0.5$ m$)$. The scatterer is well characterized by a sphere and the solution is cast in a multipole expansion (Lighthill, 1975). The most important term in describing the low–frequency behavior of the system is the monopole term.

The coordinate system for the sphere is shown in Figure 3.1, where the relationship between the Cartesian and spherical polar coordinate systems is given by the usual transformations

$$x = r \sin \theta \cos \phi, \quad y = r \sin \theta \sin \phi, \quad z = r \cos \theta, \tag{3.1}$$

and the coordinate origin is located at the center of the sphere.
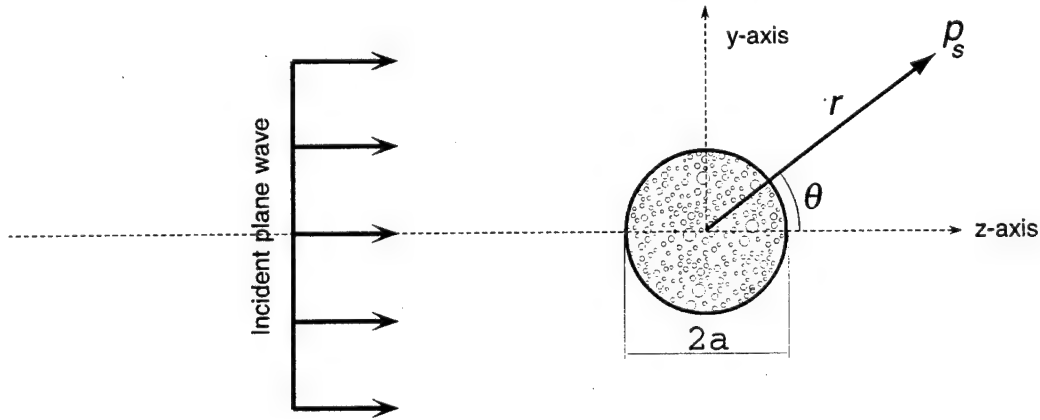
Figure 3.1: Scattering geometry. The z–axis is aligned with the direction of plane wave propagation. The coordinate system origin is located at the center of the sphere.

The sphere is assumed to consist of an isotropic fluid material of density ρ_e and sound speed c_e. Outside the sphere, an infinite fluid of density ρ and

sound speed c exists. A continuous plane wave of angular frequency ω insonifies the sphere from the z–direction. The time and spatial dependence of the incident sound is $\exp[i(\mathbf{k} \cdot \mathbf{r} - \omega t)]$, where the magnitude of the wave number is $k = \omega/c = 2\pi/\lambda$, and λ is the wavelength of the incident sound in the host fluid. Inside the sphere, the wave number is simply $k_e = \omega/c_e = 2\pi/\lambda_e$, and λ_e is the effective wavelength of sound inside the sphere.

The general solution for the pressure everywhere is

$$p = \begin{cases} p_i + p_s & r \geq a, \\ p_{\text{int}} & r < a, \end{cases} \qquad (3.2)$$

where the subscripts i, s, and int, refer to the respective incident, scattered, and internal fields. A monochromatic incident plane wave of amplitude p_o impinging on the sphere has the form

$$\begin{aligned} p_i &= p_o e^{i(\mathbf{k}\cdot\mathbf{r}-\omega t)} & (3.3) \\ &= p_o e^{i(kr\cos\theta-\omega t)}. & (3.4) \end{aligned}$$

This disturbance gives rise to both internal and external waves, p_{int} and p_s, respectively.

Exploiting the symmetry of the problem, the incident field can be expressed as a series expansion in spherical harmonics dependent on r and θ,

76

angular frequency ω, wave number k, and time t.

$$p_i(\mathbf{r}, t) = p_o \sum_{m=0}^{\infty} (2m + 1) i^m P_m(\cos \theta) j_m(kr) e^{-i\omega t}, \qquad (3.5)$$

where the $j_m(kr)$ is the spherical Bessel function of the first kind of order m; and $P_m(\cos \theta)$ is the Legendre polynomial of order m. The solution is independent of the angular direction ϕ due to azimuthal symmetry.

At the boundary of the sphere $(r = a)$, both the pressure and normal component of the particle velocity must be continuous. For the acoustic pressure, the boundary condition is

$$p_i(a) + p_s(a) = p_{\text{int}}(a). \qquad (3.6)$$

The continuity of radial component of the particle velocity on the spherical boundary is

$$u_{i,r}(a) + u_{s,r}(a) = u_{\text{int},r}(a). \qquad (3.7)$$

The relationship between the pressure and the normal velocity is

$$u_{\star,r} = \frac{-i}{\rho_\star c_\star} \left[\frac{\partial p_\star}{\partial (kr)} \right], \qquad (3.8)$$

where the subscript $\star$ denotes the incident, internal, or scattered solutions. In addition, the pressure inside the sphere must be finite everywhere, and outside the sphere the amplitude of the scattered pressure disturbance must go to zero

77

as r approaches infinity.

The acoustic pressure must satisfy the three–dimensional wave equation:

$$\nabla^2 p - \frac{1}{c^2}\frac{d^2}{dt^2}p = 0, \tag{3.9}$$

which simplifies to, $\nabla^2 p + k^2 p = 0$, after evaluating the time derivative.

The solution for the internal and scattered pressure are given by the partial wave expansion in spherical harmonics as follows:

$$p'(r < a, t) = \sum_{m=0}^{\infty} A_m P_m(\cos\theta) j_m(kr) e^{-i\omega t}. \tag{3.10}$$

$$p_s(r > a, t) = \sum_{m=0}^{\infty} B_m P_m(\cos\theta) \begin{bmatrix} j_m(kr) \\ n_m(kr) \end{bmatrix} e^{-i\omega t}. \tag{3.11}$$

Here, the $j_m(x)$ and $n_m(x)$ represent the spherical Bessel functions of the first and second kind of order m and argument x (usually called the spherical Bessel and spherical Neumann functions, respectively). The coefficients A_m and B_m are obtained by applying the boundary conditions Eq. (3.6) and (3.7). Our interest is in the scattered field, not the internal pressure field, thus

$$p_s(r) = -\frac{p_o}{2} \sum_{m=0}^{\infty} i^m (2m+1) \mathcal{R}_m P_m(\cos\theta) h_m(kr) e^{-i\omega t}, \tag{3.12}$$

where $h_m(x) = j_m(x) + i n_m(x)$ is the spherical Hankel function, and $\mathcal{R}_m$ satisfies the boundary conditions. Individual terms in the expansion Eq. (3.12) yield the monopole, dipole, quadrupole, etc., amplitudes (*i.e.*, $m = 0, 1, 2, \ldots$,

respectively). The monopole term radiates sound uniformly in all directions since $P_0(\cos\theta) = 1$, identically. Furthermore, the $m = 0$ term represents the volume or breathing mode of the sphere. Unless otherwise specified, the time dependence of the solution $\exp(-i\omega t)$ will be discarded.

The coefficient $\mathcal{R}_m$ in Eq. (3.12) is determined from the boundary conditions where,

$$\mathcal{R}_m = \frac{\rho_e c_e j_m(k_e a) j'_m(ka) - \rho c j'_m(k_e a) j_m(ka)}{\rho_e c_e j_m(k_e a) h'_m(ka) - \rho c j'_m(k_e a) h_m(ka)}, \tag{3.13}$$

and $j'_m(x)$ and $h'_m(x)$ are the derivatives of the spherical Bessel and Hankel functions.

In the far field ($kr \gg 1$), the scattered pressure in Eq. (3.12) asymptotes to

$$p_s(\mathbf{r}) \longrightarrow i\frac{p_o}{2}\frac{e^{ikr}}{kr}\sum_{m=0}^{\infty}(2m+1)\mathcal{R}_m P_m(\cos\theta), \tag{3.14}$$

$$\longrightarrow p_o\frac{a}{2r}\mathcal{F}(ka,\theta), \tag{3.15}$$

where $\mathcal{F}(ka,\theta)$ is the so called dimensionless scattering form function.

The preceding equation (3.14) deserves special attention. The amplitude of the solution falls of inversely with distance as expected from a spherical radiating source. Also, each term in the series has a strong dependence on the internal and external densities and sound speeds, as well as the driving frequency (this is because $k = 2\pi f/c$ and $k_e = kc/c_e$). In addition, the angular dependence of the scattered radiation is given by the Legendre polynomials

79

which result in preferential radiation in some directions since the boundary of the target is not driven uniformly. While it can be shown that the directionality is only of moderate importance for small ka and can be quite significant for larger ka, our interest is in the backscattered contribution. Accordingly, a further simplification by setting $\theta = 180°$ will be applied and the Legendre polynomials simplify to the well known relation $P_m(-1) = (-1)^m$.

The coefficient $\mathcal{R}_m$ contains the fundamental dependence of the scattering on frequency and material properties of the target and its host. It is a complex quantity, and thus the magnitude and phase are important. For a given density and sound speed of the host and target, resonances or peaks in the scattering spectrum will occur for singularities of the coefficient $\mathcal{R}_m$ (*i.e.*, when the denominator of Eq. (3.13) approaches zero). This will be discussed further in Section 3.4

3.3 Backscattering form function

Although the incident and scattered pressures (Eq. (3.4) and (3.14)) are experimentally measurable quantities, it is sometimes impractical and often unnecessary to report absolute levels when discussing the efficiency of the scattering by a target. Rather, coefficients of the relative scattering strength, such as the scattering form function, scattering cross section, ratio of pressure amplitudes, and target strength are generally reported.

The total scattering cross section (σ_s) is defined by the ratio of the total power scattered divided by the incident intensity. Expressed as an integral over

80

all angles, the total scattering cross section is

$$\sigma \equiv \frac{\Pi_s}{I_i} = \iint\limits_S \frac{d\sigma_s}{d\Omega}\, d\Omega, \tag{3.16}$$

where the quantity Π_s is the total power scattered over all angles; $d\Omega$ is the increment of solid angle; and $\frac{d\sigma_s}{d\Omega}$ is the differential scattering cross section. When σ is evaluated, it determines the power scattered per unit solid angle and per unit incident intensity. The differential scattering cross section has the dimensions of area is defined as

$$\frac{d\sigma_s}{d\Omega} \equiv \frac{I_s r^2}{I_i}, \tag{3.17}$$

where I_s is the scattered intensity, I_i is the incident intensity, and r is the distance from the point of interest (the receiver) to the target (Clay & Medwin, 1977). For an isotropic scatterer, $d\sigma_s/d\Omega$ is independent of direction and equal to $\sigma_{\rm bs}/4\pi$, where $\sigma_{\rm bs}$ is the backscattering cross section (*i.e.*, σ_s evaluated at $\theta = 180°$).

Closely related to the backscattering cross section is a quantity called the relative target strength level (TS) defined by (Urick, 1967)

$$TS = 10 \log_{10} \left(\frac{I_s}{I_i} \right)_{r=1\,\rm m}, \tag{3.18}$$

where the incident and scattered intensities are evaluated at a 1 m distance.

In the sonar community, the TS is the standard quantity used to indicate the scattering strength of an object. If you consider incident plane waves and

81

isotropic scattering, then Eq. (3.17) and (3.18) combine to yield

$$TS = 10 \log \left(\frac{\sigma_{bs}}{4\pi r^2} \right)_{r=R_{ref}}. \tag{3.19}$$

Further discussion of the TS and its application to scattering measurements is outlined in Appendix A.

Since acoustic intensity is proportional to the square of the pressure amplitude for both planar and spherical waves, the scattering cross section and the target strength are closely related to the pressure amplitudes in Eq. (3.14). Thus, the relationship between the backscattering cross section and the scattered and incident pressure amplitudes is given by

$$\frac{\sigma_{bs}}{4\pi} = \frac{|p_s|^2}{|p_i|^2} r^2, \tag{3.20}$$

and the magnitude of the dimensionless scattering form function is

$$|\mathcal{F}| = \frac{2r}{a} \frac{|p_s|}{|p_i|}, \tag{3.21}$$

and is dependent explicitly on ka, g, and h. The form function is a dimensionless quantity which describes the strength of a scatterer as a function of ka. Now,

$$TS = 20 \log_{10} \left(\frac{a}{2r} |\mathcal{F}| \right)_{r=1\,\text{m}} = 20 \log_{10} \left(\frac{|p_s|}{|p_i|} \right)_{r=1\,\text{m}}, \tag{3.22}$$

in contrast to Eq. (3.21), is not explicitly dependent on ka. The radius (a) and

the frequency must be known prior to computation of the TS.

To simplify the analysis, let us define the relative quantities $g \equiv \rho_e/\rho$, and $h \equiv c_e/c$, and rewrite the scattered pressure series solution (Eq. 3.14) in terms of these quantities. Then the magnitude of the backscattering form function is

$$|\mathcal{F}| = \left| \frac{1}{ka} \sum_{m=0}^{\infty} (-1)^m (2m+1) \mathcal{R}_m \right|,$$ (3.23)

and

$$\mathcal{R}_m = \frac{j_m(\frac{ka}{h})j'_m(ka)gh - j'_m(\frac{ka}{h})j_m(ka)}{j_m(\frac{ka}{h})h'_m(ka)gh - j'_m(\frac{ka}{h})h_m(ka)}.$$ (3.24)

It is important to stress that so long as the material properties of the scatterer and host are not dispersive, then the form function is strictly parameterized by the Helmholtz number, ka, and the material quantities g and h. This scaling between size and frequency is common to many problems in acoustics, and means that neither the scatterer size nor the frequency need to be known independently in order to solve the problem.

From this point forward, all references to the scattering strength will be made either through the target strength or scattering form function. Generally, the form function will be reserved for use when comparing the theoretical backscatter from targets having a non–dispersive interior (and exterior) sound speed. For such cases, calculation of the backscattering form function as a function of ka alone both generalizes and simplifies the analysis and calculations considerably.

83

On the other hand, for a bubbly mixture the velocity of sound is dependent of the acoustic frequency as shown in Chapter 2. Furthermore, the dispersion relation for the mixture sound speed is in no way dependent on the cloud dimensions, much less ka. Therefore, a plot of the backscatter form function versus ka has little meaning for a dispersive medium unless either the cloud radius or frequencies are specified. Of course, this is not the case for non–dispersive media, where for a given sound speed and density ratio, h and g, respectively, a single calculation of the form function yields valid results for any range of frequencies or sphere radii (*i.e.*, ka) considered.

To calculate the TS, the cloud radius and frequency range must be specified *a priori*. The TS will be used to compare calculated predictions with experimental measurements. In an experiment the characteristic dimensions and acoustic parameterizations (g and h) of the target are not needed to measure the TS.

Initially, the calculations were performed using *Mathematica*. Once it was determined that the calculations were accurate (by comparison with the plots in Anderson's (1950) paper), the codes were rewritten in the C/C++ programming languages and integrated with the collective oscillations code. The calculations of the special functions (spherical Bessel, spherical Neumann, and Legendre polynomials) were performed using the standard recursion relations (simple transcendental equations involving sin and cos). Since the interest in this research is confined to the lower order scattering modes (*i.e.*, small ka), no special attention was paid to the accuracy of the calculation of these special functions.

3.3.1 Case Studies

The dependence of the backscatter form function of a sphere in water as a function of ka is now explored for three cases of different material parameters. Consider first the case of the idealized hard impenetrable sphere. In this case, the internal acoustic impedance is given by $Z_e = \rho_e c_e \to \infty$. Thus in Eq. (3.24) the quantity $gh \to \infty$ and Eq. (3.23) reduces to

$$|\mathcal{F}| = \left| \frac{1}{ka} \sum_{m=0}^{\infty} (-1)^m (2m+1) \frac{j'_m(ka)}{h'_m(ka)} \right|. \tag{3.25}$$

The form function versus ka for the hard sphere is shown in Figure 3.2, where the resonances or peaks of the system are governed by the minima of $h'_m(ka)$. The peaks are due to interference between waves propagating along the fluid boundary layer on the circumference of the sphere (a phenomenon known as creeping waves) and the specular reflection. For increasing ka, the amplitude of the oscillations in the form functions diminish resulting in perfect specular reflection. And as such, the magnitude of the form function approaches unity. For specular reflection from a hard sphere the TS in the high frequency (short wavelength) limit asymptotically approaches $TS = 20\log_{10}(a/2)$, and thus a 2 m radius sphere will possess a TS=0 dB. Consequently, hard metallic spheres are often used as calibrated targets.

For the case of an idealized bubble submerged in water, that is an air filled sphere without damping, the acoustic parameterizations are $g = 0.001$ and $h = 0.22$. In Figure 3.3, the backscattering form function as a function of ka for a bubble is illustrated. Here, there is an obvious very sharp resonant

85
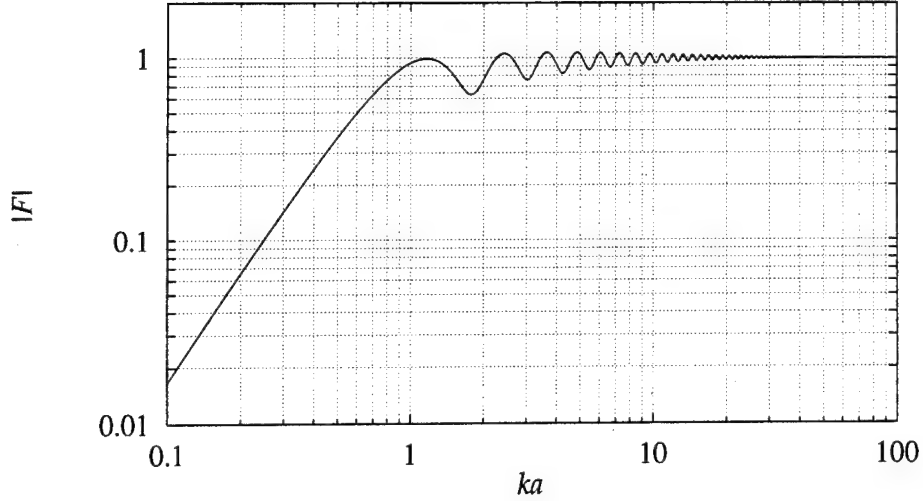
Figure 3.2: Backscattering form function versus ka for an impenetrable sphere.

peak in the spectrum at $ka = .0134$, followed by a rather smooth response and then several 'spiky' resonances at higher ka. The fundamental resonance corresponds to $f_o = 0.0134\, c/2\pi a \approx 3.2/a$ in Hz, where the radius a is given in meters. Remarkably, this peak corresponds exactly to the well know Minneart frequency given in Eq. (2.21).

The third case is that of a frequency independent low–sound velocity bubble cloud as shown in Figure 3.4. In this case the void fraction within the cloud is $\beta = 10^{-3}$ and the Wood approximations yields $c_e \approx 313\,\text{m/s}$. Accordingly, $g = 0.999$ and $h = 0.208$. Again, a peak is observed in the spectrum for $ka < 1$. Although the sound velocity ratio in this case and the previous case for the bubble are nearly identical, the resonance response is quite different. This suggests that the density ratio plays an important role in both the frequency and width of the resonance peak. We would like to have the ability to predict the resonance frequency for all target spheres. As a first
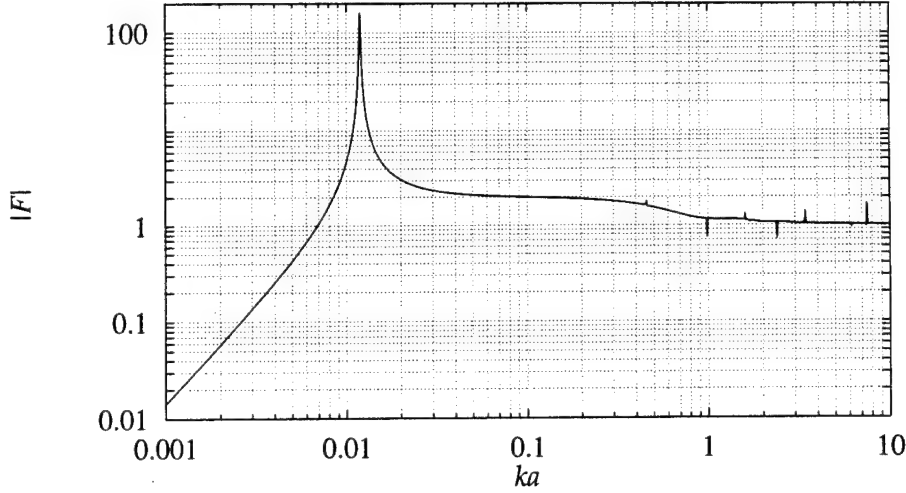
Figure 3.3: Backscattering form function versus ka for a bubble.

'guess', we begin with the Minneart relation, $f_o = (1/2\pi a)\sqrt{3\gamma P_\infty / \rho}$ for the natural resonance of a bubble, and recall that the velocity of sound in the gas is approximately $c_g = \sqrt{\gamma P_\infty / \rho_g}$. Substitution of the gas sound speed into the former equation results in

$$f_o = (c_e/2\pi a)\sqrt{3\rho_e/\rho}, \tag{3.26}$$

where the subscripts for the gas are replaced by the subscript denoting the generalize sphere. From Eq. (3.26), we have

$$ka \; = \; 2\pi a f_o/c \tag{3.27}$$

$$= \; (c_e/c)\sqrt{3\rho_e/\rho} \tag{3.28}$$

$$= \; h\sqrt{3g} \tag{3.29}$$

at resonance. For the case of the bubble cloud considered above, this suggests

87

that $ka = 0.36$. This appears to be a good approximation since the peak actually occurs at $ka = 0.355$.
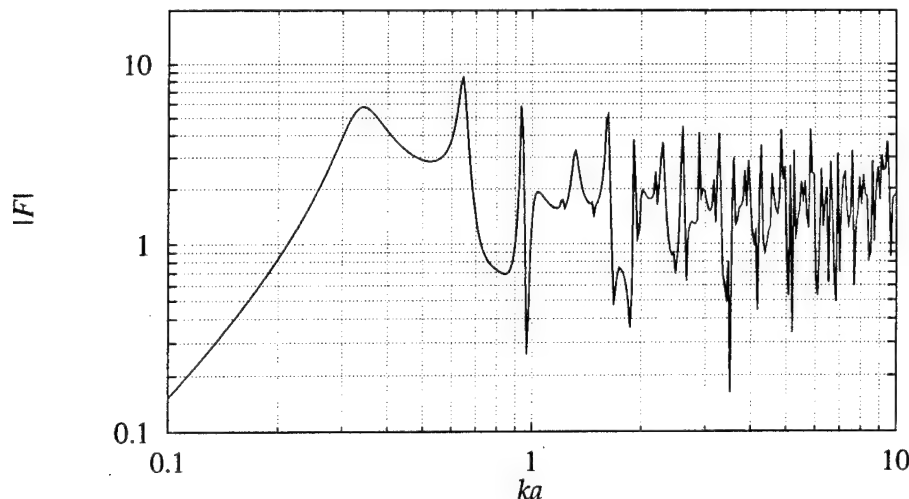
Figure 3.4: Backscattering form function versus ka for a bubble cloud having $\beta = 10^{-3}$, thus $c_e \approx 313\,\mathrm{m/s}$ (*i.e.*, $g = 0.999$ and $h = 0.208$).

The fundamental observation is that for a compressible fluid sphere, the monopole resonance is clearly indicated by the first peak in each of the curves. For $ka \ll 1$, all the cases examined exhibit a similar asymptotically increasing slope—classically termed Rayleigh scattering. Beyond the monopole resonance ($ka > 1$), in the regime known as geometrical scattering, the complex series of higher order peaks are due to internal resonances and can be explained by resonance scattering theory. These resonances (eigenmodes) are governed by minimizing the denominator of $\mathcal{R}_m$.

In the preceding development, the internal sound velocity of the sphere was not dispersive and thus scattering form function is dependent on ka rather than frequency explicitly. In order to consider the dispersive effects of a true bubbly fluid (using the collective oscillations model), a particular sphere radius

88

must be chosen to consider the frequency dependence. Recall, from Chapter 2 the discussion of the mixture sound speed in a bubble cloud having void fraction $\beta = 10^{-3}$ with a mean bubble size of $500\,\mu$m. From Figure 2.3, it is clear that the mixture sound velocity asymptotes to the Wood approximation is valid for all frequencies below $2\,$kHz and departs from this limiting value when evaluated at higher frequencies. The attenuation over this frequency range is not negligible. In the region surrounding the bubble resonance, the attenuation in the bubbly mixture is great and thus the sphere cannot be expected to scatter sound in the same manner as it would at the lower frequencies.

In Figure 3.5, the TS as a function of frequency, is plotted for a bubble cloud having radius $a = 0.25\,$m, void fraction $\beta = 10^{-3}$, and a uniform bubble distribution of radii $R_o = 500\,\mu$m. Also plotted is the TS of an individual $500\,\mu$m–radius bubble. The similar pair of curves represents the effect of using the Wood equation (lighter curve) as compared to the dispersive sound speed formalism (darker curve) obtained using the collective oscillations theory in Eq. (2.25). It is clear that introducing attenuation has reduced the overall scattering level at the lowest frequencies, as well as shifted the higher order peaks to lower frequencies. The solid curve with a single peak near $5.5\,$kHz represents the backscatter form function of a bubble having radius $R_o = 500\,\mu$m. Just above the monopole resonance of the constituent bubbles, the TS of the dispersive bubble cloud approaches that of the perfectly reflecting impenetrable sphere since the interior sound speed is increased dramatically (recall Figures 2.3 and 3.2).

89
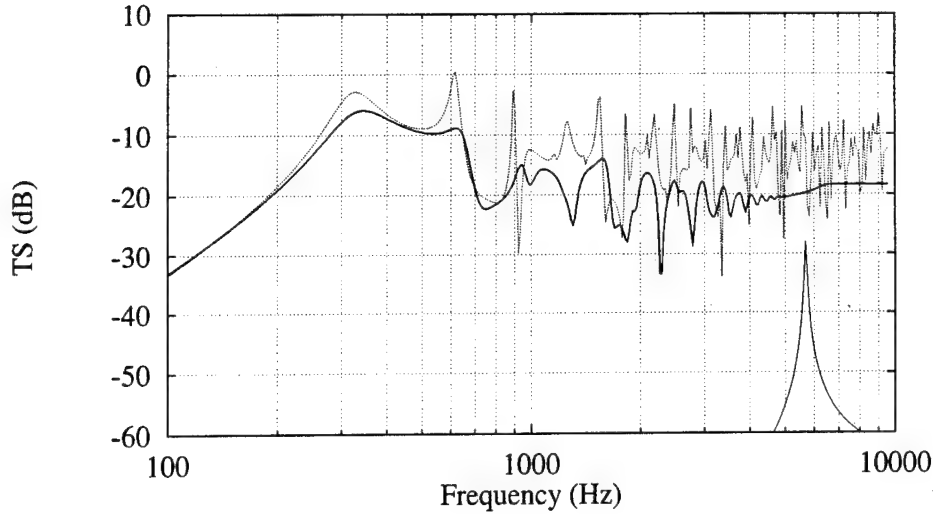
Figure 3.5: TS versus frequency. The upper two curves are for a cloud radius of $a = 0.25$ m and $\beta = 10^{-3}$. In the darkest solid curve, the dispersive internal sound velocity was used, and in the dashed curve the internal sound speed was calculated using the Wood expression (recall Figure 3.4). The thin solid line corresponds to the TS of single $500\,\mu$m radius bubble. Recall from Eq. (3.22) that a perfectly reflecting sphere ($|\mathcal{F}| = 1$) having radius $a = 2$ m possesses TS $= 0$ dB.

3.4 The low–frequency limit

From Figures 3.3 and 3.4, it is clear that the first or 'breathing–mode' resonance occurs in all cases for $ka < 1$. It would be useful to explore the behavior of the form function as a function of ka for a few of the lower order modes. In Figure 3.6, the $m = 0, 1, 2$ order terms of the backscattering form function (Eq. 3.23) are plotted along with the full solution. It is clear that the m–th order peak in the partial–wave solution arise as a direct consequence of m–th order term in the expansion of Eq. (3.23).

Also, we should remark that the lowest order peak is dependent solely on the $m = 0$, monopole term, of the series expansion. For the lowest order peak,
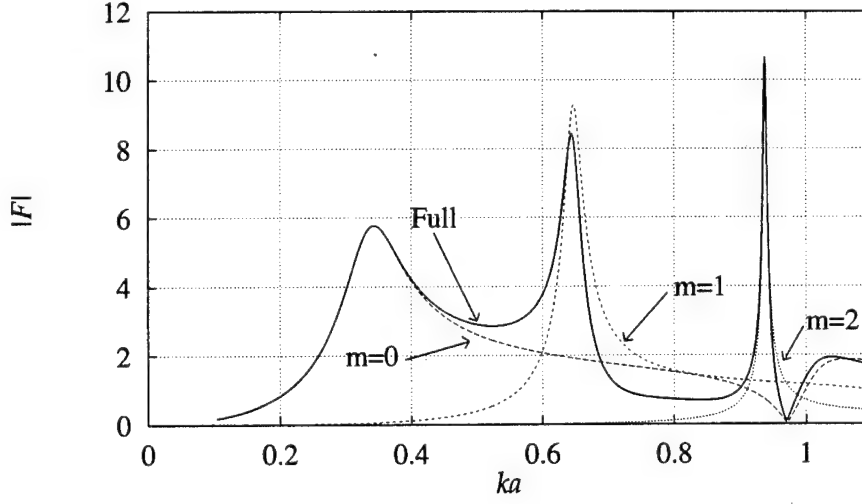
Figure 3.6: Modes of sphere with $g = 0.999$ and $h = 0.208$ plotted against ka.

an approximation to the form function is obtained by expanding the $m = 0$ term of the series (Eq. 3.24) to lowest surviving order in ka. Small argument approximations to the spherical Bessel and Neumann functions (since $h_m(x) = j_m(x) + in_m(x)$) are given by the following expansions :

$$j_o(x) = \left\{ 1 - \frac{\frac{1}{2}x^2}{3} + \frac{\left(\frac{1}{2}x^2\right)^2}{2!(3)(5)} - \cdots \right\},$$

$$n_o(x) = \frac{1}{x}\left\{ 1 - \frac{1}{2}x^2 + \frac{\left(\frac{1}{2}x^2\right)^2}{2!(1)(3)} - \cdots \right\}.$$

Upon making these substitutions and retaining only the lowest order surviving terms of ka, we find that the form function is approximated by

$$|\mathcal{F}| \approx \frac{(ka)^2}{3} \left| \frac{1 - gh^2}{\left(gh^2 - \frac{(ka)^2}{3}\right) - i\frac{(ka)^3}{3}} \right|. \tag{3.30}$$

91

Thus, for $ka < 1$, the magnitude of the slope of the form function is $(ka)^2$, exhibiting what is known as Rayleigh scattering behavior[2]. The peak in this limiting form is clearly dependent on the density and sound–speed squared ratios and the monopole resonance frequency is well approximated by equating the real portion of the denominator (Eq. 3.30) to zero. Employing this approximation, it is found that

$$0 \equiv \left(gh^2 - \frac{(k_o a)^2}{3} \right) \tag{3.31a}$$

$$k_o^2 = \frac{3\rho_e c_e^2}{a^2 \rho c^2} \tag{3.31b}$$

$$\Omega_0 = \frac{c_e}{2\pi a} \sqrt{\frac{3\rho_e}{\rho}}. \tag{3.31c}$$

In Eq. (3.31), $k_o = 2\pi \Omega_0 / c$ is the resonance wave number, Ω_0 is the monopole resonance frequency (in Hz) for a spherical scatterer of radius a. For a bubble, we set $c_e = c_g \equiv \sqrt{\kappa P_\infty / \rho_g}$, $\rho_e = \rho_g$, and $a = R_o$ so that Eq. (3.31c) simplifies to the Minneart expression. The monopole resonance frequency (Eq. 3.31c), incidentally, agrees with our previous 'guess' in Eq. (3.26).

For a bubble cloud, the sound speed is approximated by the Wood expression (Eq. 2.9) for small ka, and we find that the monopole resonance frequency is governed by a *modified* Minneart expression, namely

$$\Omega_0 = \frac{1}{2\pi a} \sqrt{\frac{3\kappa P_\infty}{\beta(1-\beta)\rho}}. \tag{3.32}$$

In this case, the additional approximation that $\rho_e \approx \rho$ was also applied.

---

[2]The Rayleigh regime is actually noted for a $(ka)^4$ slope dependence, which is indeed the case when one expands the scattering cross section and not the form function.

At the monopole resonance, the ratio of scattered to incident pressure amplitudes (the argument of the TS in Eq. (3.22)) is:

$$\frac{|p_s|}{|p_i|} = \frac{a}{2r} \, |\mathcal{F}| \propto \frac{1}{\Omega_0 r} \left| \frac{\rho_e c_e^2}{\rho c^2} - 1 \right|. \tag{3.33}$$

As illustrated in Figure 3.7, the low frequency approximation of the form function predicts, qualitatively and semi–quantitatively, both the amplitude and resonance frequency of the scatterer. Higher order modes of the system can be solved in a similar manner (Flax *et al.*, 1981). However, it is doubtful that equations with more physical insight than Eq. (3.32) and (3.33) will be obtained.
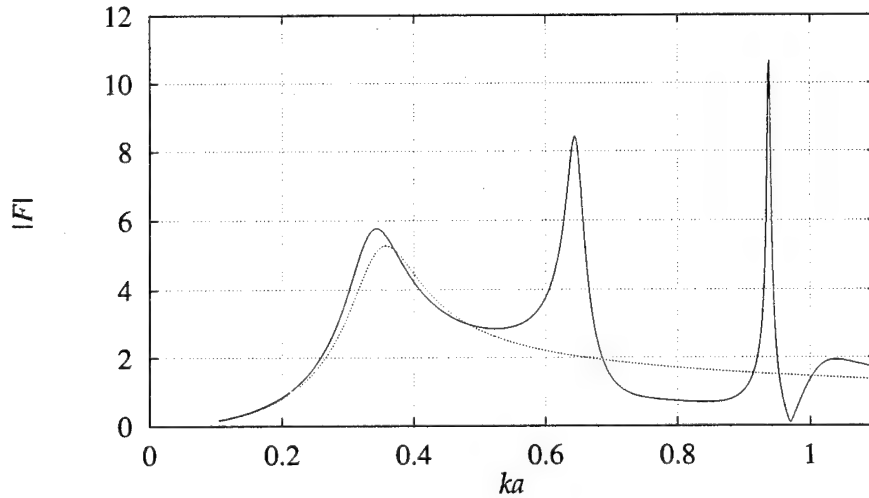
Figure 3.7: A comparison of the asymptotic form function with the exact calculation

The simple analytic expressions Eq. (3.30) and (3.31c) along with the Wood equation lead to the following conclusions for scattering at resonance: (1) For a given cloud radius, increasing the void fraction results in decreased

93

sound speed and a decrease in the monopole resonance frequency (Figure 3.8(a)). A corresponding increase in the monopole scattering amplitude is also observed (Figure 3.8(b)). (2) For a fixed volume fraction (*i.e.*, fixed sound speed), the resonance frequency decreases with increasing cloud radius (Figure 3.9(a)) and the scattering amplitude increases (Figure 3.9(b)). A particularly useful feature of these equations is their ability to predict the scattering behavior near the monopole resonance base only on the cloud radius and the void fraction. In Figures 3.8(a)–3.9(b) the solid line is calculated using the full wave expansion (Eq. 3.23) and the dashed line from the asymptotic expression (Eq. 3.30).

The asymptotic equations in Eq. (3.32) and (3.30) adequately predict the behavior of the scatterer at frequencies near the monopole peak even though the expansion used to obtain Eq. (3.33) is not mathematically valid for the $k_e a > 1$, as will usually be the case for a low sound speed scatterer. Perhaps the most interesting result is that using simple asymptotic expressions we can easily predict Ω_0 (Eq. 3.32), the TS surrounding the resonance frequency (Eq. 3.30), and c_e (Eq. 2.10b) to within an acceptable margin having knowledge of only the cloud radius and the void fraction. Furthermore, the monopole resonance for other cloud geometries (cylinders, spheroids, etc) should be well approximated by these simple expressions provided that the aspect ratio does not vary considerably from unity. For such cases, we need only the total gas volume in the cloud and total liquid volume enclosing the mixture to determine the equivalent radius, void fraction, and therefore determine Ω_0, TS, and c_e.

From Figure 3.9 it is evident that a 0.1 m-radius cloud with void fraction
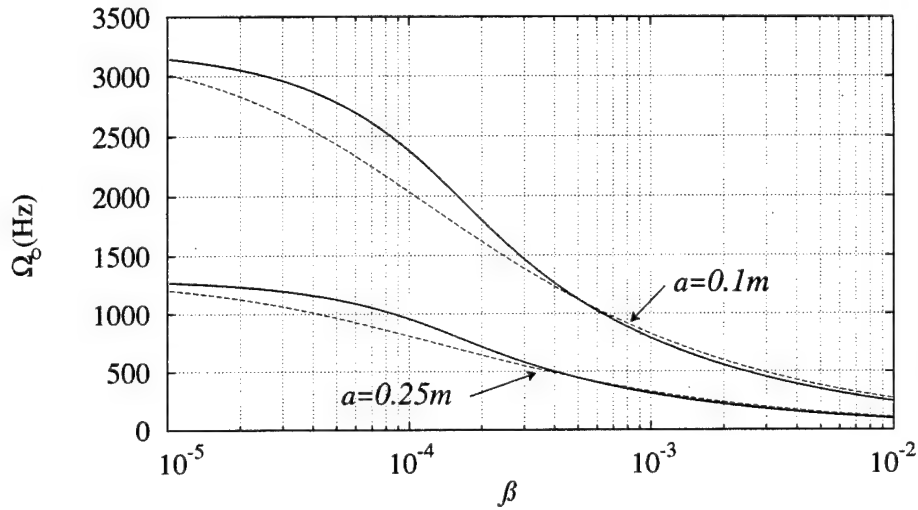
(a) Peak monopole resonance frequency.
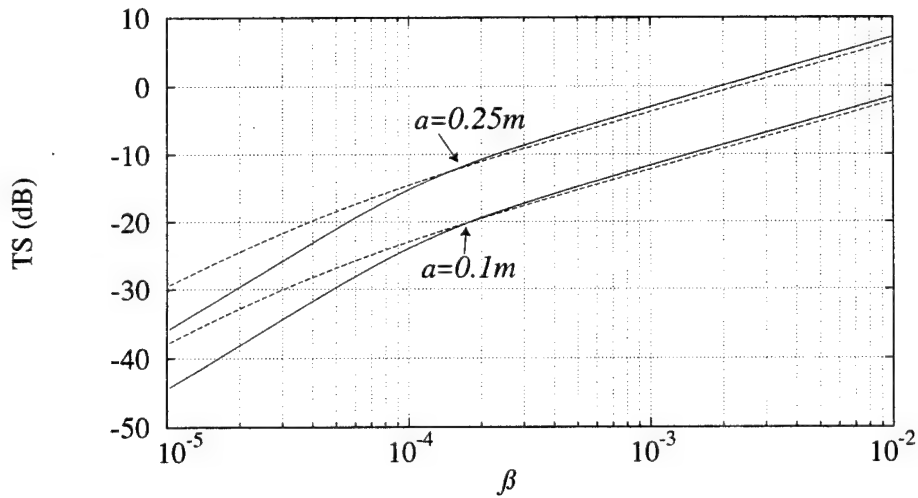
(b) Peak TS evaluated at monople resonance frequency.

Figure 3.8: Peak monopole TS and frequency as a function of void fraction for cloud radii $a = 0.1\,\text{m}$ and $a = 0.25\,\text{m}$ using the exact series expansion (solid) and the asymptotic expression (dashed).
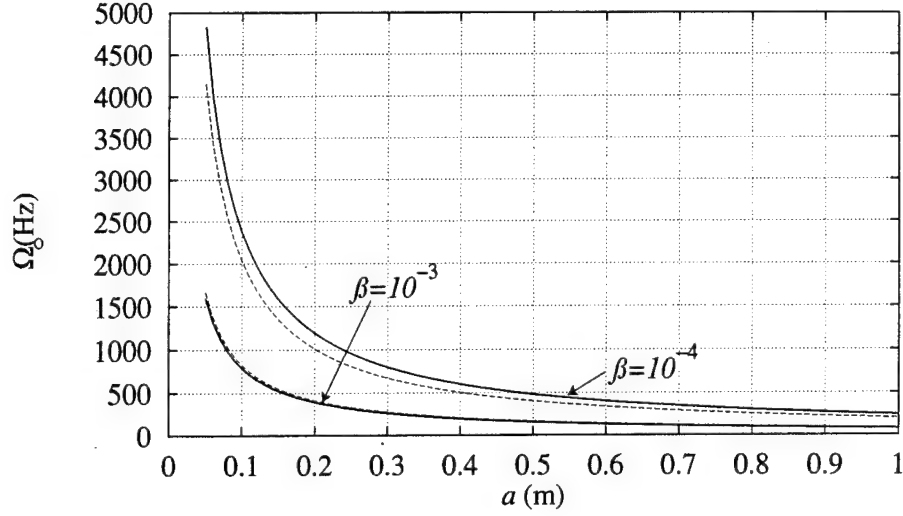
(a) Peak monopole resonance frequency.
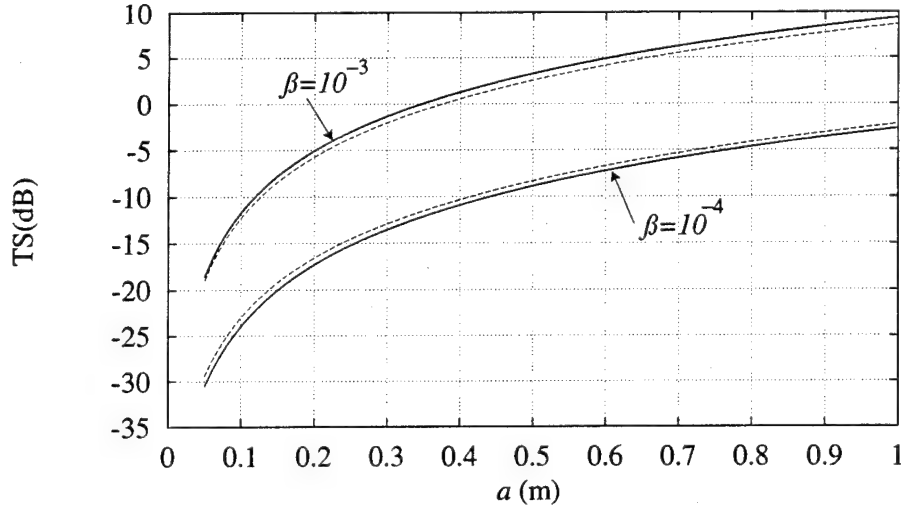
(b) Peak TS evaluated at monople resonance frequency.

Figure 3.9: Peak monopole TS and frequency as a function of cloud radius for a void fraction of $\beta = 10^{-4}$ and $\beta = 10^{-3}$ using the exact series expansion (solid) and the asymptotic expression (dashed).

96

10^{-3} resonates at about 800 Hz with a target strength of about -11 dB. The latter two numbers are consistent with the observations of Adair and Huster (Figure 1.4). Furthermore, the cloud size and void fraction suggested here are not outside the realm of possibility (Monahan & Lu, 1990; Lamarre & Melville, 1992). It would appear then that this model may have some validity. To examine this hypothesis further, a carefully controlled experiment was recently conducted in a fresh water lake in New York state (see Part II of this document).

3.5   Discussion and Summary

In this chapter the theory for acoustic scattering from a compliant sphere in the free–field was presented. The solution for the scattered pressure at every point in the sphere's exterior is given by the normal mode expansion (Eq. 3.12). The classical solution was obtained by simply meeting the requirements on the boundary of the sphere of continuous pressure and continuous normal particle velocity and by exploiting the symmetry of the problem. Although not limited to scattering from acoustically compact bubble clouds, this problem yields itself to a simple and straightforward analysis using the well established collective oscillations model for the effective sound speed and effective density as outlined in Chapter 2.

In addition to the partial wave expansion, simple analytical expressions were derived which approximate qualitatively, and semi–quantitively, the monopole resonance frequency Ω_0 (Eq. 3.32) and the TS (Eq. 3.33) at this

97

resonance of a bubble filled sphere. It was determined that the resonance frequency and TS depend only on two physical characteristics of the bubble cloud: the radius (a) and the void fraction (β). It is important to stress that the monopole TS level and Ω_0 can always be obtained without a detailed knowledge of the bubble size distribution.

Since upper ocean dynamics (or even laboratory experiments) will not likely produce spherical bubble clouds, it is obvious that other geometries (cylinders, cones, ellipsoids, or arbitrary shaped volumes etc.) should be explored. As in the solution presented in this chapter, the scattering form function for other geometrical shapes can also be expressed as a series expansion of monopole, dipole, quadrupole and higher order terms. But for long wavelengths (*i.e.*, $\lambda > 2\pi a$), the monopole (volume) mode is the most important and thus the object can be assumed spherical. Then the scattering can be expressed as a simple function, dependent only on the void fraction and *equivalent* (spherical) radius. A comparison of a measurement with the model presented here can be made if the total cloud volume and total volume of gas injected into the bubble cloud are known, since the void fraction and equivalent spherical radius are determined from these quantities.

The prime motivation in this effort was to solve the problem of sub–kilohertz backscattering of sound from bubble clouds. At such frequencies, the wave length of sound in water can be considerably greater than the gross dimensions of the cloud. As such, the choice of a sphere is appropriate. Selecting a more complex geometry will not likely enhance the physical understanding of the problem, except of course at higher frequencies. Furthermore, the assump-

tion of uniform void fraction throughout the interior of the sphere, although non–physical from an oceanographic stand point, is nevertheless a first step at understanding the problem.

Part II

Acoustic scattering from bubble clouds in the absence of boundaries: Experiment

Chapter 4

The Lake Seneca experiment: Project overview and bubble cloud generation

4.1 Introduction

The Office of Naval Research in the fall of 1988 initiated the Sea Surface
Scattering Special Research Program. From this program evolve a small
consortium of investigators advocating laboratory and lake experiments de-
signed to determine the mechanisms governing low–frequency sound scatter-
ing from bubble clouds. As a result, an experiment was designed to measure
the frequency–dependent backscatter from a bubble cloud in fresh water (Lake
Seneca, NY) in the absence of boundaries and under known propagation con-
ditions. In these efforts we did not set out to duplicate *realistic* salt–water

clouds, but rather to obtain data to test and validate a low–frequency bubble cloud scattering theory.

A series of three experiments were performed in the Fall–'90, Summer–'91, and Fall–'91. The experiments were conducted under conditions that were generally calm: daily sound velocity profile measurements were taken which showed isovelocity conditions from a depth of 65 m down to the bottom of the lake. The lake was roughly 160 m deep at the test location, with an additional 120 m of soft mud below this; the distance to the nearest shore was over 1.5 km. The initial experiment, performed at 25 m–depth, successfully served as a qualitative proof of principle that bubble clouds are indeed efficient scatterers of sound at frequencies below individual bubble resonance. However, neither the cloud volume nor the bubble size distribution within the cloud could be measured *in situ* , and therefore a subsequent modeling effort proved untenable. In addition, the source used to insonate the cloud, a parametric source (PS), relies on a nonlinear interaction of two colinear sound beams in the water to produce a highly directional low frequency sound beam at the difference frequency. Concern existed that the observed scattering returns were due to nonlinear 'enhancement' of the parametric source level caused by the highly nonlinear bubbly fluid, rather than due to scattering from an effective medium possessing low sonic velocity at frequencies below bubble resonance (recall the collective oscillations model). This hypothesis, although deemed unlikely, warranted further exploration using a conventional sound source to substantiate the parametric source measurements. This required that the experiment be performed at greater depth to insure that reverberation

102

from the lake surface did not contaminate the measurements.

To resolve these issues, a second test was performed in which a submersible video camera and both the PS and conventional sources (CS) were deployed. The camera was mounted on the surface of the bubble maker to record the size distribution of bubbles ejected from the needle tips and was also used to image the cloud characteristics (*i.e.*, shape, size, rise velocity, and void fraction). The conventional sources played an important, but limited, role in the scattering measurements. The objective was to compare the measurements from the PS and CS in order to belay the notion that parametric enhancement occurred. The advantage of a parametric source is that it provides a highly directional low frequency beam (at the expense of reduced source level). This directionality results in reduced volume reverberation from unwanted scattering sources in the vicinity of the test range[1]. This effort confirmed that a PS is a viable tool to perform directional low frequency scattering experiments from artificially generated bubble clouds.

The data collected during the second experimental effort verified that excessive nonlinear enhancement did not occur and thus the PS was a viable research tool for performing target strength (TS) level measurements. However, the parametric–source based scattering data was limited to frequencies above 800 Hz due to low signal to noise levels. The third and most important experiment was performed in the Fall of 1991 after reconditioning the PS to enhance its output capability. In this effort, measurable scattering was observed down to frequencies as low as 250 Hz. The data collected during the

---

[1]Fish and possibly other unknown apparatus deployed from the test platform. Ours was not the only experiment being conducted at the time.

final experimental effort clearly indicated that the bubble cloud possessed a broad monopole resonance peak having a TS near -4 dB at frequencies between 300 and 350 Hz. Both the TS and the monopole resonance frequency of the cloud (Ω_0) agreed to within experimental uncertainty with results from the simple analytical model outlined in Chapter 3, given a measured bubble cloud radius of $a = 0.38$ m and void fraction $\beta = 5.4 \times 10^{-3}$. Recall that a perfectly reflecting sphere having radius $a = 2$ m possesses a target strength of 0 dB. The fact that a 300 Hz sound wave incident on an acoustically compact bubble cloud ($a < 0.5$ m) can scatter sound in the free field so effectively is remarkable.

Besides the PS, the most critical piece of equipment employed in these efforts was the National Center for Physical Acoustics (NCPA) bubble cloud generator, for without it this experiment could not have been performed. It consisted of a pressurized steel air reservoir which was vented to the lake by three concentric rings of 22–gauge hypodermic needles (48 needles total). The bubbler could be operated in either a continuous mode in which a steady column of bubbles was produced, or in a transient pulsed mode in which bubble cloud bursts were introduced into the lake on demand. Air was supplied to the bubble maker from a compressor located on the barge and the internal over–pressure in the bubble maker and burst duration (the time that air was allowed to flow freely through the needles) were regulated from the surface, allowing bubble clouds to be generated on demand. The operation of the bubble maker is discussed in detail in Section 4.2.

In this chapter, the operation of the transient bubble maker and bubble

104

cloud characterization measurements are detailed. The total cloud volume, the total gas volume injected into the cloud, the rise velocity, and the bubble size distribution were measured non–acoustically using the video tape data. These parameters are needed to estimate the void fraction and radius of an equivalent volume sphere. Finally, these measurement allow us to make a comparison of the scattering measurements (see Chapter 5) with the simple analytical model presented in Chapters 2 and 3.

4.1.1 Sound speed profile

Shown in Figure 4.1 are measured sound speed profiles obtained during the Summer and Fall–'91 efforts. Profiles were measured daily during the test by lowering a thermistor chain from the edge of the test platform. The near sur-face sound speed profile (< 10 m) was variable as one might expect. Figure 4.1 clearly illustrates that at depths below 61 m iso–velocity conditions prevailed. This assured us that significant refraction of sound rays propagating across the test range did not occur. Consequently, a ray launched at a declination angle of 35.2° at a depth of 61 m will, in accordance with Snell's law, have a declination angle of 35.2° at a depth of 87.6 m (300 ft). For the calculations presented herein, a sound speed of 1421.5 m/s was used.

4.2 Bubble maker deployment and operation

The heart of the experiment was the bubble cloud generator. Illustrated in Figure 4.2, the bubble maker consisted of a submersible pressurized steel air
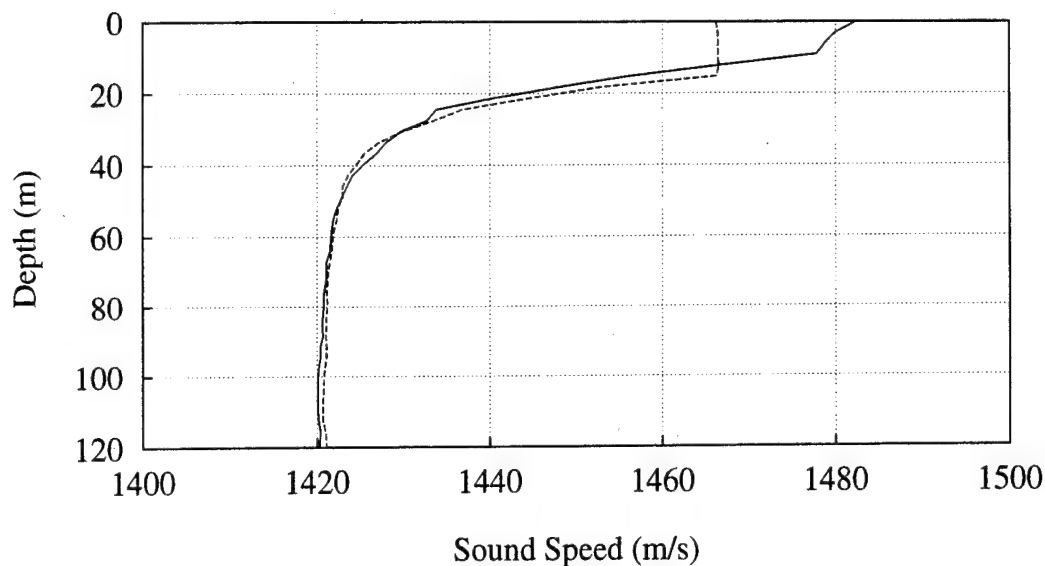
Figure 4.1: Sound speed profile at Lake Seneca test site. The dashed line represents sound speed for the Summer–'91, and the solid line the Fall–'91. At a depth of 87.6 m (300 ft) the sound speed was 1421.5 m/s.

reservoir which was vented to the lake by three concentric rings of 28–gauge hypodermic needles (8, 16, and 24 needles per ring; 48 total). It could be operated in either a continuous mode in which a steady column of bubbles was produced, or in a transient pulsed mode in which artificial cloud bursts were released into the lake. Air was supplied to the bubble maker from a compressor located on the barge. The internal over–pressure in the bubble maker and burst duration (the time that air was allowed to flow freely through the needles) were regulated from the surface, allowing bubble clouds to be generated on demand. A diagram illustrating the bubble maker is shown in Figure 4.3 and its operation is described below.

The bubble maker was lowered over the edge of the barge to a depth of 91.4 m beneath the lake surface, or 3.8 m beneath the expected backscat-
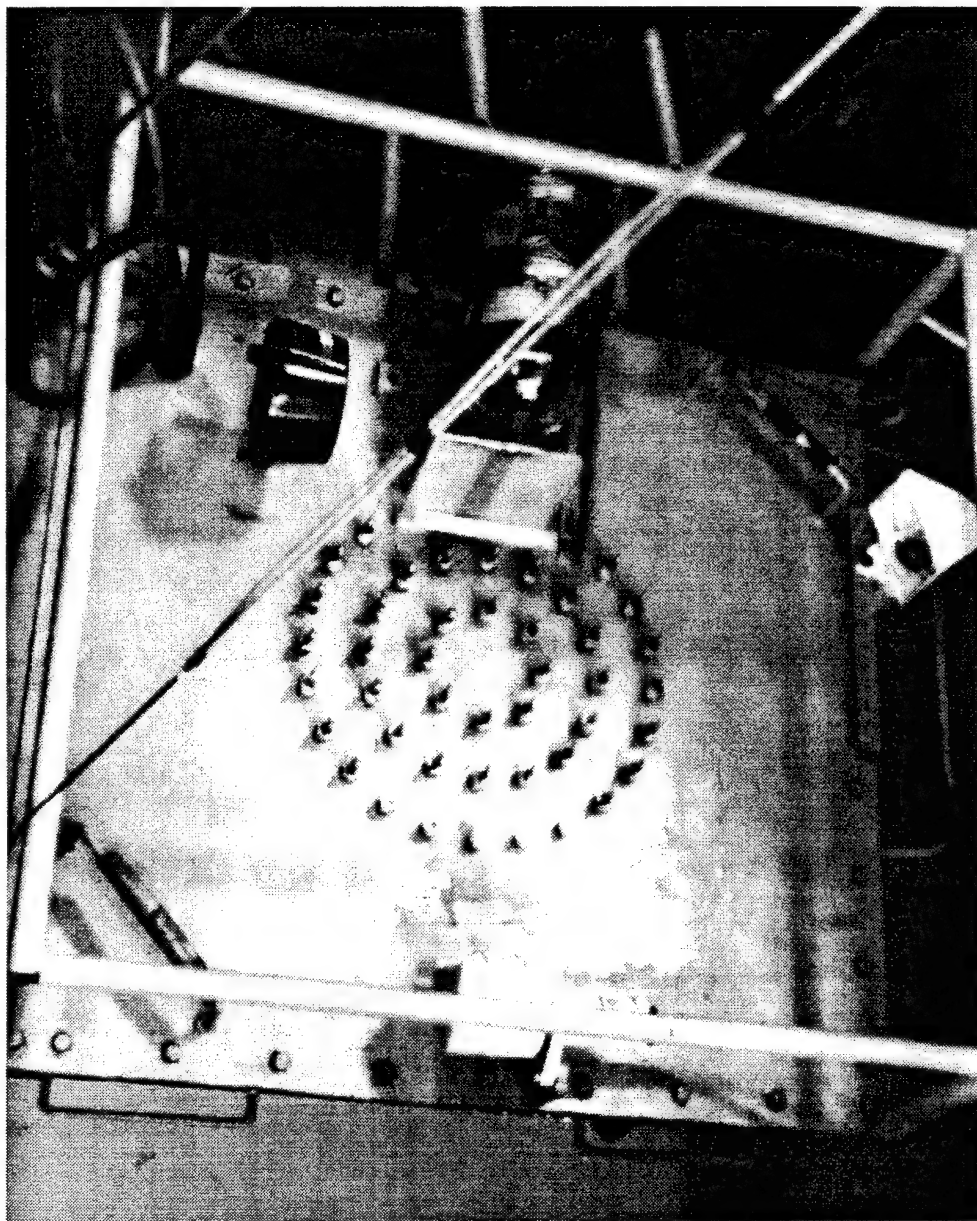
Figure 4.2: Photograph of the bubble maker.

ter target position (see Figure 5.1 for the layout of the test range) . It was

supported by a davit mounted on the top face of the barge with a 1/4–inch

steel cable. The depth of the bubble maker was determined using the cable
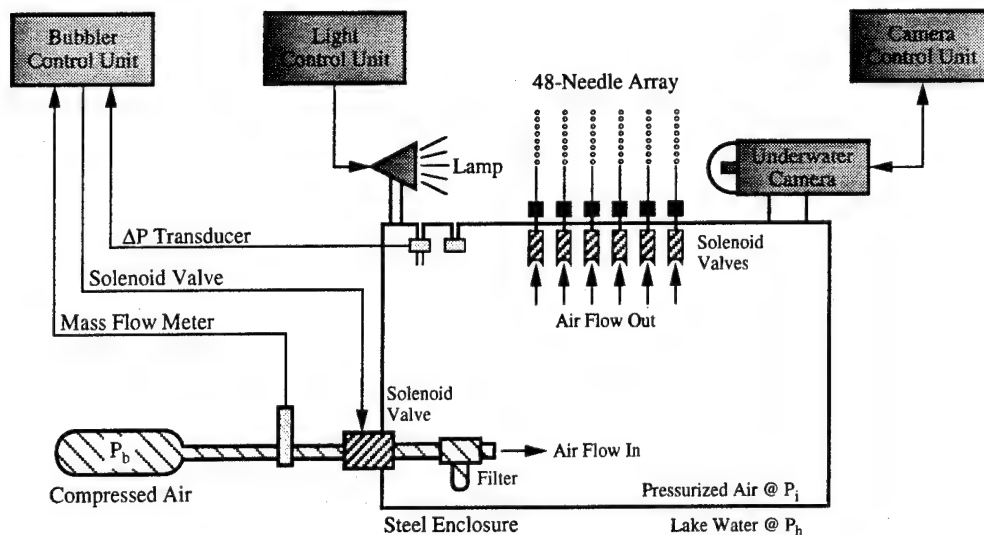
Figure 4.3: Schematic of the Seneca Lake bubble maker.

meter used to deploy the hydrophones and the steel target sphere. In addition, an absolute electronic pressure transducer was mounted on the interior of the bubbler, but exposed to its exterior. This provided a secondary means of determining the depth by measuring the ambient hydrostatic pressure. Electrical power was provided to this pressure transducer and the other electronic elements (solenoid valves, and the $\triangle P$ transducer) via a 10 conductor submersible cable connected to the Bubbler Control Unit (affectionately named *Deep Thought*) located inside the barge.

Since the hydrostatic pressure increases with depth, the bubbler depth and internal pressure were increased incrementally, to prevent implosion. At each 5 m depth increment the lowering process was halted and several clouds were released from the bubbler in order to purge water from the syringe nee-

108

dles and to insure re–equilibration of the internal pressure to a level 10 psi greater than the hydrostatic pressure at depth. Individual cloud releases were visually monitored with the PhotoSea Cobra submersible video camera which was mounted on the surface of the bubble maker (see Figures 4.2 and 4.3) in order to confirm that air flowed freely through all the needles.

During the deployment phase, the internal pressure of the bubble maker was maintained at 10 psi above the ambient hydrostatic pressure at a given depth. To consistently and accurately maintain the over–pressure inside the bubbler an electronic "regulator" system was designed which consisted of the following components: an electric differential pressure transducer ($\triangle P$); an electronic input solenoid valve (normally closed); an air supply line pressurized 30 psi over the ambient pressure at depth and connected to the input solenoid; and the bubble maker controller, *Deep Thought.*

The $\triangle P$ transducer measured the difference in the external hydrostatic pressure relative to the interior of the bubble maker, transmitting it as a voltage to *Deep Thought.* The overpressure was configured automatically controlled and nominally set to 10 psi maximum and 9.5 psi minimum. Throughout the experiment, *Deep Thought* continuously monitored the $\triangle P$ to assure that the over–pressure did not drop below the preset value of 9.5 psi. As a precautionary measure, an analog pressure gauge displaying the difference in internal and external pressure of the bubble maker was installed on the surface of the bubble maker and was occasionally monitored using the underwater video camera. Data from this pressure gauge was not recorded since the electronic transducers performed as expected.

When $\triangle P$ fell below 9.5 psi, the bubble maker controller activated the normally–closed "input solenoid" mounted inside the bubbler allowing air to flow into the reservoir. Once the input solenoid was activated, the inflow of air continued until $\triangle P$ reached 10 psi. The pressurized air was provided by a compressor located on the barge surface; as a safety backup, a compressed nitrogen cylinder was also placed inline. The air source was pressurized to 30 psi above the internal pressure of the bubbler in order to fill it quickly as clouds were produced. In addition, air filters (designed trap particulates and fluids) were placed inline at the compressor output and the bubble maker input.

Three concentric rings containing 8, 16, and 24 needles (22–gauge) were mounted on the surface of the bubble maker (see Figure 4.2). Each pair of needles, opposite one another on a given ring, were controlled via a single normally–closed solenoid valve mounted in the interior of the bubble maker. The burst duration, the time that air was allowed to freely flow from the needle tips, and the opening of a single, pair, or all rings of needles were controlled remotely from *Deep Thought*. The cloud production parameters are summarized in Table 4.1.

$\triangle P = 10$ psi	# Needles = 48
$t_{\text{burst}} = 3.4$ s	Depth = 91.4 m

Table 4.1: Cloud generation parameters.

In Figure 4.4, the digitized and scaled output from the $\triangle P$ transducer is displayed. A single cloud was released at $t = 0$ s at which point the internal over–pressure was 9.9 psi. As air exited the bubble maker, the internal pressure

decreased. When the internal pressure reached 9.5 psi, the air supply input solenoid valve was opened forcing air into the bubble maker; a corresponding increase in the over–pressure is observed. To end bubble cloud production (at time $t_{burst} = 3.4$ s), the solenoid bank controlling the needle ports was deactivated. Air from the supply line continued to fill the bubbler and $\triangle P$ quickly returned to 10 psi, at which point the input solenoid was closed. Note that in Figure 4.4, the over–pressure decreases slightly during the next 40 s after the bubble cloud generation. This was casued by a pair of needles which continuously released a few bubbles per second as viewed on the video monitor. This leak was small and of negligible importance.
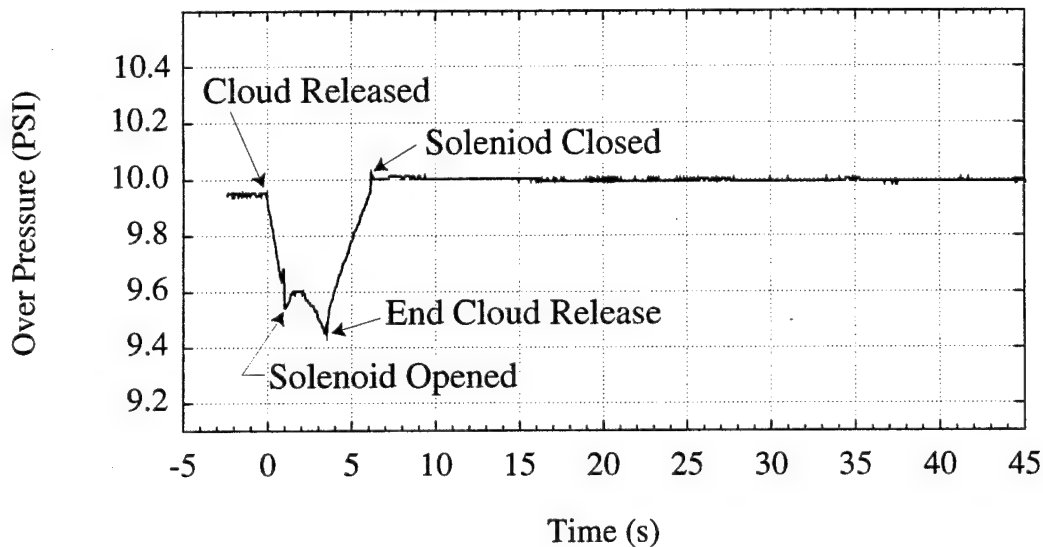
Figure 4.4: Pressure difference ($\triangle P$) between the lake and the bubble maker at a depth of 91.6 m as a function of time during a cloud release. The cloud was released at $t = 0$ at which point the internal pressure decreased. The electronic regulator was set to a 0.5 psi threshold at which point the input solenoid was opened allowing air to enter the bubble maker.

4.3 Bubble cloud characterization

In order to make a comparison between the transient bubble cloud scattering measurements and the model, it is necessary to have a detailed knowledge of the cloud shape and volume, bubble size distribution, rise velocity, and position. Since our interest is in backscattering, these values need only be known when the bubble cloud passes through the backscatter target position (recall Figure 5.1). With this information, the effective phase speed of sound in the bubbly mixture can be estimated. Furthermore, by solving the boundary value problem of the system, the backscatter TS as a function of frequency can be determined. The solution of this problem will result in the resonance frequencies or modes of the system, as well as the scattering cross section (or target strength) as a function of frequency. However, our ability to measure the physical attributes of the bubble cloud (especially the shape and spatial distribution of bubbles) with accuracy was limited by various physical constraints. Therefore explicit agreement of the scattering model presented in Chapters 2 and 3 with the measurements (Chapter 5) is difficult, except at the lowest frequencies (*i.e.*, $ka < 1$).

For low frequencies, where the bubble cloud is considered acoustically compact, the shape is of secondary concern provided the aspect ratio does not vary appreciably from unity. Recall that the lowest order mode of an acoustically compact scatterer is dependent on the volume of the target and thus the spherical model outlined earlier should be sufficient to predict the monopole scattering characteristics of the bubble cloud. To estimate the TS of a bubble cloud in the free–field at the lower frequencies, only the volume

fraction (β) and cloud radius (a) need to be known. These two quantities were obtained by measuring the total cloud volume (V_{cloud}) and the total volume of air (V_{gas}) injected into the cloud, since $\beta = V_{gas}/V_{cloud}$ and $V_{cloud} = 4\pi a^3/3$. For an acoustically compact bubble cloud, the bubble size and spatial distribution is of minimal importance as long as the frequency of the incident wave is much less than the resonance frequencies of the constituent bubbles (*i.e.*, $kR_o \ll ka < 1$). To verify that the prior condition was satisfied, the bubble radius distribution was also measured as well.

4.3.1   Bubble cloud rise time

The rising bubble clouds viewed on the monitor at a height of 3.8 m above the bubble maker appeared to be nominally cylindrical shaped with a blunt leading edge and a trailing skirt of bubbles. The distinction between the 'skirt' and the more densely populated regions of the bubble cloud was not obvious and therefore an "educated–guess" was made. The video camera was deployed in the configuration shown in Figure 4.5. It was not possible to view an entire bubble cloud at any instant in time. This was due to the short separation distance between the bubble cloud and the submersible camera (< 0.6 m). These measurements were performed on the last scheduled day of the experiment, preventing redeployment of the camera and lighting rig.

To determine the rise velocity, shape, and total volume of the bubble cloud as it crossed the axis of the test range, video recordings were made. During these measurements, the Photosea Cobra underwater video camera and lighting system were mounted at the backscatter target position on the

113
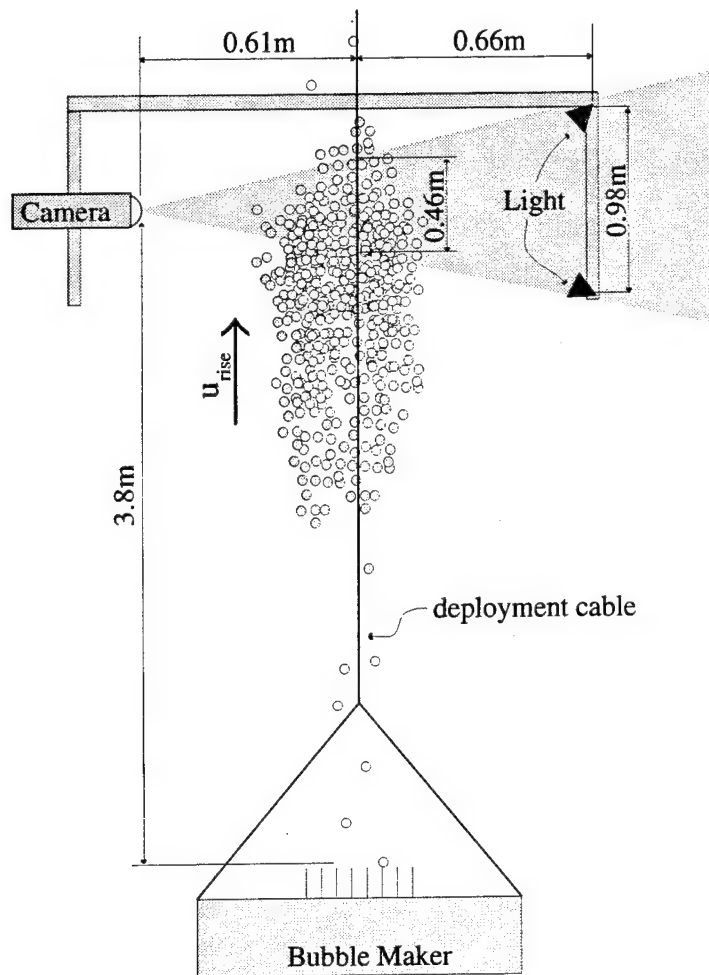
Figure 4.5: Video rig used to measure physical parameters of cloud at depth.

suspension cable 3.8 m above the bubble maker. A diagram illustrating the geometry of the camera and lighting station used to perform the rise time, and cloud volume and shape measurements is shown in Figure 4.5. The video camera was focussed on the plane perpendicular to the suspension cable and the field of view was approximately 0.46 m vertical and horizontal in the focal plane. The viewing area is indicated in the Figure 4.5 by the triangular region.

The bubble cloud rise–time into the backscatter position was measured

from a series of 30 bubble cloud releases separated by 10 s intervals. From the rise–time measurements, the cloud rise velocity and cloud length were inferred. The rise–times for the upper and lower cloud boundaries to pass the video camera relative to the beginning of cloud release ($t = 0$) were measured using a digital stop watch. The top rise time was $t_{\text{top}} = 9.1 \pm 0.5 \, \text{s}$ and the bottom rise time was $t_{\text{bottom}} = 13.6 \pm 0.5 \, \text{s}$, where the error indicates standard deviation in the measurements.

4.3.2 Bubble cloud rise velocity

The velocity of the upper and lower boundaries of the bubble cloud were deduced by dividing the rise distance ($z = 3.8 \, \text{m}$) by the appropriate rise times as follows: $u_{\text{top}} = z/t_{\text{top}}$, and $u_{\text{bottom}} = z/t_{\text{bottom}} - t_{\text{burst}}$, where $t_{\text{burst}} = 3.4 \, \text{s}$ is the burst duration (the length of time that air was allowed to escape from the bubble maker needle tips). Consequently, $u_{\text{top}} = 0.41 \pm 0.034 \, \text{m/s}$ and $u_{\text{bottom}} = 0.37 \pm 0.012 \, \text{m/s}$, where the error is estimated using a modified Taylor expansion as described in Appendix D.

The mean velocity of the bubble cloud, $u_{\text{rise}} = 0.39 \pm 0.023 \, \text{m/s}$, is the average of u_{top} and u_{bottom}. It should be noted that the cloud boundaries—top, radial, and especially bottom—are not well defined and thus an "educated" guess was made.

4.3.3 Bubble cloud length

The cloud length is given by the simple expression: $L = u_{\text{rise}} (t_{\text{bottom}} - t_{\text{top}})$. For the rise times and cloud velocity given above, the cloud length is: $L =$

1.7 ± 0.18 m.

4.3.4 Bubble cloud shape and volume

In addition to the difficulty of accurately determining the upper and lower boundaries of the bubble cloud, the sides of the bubble cloud was not well defined. Furthermore, the width of the rising bubble cloud exceeded the field of the view on the video monitor because of the inadequate spacing between the video camera and the rising bubble cloud (see Figure 4.5). To compensate for this fact, the video camera was panned to the left of the cloud in order to record an image of the right edge of the several rising clouds; similarly, the camera was panned to the right to view an image the left half of several rising clouds. In both cases, the cable used to lower the bubbler and to support the video camera and lighting rig was kept in the field of view and used as a fixed point of reference.

To determine the cloud shape and volume, the video tapes were played back and the distance between the reference point (the support cable) and a edge of the bubble cloud was measured as a function of cloud height (actually rise time). Since the entire cloud did not fit into the field of view, a sequence of photographs were taken directly from a video monitor. The 35 mm camera used to take these snapshots was mounted on a tripod and focussed on the video monitor. During the playback of a rising bubble cloud, the video tape was paused when upper boundary of the cloud was near the top of the field of view and a single photograph taken. Next, the video tape was advanced 1.4 s (*i.e.*, the amount of time required for a portion of the cloud visible on

116

the lower part of the video monitor to rise above the field of view), paused, and another snapshot taken. This process was repeated until an entire bubble cloud had passed through the viewing area.

A total of seven photographic sequences of rising bubble clouds were obtained (four right–side images, and three left–side images). A pair of these sequences, shown in Figure 4.6, were assembled and roughly illustrate the shape of a single rising bubble cloud.

It is clear from Figure 4.6 that the spatial distribution of bubbles within the cloud is not uniform, an assessment that is confused by the non–uniform lighting used to illuminate the cloud. Thus, an attempt to estimate the spatial bubble population density within the cloud was not made. In Figure 4.6, the curvature or "bulges" indicated in each photograph of this mosaic is due to distortion of the image by the video camera lens or its perspex pressure dome. When viewed on the video monitor, the cloud appeared to "roll" rather than rise.

The bubble cloud image in Figure 4.6 was divided into 32 segments equal segments about the cloud length ($dL \approx 5\,\text{cm}$) and the radial versus height profiles of the left and right hand edge of several clouds were estimated relative to the suspension cable. This radius–height profile was then used to determine the total volume of the bubble cloud by accumulating the volumes of conical frustum bounded by adjacent radii and height dL. A sample frustum is illustrated in Figure 4.7, and the total cloud volume is given by

$$V_{\text{cloud}} = \frac{\pi}{3} \sum_{i=1}^{32} (a_i^2 + a_i a_{i+1} + a_{i+1}^2) dL \,,$$

117
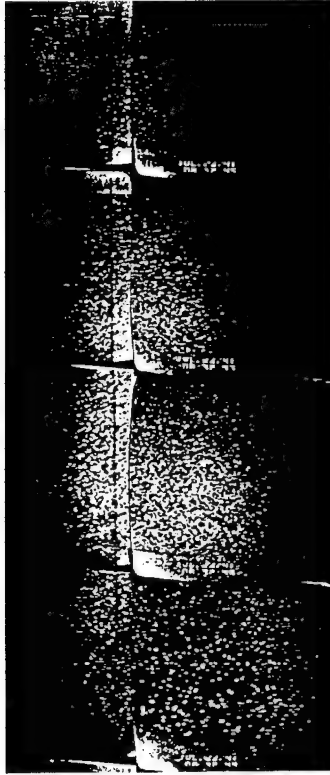
Figure 4.6: Mosaic of a bubble cloud. A series of snapshots were taken directly from the video monitor during tape playback. The images to the left and to the right were not taken from the same cloud. However, the sequence of photos in each column were obtained from a single rising bubble cloud. In each column, each consecutive snapshot is separated in time by approximately 1.4 s. Notice the variation in bubble population density. The dark vertical stripe in the left portion of the image is the suspension cable used to lower the bubble maker. Thus it is clear that the bubble cloud rose slightly off axis due to a slight current in the lake.

where a_i refers to the i–th radial element. The total cloud volume then is

$$V_{\text{cloud}} = 222 \pm 0.027\, l,$$ where the radius–height profile is given in Table 4.2.
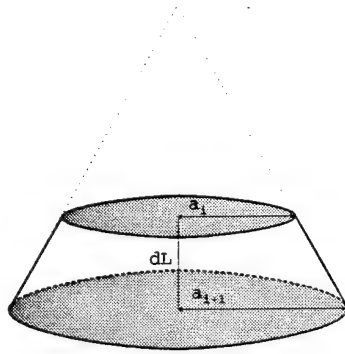
Figure 4.7: Frustum of a cone. The total volume of the bubble cloud was determined by accumulating 31 frustum volumes using the radial measurements in Table 4.2

4.3.5 Effective bubble cloud radius

Although the bubble cloud image in Figure 4.6 is clearly non–spherical, the monopole scattering response (volume mode) can be estimated using the sphere model outlined in Chapter 3. Thus for a spherical cloud of volume $V_{cloud} = 222 \pm 0.027 \, l$, the radius of the cloud is $a = 0.37 \pm 0.014 \, \text{m}$. We are now left to determine the net void fraction of the bubble cloud.

4.3.6 Total gas volume measurement

To determine the total volume of gas injected into a single bubble cloud, an precision electronic flow meter (Porter Instrument Co., Model 113) was mounted inline with the bubble maker air supply line on the barge surface. V_{gas} is a critical quantity needed to determine the void fraction, and thus used to make an unbiased comparison of the model with the acoustic scattering measurements. The voltage output from the flow meter is proportional to the

119

Table 4.2: Radius versus height profile of the Lake Seneca bubble cloud.

Height (m)	Radius (m)	Volume (l)	Height (m)	Radius (m)	Volume (l)
0.00	0.106	2.150	0.85	0.234	8.6
0.05	0.121	2.506	0.96	0.238	9.3
0.11	0.124	3.044	1.0	0.24	9.2
0.16	0.146	3.949	1.1	0.23	9.1
0.21	0.162	4.755	1.1	0.23	9.2
0.27	0.176	5.391	1.2	0.23	9.0
0.32	0.183	5.777	1.2	0.23	8.6
0.37	0.188	5.961	1.3	0.22	8.2
0.43	0.189	6.227	1.3	0.22	7.9
0.48	0.197	6.725	1.4	0.21	7.6
0.53	0.204	7.113	1.4	0.21	7.2
0.58	0.208	7.436	1.5	0.20	6.8
0.64	0.214	7.777	1.5	0.20	6.2
0.69	0.218	8.058	1.6	0.19	5.9
0.74	0.221	8.437	1.7	0.19	6.0
0.80	0.228	8.931	1.7	0.19	

Note: In the middle columns, the cloud radius as a function of height is given. In the third columns, the volume element (in liters) of a slice of a right circular cone is given for consecutive radial pairs. The total cloud volume is obtained by summing the volume elements (see Figure 4.7).

mass flow of gas in standard liters[2] through the apparatus. During a cloud release, the voltage output from the flowmeter was digitized and integrated with respect to time, and scaled to yield the total volume of gas in standard liters (V_{std}). Then $V_{\text{gas}} = (V_{\text{std}}/P_h) \cdot 10^5 \, \text{Pa}$, by the ideal gas law. Here, $P_h = 9.82 \times 10^5 \, \text{Pa}$ is the ambient hydrostatic pressure at a depth of 87.6 m beneath the lake surface.

As a bubble cloud was released from the bubble maker, $\triangle P$ immediately

---

[2]One standard liter is equivalent to one liter at atmospheric pressure (*i.e.*, , re $10^5 \, \text{Pa}$)

decreased (recall Figure 4.4). When $\triangle P$ reached 9.5 psi, the input solenoid was opened allowing air to flow into the bubble maker. The air flow entering the bubble maker, as illustrated in Figure 4.8, increased rapidly after the input solenoid was opened ($t = 1.2$ s), leveled off ($t = 3.4$ s), and decreased after the bubble maker reached its equilibrium internal over–pressure when the input solenoid was closed ($t = 6$ s).
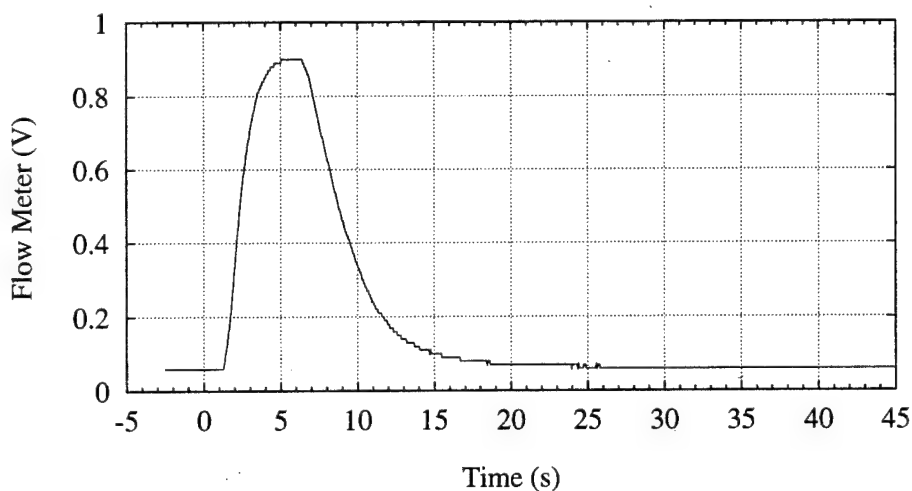
Figure 4.8: Digitized flow meter output as a function of time during a cloud release. The output was integrated and scaled to yield the total air volume injected into the cloud, nominally $1.22 \pm .014\,l$.

During the Seneca–2 experiment, the mass flowmeter output from total of 112 cloud releases was digitized at 10 points per second. The data from each cloud release was integrated and scaled to yield the cumulative mass flow in standard liters. This quantity was then converted to the equivalent gas volume at a depth of 87.6 m beneath the lake surface (the expected backscatter position of the bubble cloud). Over the course of the experiment, and for the cloud generation parameters listed in Table 4.1, the measured total gas volume

121

injected into the Lake Seneca bubble cloud was $V_{\text{gas}} = 1.22 \pm .014\,l$, where the error is the standard deviation of the measurements (recall that the total cloud volume was $V_{\text{cloud}} = 222 \pm 0.027\,l$). Thus, the mean void fraction for a single Lake Seneca bubble cloud was $\beta = 0.0055 \pm 0.001$.

As discussed in Chapter 2, the sound velocity in the bubbly mixture is well approximated by the Wood expression (Eq. 2.9) and is only dependent on the void fraction when the driving frequency of the acoustic wave is well below the fundamental resonance frequencies of the constituent bubbles. However, for large ambient pressures, like that experienced by the bubbles during the this experiment, the mixture sound speed is known to diverge from the low frequency limiting expression (Commander & Prosperetti, 1989). After simple algebraic manipulation and an order of magnitude analysis, it is clear that an improved approximation to the Wood equation can be derived from Eq. (2.24)

$$
c_e \rightarrow \left(\frac{\kappa P_\infty}{\frac{c^2}{\kappa P_\infty} + (1 - \beta)\beta\rho} \right)^{\frac{1}{2}}. \tag{4.1}
$$

Eq. (4.1) is termed the *modified* Wood expression.

Using the estimated values of the void fraction and cloud radius and applying Eq. (4.1), (3.32), and (3.33), the low frequency phase speed (c_e), monopole resonance frequency (Ω_0) and backscatter TS of the Lake Seneca bubble cloud can be estimated—assuming a spherical cloud. A further assumption made here is that the resonance frequencies of all the bubbles contained in the Seneca cloud are much greater than Ω_0 (this will be discussed in the next section).

122

4.3.7 Bubble radius distribution measurements

With the video camera and lighting rig deployed 3.8 m above the bubble maker as in Figure 4.5, it was not possible to accurately measure the bubble size distribution *in situ* . However, with the video camera mounted on the top surface of the bubble maker (as shown in Figure 4.2), imaging the size distribution of bubbles produced at a single needle tip was possible.

The Photosea Cobra video camera could be focussed down to very short distances (even onto its own perspex pressure dome), enabling us to place it very close to a single needle tip and observe single bubbles as they were released. In addition, the camera was shuttered so that the rising bubbles were not blurred depreciably, and we could therefore make precise BSD measurements. A frosted semi–opaque screen was mounted a few cm behind one of the needles and used to diffuse the background lighting from the 500 Watt Halogen bulbs. On the diffuser, a millimeter scaled ruler was secured as a second reference calibration for the measurements. In addition, the diameter of the 22 gauge needle, 0.7 mm, was used as a reference measurement. In Figure 4.9 a digitized image as viewed from the submersible video camera mounted on the surface of the bubble maker and focused on a single needle tip is shown. As was generally the case, only a few bubbles per image were in focus due to the narrow field of view. The internal over–pressure in the bubble maker was set to 10 psi and the bubble maker was pulsed for 3.4 s to generate a cloud.

Images of newly formed and rising bubbles were recorded on video tape. The size distribution of in–focus bubbles emerging from the needle tip were then measured directly from the surface of a video monitor during tape play-

<div align="center">123</div>
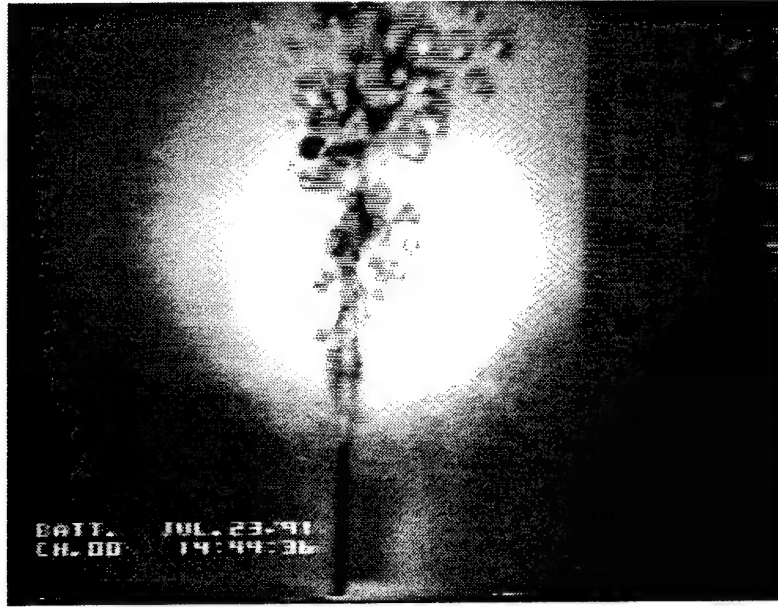
Figure 4.9: Bubbles released from single needle tip as viewed from the submersible video camera. The scaled ruler (mm gradations) is visible on the right. The bright spot in the center is due to the intense lighting needed to illuminate the rising bubbles.

back. A digitized video image is shown in Figure 4.9. Here, it is clear that the newly formed bubbles had not yet reached an equilibrium shape, and many of the bubbles are blurred due to the narrow focal plane. Because the majority of the bubbles were not spherical, it was essential to measure both the major and minor axis of the bubbles. The bubble volume was estimated using simple geometric formulas for the volume of oblate and prolate spheroids:

$$
\begin{aligned}
V_{\text{oblate}} &= \frac{4\pi}{3} a^2 b, \\
V_{\text{prolate}} &= \frac{4\pi}{3} a b^2,
\end{aligned}
$$

where, a and b are the semi–minor and semi–major axis respectively.

It is likely that the observed spheroidally shaped bubbles were prolate (*i.e.*, link sausages), rather than oblate (*i.e.*, pancakes), since they were forcefully ejected from the needle tip and had not yet obtained an equilibrium shape. Once the bubble volume was determined, the equivalent spherical bubble radius and corresponding statistical distribution were calculated and are illustrated in Figure 4.10 and listed in Table 4.3.

Since the radius of these bubbles are in the range 0.42 mm to 2.93 mm, then at a depth of roughly 91 m the range of bubble resonance frequencies is bounded roughly by 2.9 kHz and 20 kHz, according to the Minneart resonance frequency (Eq. 2.21). Thus, for all acoustic frequencies below about 2.0 kHz, the speed of sound in a cloud composed of these bubbles should be well approximated by the modified Wood expression (Eq. 4.1).

Mean	1.55 mm	Min	0.42 mm
Std. Dev.	1.40 mm	Max	2.92 mm
Counts	159	Range	2.5 mm

Table 4.3: Statistics from *in situ* BSD measured slightly above a single needle tip at Lake Seneca.

In Figure 4.10, there are clearly three visible peaks located at $R_{o,1} = 0.39$ mm, $R_{o,2} = 1.45$ mm, and $R_{o,3} = 1.95$ mm. This BSD data was fitted to a triple–Gaussian curve

$$f(a) = A_1 e^{-\left(\frac{(a-R_{o,1})}{\sigma_1}\right)^2} + A_2 e^{-\left(\frac{(a-R_{o,2})}{\sigma_2}\right)^2} + A_3 e^{-\left(\frac{(a-R_{o,3})}{\sigma_3}\right)^2} \qquad (4.2)$$

using a nonlinear least–squares method. The parameters obtained by the fit are given in Table 4.4.

125
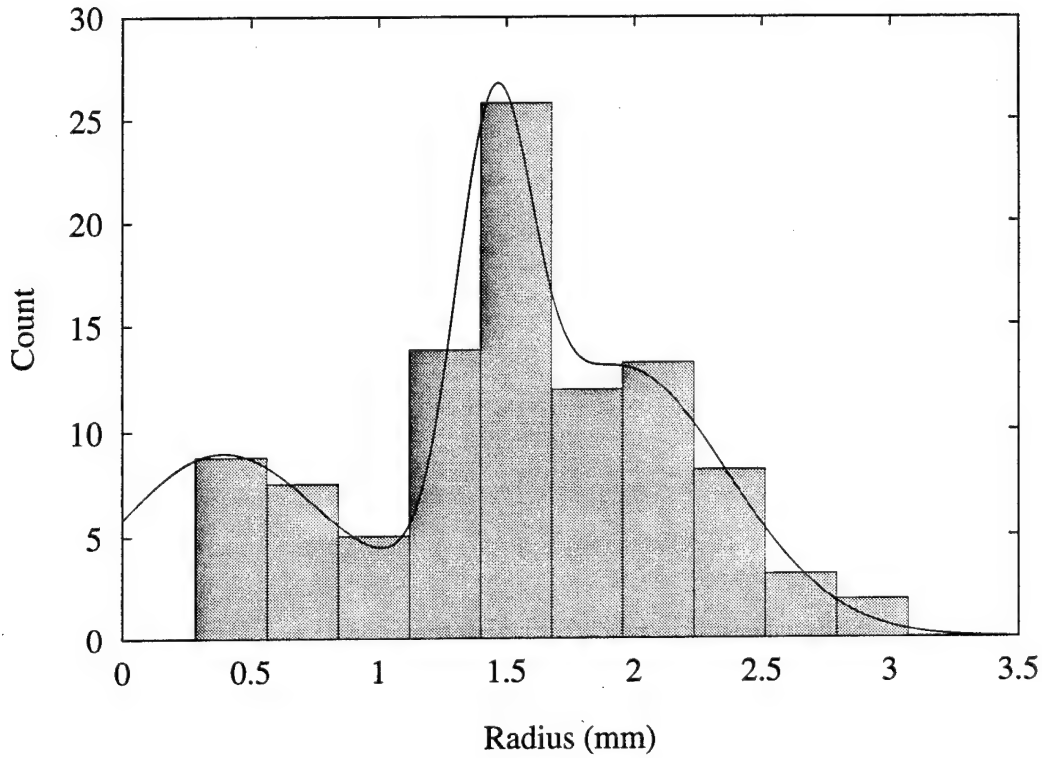
Figure 4.10: Bubble size distribution measured just above a single needle tip at Lake Seneca. The curve represents a triple-gaussian non-linear least squares fit to the measured data. For phase speed calculations the fit is truncated between 0.1 mm and 3.2 mm.

	Mean (mm)	Std. Dev. (mm)	Amp.
Peak 1	0.391946	0.59941638	8.962
Peak 2	1.44917	0.2074013	19.679
Peak 3	1.947760	0.60210049	12.982

Table 4.4: Parameters obtained from a nonlinear least–squares fit of the *in situ* BSD to a triple–Gaussian curve.

In Fig. 4.11, the frequency dependent phase speed versus frequency curve for the Lake Seneca bubble cloud is shown for each of the measured bubble size distributions (*i.e.*, monodispersed, discrete, and Gaussian). For the

monodispersed distribution, the equilibrium bubble radius is $R_o = 1.55\,\text{mm}$, the volume fraction is $\beta = 0.54 \times 10^{-2}$, and the ambient pressure is $P_\infty = 9.82 \times 10^5\,\text{Pa}$. For the discrete distribution, the mixture sound speed is calculated using the radius and amplitude values shown in the histogram of Figure 4.10. Finally for the Gaussian fitted bubble radius distribution, the triple Gaussian fit (Table 4.4) to the histogram in Figure 4.10 is applied. Note that in all cases, the phase speed is independent of frequency well below the bubble resonance frequency. In the low frequency limit the calculation of the mixture sound speed yields $c_e = 464\,\text{m/s}$. This compares favorably with the modified Wood expression (Eq. 4.1) value of 468 m/s in the adiabatic limit ($\kappa \to \gamma$). In the isothermal limit ($\kappa \to 1$), the modified Wood expression predicts a sound speed of 402 m/s.

4.4 Summary

Artificial transient bubble clouds were generated at a depth of 87.6 m beneath the surface of a freshwater lake for the purpose of conducting an acoustic backscattering experiment. Although the bubble cloud image in Figure 4.6 is clearly non–spherical, the monopole scattering response (volume mode) can be estimated using the sphere model outlined in Chapter 3. Thus for a spherical cloud of volume $V_{\text{cloud}} = 222 \pm 0.027\,l$, the radius of the cloud is $a = 0.376 \pm 0.014\,\text{m}$. In Table 4.5, the values obtained during the processes described herein are summarized.
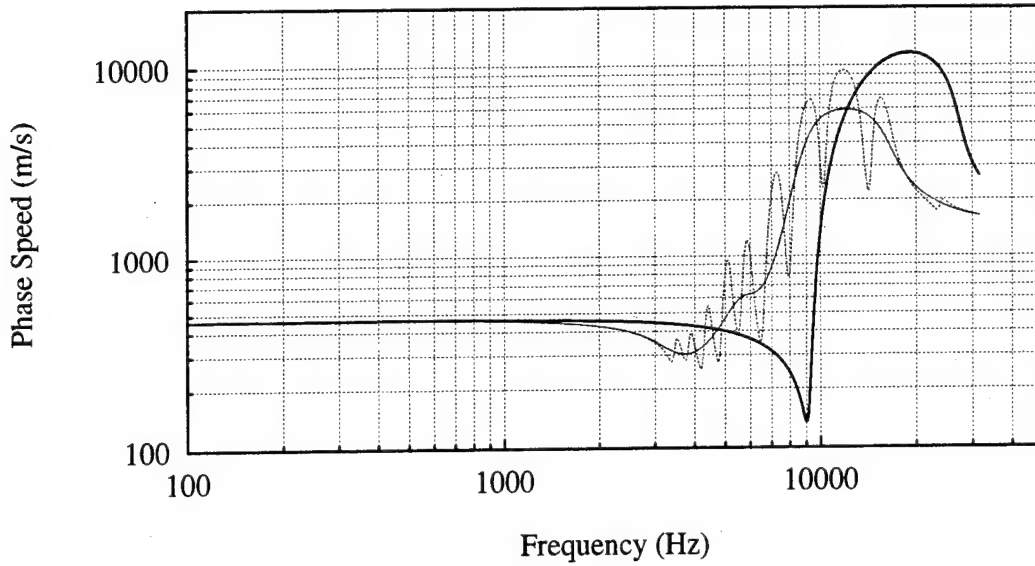
Figure 4.11: Effective phase speed versus frequency for the Lake Seneca bubble cloud using monodispersed (solid line), discrete (jagged–dashed line), and Gaussian (smooth–dashed line) bubble size distributions. Here the void fraction is $\beta = 0.55 \times 10^{-2}$, and $P_\infty = 9.82 \times 10^5$ Pa. For all frequencies of interest in this experimental analysis (*i.e.*, below 2000 Hz, the sound velocity in the mixture asymptotes to 460 m/s.

Table 4.5: Lake Seneca experimental precision analysis.

(a) Measurement

Parameter		Mean Value	Uncertainty	Relative Uncertainty (%)
P_o	(Pa)	958774	15336	1.60
V_{cloud}	(l)	222	2.7	12.28
V_{gas}	(l)	1.2	0.1	11.48
c	(m/s)	1421.5	0.000	0.00
a	(m)	0.376	0.014	3.72
β		0.55	0.001	16.80

(b) Predictions

ρ_e	(kg/m^3)	994.73	0.928	0.09
c_e	(m/s)	402.05	31.049	7.72
Ω_0	(Hz)	294.088	25.213	8.57
$k_o a$		0.489	0.046	9.35
TS	(dB)	-2.998		

128

Chapter 5

The Lake Seneca experiment: acoustic backscattering measurements and analysis

5.1   The experimental test plan

The Lake Seneca facility consisted of two moored barges in a water depth of 130 m, with the smaller barge (called the TCP barge; 10.7 m x 42.7 m) serving as the platform for the test range. Equipment was deployed with the use of davits, a cable meter, and the edge of the barge, with the resulting vertical geometry shown in Figure 5.1. Transmitters and receivers were oriented co–linearly, with the axis of the range intersecting the path of a rising bubble cloud. A depth of 87.6 m was chosen for the target backscatter position in order to minimize both surface reverberation and volume reverberation (*i.e.*,

from fish, etc.) in the vicinity of the staging. Because of the deployment depth and the extent of the test range, the lake surface did not play a role in the backscattering and thus a comparison of the scattering measurements with the free–field model presented in Chapter 3 is facilitated.
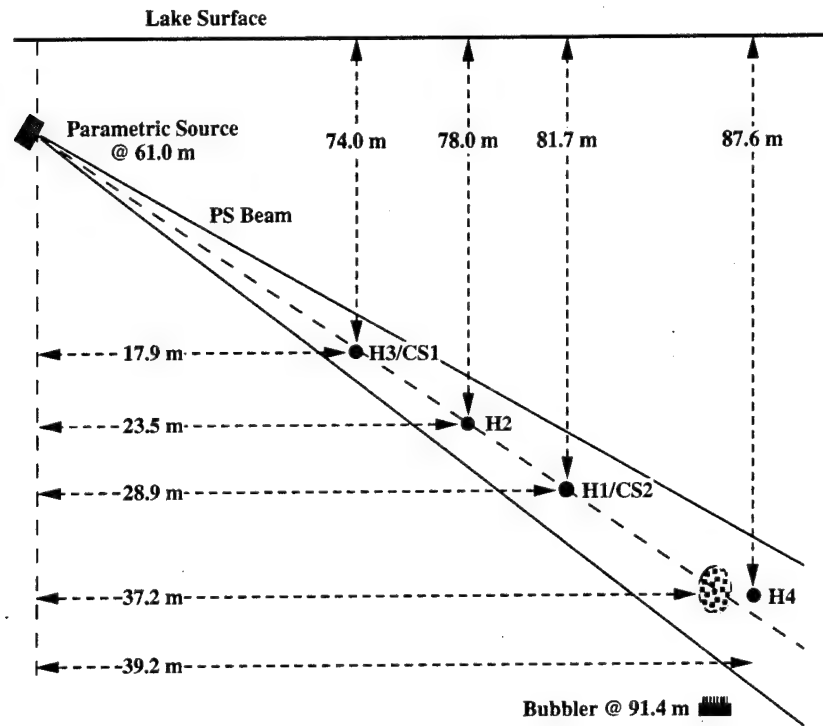
Figure 5.1: Layout of the test range. The receivers in the backscatter direction are denoted by H1, H2, and H3. Hydrophone H4 is in the forward direction and was used primarily to measure noise emissions from newly formed bubble clouds (Nicholas *et al.*, to be submitted). H3 and H1 were also used as a conventional sources (CS1 and CS2, respectively) during some of the tests. The PS beamwidth is indicated approximately by the region between the solid lines.

The backscatter target strength of the rising bubble cloud was measured over frequencies ranging from 250 Hz to 14 kHz using both conventional

130

and parametric sources. Over the course of the measurements, the source repetition frequency was fixed at either 1 or 2 Hz and the incident pulse length made to vary from 8 to 15 ms. Calibrations of both the frequency–dependent source level and beamwidth were performed *in situ* and were nominally 177 dB (re: 1 μPa at 1 m) and 8.0°, respectively (at 1.0 kHz). In addition, H1/CS2 and H3/CS1 were used as conventional sources in some of the tests.

5.1.1 The parametric source

Accurate target strength measurements are difficult to acquire as the frequency of the source is lowered, primarily because of the difficulty of radiating sound with narrow beam widths in order to avoid boundary reflections and excess volume reverberation within the sea. Conventional acoustic projectors (i.e., piston sources) capable of the necessary beam widths ($< 10°$) are both cumbersome and expensive. Furthermore, a conventional source radiates a significant amount of energy into the sidelobes. For a conventional projector, a 10- m diameter transducer aperture would be required to produce a 10° -3 dB[1] beam width at 1000 Hz (Konrad & Geary, 1991).

With a parametric source, a narrow beam with negligible side lobes is produced from a manageable sized projector. A 10° beam width at 1000 Hz can be achieved using a 0.75 m diameter aperture. In addition, the same source can be effectively used at frequencies between 500 and 7000 Hz. The PS produces these unique characteristics by simultaneously radiating sound at two much higher frequencies (called primaries) in collinear beams, and capitaliz-

---

[1]A -3 dB beam width refers to the half power points on the main lobe of the beam.

ing on the inherent nonlinearity of the water to convert some of the primary energy into sound at the difference frequency of the two primary waves. The resulting sound beam is a combination of the large amplitude primary waves and the somewhat lower amplitude (about 40 dB down) "sum" and "difference" frequencies. Acoustical mixing occurs only within the overlap zone of the primary beams, and thus the difference frequency is generated in a long virtual end–fire array extending outward from the source. The fundamental disadvantage of this source is its low efficiency, typically less than 5%, and consequent need for relatively high input powers. However, in the generation of short pulses on the order 100 ms and for duty cycles under 5%, the energy requirements are relatively easy to meet.

The parametric source used in this experiment was Section–4 of NUWC's[2] (formerly NUSC[3]) TOwed Parametric Source (TOPS), which is well characterized in *Scientific and Engineering Studies: Nonlinear Acoustics 1954 to 1983*. The source was deployed to its maximum depth of 61 m (200 ft), using sections of 6" diameter steel pipe. The fundamental design frequency of TOPS was 22 kHz. The two primary frequencies are symmetrically up and down shifted relative to 22 kHz. The signals were time gated and amplified by a 20 kW drive amplifier. Thus, to deliver a difference frequency $f_\triangle = 500\,\text{Hz}$ into the test range, the source was simultaneously driven at primary frequencies of $f_1 = 21.75\,\text{kHz}$ and $f_2 = 22.25\,\text{kHz}$. The source is compact, quite directional, and has a negligible side lobe structure compared to a CS. To perform the measurements described herein at difference frequencies less than

---

[2]Naval Undersea Warfare Center
[3]Naval Underwater Systems Center

2 kHz, a low–pass filter (2 kHz) was inserted at the output of each hydrophone in order to remove the primary source frequencies. A measured beam pattern for the PS driven at $f_\triangle = 500\,\mathrm{Hz}$ is illustrated in Figure 5.2. The beam pattern was obtained at receiver H1 (recall Figure 5.1) by tilting the PS about the polar (vertical) axis. In Table 5.1, the -3 dB beamwidth is listed for frequencies between 500 and 4000 Hz.
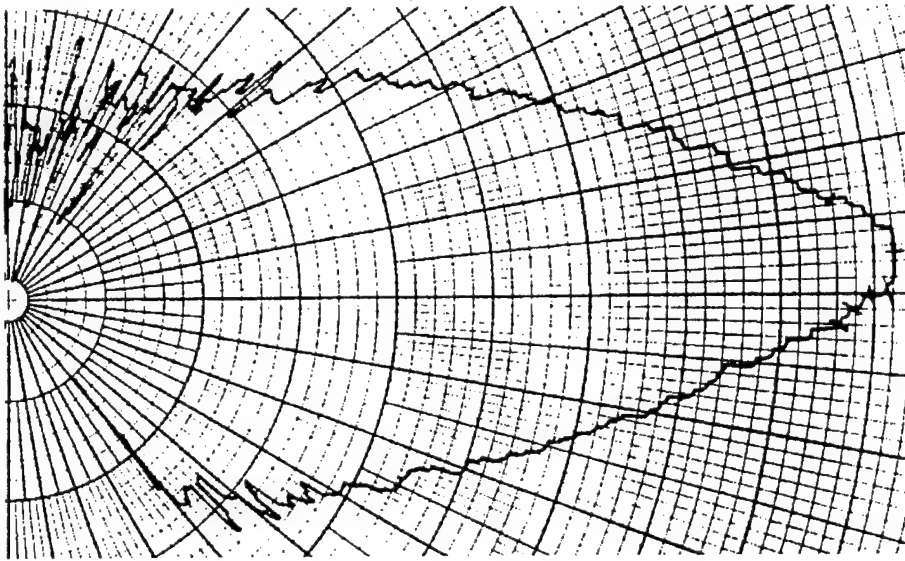
Figure 5.2: Parametric source beam pattern obtained for $f_\triangle = 500\,\mathrm{Hz}$. The source was tilted about its vertical axis and the resulting beam pattern measured at receiver H1. The smallest angular and radial units on the grid are separated by 1° and 1 dB respectively. Thus, the $-3\,\mathrm{dB}$ beamwidth at 500 Hz is $\pm 4.25°$ or 8.5° total.

5.1.2 Bubble cloud generation

The heart of this experiment was the bubble cloud generator (Figure 4.3). Air from a steel enclosure, pressurized to $\triangle P = 10\,\mathrm{psi}$ above the ambient pressure in the lake (*i.e.*, $\triangle P = P_{\text{internal}} - P_{\text{hydrostatic}}$), was vented into the lake through

133

Fq (Hz)	SL (dB)	BW (-3 dB)
500	167	8.5°
1000	177	8.0°
2000	185	7.0°
4000	193	6.5°

Table 5.1: Frequency dependent source level and beam width for the parametric source. These measurements were performed by tilting the PS about the vertical and using receiver H1.
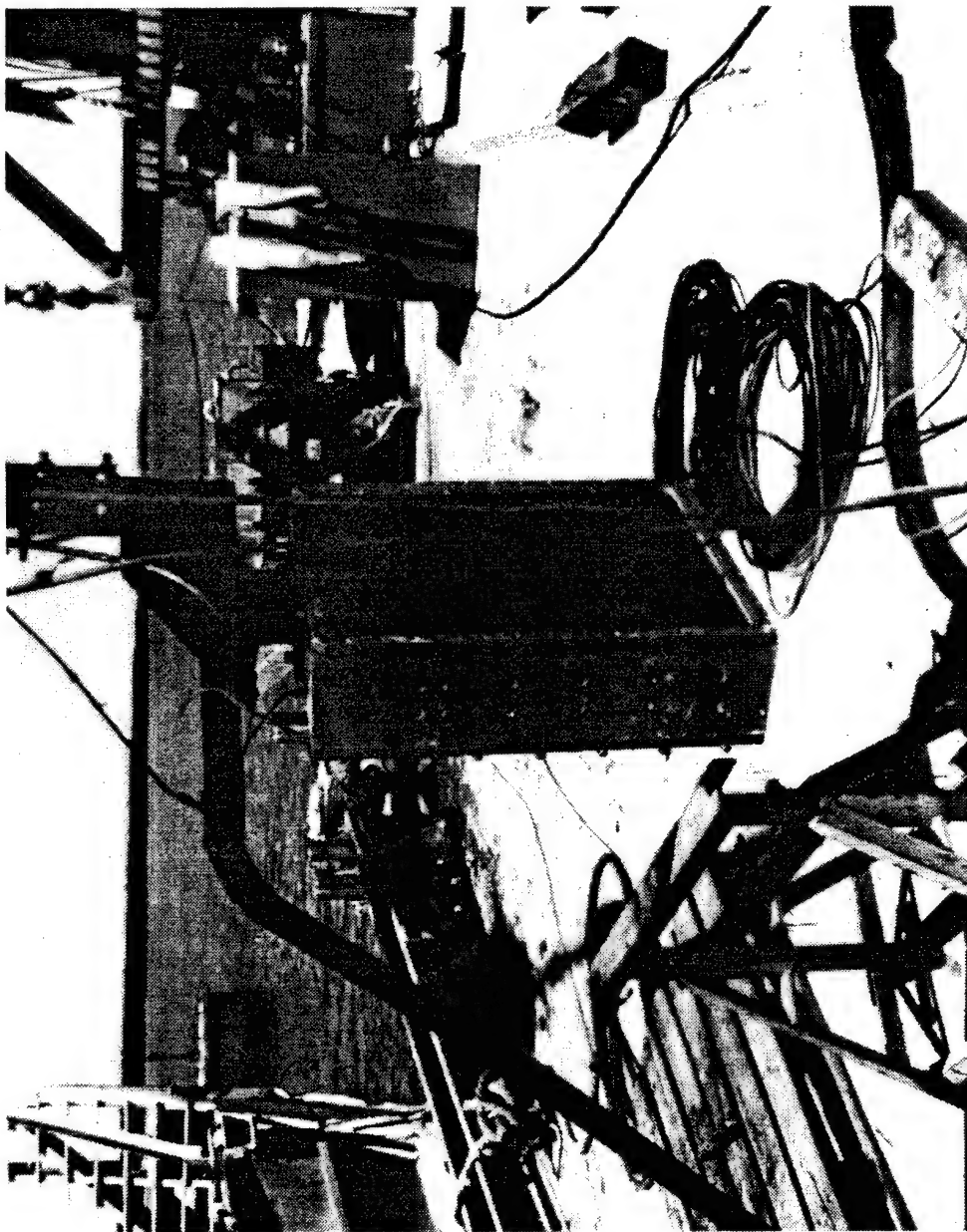
Figure 5.3: Photograph of the parametric source. The projector surface is approximately 0.75 m square.

135

an array of ports opened via solenoid valves controlled from the surface (see Section 4.2 for a more comprehensive discussion). Each port was capped with a 22–gauge hypodermic needle, the end of which was cut perpendicular to the needle shaft ("pipetting needles"). In all there were 48 ports arranged in a circular array of three concentric rings of radii 6.4 cm (containing 8 ports), 12.8 cm (containing 16 ports), and 19.2 cm (containing 24 ports).

Pressurized air was supplied to the steel enclosure from a compressor located at the surface. After suitable pressure regulation and filtering, the total mass of air supplied to the apparatus was recorded using a precision mass flowmeter. The relative pressure between the air in the enclosure and the ambient lake pressure ($\triangle P$) was continually monitored using an electronic differential pressure transducer; during the venting process, if $\triangle P$ dropped below a preset tolerance, a solenoid valve was opened which enabled compressed air from the supply to enter the pressurized steel enclosure and thus to reestablish the operating overpressure. The regulated air pressure at the compressor was typically 20 psi greater than the internal pressure in the bubble maker.

Bubble clouds were generated in the following manner: At the surface, the overpressure and burst duration (the time that the solenoid bank was opened) were configured to 10 psi and 3.4 s respectively. Clouds were released on demand (by pressing a button), resulting in the formation of rising bubble cloud. The bubble clouds were nominally cylindrically shaped with at blunt leading edge and a trailing skirt of bubbles. The rise velocity of the cloud was approximately 0.4 m/s, and the total cloud volume and total gas volume contained within the cloud were $V_{cloud} = 222l$ and $V_{gas} = 1.22l$, respectively.

The total cloud volume and rise velocity were determined from video recorded data, and the total gas volume from the electronic precision mass flow meter. Although the spatial distribution of bubbles in the cloud was not uniform (recall Figure 4.6), the average void fraction was determined to be $\beta = 0.0055$ and the equivalent volume spherical radius was $a = 0.376\,\text{m}$.

5.2   The measurement of target strength

In Appendix A the standard definition of the backscatter target strength is given and the process of performing an experimental measurement is described. The relationship between the theoretical backscatter TS and its measurement is given by:

$$\text{TS} = 20\log\left|\frac{p_s}{p_i}\right|_{r=1\,\text{m}},$$

$$= 20\log\frac{\text{EV}}{\text{MBV}} - 20\log\frac{R_{SH}}{R_{ST}R_{TH}} - (G_{\text{echo}} - G_{\text{mb}}), \qquad (\text{A}.10)$$

where the terms MBV and EV refer to the respective "steady–state" main bang and echo voltage amplitudes measured from a particular hydrophone; the term $20\log\frac{R_{SH}}{R_{ST}R_{TH}}$ accounts for the total transmission loss in dB (each factor in this term is assumed to be divided by the reference distance of $1\,\text{m}$); and the difference in receiver gain settings for the echo versus main bang measurement is given by the G terms. Note that the TS measurement is independent of the source level and the hydrophone calibration coefficients as long as the main

137

bang and echo signals are processed from a the same receiver.

5.3 Test range layout

In Tables 5.2(a) and (b) the layout of the test range is specified for the Seneca–2 and Seneca–3 tests respectively. Four receivers (ITC #7001, 6" spherical ball), labeled H1–H4 were lowered over the edge of the TCP barge to the depths indicated in Tables 5.2(a) and (b). The hydrophones were first lowered over the side of the barge and the horizontal spacing on the surface measured relative to the PS (column H). The parametric source was deployed to a depth of 69 m (200 ft) using lengths of 6 in diameter steel pipe. The hydrophones were then lowered, resulting in the alignment indicated in Figure 5.1. In Column V of Tables 5.2, the vertical depth of each receiver (measured with a Durant Model 5–d–8–1–CL cable meter) relative to the PS source depth is indicated. Slight adjustments to the depth of each phone were made to insure that they were located on the main response axis of the PS.

The slant range distance R_{SH}, and thus the depth, of each hydrophone were accurately determined by performing several time–of–flight measurements of short pulses propagated from the PS using the 22 kHz carrier beam. The slant range distances between the source and each receiver ($R_{SH} = \sqrt{H^2 + V^2}$) are summarized in column R_{SH} of Table 5.2.

In Table 5.2, $\triangle t = t_{\text{echo}} - t_{\text{mb}}$ refers to the expected time delay for an *echo return* relative to the passing of the incident *main bang* pulse at a particular hydrophone. The transmission loss factors (TL) account for the $1/R$ de-

Table 5.2: Range layout and transmission loss factors.

(a) Seneca–2

	H (m)	V (m)	R_{SH} (m)	$\triangle t$ (ms)	θ (deg)	TL_{SH} (dB)	TL_{ST} (dB)	TL_{TH} (dB)	TLF (dB)
PS	00.00	00.00	00.00						
H3	17.90	13.02	22.13	33.26	36.03	26.90	33.21	27.47	-33.78
H2/CS2	23.53	17.01	29.03	23.55	35.86	29.26	33.21	24.47	-28.43
H1	28.92	20.73	35.58	14.34	35.63	31.02	33.21	20.16	-22.35
Target	37.20	26.67	45.77		35.64				
H4	39.21	26.67	47.42		34.22				
Bubbler	37.20	30.69	48.23		39.53				

(b) Seneca–3.

	Horiz (m)	Vert (m)	R_{SH} (m)	$\triangle t$ (ms)	θ (deg)	TL_{SH} (dB)	TL_{ST} (dB)	TL_{TH} (dB)	TLF (dB)
PS	0.00	0.00	0.00						
H3	17.83	12.78	21.94	33.19	35.62	26.82	33.17	27.46	-33.80
H2	23.34	16.73	28.72	23.65	35.63	29.16	33.17	24.51	-28.52
H1	28.72	20.58	35.33	14.35	35.63	30.96	33.17	20.17	-22.38
Target	37.01	26.52	45.53		35.62				
H4	43.07	30.86	52.98		35.63				
Bubbler	37.01	30.21	47.77		39.22				

Note: The items deployed are listed in the first column. Column–H lists the horizontal separation of each item relative to the PS location; Column–V lists the depth of each item beneath the PS; Column–R lists the direct path between the PS and each element; $\triangle t$ is the expected time delay between the reception of incident and scattered pulse at a particular hydrophone; θ is the declination angle between the PS and the element, relative to the horizontal. The transmission loss factors for the distances R_{SH}, R_{ST}, R_{TH} and the total transmission loss factor, TL are listed in the remaining columns (refer to Figure 5.4).

crease in signal amplitude due to spherical spreading of the signal between the source–hydrophone (R_{SH}), source–target (R_{ST}), and target–hydrophone distances (R_{TH}), as indicated in Figure 5.4. (The sonar equations which describe the transmission loss factors and the backscatter target strength measurement are presented in Appendix A.)
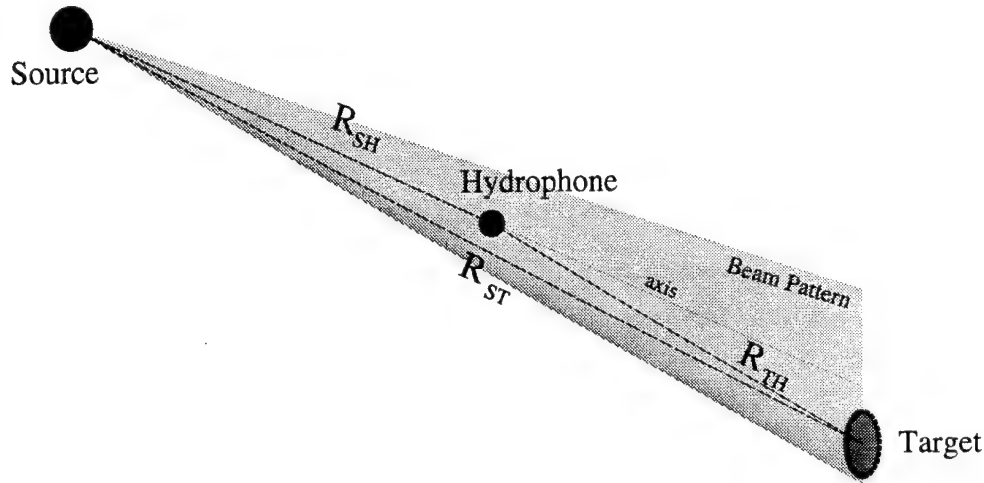
Figure 5.4: Scattering geometry for a single hydrophone and the target not in the backscatter position. R_{SH} is the distance between the source and the receiver; R_{ST} is the distance between the source and the target; and R_{HT} is the distance between the target and the hydrophone. When the target is in the backscatter position, $R_{ST} = R_{HT} + R_{SH}$.

The transmission loss factors between the source–target and target–hydrophone are listed Columns TL_{ST} and TL_{TH} of Table 5.2, where $TL_{ST} = 20\log_{10}(R_{ST})$ and $TL_{HT} = 20\log_{10}(R_{TH})$. The total transmission loss factor for the target in the backscatter position is $TLF = 20\log_{10}(\frac{R_{SH}}{R_{ST}R_{TH}})$ are given in Column TLF. For the case of a rising bubble cloud, however, the target is not stationary. The bubble cloud is assumed to rise vertically (see Section 4.3.1), and thus the separation distances R_{ST} and R_{TH} (and therefore, the TLF) are

simple functions of the rise time and vertical rise velocity of the bubble cloud (horizontal drift was not accounted for).

The test range parameters given in Table 5.2 describe the special case when the bubble cloud crosses the axis of the test range (*i.e.*, backscattering). However, since the bubble cloud position is not held fixed (since it is rising), the transmission loss factors that are needed to determine the time–evolving target strength are functions of cloud position, and therefore, functions of time relative to the cloud release. In general, the total transmission loss factor for the experimental geometry described here is given by $TLF = \mathrm{TL}_{SH} - \mathrm{TL}_{ST} - TL_{TH}$, where the subscripts SH, ST, and TH refer to the distance between source–receiver, source–target, and target–receiver, respectively (for example $\mathrm{TL}_{ST} = 20\log(R_{ST})$). For a rising bubble cloud, however, the range distances R_{ST} and R_{TH} can be determined as a function of time relative to cloud release, and therefore, the total transmission loss factor is calculated at each increment of time. Assuming that the cloud rises vertically, then the distances R_{ST} and R_{TH} are given by

$$R_{ST} = \left[(X_{\mathrm{bubbler}})^2 + (Y_{\mathrm{bubbler}} - u_{\mathrm{rise}} \cdot t)^2\right]^{\frac{1}{2}} \tag{5.1}$$

$$R_{TH} = \left[(X_{\mathrm{bubbler}} - X_{\mathrm{rec}})^2 + (Y_{\mathrm{bubbler}} - u_{\mathrm{rise}} \cdot t - Y_{\mathrm{receiver}})^2\right]^{\frac{1}{2}}, \tag{5.2}$$

where the X and Y coordinates are given in Table 5.2 relative the PS origin, and $u_{\mathrm{rise}} = 0.39\,\mathrm{m/s}$. Shown in Figure 5.5 are the calculated rise–time dependent total transmission loss factors used to determine the target strength. Note that at $t \approx 11\,\mathrm{s}$, the total transmission loss factor corresponds to the

141

values given in Tables 5.2(a) and 5.2(b), respectively.
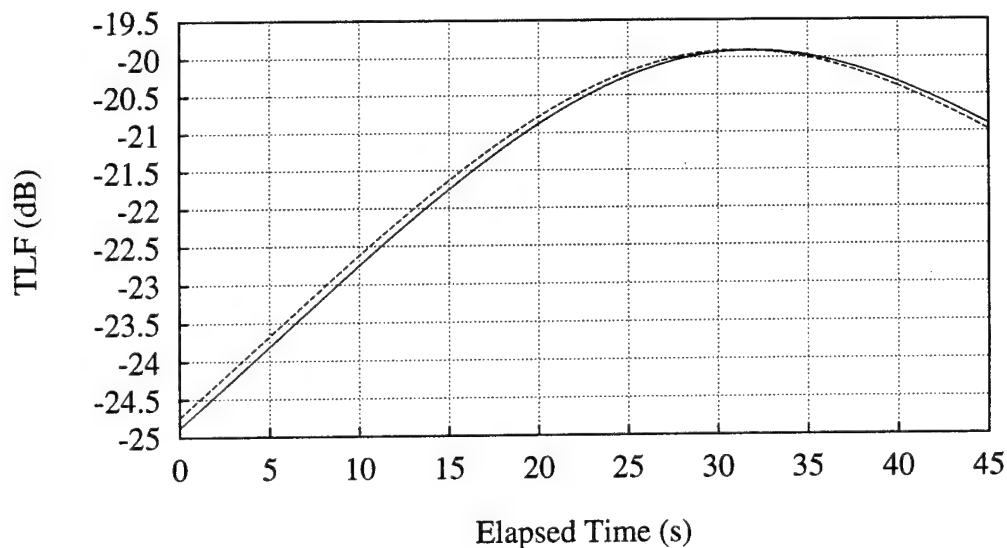
Figure 5.5: Total transmission loss factor for receiver H1 as a function of bubble cloud rise–time relative to cloud release. The dashed line corresponds to the total transmission loss correction applied to the Seneca–3 data, and the solid line for the Seneca–2 data. When the cloud is in the backscatter position, $t \approx 11$ s, the TLF corresponds to the values given in Table 5.2.

5.4 Signal conditioning and recording

The receivers deployed axially along the PS beam were used to measure the incident main bang signal and scattered or *echo* signals. A schematic illustrating the instrumentation used to acquire the data from a single hydrophone is shown in Figure 5.6. Its operation is described as follows: First, the source was configured to send a steady stream of pulses of specified pulse width and difference frequency (f_Δ) at a repetition rate of either 1 or 2 Hz. The main bang signals were received on each of the hydrophones H1–H3, and continued

to propagate toward the target. The target responds by scattering sound in all directions, and the backscattered echo contribution (EV) was recorded from hydrophones H1–H3. In order to remove the large amplitude PS primaries ($\approx 22\,$kHz) from the received waveforms, a $2\,$kHz passive low–pass filter (a single pole RC filter with -6 dB/octave insertion loss) was placed inline prior to pre–amplification; during the conventional source tests these filters were removed. The signals acquired at each hydrophone were fed into an Ithaco (model 453) pre–amplifier set to variable gain and including a 100 Hz high pass filter. The pre–amplifier gain was adjusted to maximize the main bang and the echo voltages generated by each hydrophone within a $1\,$V$_{peak}$ range (the input range of the recording tape deck).

Following pre–amplification, a KronHite (model #3343) active low pass filter set one to two decades above the difference frequency was installed to insure that the signal recorded on the tape deck lacked frequency components outside the range of the recorder at its lowest possible recording speed at a given driving frequency. In addition, this filter served as an anti–aliasing filter, since the tape recorded data was to be digitized after returning to the laboratory. The incoming main bang and echo signals from hydrophone H1 were monitored *in situ* using a LeCroy 9450 digital oscilloscope in order to confirm correct range alignment and to confirm that scattering did indeed occur as the cloud ascended through the main lobe of PS beam.

The signals were recorded on a 3/4-inch reel–to–reel tape deck (Teac SR31–DF) with 7 recording tracks. The tape deck was capable of operating at one of nine variable speeds and each channel was recordable in either a FM or Direct
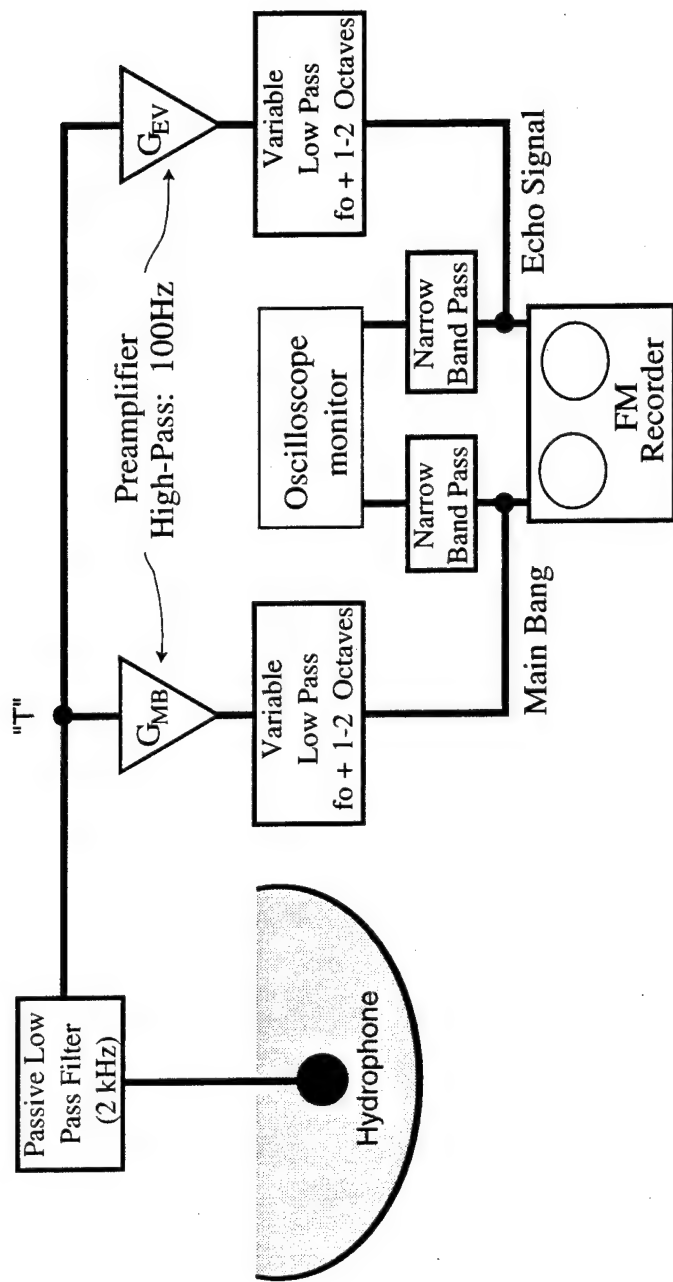
Figure 5.6: Instrumentation setup for a single hydrophone during the Seneca–3 experiment. The large amplitude ≈ 22 kHz primaries from the parametric source were removed using the 2 kHz passive low–pass filter. Then the signal was split into two channels using a "T" and fed into a pair of pre–amplifiers and active low–pass filters prior to recording to individual main bang and echo channels on the reel–to–reel tape deck. The pre–amplifier gain was set to optimally amplify either the incident or scattered echo pulse respectively in a 1 V_{peak} range prior to recording. During the Seneca–2 experiment, the main bang and echo signals were recorded from separate data runs, thus the "T" was not inserted. Online processing was performed by monitoring narrow band passed signals on a LeCroy 9450 digital oscilloscope.

144

recording mode. The frequency response and signal to noise ratio for these operating speeds is shown in Table 5.3. For the majority of the data recorded, the tape speed was set to 38 cm/s however, tapes speeds of 19 and 76 cm/s were also utilized. For the echo measurements, the preamplifier gain was set high enough such that the incident main bang signal saturated the amplifier output and the tape deck input. This did not have a detrimental effect on the recorded data as the equipment had sufficient time to recover from these saturations.

FM mode					Direct mode				
Speed (cm/s)	Frequency Range (kHz)		S/N ratio (dBrms)		Speed (cm/s)	Frequency Range (Hz) — (kHz)			S/N ratio (dBrms)
152.40	DC —	40	49		152.40	300	—	300	30
76.20	DC —	20	49		76.20	200	—	150	30
38.10	DC —	10	49		38.10	100	—	75	30
19.05	DC —	5	48		19.05	100	—	37	30
9.52	DC —	2.5	46		9.52	100	—	18	30
4.76	DC —	1.25	44		4.76	100	—	9	30
2.38	DC —	0.625	44		2.38	100	—	4.5	30
1.19	DC —	0.313	42		1.19	100	—	2.25	30
0.59	DC —	0.156	40		0.59		—		—

Table 5.3: Tape deck (Teac SR31–DF) specifications.

Shown in Figure 5.7(a), is a cartoon of a tape segment illustrating a sequence scattering measurements recorded to tape for a particular driving frequency. The reel–to–reel recorder were capable of recording 7–tracks of data simultaneously, only the first four are shown in the figure. During the Seneca–2 experiment, a recording of the incident main bang signal was made from all hydrophones prior to a series of cloud releases. The pulse repetition frequency was set to 2 Hz, the preamplifier gain was set to G_{mb} (arbitrary, but dependent on the driving frequency) and roughly 60 pulses or 30 s of data were recorded to the analog reel–to–reel tape. At this gain setting, the specular echo

145

from the target often appeared to be buried in the background noise.

Prior to recording the sequence of scattering measurements from rising bubble clouds, the preamplifier gain (G_{echo}) was adjusted in order to maximize the specular return of the backscatter signal within a $1\,V_{peak}$ range. Typically, the difference in preamplifier gain settings ($\triangle G = G_{echo} - G_{mb}$) exceeded $20\,dB$, or a factor of 10 in signal amplitude. After determining the appropriate gain setting for the backscatter measurement at a given driving frequency, a minimum of three cloud releases were recorded to the reel–to–reel tape units. Following this sequence of measurements, the source frequency was modified and the process repeated. In Appendix B, a table listing the recording parameters and test schedule for the Seneca–2 test can be found.

In contrast, during the Seneca–3 test the main bang and backscatter echo signals were recorded simultaneously as illustrated in Figure 5.7(b). This obviously required double the number of pre–amplifiers and filters, but less overall time per frequency run (recall Figure 5.6). In addition, the advantage of this recording configuration is a 1:1 correspondence between the main bang pulse and the backscattered echo pulse. In Appendix C, a table listing the recording parameters and test schedule for the Seneca–3 test can be found. The data tapes from both experiments were digitized and processed after returning to the lab. In Chapter 5, the digitizing process and subsequent data analysis is described.

In Figure 5.8, a photograph of the main equipment rack used during this experiment is shown. It contained the pre–amplifiers (bottom) and a set of three active low–pass filters (KronHite #3343) used to condition the incom-

146

7 Tracks

	No Cloud	Cloud 1	Cloud 2	Cloud 3
	H1 G_{mb}	H1 G_{ev}	H1 G_{ev}	H1 G_{ev}
	H2 G_{mb}	H2 G_{ev}	H2 G_{ev}	H2 G_{ev}
	H3 G_{mb}	H3 G_{ev}	H3 G_{ev}	H3 G_{ev}
	H4 G_{mb}	H4 G_{ev}	H4 G_{ev}	H4 G_{ev}

Time ⟶

(a) Seneca–2 tape segment.

7 Tracks

	Cloud 1	Cloud 2	Cloud 3	Cloud 4
	H1 G_{mb}	H1 G_{mb}	H1 G_{mb}	H1 G_{mb}
	H1 G_{ev}	H1 G_{ev}	H1 G_{ev}	H1 G_{ev}
	H2 G_{mb}	H2 G_{mb}	H2 G_{mb}	H2 G_{mb}
	H2 G_{ev}	H2 G_{ev}	H2 G_{ev}	H2 G_{ev}
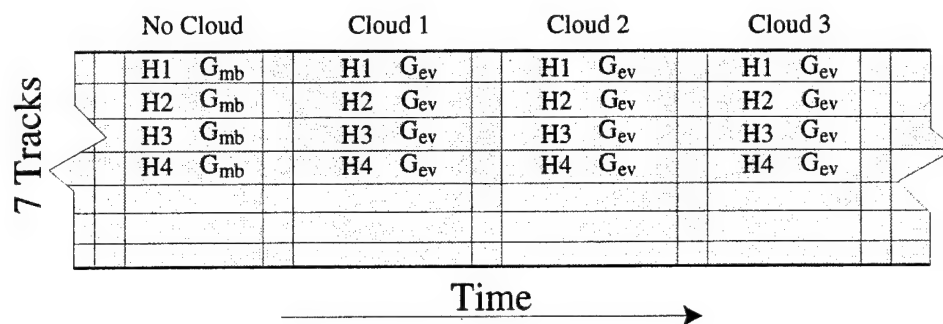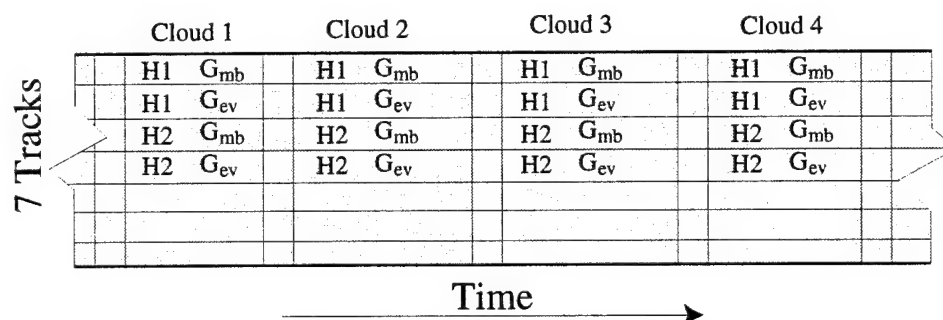
Time ⟶

(b) Seneca–3 tape segment.

Figure 5.7: Sample reel–to–reel tape segments (elapsed time) for the Lake Seneca experiments. The tape deck was capable of recording 7 data tracks simultaneously and the signals recorded to each track is listed above. The signals recorded and preamplifier gain settings used are indicated here only for tracks 1-4. Signals were recorded to tape for approximately 60 s per cloud release. In the region between data runs a 2 s calibration tone was recorded. Note: Due to the instrumentation setup used in the Seneca–2 effort, a single main bang recording was conducted prior to a series of cloud releases. During the Seneca–3 experiment, the main bang and echo recordings were made simultaneously.

ing signals prior to recording on the analog tape deck. Above the recording filters are located a trio of WaveTek #753A "Brick–Wall" filters which were configured to narrow band–pass the conditioned signals in order to monitor

147

the backscattering results "on–line" with the LeCroy 9450 digital oscilloscope. Above the oscilloscope is a signal generator and the *Deep–Thought* bubble maker controller unit. On top of the equipment rack is a digital volt meter used to monitor the differential pressure transducer mounted inside the bubble maker.

5.5   Test range calibration

Prior to lowering the bubble maker and performing backscattering measurements from rising bubble clouds, a test target was deployed in the expected backscatter position of the test range in order to verify range alignment (recall Figures 5.1 and 5.4). This calibration was important in order to correctly account for the transmission loss factors needed to determine the target strength in Eq. (A.10), and to ground truth the experimental procedure. In order to determine the total transmission loss factor (TLF), the distance between the source–hydrophone (R_{SH}), source–target (R_{ST}), and target–hydrophone (R_{TH}) need to be known accurately for each receiver.

The test target was a hollow (air–filled) steel sphere of radius $a = 1.12\,\mathrm{m}$ weighted with 800 lbs of ballast (lead and steel) and lowered to the backscatter position at a depth of 87.6 m (depth determined using the cable meter). To determine the distances R_{ST} and R_{TH}, the time delay between the reception of an incident main bang pulse and scattered return (specular reflection) from the steel sphere was measured and compared to the expected values listed in Column $\triangle t$ of Table 5.2. For Hydrophone 1 (H1), the expected time delay

148
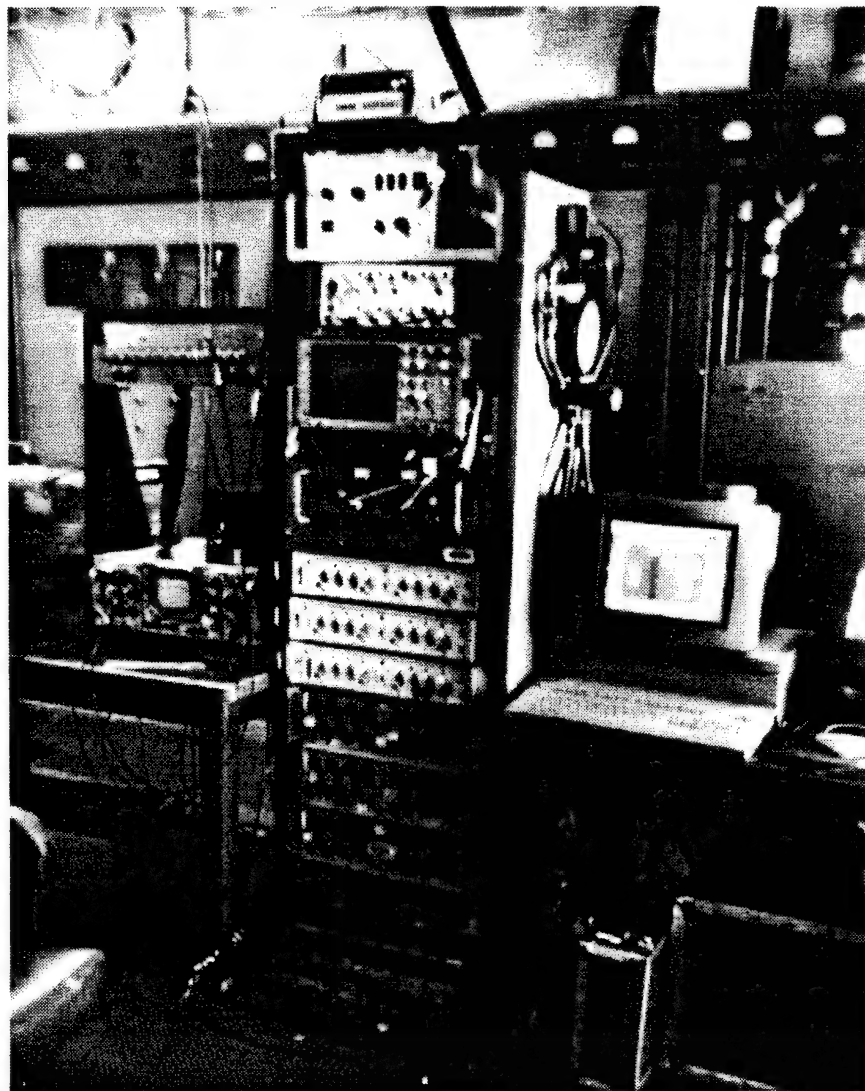
Figure 5.8: Photograph of instrumentation setup. Located on the top of the equipment rack is a digital voltmeter used to monitor the internal over pressure of the bubble maker. Beneath this, the *Deep Thought* bubbler controller unit is mounted in the upper most location of the equipment rack. A signal generator and the LeCroy 9450 digital oscilloscope are next, followed by a bank of three WaveTek #753A "brick–wall" filters, and three KronHite #3343 filters set to low–pass mode. Finally, the Ithaco pre–amplifiers are located at the bottom of the rack. The computer on the right of the equipment rack was used to remotely control the recording tape deck and digitize and store the outputs from the precision electronic mass flow meter and the pressure transducers mounted in the bubble maker.

149

was $\triangle t_{\text{expected}} = 14.3\,\text{ms}$ and the measured time delay $\triangle t_{\text{meas}}$ varied roughly between 13 and 16 ms. The variation is presumably due to slight currents in the lake which cause either the hydrophones or the target to move slightly off axis. Because of the agreement between the measured and expected time delays, it was concluded that the test range was laid out to the best of our ability. The locations and expected time–delays for the sources and receivers hydrophones deployed during this experiment are indicated in Table 5.2.

Aside from calibrating the test range, the steel target allowed us to test our ability to perform a quantitative backscatter TS measurement using Eq. (A.10). The PS was configured to send 12 ms pulse of sound every 1 s at difference frequency $f_\triangle = 500\,\text{Hz}$ and pulse length of 10 ms. The incident main bang and backscattered echo signals were recorded to analog reel–to–reel tape for each receiver in the backscatter direction using the method described in Section 5.4. An example of a single incident main bang and scattered echo pulse recorded from receiver H1 (the nearest hydrophone in the backscatter direction) is shown in Figure 5.9. The echo arrived at the receiver $\triangle t = 14.5\,\text{ms}$ after the reception of the leading edge of the incident pulse. The preamplifier gain setting for the incident main bang channel was $G_{\text{mb}} = 46\,\text{dB}$; and for the echo return, the quantity of $G_{\text{echo}} = 66\,\text{dB}$ gain was added. The rms voltage amplitude was measured over an 8 ms "steady–state" portion of the received main bang and scattered echo pulse wave forms (e.g., MBV $= 0.27\,\text{V}_{\text{rms}}$ and EV $= 0.09\,\text{V}_{\text{rms}}$) after the data streams were band–pass filtered at $500 \pm 50\,\text{Hz}$ (Note: Here the term "steady state" refers to the middle portion of the pulse). These voltages were entered into the equation for the target strength (Eq. A.10)

along with a transmission loss factor of $-22.38\,$dB and the pre–amplifier gain factors in order to determine TS. In this example, for a driving frequency of $500\,$Hz, the measured TS by receiver H1 is $-7.4\,$dB.

For the PS driven at $f_\triangle = 5000\,$Hz, the measured TS was $-12.3\,$dB. This is in close agreement with the expected TS of a perfectly reflecting sphere of the same radius at high frequencies, $-11.1\,$dB (recall that $TS_{rigid} = 20\log_{10}(a/2)$). The comparison of the theoretical TS of a perfect reflector at high frequencies to the hollow steel spherical shell is likely valid (Urick, 1967) and suggests that our ability to measure the TS is good.

5.6   "On–line" data processing

In this section, the preliminary Lake Seneca "on–line" analysis of the target strength measurements from rising bubble clouds is presented. As shown in Figure 5.6, a LeCroy 9450 digital oscilloscope was utilized to monitor the received and pre–processed signals. The primary reason to conduct on–line monitoring is to insure that the experimental measurements and associated equipment are performing adequately. Another motivation for conducting this analysis was to obtain a rough estimate of the frequency dependent target strength and to establish the viability of the parametric source as a research tool which could be utilized to conduct scattering experiments from bubble clouds. Thus comparisons between the target strength measurements utilizing both the parametric source and the conventional sources were made over a range of frequencies spanning $500\,$Hz to $7\,$kHz. Below $500\,$Hz, the conven-
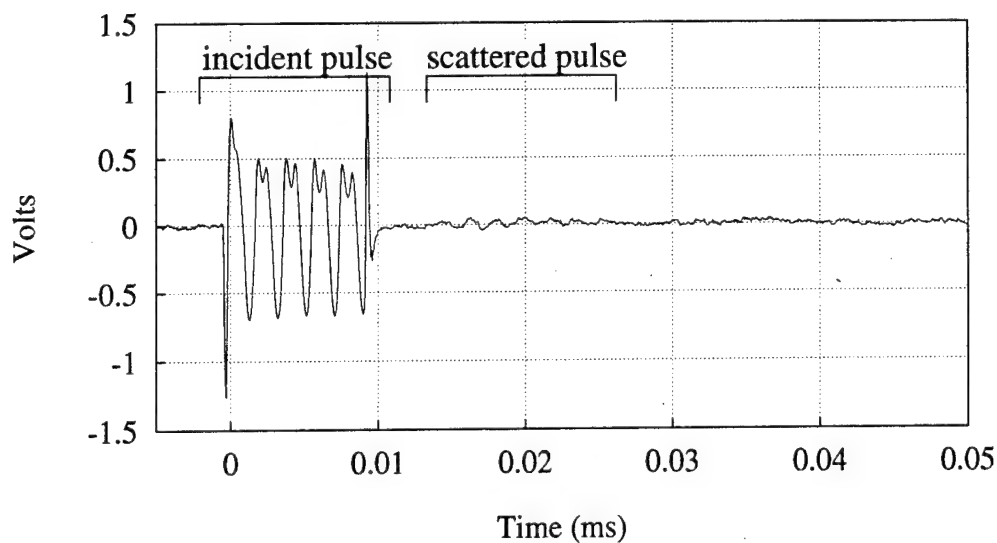
(a) Main Bang waveform
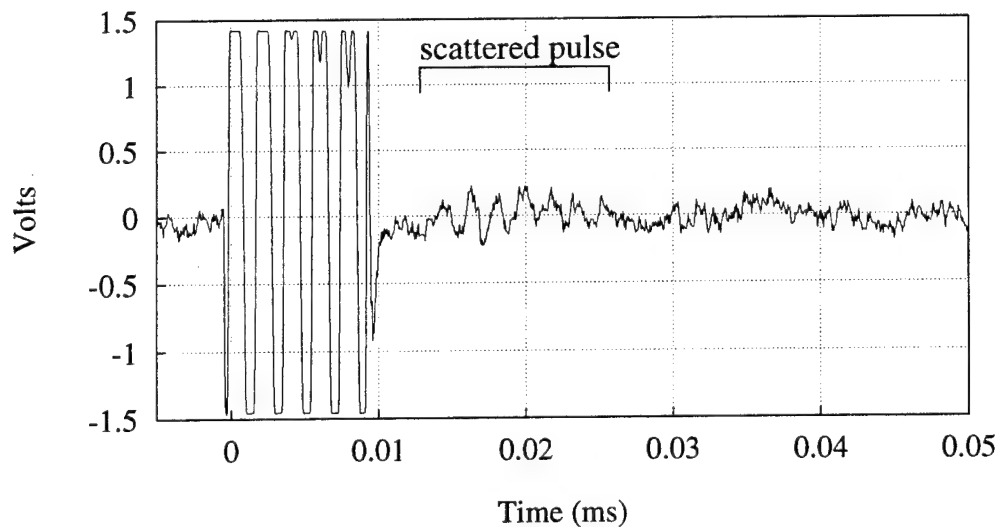
(b) Backscattered waveform

Figure 5.9: Incident main bang (a) and backscattered (b) waveforms from the steel target sphere measured at receiver H1. Here, the driving frequency is 500 Hz and the backscatter return is received at $\triangle t_{\mathrm{meas}} = 14.5\,\mathrm{ms}$, relative to the incident pulse. To enhance the echo, an additional 20 dB of gain was added to (b).

tional sources were ineffective due to low source level, and thus the signal to noise ratio and reverberation increased correspondingly. The parametric source, however, was utilized down to 250 Hz, at which point it too suffered from a significant drop in signal level. For the frequency range between 500 and 3000 Hz, the scattering results using both sources were found to be in agreement.

Shown in Figure 5.6 is an illustration of the signal processing instrumentation used to prepare raw signals received at each hydrophone. While conducting the experiment, receiver H1 was monitored and processed on–line in the following manner:

Once the range was aligned and calibrated and the source frequency and pulse duration set, the bubble–maker solenoids were activated for 3.4 s, resulting in a rising bubble cloud. The cloud rose from the bubbler and ascended through the source beam axis yielding a time–varying backscattered echo level. Because the rise velocity of the bubble cloud was not measured until the final day of the experiment, it was assumed that the bubble cloud crossed the axis of the test range when a peak in the scattered voltage amplitude occurred. This location of the peak varied by as much as 6 s depending on the driving frequency. For the lower frequencies (250 to 600 Hz) the peak occurred at approximately 6 to 8 s after cloud release, and for higher frequencies (> 1000 Hz) this peak occurred at about 12 s after cloud release. The latter is in good agreement with the expected time needed for a cloud to cross the backscatter location after cloud generation, while the former is presumably due to several factors, most notably the decreasing signal to noise ratio as the source driving

153

frequency was lowered. This decrease is due to the fact that the signal level introduced into the test range by the parametric source (or nearly any source, for that matter) decreased as the frequency was lowered.

Furthermore, at some frequencies, there were multiple peaks. This would seem to suggest that: (a) angular dependent scattering had occurred, (b) perhaps interference with the bubble maker was a problem, or (c) the bubble clouds generated were not rising in a repeatable manner. The latter conclusion was ruled out after performing the rise time measurements. It was clear then that our initial assumption (that the cloud crossed the axis of the test range when the peak scattering level was measured) was in error. It should be noted, however, that for a given driving frequency the elapsed–rise–time–dependent scattering amplitudes for several subsequent cloud releases were well correlated. The pulse length, and thus pulse bandwidth, rather than the number of cycles was held fixed for the various driving frequencies during the experimental effort. The reason for this is that at the lower driving frequencies, we wanted to insonate the target with as much energy as possible. However, due to the spacing between the first hydrophone (H1) and the bubble cloud, the maximum pulse length was limited to 14 ms (for longer pulses, an overlap in the main bang and scaterred signals would occurr).

For the majority of the scattering data runs the incident pulse duration was set to 12 ms. The pulse repetition rate was set to 2 Hz for the Seneca–2 test and 1 Hz during the Seneca-3 test. The oscilloscope was set to trigger on the leading edge of the incident main bang pulse. Range gating of the echo signal was performed by configuring the oscilloscope to capture and store

154

a 10 ms window centered on the expected location of the backscatter pulse waveform. For receiver H1, the 10 ms echo–gate was fixed to acquire data from 15.5 to 25.5 ms after the leading edge of the incident main bang waveform. A sequence of the range–gated echo voltage returns, one for each incident pulse propagated across the test range during the ascent of a single bubble cloud, were stored in the oscilloscope memory. After the cloud had risen for approximately 45 s, sufficient time for it to exit the test range, the sequence of stored backscatter waveforms were recalled from memory, and displayed on the oscilloscope monitor.

Finally, for at least one bubble cloud release at each driving frequency, a hard copy of the LeCroy oscilloscope display screen was made. In Figure 5.10, an image of the LeCroy console containing the time–elapsed, time–gated backscatter echo from resulting from a single rising bubble cloud is shown for a driving frequency of 3.0 kHz. As expected, the echo voltage amplitude varied as the cloud traversed through the source beam, reaching a maximum 10 s after release. As the bubble cloud continued to rise, the backscatter echo voltage amplitude eventually diminished after exiting the test range. Individual scattering returns (bins) in the echo time sequence in Figure 5.10 could be displayed and were used to determine the target strength of the bubble cloud.

A similar sequence of time–gated main bang waveforms were also stored. The maximum rms voltage amplitude of the echo in a time sequence (EV) and the average rms amplitude of the main bang sequence (MBV) were recorded in the experimental log book along with the preamplifier gain settings. Finally, using Eq. (A.10), the target strength was calculated (also recall Table 5.2).

155
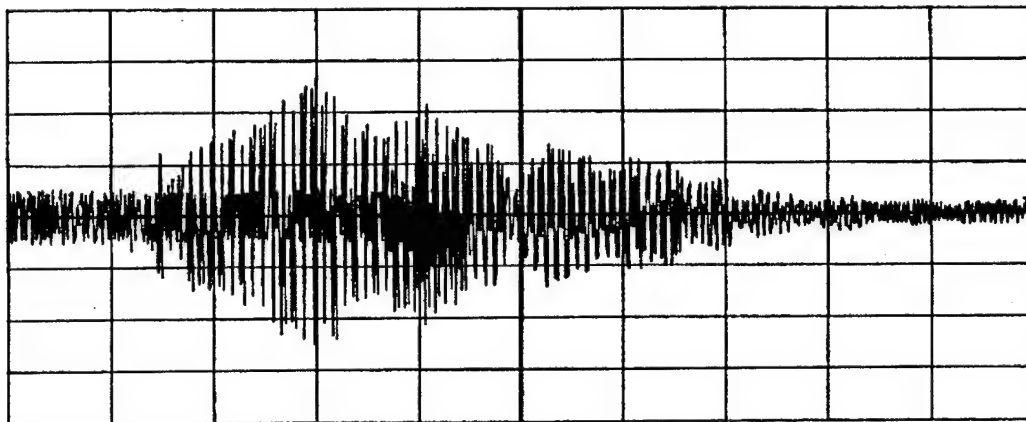
Figure 5.10: Time gated echo response from a rising bubble cloud measured by receiver H1. Here, the PS was driven at 3000 Hz. The time duration of this oscilloscope trace is 50 s. For each incident main bang pulse, a 10 ms window centered over the expected backscatter signal position (between 15.5 and 25.5 ms) after the leading edge of an incident main bang pulse) was digitized and stored to memory. The pulse repetition frequency was 2 Hz and thus 100 such echoes are displayed in a compressed form (10 echoes per division). The cloud was released within ±1 s of the initial trace and the peak echo response occurs between the 10–15 s mark.

In Figure 5.11, the preliminary target strength measurements for frequencies below 1600 Hz are shown. These data sets were conducted utilizing the conventional source (CS1: 500 to 1250 Hz), and the parametric source (250 to 1600 Hz). The conventional source data was collected during the Seneca–2 test and the target strength increased as the driving frequency was lowered from 700 Hz down to 350 Hz. This increase in the target strength was indicative of a resonance at a lower frequency and these promising results were the prime motivation for reconditioning the parametric source and performing the Seneca–3 tests (recall that during the Seneca–2 experiment the parametric source was usable only down to 800 Hz). Unfortunately, the conventional sources could not be driven below 350 Hz due to decreasing signal level. The

156

substantial error–bars and lack of agreement with the PS measurements in the conventional source measurements are due to excess reverberation; clearly at the higher frequencies this was less of a problem.
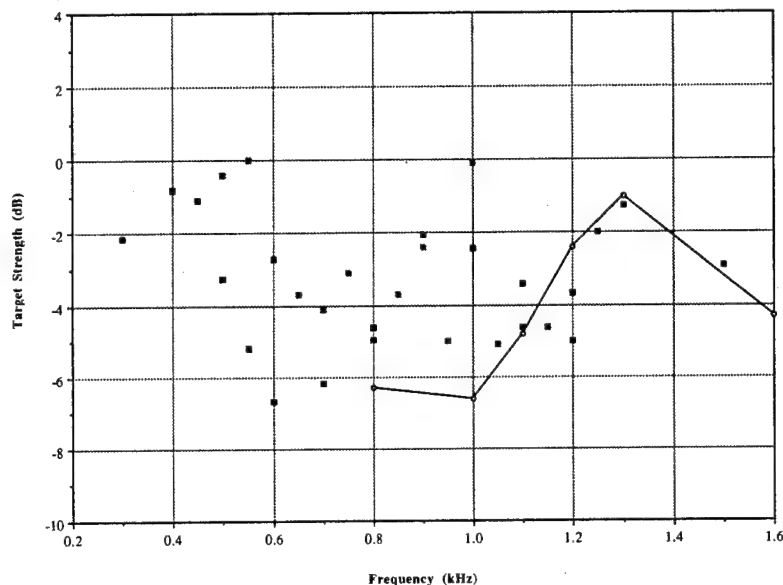
Figure 5.11: Backscatter target strength measured below 1600 Hz. The hollow squares were obtained using the parametric source; the solid squares using the conventional source. The error bars indicate the extent of deviation in the backscatter target strength over a consecutive series of three bubble cloud releases. Note: The curve joining the points is only used to train the eye.

The peak centered at 300 Hz and having TS ≈ −1 dB is strongly suggestive of a resonance. Recall that the measured TS of the 1.12 m-diameter steel sphere at 500 Hz was only -7 dB. Even though it was not known until a later date that the dimensions of the bubble cloud were on the same order of magnitude of the steel sphere, it still seems remarkable that the measured TS was so large. From Figure 3.2, a rigid sphere of this dimension ($ka = 1.1$) would possess a target strength of ≈ −13 dB. Incidentally, the measured tar-

157

get strength of the hollow steel sphere for a driving frequency of 500 Hz is approximately -7 dB—the difference in the measured and predicted value for the steel sphere is hypothesized to be due to the fact that at 500 Hz, this sphere does not appear to be impenetrable (at large ka it does), or it is even more likely that at this low frequency in which the source level decreases dramatically, that the reduced signal–to–noise ratio made an accurate measurement impossible.

For the bubble cloud characterization described in Section 4.3 and for frequencies below 600 Hz, the Lake Seneca bubble cloud is an acoustically compact scatterer, and thus can be treated as a sphere of radius $a = 0.376$ m with void fraction $\beta = 0.0055$. Such a cloud would possess a resonance frequency of $\Omega_0 \approx 326$ Hz and monopole $TS \approx -3$ dB at a depth of 87.6 m, according to Eq. (3.32) and (3.30). Although the preliminary measurement analysis did not agree quantitively with the model predictions, the presence of the scattering peak at approximately the predicted frequency (300 Hz) in the Figure 5.11 is encouraging.

5.7 Post–experimental analysis

5.7.1 Digitizing the data tapes

The data tapes were digitized and processed as illustrated in Figure 5.12. The tapes were mounted on the tape deck for playback. Recall that prior to recording the signals, the waveforms were pre–conditioned (low–pass filtered one to two decades above the driving frequency and 100 Hz high–pass filtered). How-

ever, to insure that no signal aliasing occurred during the digitizing process, the tape deck output was filtered at one–half the data acquisition rate (dependent on the driving frequency). The filter used was a Stewart Brickwall Model VBF-8 with 132 dB rolloff per decade. The amplitude of each output channel on the tape deck was calibrated by adjusting the output level of a pre–recorded calibration tone to $1\,V_{peak}$ as suggested in the Teac SR31–DF manual. This two–second calibration tone was automatically recorded prior to each data run during the experiment. Also, a sequence of calibration tones were recorded to the tape deck each morning during the experimental effort.
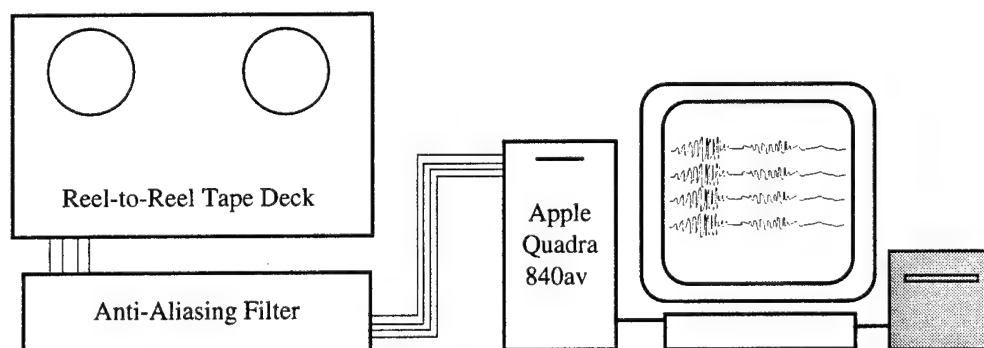
Figure 5.12: The data tapes were mounted on the reel–to–reel tape deck and digitized. Prior to digitizing, an anti–aliasing filter set to one–half the data acquisition rate was placed between the tape deck output and the digitizer input. The computer (Apple Macintosh Quadra 840av) was outfitted with a National Instruments NB–MIO–16 multifunction I/O board and performed the waveform digitizing. The digitized waveforms were stored to files on magneto–optical disks for future processing.

For the majority of the recorded data, the National Instruments NB–MIO–16 expansion board (maximum digitizing rate, 100 kHz) in the Apple Macintosh Quadra 840av computer was configured to digitize data at a rate of at least 10 points per cycle, however, the sampling rate often exceeded 20

points per cycle. For frequencies below 1000 Hz, the sampling rate was set to 20 kHz, and four channels of the tape deck output were digitized simultaneously.

Shown in Figure 5.13 is a pair of digitized main bang and echo wave forms recorded from receiver H1 for a source driving frequency of 1400 Hz during the Seneca–3 experiment. The waveform in Figure 5.13(a) was pre–amplified at $G_{\mathrm{mb}} = 20$ dB, and in Figure 5.13(b) the gain was set to $G_{\mathrm{echo}} = 43$ dB, in order to maximize the respective main bang and scattered echo signal in a ± 1 V_{peak} range (the input range of the recording tape deck).

The software used to control the digitizing process, National Instruments LabView 3.0, was configured to capture 150 ms of data after pre–triggering 10 ms prior to an incident main bang pulse. Recall that for receiver H1, the backscattered echo was expected to arrive approximately 14.3 ± 2.0 ms after the leading edge of the main bang pulse. For frequencies below 1 kHz, the main bang from receiver H1 was used as the trigger channel. Once the voltage output of this channel exceeded the specified amplitude, all four channels were simultaneously digitized. For the higher frequencies, different output channels were used to trigger the digitizing process. The computer software controlling the digitizing process was initiated manually (*i.e.*, a simple "mouse click") at the point of cloud release by monitoring the playback of a single tape deck output channel on an external speaker (the activation of the solenoid bank resulting in the release of a cloud from the bubble maker was audible).

The digitizing process continued until at least 30 s had passed and was stopped prior to the 60 s mark, or when the next cloud was released from

the bubble maker. The bubble cloud rise velocity was 0.39 m/s, thus in 30 s a bubble cloud should rise approximately 11 m above the bubble maker. For the Seneca–2 data tapes, at least 60 waveforms per data run were digitized (*i.e.*, the pulse repetition rate was 2 Hz); and for the Seneca–3 data tapes, at least 30 waveforms were acquired for each data run. The digitized signals were stored to files on magneto–optical disks for future analysis. This process was repeated for each driving frequency, and each cloud release recorded to the reel–to–reel tapes.

Shown in Figure 5.14 is the echo voltage response measured by receiver H1 for a single rising bubble cloud at a source driving frequency of 1400 Hz during the Seneca–3 experiment. Consecutive waveforms (bins) are separated by 1 s, and are to be read down first, then across. The length of each time trace in Figure 5.14 is approximately 50 ms. The bubble cloud was generated within ± 0.5 s of the upper left waveform. The scattering response increased as the bubble cloud traversed through the axis of the source beam, reaching a maximum in bins 11–14. This time–frame is within the 3.8 m (backscatter position) rise–time measurements discussed in Section 4.3.1. The clipped pulse early in each bin is the incident main bang waveform. The reason for the clipping is due to the enhanced pre–amplifier gain applied to the received signal in order to maximize the echo pulse in a $\pm 1 \, V_{peak}$ range prior to recording. A separate channel with the pre–amplifier gain set to maximize the main bang pulse in this voltage range was also recorded. Typically, the difference in gain settings between the main bang and echo channels exceeded 20 dB.

161
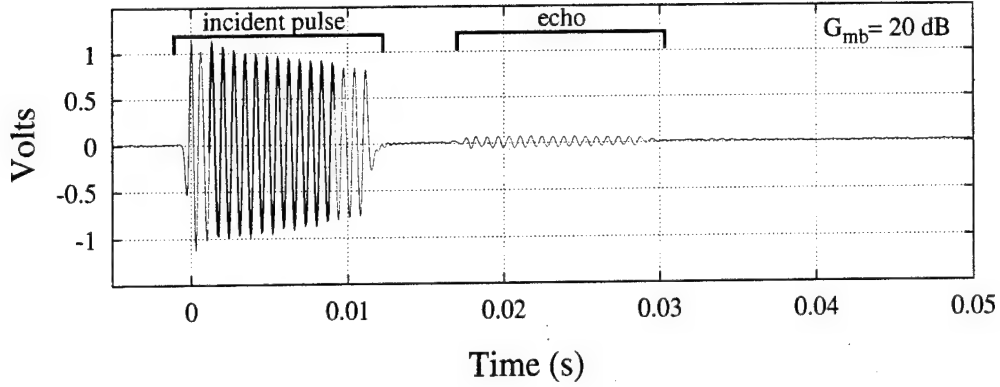
(a) Incident main bang signal
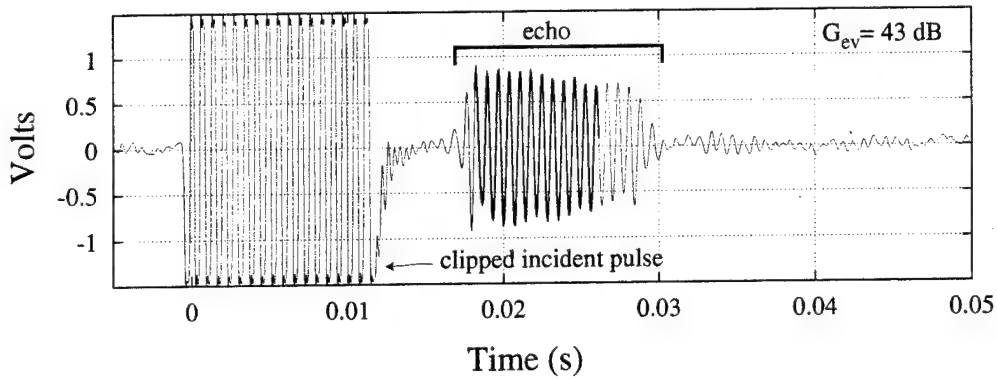
(b) Backscattered echo signal

Figure 5.13: Sample incident and scattered pulse $\approx 11\,\mathrm{s}$ after cloud release (backscatter position) for a driving frequency of $1400\,\mathrm{Hz}$ and measured at H1. To increase the resolution of the scattered echo, the signal was pre–amplified $43\,\mathrm{dB}$ prior to recording. The main bang signal was pre–amplified separately by $20\,\mathrm{dB}$. The incident pulse length is $12\,\mathrm{ms}$. The darker region in each plot corresponds to an $8\,\mathrm{ms}$ window over which the rms measurements were made. In this case, the rms voltages are $\mathrm{MBV} = 0.6\,\mathrm{V_{rms}}$, $\mathrm{EV} = 0.46\,\mathrm{V_{rms}}$. Thus for a total transmission loss factor of $TLF = -22.38\,\mathrm{dB}$ (recall Table 5.2) and the preamplifier gain settings listed above, the measured target strength as given by Eq. (A.10) is $\mathrm{TS} = -2.9\,\mathrm{dB}$.

162
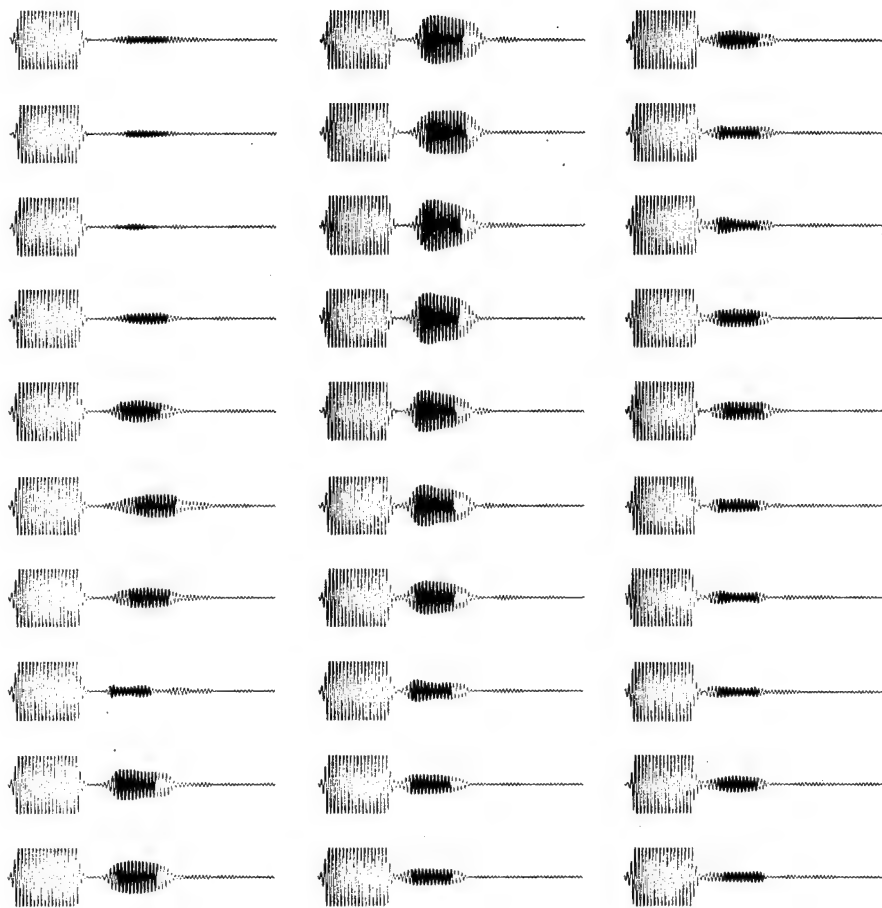
Figure 5.14: Echo response (voltage versus time) after a cloud release at a driving frequency of 1400 Hz. Consecutive time traces are separated by 1 s and are to be read down first then across. Each trace is 50 ms in duration. The cloud is released within ±0.5 s the upper left signal. As the cloud rises through the target area, significant scattering is observed with the expected backscatter position in the upper four traces in the middle column. The darker region (8 ms) contains the maximum rms voltage in the "steady–state" portion of the echo and is used for the TS measurements. The larger amplitude 'clipped' incident main bang ping is due to optimal amplification of the echo.

5.7.2 Data analysis

Because of the relatively low Q (wide bandwidth) of the incident pulses at the lower frequencies, the archived data files were processed using two methods.

163

The "steady–state" rms amplitude of the main bang and scattered waveforms were used to determine the target strength at each driving frequency using an algorithm similar to the on–line analysis. This method, however, only results in a single backscatter data point for each driving frequency, which is effectively the "average" value over the pulse bandwidth. For example, consider the target strength versus frequency curves shown in Figure 3.5, in particular consider the dashed curve with the sharp resonance peak at approximately 600 Hz. To resolve this high–Q resonance peak using amplitude measurements from broad–band (low–Q) pulse is impossible. Rather, this method would result in an "average" response, which tends to lower resonance peaks and increase the dips.

However, utilizing Fourier analysis techniques, the broad–band pulses can be used to determine the frequency response of the scatterer. Further-more, when the bandwidth of the incident pulses at several different driving frequencies overlap (as is the case in this experiment), a much higher resolution frequency response curve can be obtained.

Steady–state rms analysis

In performing the preliminary experimental analysis, the rise velocity of the bubble cloud was unknown and the peak rms amplitude of the main bang and scattered echo voltage provided by hydrophone H1 was used to determine the backscatter target strength of the bubble cloud. During the experiment, it was expected that the strongest scattering returns from the bubble cloud would arrive when the bubble cloud crossed the axis of the test range. The

expectation was that the scattering level would be lower prior to and after the cloud passed through the backscatter location. This was not observed for all driving frequencies. Rather, for some source driving frequencies, the amplitude of the scattered return was observed to increase many seconds prior to the time needed for the cloud to cross the axis of the source beam (12 s), decrease for a few seconds, and then increase again. These unusual observations were repeatable for each of the several clouds released during a given frequency run. Thus, it was clear that some unexpected phenomenon was effecting the scattering observations. At the time, it was postulated that either angular dependent scattering (*i.e.*, not normal incidence backscatter) or perhaps acoustic interference with the bubble maker had occurred.

Another limitation in the preliminary analysis was that the transmission loss factor used to determine the TS level was fixed. This was due to the fact that only a single measurement, the backscatter target strength, was being performed. In this analysis, the rise–time dependent transmission loss factors from Figure 5.5 will be used to determine the elapsed time target strength.

Recall Figure 5.14 in which the evolution of the backscattered echo response of a single rising bubble cloud is displayed. The echo location in each waveform varies as a function of elapsed rise–time, and thus constant range–gating of the scattered echo cannot be used as it was during the "on–line" analysis. Moreover, even though consecutive scattering runs at a given driving frequency were highly repeatable, deviations in the echo delay of 1 to 2 ms were not unusual between cloud releases. These deviations are thought to be due to lake currents which result in the horizontal displacement of the

bubble cloud and/or the receivers.

The peak rms steady–state amplitude of the backscattered echo signal was measured for each incident pulse (see the darker region) in order to determine the target strength as a function of rise time. A simple algorithm was designed to locate the echo pulse in these waveforms. First, the rms amplitude over an 8 ms window beginning 35 ms after the trigger on the main bang pulse ($t = 0$ s) was calculated. Second, this measurement was compared with the rms amplitude over a window of the same width beginning 0.5 ms prior to the 35 m/s delay. The second step of this procedure was repeated until the echo measurement window reached the tail of the incident main bang pulse, and then the peak rms echo amplitude was determined. This peak echo voltage amplitude, along with the average rms amplitude of the incident main bang pulse waveforms, the pre–amplifier gain factors, and the total transmission loss factors from Figure 5.5 were used to determine the target strength as a function of rise time using Eq. (A.10).

Shown in Figure 5.15 are the bubble cloud rise–time dependent target strength measurements for a consecutive sequence of three bubble cloud releases. For this data run, the source driving frequency was set to 1400 Hz, and the measurements were performed using receiver H1, the closest to the target. The average target strength for these three runs is indicated by the dashed line. It is clear that there is a significant deviation in the measured TS in the first few seconds after cloud release, and again after 20 s. This variability is likely due to the fact that the bubble cloud was not within the -3 dB beam–width of the parametric source. The variation is thereby casued by the

166

variability associated with the low signal to noise ratio conditions. However, in bins 5–15, the measured TS for the three clouds is highly repeatable since the bubble cloud is definitely crossing through the main lobe of the parametric source, resulting in an improved signal to noise ratio. In Appendix E, the remainder of the rise–time dependent target strength measurement sequences are illustrated.
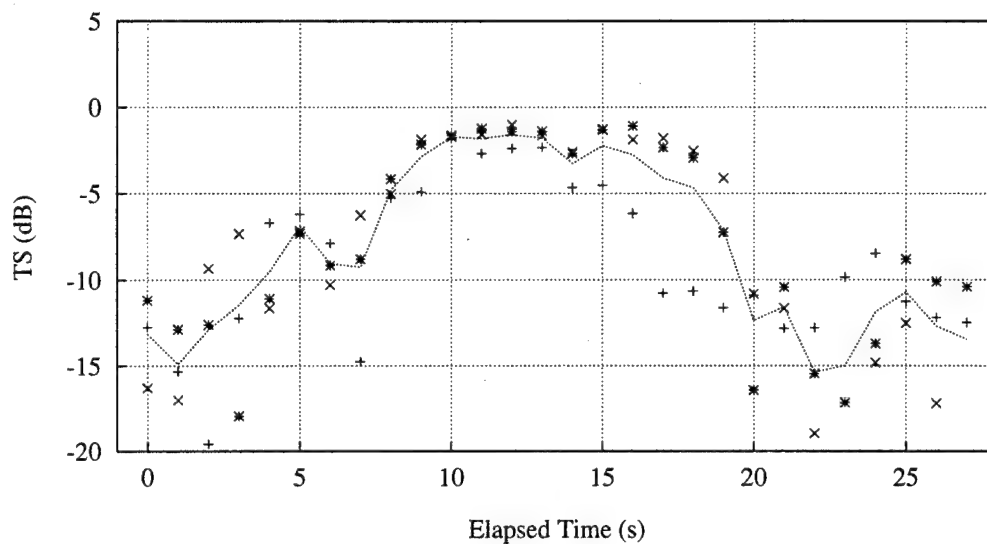
Figure 5.15: Time elapsed target strength for a driving frequency of 1400 Hz during the Seneca–3 experiment. The crosses, stars, and plus signs are the elapsed time dependent TS measurements for individual cloud releases. The boxed points and the dashed line joining these points indicate the average elapsed time TS. The minimum measurable signal in the absence of a rising bubble cloud was -26 dB.

In Figure 5.16 the elapsed time target strength averaged over three consecutive cloud releases is shown for each of the source frequencies used during the Seneca–3 experiment. This figure illustrates some important points. In the frequency range 250 to 500 Hz, the target strength of the rising bubble cloud is relatively strong during the first 20 s after cloud release. This is in part due
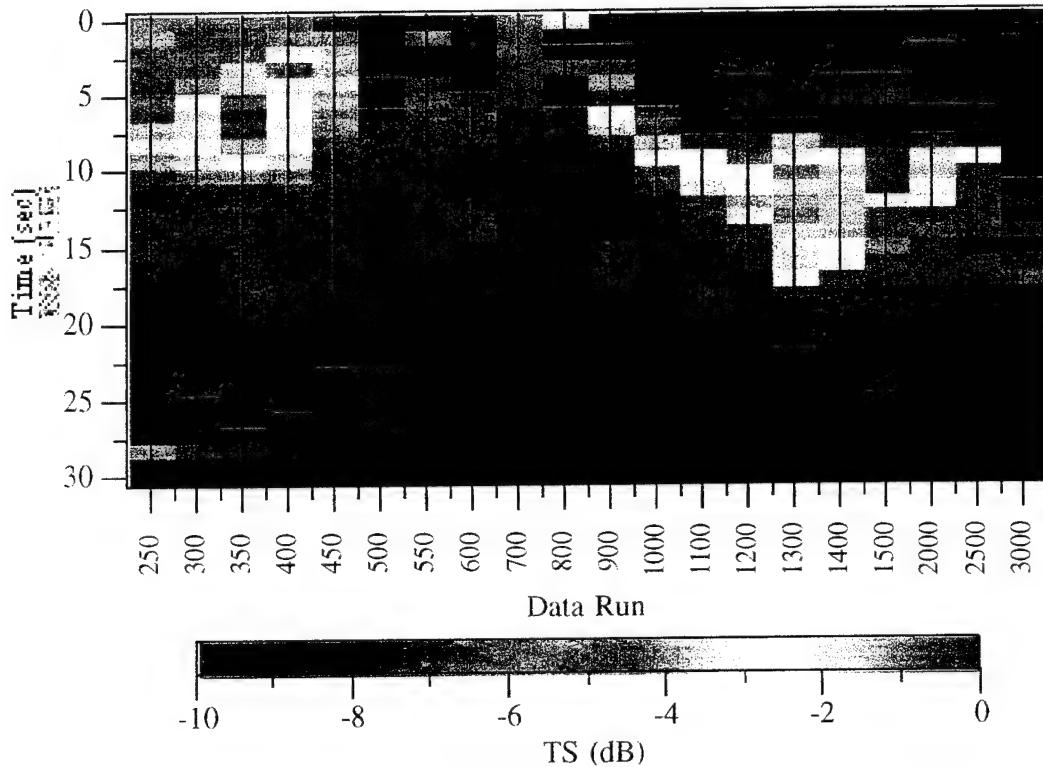
Figure 5.16: Summary rise–time dependent TS measurements. Here, the target strength is computed from the average echo voltage return from a sequence of three rising bubble clouds. The individual data runs are plotted in Appendix E.

to the lower signal to noise level at these frequencies compared to the higher frequency data sets. The PS is less efficient at the lower difference frequencies, and thus our ability to measure the scattered echo over the background spectrum was reduced. It is clear, however, that a peak in the TS versus frequency curve exists between 300 and 350 Hz at approximately 7 s after cloud release, at least 3 s earlier than expected.

The reason for the earlier than anticipated echo return could be due to

the long sonic wavelengths and the proximity of the bubble cloud to the bubble maker (interference phenomenon). It is plausible that the two are acoustically coupled, resulting in an enhanced echo return. The higher frequency data (> 1000 Hz), on the other hand, clearly demonstrates that the bubble cloud crossed the axis of the test range between 9 and 17 s after cloud release. This is in good agreement with the measured rise–time data which suggest that the head of the cloud ascended to the backscatter target location in approximately 9 s and the lower boundary of the cloud passed through this position nearly 14 s after being released into the lake.

According to the rise–time measurements, the bubble cloud should cross the axis of the test range between 9 and 14 seconds after generation. Thus, to determine the backscatter TS, the rms voltage in bins 10–13 were smoothed and averaged over each of the three cloud releases, resulting in the target strength versus frequency curve given in Figure 5.17. The uncertainty in the backscatter TS measurement is derived from the maximum and minimum deviation with respect to the averaged value and are not determined statistically (due to the limited number of observations).

Figure 5.17 plots the smoothed–averaged backscatter target strength measurements at each source driving frequency below 1600 Hz along with the prediction from the simple model presented in Chapter 3. The solid line is a calculation of the target strength using the asymptotic expression (Eq. 3.30), and the dashed line a calculation using the full wave solution of Eq. (3.14). The non–acoustically determined parameters, $P_o = 9.82 \times 10^5$ Pa, $c = 1421.5$ m/s, $\beta = 0.0055$, and $a = 0.376$ m, are used respectively for the ambient hydro-
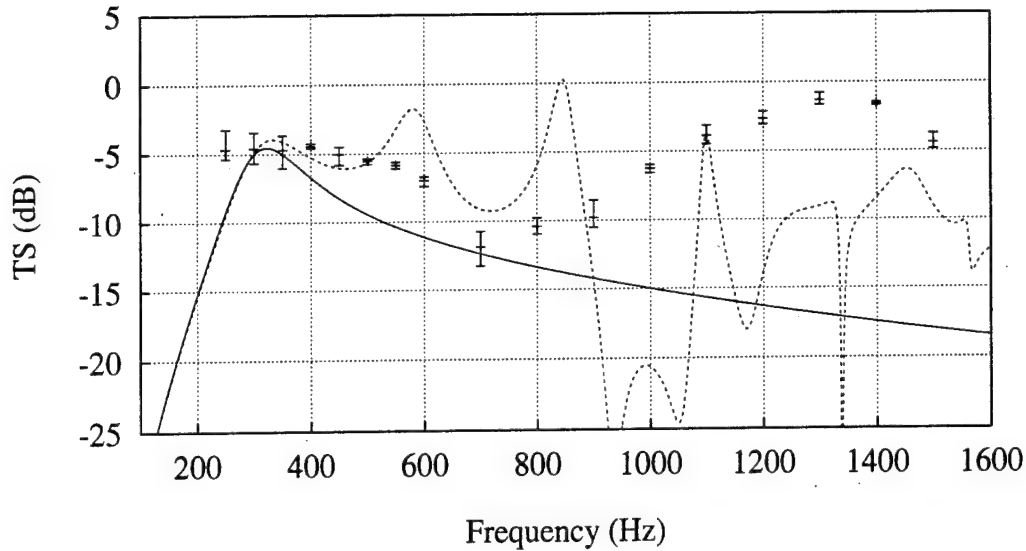
Figure 5.17: Backscatter TS measurements (rms voltage method) performed during the Lake Seneca experiment and comparison with the model. The curves are calculations based on the non–acoustically determined parameters obtained in Chapter 4.3.

static pressure, the sound speed of the water surrounding the sphere, the void fraction, and the radius of the spherical bubble cloud. The error–bars at each source driving frequency indicate the maximum and minimum measured target strength for a sequence of three bubble cloud releases as they crossed the axis of the test range (bins 10–13).

The acoustic scattering measurements agree quantitatively with the prediction of the simple model near the monopole resonance peak ($\approx 300\,\text{Hz}$) as shown in Figure 5.17; this agreement of the experimental measurement with the monopole model is indicated in Table 5.4. Furthermore, in Figure 5.17 there is semi–qualitative agreement out to frequencies as high as 800 Hz. However, the measurements and model diverge at the higher frequencies. This disagreement is likely due to shape dependencies and non–uniform bubble density

170

	Eq. (6.4) ($m = 0$)	Eq. (6.5)	Measured
Ω_0	$326 \pm 25\,\mathrm{Hz}$	$294 \pm 25\,\mathrm{Hz}$	$325 \pm 25\,\mathrm{Hz}$
TS_{ff}	$-2.9 \pm 0.7\,\mathrm{dB}$	$-3.0 \pm 0.7\,\mathrm{dB}$	$-3.4 \pm 0.9\,\mathrm{dB}^a$

[a]The measured value of TS_{ff} was obtained at 300 Hz, and not at Ω_0

Table 5.4: Monopole resonance frequency and target strength for the Lake Seneca bubble cloud.

within the Lake Seneca bubble cloud. For the model, the shape of the bubble cloud is taken to be spherical and the bubble population is uniform throughout; at frequencies above 600 to 700 Hz, this cloud is *not* a uniform sphere. It is likely that if the shape of the bubble cloud were more nearly spherical and that if the bubble population were uniform, then better agreement at all frequencies would have been obtained. Furthermore, the data was obtained over a sparse set of driving frequencies and thus one cannot expect to resolve the sharper peaks and valleys in the higher frequency spectrum without resorting to a frequency spectrum analysis (to be addressed in presentation).

However, for frequencies below 600 Hz the cloud *is* acoustically compact ($ka < 1$) and the trends observed in the Lake Seneca measurements agree semi–qualitatively with those of the partial wave expansion model. The lowest driving frequency was 250 Hz, and a sharp decrease in the target strength predicted by the model (*i.e.*, the Rayleigh scattering regime) below the monopole resonance frequency was not observed. This, in part, is due to the decrease in source level with frequency. The decreasing source level results in a lowered signal to noise ratio, as is evident by the nearly flat elapsed–time response (Figure 5.16) at all frequencies below 550 Hz, with the exception of those frequencies near resonance. Still another possibility for the sooner than expected

171

scattering return near the monopole resonance is that the receiver was not in the far field at these low frequencies. The distance between the target and receiver at the backscatter location was 20.4 m, and the wavelength is greater than 2.5 m.

Part III

Backcattering from acoustically compact bubble clouds near the sea surface

Chapter 6

Acoustic backscattering from compact bubble clouds beneath the ocean surface

6.1 Introduction

Recent studies indicate that bubble layers, plumes, and clouds are produced when waves break (wind speed, $U > 6\,\text{m/s}$), and that these assemblages are convected to depth by Langmuir circulation (Thorpe, 1982; Monahan & Niocaill, 1986). A fundamental question to be answered is what role, if any, do bubble assemblages play in the near–surface production and scattering of sound in the low to mid–frequency range (20 Hz to 2 kHz). There exists ample experimental evidence to suggest that mid–frequency ambient noise levels dramatically increase when waves begin to break (Carey & Browning, 1988;

Hollet, 1994) and that sound scattering from the sea surface possesses a characteristic which is different from that expected by Bragg scattering from gravity waves (McDaniel, 1988). The commonly held view is that persistent bubble clouds, plumes or layers brought on by breaking wave activity can act as efficient scatterers of sound. Indeed, recently published works by Henyey (1991), McDonald (1991), Gragg and Wurmser (1993), Carey and Roy (1993), Gilbert (1993), Sarkar and Prosperetti (1993) indicate a significant role for bubble assemblages in surface backscatter.

In response to these observations a hypothesis has been stated that if bubble clouds and plumes with void fractions, β, ranging from 10^{-5} to 10^{-2} are entrained by surface wave activity, then low–frequency radiated noise can be produced and scattering can occur with little Doppler shift and ample Doppler spread. It has been argued by Prosperetti (1988b) and by Carey and Browning (1988) that, at low frequencies, it is not the individual bubbles driven at their natural resonance frequencies that contribute the most to the scattering cross section of a bubble plume. Rather, sound is scattered primarily by the bubble plume itself via a process in which the bubbles pulsate together in a collective mode of oscillation. This hypothesis is based on the classical theory that when a large number of small bubbles occupy an acoustically compact region, coupled oscillations result and the propagation of sound is determined by the properties of the mixture; the free gas establishes compressibility and the water provides inertia. In such a case, a damped resonant oscillation can result in which the eigenfrequency is determined by the phase speed within the "effective" medium (typically less than $500\,\mathrm{m/s}$) and the characteristic length

175

scale of the plume. Ample evidence of this phenomena, which was originally proposed by d'Agostino and Brennen (1983) has been obtained from the study of low–frequency noise produced by steady–state bubble columns (Yoon *et al.*, 1991) as well as transient bubble plumes (Kolaini *et al.*, 1993; Carey *et al.*, 1993).

6.1.1   Prominent, near–surface scattering features

Recent tests of low–frequency active sonar systems (CST–4)[1] indicate the presence of prominent, near–surface targets during conditions of high sea state (Gauss *et al.*, 1993). Those investigators concluded that prominent returns in the 800–1200 Hz range were due to bubble clouds with lifetimes less than 45 seconds. Similar results were obtained at CST–7 by Adair *et al.* (1992), who observed strong returns (target strength $> -5\,$dB) from seemingly short lived targets positioned within a few meters of the surface. Henyey (1991) and McDonald (1991) have developed scattering models based on the application of weak scattering theory to so–called tenuous bubble clouds (β order 10^{-8}). However, tenuous clouds should persist for more than 45 seconds and are probably not the source of these bright targets.

It is more likely that these short–lived, near–surface targets are the result of bubble plumes generated beneath plunging breakers. Such plumes possess length scales of up to 1 m, void fractions on the order of 10^{-3}, and lifetimes on the order of seconds (Monahan, 1988). If the plumes detach, a three–dimensional, high void fraction bubble cloud is momentarily submerged

---

[1]CST = Critical Sea Test, a research program sponsored by the Office of Naval Research.

at a depth of order 1 meter or possibly more. The contention here is that such a cloud could exhibit resonance scattering properties that translate to high target strengths at low frequencies for short periods of time.

Since the burden of proof lies with the experimentalist, a lake test was carried out in the fall of 1991. (See Chapters 4 and 5 for a detailed description of this effort.) The rational behind the experiment was to measure the frequency–dependent backscatter target strength (TS_{ff}) of a submerged bubble cloud of known properties in the free field under known propagation conditions. The test, which was performed at the NUWC[2] Seneca Lake Sonar Test Facility, involved the production of a bubble cloud of known geometry and void fraction 90 m beneath the surface of the lake. Using a parametric sound source, the target strength of the cloud was measured for frequencies ranging from 250 Hz to over 10 kHz. The test results indicated the presence of a prominent scattering resonance whose level ($\mathrm{TS} \approx -3\,\mathrm{dB}$) and frequency ($\Omega_0 \approx 325\,\mathrm{Hz}$) are well predicted using classical scattering theory coupled with an effective medium approximation and subject to a priori knowledge of the bubble cloud properties. This theory, which is reviewed below, assumes monopole scattering and free–field conditions. The generalization of this model to near–surface conditions is the topic of this chapter.

---

[2]Naval Undersea Warfare Center

6.2 Theoretical model

6.2.1 Scattering from bubble clouds in the free field

Here, the usual assumptions are taken in which plane waves are incident on a compliant sphere of radius a surrounded by a continuous medium of density ρ and sound speed c respectively. Likewise, the sphere is considered to be a homogeneous medium of density ρ_e and sound speed c_e respectively. The sphere (bubble cloud) is composed of many air–filled bubbles; thus, the medium is dispersive with an effective density and wave number given by (Commander & Prosperetti, 1989),

$$\rho_e \equiv (1-\beta)\rho + \beta\rho_g, \tag{6.1}$$

$$k_e^2 = \frac{\omega^2}{c^2} + \frac{4\pi\eta R_o\omega^2}{\omega_0^2 - \omega^2 + 2ib\omega}, \tag{6.2}$$

where k_e is the wave number in the liquid, R_o is the radius of individual bubbles (considered to monodispersed in size), η is the number of bubbles per unit volume, ω_0 is the angular resonance frequency of the bubbles, β is the void fraction, and b is the complex frequency dependent damping constant. For $\omega \ll \omega_0$, one can show that the real portion of the complex phase speed in the mixture is given by,

$$c_e = \sqrt{\gamma P_\infty/\beta\rho} \tag{6.3}$$

Here, P_o is the ambient pressure and γ is the ratio of specific heats of the air. Note that c_e decreases with increasing void fraction. Indeed, for β greater than

178

approximately 10^{-2}, the effective sound speed of the mixture is less than that encountered in either air or water alone.

For the scattering problem in an infinite medium the Helmholtz equation is solved subject to the boundary conditions of continuous pressure and normal velocity. The far–field solution is a superposition of incident plane waves and scattered spherical waves, the latter of which are represented by an expansion in Legendre polynomials given by

$$p_s(\mathbf{r}) \longrightarrow i\frac{p_o}{2}\frac{e^{ikr}}{kr}\sum_{m=0}^{\infty}(2m+1)\mathcal{R}_m P_m\left(\cos\theta\right). \tag{6.4}$$

The coefficients $\mathcal{R}_m$ in Eq. (6.4) satisfy the boundary conditions and describe the reflectivity of the sphere. For acoustically compact scatterers, where $ka \ll 1$, the monopole term in the expansion dominates and the far–field backscattered pressure amplitude is approximated by

$$|p_s| \approx p_o\frac{(ka)^2}{3}\left|\frac{1 - gh^2}{\left(gh^2 - \frac{(ka)^2}{3}\right) - i\frac{(ka)^3}{3}}\right|, \tag{6.5}$$

where $g = \rho/\rho_e$, and $h = c/c_e$.

The second term in the denominator accounts for radiation damping while the first term, when set equal to zero, defines a resonance condition. This results in a monopole resonance frequency and scattered pressure amplitude given by

$$\Omega_0 \;=\; \frac{1}{2\pi a}\sqrt{\frac{3\gamma P_\infty}{\beta(1-\beta)\rho}}. \tag{6.6}$$

Note that the expression for Ω_o has the same form as the Minneart expression (Eq. 2.21) defining the monopole resonance frequency of a spherical bubble; here β accounts for the velocity defect associated with the two–phase mixture. To obtain the free–field backscattered target strength one can substitute either Eq. (6.4) or, for low–frequency scattering, Eq. (6.5) into

$$\mathrm{TS}_{ff} = 20 \log_{10} \left| \frac{p_s}{p_o} \right|_{r=1\,\mathrm{m}} . \tag{6.7}$$

In Table 5.4 the predicted and resonance TS_{ff} are compared with the measurements obtained at Lake Seneca. Since the concern here is with the monopole resonance response, only the $m = 0$ term was calculated in the expansion. The good agreement between theory and measurement supports the view that an effective media approximation is a reasonable way to model low–frequency bubble cloud scattering; indeed, it appears that one can predict the resonance using the simple algebraic expressions given in Eq. (6.5). It is important to note that the model and the measurements agree despite the fact that the Seneca cloud was spheroidal rather than spherical. This is because a monopole response corresponds to a volume–dependent, breathing mode oscillation. For an acoustically compact scatterer, the monopole resonance behavior is well approximated by a sphere of equal volume. In the case of the Lake Seneca cloud, this corresponds to a sphere $\approx 0.38\,\mathrm{m}$ in radius.

6.2.2 Scattering from bubble clouds near the ocean surface

At low frequencies we chose to model the acoustically compact target as a monopole scatterer positioned a distance d beneath a plane horizontal surface characterized by a reflectivity coefficient μ which can vary between -1 and 0. The primary assumptions here are incident plane waves and far–field propagation. A standard application of the method of images yields the following expression for the near–surface, backscatter target strength:

$$\text{TS}_{\text{ns}} = \text{TS}_{f\!f} + 10 \log \left| 1 + \mu^2 + 2\mu - 4\mu \sin^2\left(kd \sin \phi_g\right) \right|^2, \qquad (6.8)$$

where ϕ_g is the grazing angle measured relative to the horizontal. The reflection coefficient describes the roughness of the sea surface; $\mu = -1$ corresponds to a smooth pressure release surface and $\mu = 0$ corresponds to an extremely rough surface (effectively equivalent to an unbounded medium).

6.2.3 The method of images

The solution in Eq. (6.8) is derived using the method of images. Consider the scattering geometry of Figure 6.1. Here, acoustic waves of frequency ω and pressure amplitude p_{i} are incident on the sea surface at grazing angle ϕ_g. The incident waves are generated by the source S which is located at point $S = (-x, -y, -z)$. The surface can be smooth and pressure release, in which case the amplitude reflection coefficient is $\mu = -1$, or it can be roughened by wave action, effectively lowering the magnitude of the reflection coefficient as

181
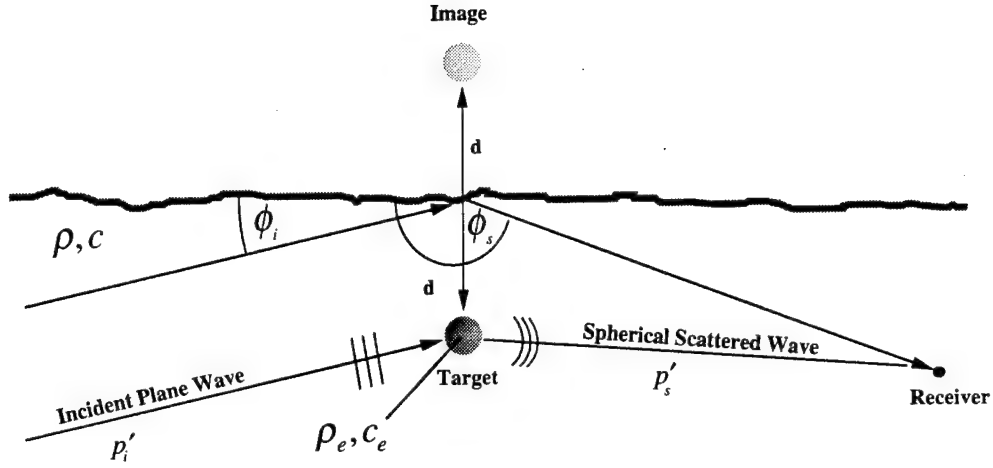
Figure 6.1: Near surface scattering geometry. It is important to note that for backscattering $\theta_i = \theta_s \equiv \phi_g$.

alluded to above (this will be discussed more formally in Section 6.2.4).

The 2-D scattering geometry is given in Fig. 6.1, where the $z-axis$ is the vertical direction, and the $x-axis$ denotes the horizontal range. We assume a plane wave incident on a monopole point scatterer a distance d beneath a surface of reflectivity μ. For far-field measurements, a monopole scatterer $(kd < 1)$ near a reflecting surface behaves like an acoustic dipole (applying the method of images), thus:

$$P_{inc}(\mathbf{r}) = p_i \left[1 + \mu e^{-i2kd\sin\phi_g}\right] e^{i(kx\cos\phi_g + kd\sin\phi_g)}, \tag{6.9}$$

$$P_{scatt}(\mathbf{r}) = p_s \left[1 + \mu e^{+i2kd\sin\phi_g}\right] e^{-i(kx\cos\phi_g + kd\sin\phi_g)}, \tag{6.10}$$

$$\left|\frac{P_{scatt}}{p_i}\right| = \mathcal{F}\left|1 + \mu^2 + 2\mu\cos\left(2kd\sin\phi_g\right)\right|. \tag{6.11}$$

182

Here, P_{inc} and P_{scatt} refer to the total incident/scattered fields (actual plus image), and p_i and p_s are the magnitudes of the incident/scattered signal in the absence of a reflecting surface. The ratio p_s/p_i on the right side of Eq. (6.11) is the backscatter form function, as derived previously, and should be replaced with Eq. (3.14), or its asymptotic form, Eq. (3.30). However, the data will be presented as TS, so that:

$$\text{TS}_{\text{ns}} = \text{TS}_{ff} + 10\log\left|1 + \mu^2 + 2\mu - 4\mu\sin^2\left(kd\sin\phi_g\right)\right|^2, \tag{6.12}$$

where the second term on the right is generally referred to as the transmission anomaly (TA)(Urick, 1967; Kinsler *et al.*, 1982). It is easy to show that for $\mu \approx -1$, and for clouds that are acoustically close to the surface ($kd \ll 1$), that the argument of the TA can be simplified to $\left((kd)^4\sin^4\phi_g\right)$, which suggests a dipole interference pattern. Thus, high void fraction clouds, which exist only very near the sea surface and have significant low-frequency TS's in the free-field, may not be acoustically "important" due to the effect of surface dipole cancellation. On the other hand, for deeper scatterers, the volume fractions are necessarily lower (by design of nature) and may not resonate at all. It seems plausible that an optimum combination of depth, void fractions and cloud sizes may exist; a notion that we are currently exploring.

6.2.4 The Kirchoff approximation

The Kirchoff approximation given by (Urick, 1967; Thorsos, 1990) relates the reflection coefficient to the windspeed, U, as follows:

$$\mu = -e^{-2(kh\sin\phi_g)^2},$$ (6.13)

where,

$$h^2 = \frac{\alpha_1 U^4}{4\alpha_2 g^2}$$ (6.14)

is the rms–squared wave height predicted by the "Pierson-Moskowitz" wave-height frequency spectra(Pierson & Moskowitz, 1964). Here, U is the wind speed measured 10 m above the sea surface, α's are empirical constants, and $g = 9.8$ m/s^2. The range of the reflection coefficient is $-1 < \mu < 0$. $\mu = -1$ corresponds to a smooth pressure release surface (*i.e.*, low frequencies and/or low wind speeds). Similarly, at high frequencies or high wind speeds the surface appears acoustically rough, which disrupts coherent surface reflection yielding free–field acoustic behavior (*i.e.*, $\mu \to 0$).

It is evident from Eq.(6.5), (6.8), and (6.13) that the resonance backscatter target strength for a near–surface bubble cloud is a complex function of the various parameters. From Eq. (6.5) it is clear that increasing either a or β reduces Ω_0 and increases the TS$_{ff}$. However, the proximity of the surface is parameterized by kd, *i.e.*, depth is relative to the acoustic wavelength. For $kd \ll 1$ and $\mu = -1$, the scattered pressure scales with $(d/\lambda)^4$. From this it

184

is clear that, although large, high–β clouds possess significant cross sections at resonance, they are also subject to substantial dipole interference owing to their close proximity (both oceanographically and acoustically) to the surface. It would appear that there are optimum combinations of physical and environmental parameters leading to significant target strengths (say, larger than -10 dB).

6.3   Results and discussion

At this point a "case study" is considered, in which the scattering characteristics of a 5 cm radius cloud of very small bubbles is explored. The grazing angle is fixed at 10°. Within the bounds of this simple model, the remaining parameters influencing the scattering characteristics of this cloud are the void fraction, depth, and windspeed. Both free–field and near–surface scattering will be considered. All calculations employ only the $m = 0$ term from Eq. (6.4), thus only the low–frequency (*i.e.*, monopole) backscattering behavior will be considered.

Shown in Figure 6.2(a) is the target strength versus frequency for this cloud resident at a depth of 2 m and possessing a void fraction of $\beta = 5 \times 10^{-3}$. Note the monopole resonance peak at 786 Hz, where TS_{ff} is -9.5 dB. A windspeed of 20 m/s does little to modify the response, for the surface is very rough. It is interesting to note, however, that lowering the windspeed to 7 m/s increases the target strength to +1.95 dB. This is due to "constructive" interference between the real and image scatterers. To see this more clearly,

185

consider the plot of resonance versus depth show in Figure 6.2(b). The "Lloyds Mirror" interference pattern is clearly the cause of the elevated target strength.
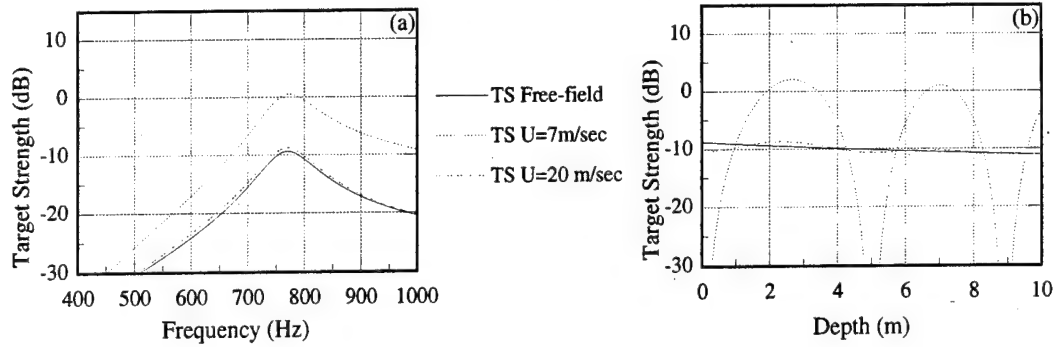
Figure 6.2: Low–frequency backscatter from 5 cm radius cloud for $\beta = 5 \times 10^{-3}$ and $\phi_g = 10°$: (a) depth = 2.0 m; (b) frequency = 786 Hz.

The global scattering properties of this cloud are illustrated in the surface plots of Figure 6.3. Figure 6.3(a) is a plot of the TS at resonance versus depth and void fraction. As predicted in Eq. (6.5), increasing the void fraction results in a significant increase in TS and decrease in Ω_0. There is also a weak dependence on submerged depth, as evidence in Eq. (6.3). Figures 6.3(b) through (d) depict the influence of the surface. The surface–dipole interference pattern is most evident at 7 m/s, where over the entire frequency range. Target strengths as high as +10 dB are observed for clouds with void fraction $\beta = 5 \times 10^{-3}$ positioned at depths ranging from 7–8 m. However, such clouds are not likely to exist in the open ocean.

A sequential consideration of Figs. 6.3(b) through (d) serves to illustrate the effect of increasing windspeed. As the wind speed increases, the surface become rougher and therefore less influential. Indeed, it appears that at 20 m/s free–field conditions prevail for all but the lowest resonance frequencies (*i.e.*,

186
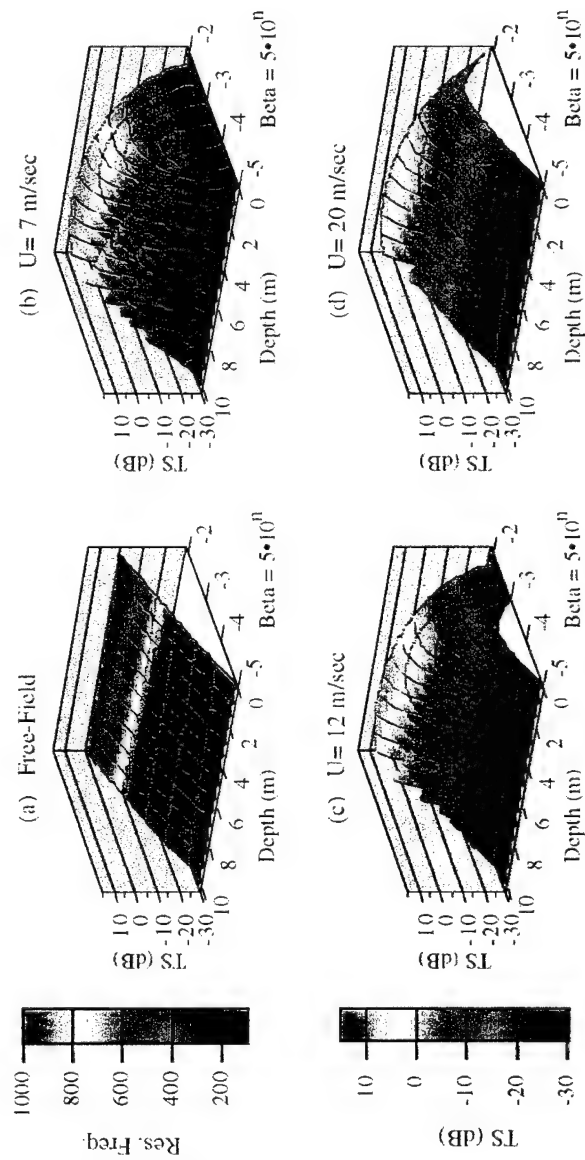
Figure 6.3: Monopole resonance backscatter from 5 cm radius cloud for $\phi_g = 10°$. The color scale denotes (a): monopole resonance frequency; (b) through (d): TS at resonance.

highest void fractions). The notion of an optimal combination of void fraction and depth is clearly evident in these plots, which exhibit pronounced peaks and valleys as these parameters vary.
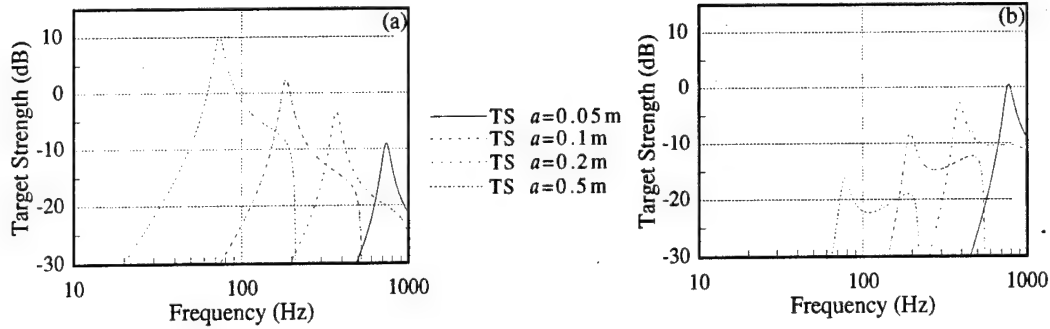
Figure 6.4: Low–frequency backscatter from various clouds for $\beta = 5 \times 10^{-3}$ and $\phi_g = 10°$: (a) free–field calculations; (b) depth = $2.0\,\mathrm{m}$ and $U = 7\,\mathrm{m/s}$.

Now the role played by increasing the size of the bubble cloud is considered. Figure 6.4(a) shows a plot of $\mathrm{TS}_{\textit{ff}}$ versus frequency for clouds with radii ranging from 5 to 50 cm. All four clouds possess a void fraction of $\beta = 5 \times 10^{-3}$. As expected, increasing cloud size equates to decreasing resonance frequency and increasing target strength in the free field. Conversely, Figure 6.4(b) illustrates the backscatter $\mathrm{TS}_{\mathrm{ns}}$ for the same clouds at a depth of $2\,\mathrm{m}$ and a surface grazing angle of $10°$. Now, the smaller clouds exhibit the higher target strengths at resonance. In general, this is due to the fact that these smaller clouds resonate at higher frequency, which means that the surface is further removed (acoustically speaking) and therefore less influential. However, in this particular instance, the contribution of constructive interference between the real and image scatterers plays a role as well. Regardless, one should not be too quick to ascribe free–field scattering properties to bubble clouds resident near the surface. In some instances, it may be the smallest clouds that make

188

to largest contributions.

6.4 Summary and conclusions

In this study, a simple model describing the low–frequency scattering proper-
ties of high void fraction bubble clouds in both the free field and near the
ocean surface was developed. This model, which is based on an effective
medium approximation and acoustically compact scatters, successfully pre-
dicts the results of the bubble cloud scattering experiment carried out at Lake
Seneca (Roy *et al.*, 1992). The introduction of the surface is facilitated by
the method of images and is subject to the same constraint of low–acoustic
frequency imposed by the compact scatterer assumption. This model is not
intended to serve as a exact replicate of oceanic bubble cloud scattering. Such
an endeavor offers limited utility, for the accuracy of any model is ultimately
bounded by the quality of the input data. The model herein was kept simple
by design, for only then can the complex physical behavior be expressed in
a simple analytical form. Simple, analytic theories facilitate the exploration
of parameter space, and more importantly serve to illuminate the underlying
physics.

    The bubble cloud appears to resonate somewhat like a free bubble
(Eq. 6.5). Increasing the size of the cloud decreases the resonance frequency
and increases the free–field target strength at resonance. Increasing the void
fraction has the same effect due to the reduction in sound speed within the
cloud. For example, a $0.5\,m$ radius cloud ($\beta = 5 \times 10^{-3}$) resonates at $75\,Hz$

189

and possesses a free field target strength of $+10\,$dB at resonance, whereas a $0.1\,$m radius cloud with the same void fraction resonates at $370\,$Hz and has a target strength of $-3.5\,$dB.

Introduction of the surface leads to a dipole interaction. For a perfectly smooth surface, the target strength can either increase or decrease depending on the frequency and the depth. Since the resonance frequency is also a function of cloud size and void fraction, the manifold of possible behavior is quite broad. In general, larger clouds are more effected due to the fact that they resonate at lower frequencies; the proximity of the surface is defined relative to the acoustic wavelength. Incoherent scattering brought on by surface roughness reduces the impact of dipole interaction. As the wind picks up, or as the acoustic frequency increases, the environment asymptotes to that of a free field. It is interesting to note that the same environmental conditions that lead to a diminishment of surface dipole interaction also result in high void fraction bubble clouds entrained by breaking waves.

A case study of a $5\,$cm radius cloud revealed target strengths as high as $+10\,$dB at depths exceeding $7\,$m and for a windspeed of $7\,$m/s. For the case of a void fraction cloud at a depth of $2\,$m, the calculated resonance frequency and target strength was $786\,$Hz and $0\,$dB respectively. It is important to recognize that the notion of such a cloud temporarily residing at a depth of 2 meters beneath a breaking wave event is well within the bounds of reason. A $0\,$dB target strength is quite significant, and we conclude that these small, high void fraction clouds may indeed be the source of the short–lived, near–surface scattering features observed by investigators such as Gauss *et al.* (1993) and

190

Adair *et al.* (1992).

Chapter 7

Concluding remarks

The presence of bubbles in water dramatically effects the propagation of sound waves. When a bubble is formed (or "birthed"), it radiates a characteristic damped harmonic acoustic signature at the well known Minneart (monopole) resonance frequency given by $f_0 = (1/2\pi R_o)\sqrt{3\gamma P_\infty/\rho}$. In addition to radiating sound, a bubble is an excellent absorber and scatterer of sound as well. In sufficient concentrations, a mixture bubbles in water effectively lowers or raises the sound velocity depending on the acoustic frequency and the sizes of the bubbles.

Substantial laboratory and field evidence suggests that high–void fraction bubble clouds radiate a sound when produced. The acoustic signature, however, is not limited to the relatively high bubble resonance frequencies. Recently, Hollet (1994) and Farmer and Vagle (1989) observed a significant contribution of low–frequency sound ($< 1\,\mathrm{kHz}$) coincident with the production of a bubble cloud in the ocean. In addition, many laboratory and well

controlled field experimental efforts have established that bubble cloud production is a viable source of low frequency sound in the ocean (Roy *et al.*, 1992; Carey *et al.*, 1993; Kolaini *et al.*, 1994; Yoon *et al.*, 1991; Nicholas *et al.*, to be submitted) and is in good agreement with the simple theoretical models (Carey & Fitzgerald, 1993; Lu *et al.*, 1990).

Interestingly enough, prior to 1985 there was little or no mention of the possibility that bubble clouds contributed to ambient noise in the ocean below 2 kHz. Currently, this idea is widely accepted. The recent field measurements of Hollet and of Farmer and Vagle, when considered along with the good agreement between the theory and results of Carey's tipping–trough and Kolaini's bucket–drop experiments suggest that the bubble clouds generated beneath breaking waves are a fundamental contributing source of natural low frequency noise in the ocean.

Since a good radiator of sound is a good scatterer of sound, it seems plausible that acoustically compact bubbly regions (clouds) can behave as scatters of sound. The application of a classical theory coupled with the homogeneous mixture assumption based on the low frequency air–water mixture properties produces an analogous single–bubble description of the bubble cloud in which the resonance frequency of the volume mode is described by a modified Minneart formula (Eq. 3.32) and a simplified monopole expression exists for the backscatter target strength (Eq. 3.33). Bubble clouds produced near the sea surface are important in both the production and scattering of low frequency sound.

7.1 Collective bubble oscillations

The propagation of acoustic waves in fluids is highly influenced by properties such as absorption and scattering. In fact, for a two–phase fluid consisting of water mixed with a sufficiently large concentration of air bubbles, the sound velocity is frequency dependent. This dependence is a consequence of the marked change of the fluid's natural compressibility when mixed with bubbles (Brekhovskikh & Lysanov, 1991). For frequencies below the fundamental resonance of the individual bubbles, the sound speed can be lowered dramatically. This dependence is solely on the fractional volume or void fraction of bubbles in the fluid (Wood, 1941). The physics behind the lowering of the sound speed is that the bubbly region possesses a density close to that of the liquid, but a much greater compressibility. The free gas establishes the compressibility, while the water provides inertia. If one recalls that the sound speed in a fluid medium is proportional to the square–root of the inverse product of the these quantities, the physical basis for the sound speed defect becomes obvious.

For the low–frequency limiting case, the speed of sound in the mixture is primarily governed by the void fraction β. For β in the range 10^{-4} to 10^{-2}, the mixture sound speed can be lowered to values that fall well beneath the sound speed in the liquid, and even to values below the speed of sound in the gas. This indeed is remarkable! It was demonstrated that the real portion of the complex phase speed in the mixture is given by,

$$c_e = \sqrt{\gamma P_\infty / \beta \rho} \qquad (7.1)$$

for frequencies below bubble resonance. Here, P_o is the ambient pressure and γ is the ratio of specific heats of the air. Note that c_e decreases with increasing void fraction. For β greater than approximately 10^{-2}, the effective sound speed of the mixture is less than that encountered in either air or water alone.

Compared to a bubble, the wavelength of the sound at low frequencies is, by definition, much greater than the bubble radii (and their respective spacing), and thus a bubbly mixture can be considered an effective fluid having a density near that of water and a sound speed that is dependent only on the void fraction and not on the details of the bubble population statistics.

7.2   Scattering

In Chapter 3 the classical theory for acoustic scattering from a compliant sphere in the free–field was presented. The solution for the scattered pressure at every point in the sphere's exterior was given by a normal mode expansion (Eq. 3.12). The solution was obtained by simply meeting the requirements on the boundary of the sphere of continuous pressure and continuous normal particle velocity and by exploiting the symmetry of the problem. Although not limited to scattering from acoustically compact bubble clouds, this problem yields itself to a simple and straightforward analysis using the well established collective oscillations model for the effective sound speed and effective density as outlined in Chapter 2.

In addition to the full wave expansion, simple analytical expressions were derived which approximate the monopole resonance frequency (Ω_0) and

195

the target strength (TS) at this resonance of a bubble filled sphere (see Chapter 3.4). It was determined that the monopole resonance frequency and TS depend only on two physical characteristics of the bubble cloud: the total volume and the void fraction (β). It is important to stress that the monopole TS level and Ω_0 can always be obtained without a detailed knowledge of the bubble size distribution so long as β and the cloud dimensions are known.

7.3 The burden of proof

Since the burden of proof lies with the experimentalist, a lake test was carried out in the fall of 1991 (See Chapters 4 and 5 for a detailed description of this effort). The rational behind the experiment was to measure the frequency–dependent backscatter target strength (TS_{ff}) of a submerged bubble cloud of known properties in the free field under known propagation conditions. The test, which was performed at the NUWC[1] Seneca Lake Sonar Test Facility, involved the production of a bubble cloud of known geometry and void fraction 90 m beneath the surface of the lake. Using a parametric sound source, the target strength of the cloud was measured for frequencies ranging from 250 Hz to over 10 kHz. The test results indicated the presence of a prominent scattering resonance whose level (TS ≈ -3 dB) and frequency ($\Omega_0 \approx 325$ Hz) are well predicted using classical scattering theory coupled with an effective medium approximation and subject to a priori knowledge of the bubble cloud properties. This theory, which is described in Chapters 2 and 3, assumes monopole scattering and free–field conditions, and models the acoustically compact cloud

---

[1]Naval Undersea Warfare Center

as a sphere.

The acoustically compact cloud produced during the Lake Seneca experiment possess higher–order poles which are not easily described by the simple analytical approach outlined in this dissertation. This is presumably due to the fact that the cloud was neither a perfect sphere nor a perfect cylinder. Unlike the monopole mode, the higher order resonances are dependent on the shape of the cloud and the localized void fraction distribution within the cloud.

Based on the relatively good theoretical agreement with experimental findings of the Lake Seneca experiment (and recent ambient noise experiments), it is quite plausible that bubble clouds are an important mechanism related to the increase in surface scattering levels observed in the ocean during periods of high sea state and for frequencies between 20 and 2000 Hz. In the free–field, an acoustically compact bubble cloud scatters sound effectively in its monopole mode and in quantitative agreement with the model based on a spherical bubble cloud of uniform void fraction. To our knowledge, this is the first report of monopole resonance scattering from a bubble cloud.

7.4 Scatter from subsurface bubble clouds

Although detailed experimental studies of the frequency dependent acoustic scattering from individual bubble clouds immediately beneath the sea surface have not been conducted, the simple model presented in Chapter 6 (Lloyd's Mirror) suggests that near–surface bubble clouds are strong scattering targets, even at the low frequencies. The most important determining factor in this

197

case is the monopole resonance frequency of the cloud (dependent on β and a) and the cloud depth beneath the surface relative to the wavelength; for small d/λ or small grazing angle, the TS is proportional to $(d/\lambda)^4$. A monopole bubble cloud scatterer beneath the pressure release sea surface is acoustically coupled to the surface and behaves as a simple dipole scatterer (method of images).

In modeling the acoustic scatter from bubble clouds beneath the sea surface, we are presented with an optimization problem which can be summarized as follows: The free–field scattering model suggests that the monopole resonance frequency decreases and the TS of the cloud increases as the cloud radius is increased (all other parameters held fixed). Near the sea surface, however, a cloud having a lower resonance frequency (and thus larger TS) is less important due to destructive dipole interference. Furthermore, a cloud with a low resonance frequency (say $\Omega_0 = 100\,\text{Hz}$ or $\lambda = 15\,\text{m}$) is physically unlikely to penetrate to depths in which the destructive dipole interference is overcome. These high void fraction clouds are more likely to be present at high sea states. Moreover, as the sea state becomes rougher, the dipole interference effects become less important since the reflectivity of the sea surface decreases as it diverges from its smooth pressure release value. Thus, the larger or higher void fraction clouds play an increasing larger role as the sea state increases.

It should be noted that as with the Chapman–Harris and Chapman–Scott sea surface scattering results and the associated empirical curves, any surface scattering model will likely display a "dipole–like" dependence similar to that illustrated in Chapter 6 (*i.e.*, $(d/\lambda)^4 \sin^4 \phi_g$). However, the hypothesis

that relatively densely populated bubble clouds are the source of the scattered sound is on an especially strong physical footing since the low–frequency sea surface scattering levels are observed to increase dramatically at the moment waves begin to break. Indeed, as is the case with underwater ambient noise production, indications are that two distinct mechanisms are likely responsible for the anomalous scattering results—one prior to, and one after wave breaking. Finally, the recent surface scattering results reported by Adair and Huster indicate that transient, spatially discrete, high target strength scattering centers exist in the upper 5 m of the ocean surface during periods of high sea state. These factors are not only strongly suggestive of bubble clouds, but are also consistent with the simple model described in Chapter 6.

7.5   Remarks

The bubble cloud appears to resonate somewhat like a free bubble. Increasing the size of the cloud decreases the resonance frequency and increases the free–field target strength at resonance. Increasing the void fraction has the same effect due to the reduction in sound speed within the cloud. For example, a 0.5 m radius cloud ($\beta = 5 \times 10^{-3}$) resonates at 75 Hz and possesses a free field target strength of +10 dB at resonance, whereas a 0.1 m radius cloud with the same void fraction resonates at 370 Hz and has a target strength of −3.5 dB.

Introduction of the surface leads to a dipole interaction. For a perfectly smooth surface, the target strength can either increase or decrease depending on the frequency and the depth. Since the resonance frequency is also a

function of cloud size and void fraction, the manifold of possible behavior is quite broad. In general, larger clouds are more effected due to the fact that they resonate at lower frequencies; the proximity of the surface is defined relative to the acoustic wavelength. Incoherent scattering brought on by surface roughness reduces the impact of dipole interaction. As the wind picks up, or as the acoustic frequency increases, the environment asymptotes to that of a free field. It is interesting to note that the same environmental conditions that lead to a diminishment of surface dipole interaction also result in high void fraction bubble clouds entrained by breaking waves.

In this study, a simple model describing the low–frequency scattering properties of high void fraction bubble clouds in both the free field and near the ocean surface was developed. This model, which is based on an effective medium approximation and acoustically compact scatters, successfully predicts the results of the bubble cloud scattering experiment carried out at Lake Seneca for frequencies consistent with the model assumptions (Roy *et al.*, 1992). The introduction of the surface is facilitated by the method of images and is subject to the same constraint of low–acoustic frequency imposed by the compact scatterer assumption. This model is not intended to serve as an exact replicate of oceanic bubble cloud scattering. Such an endeavor offers limited utility, for the accuracy of any model is ultimately bounded by the quality of the input data. The model herein was kept simple by design, for only then can the complex physical behavior be expressed in a simple analytical form. Simple, analytic theories facilitate the exploration of parameter space, and more importantly serve to illuminate the underlying physics.

Appendix A

Target Strength

A.1   Definition of target strength

Measurement of the scattering of acoustic waves from a submerged target is a complex process for which one does not always know the shape, volume, orientation, or composition of the target. For this reason, the sonar community has defined the relation *target strength*, which refers to the relative echo strength returned by an underwater target. The targets may be of military interest, such as mines, torpedoes, or submarines; of commercial interest, such as schools of fish sought by fish finding sonar's; or of academic interest, as in the case for a *spherical* bubble cloud. The target strength, as defined by Urick (1967), is

$$TS \;=\; 10\log_{10}\left(\frac{I_s}{I_i}\right)_{R_{\mathrm{ref}}=1\,\mathrm{m}}, \qquad (\text{A.1})$$

201

where I_i and I_s are the incident and scattered acoustic intensities, respectively. Furthermore, these values are evaluated at a reference distance of 1 m from the apparent origin of the scattered sound. Since the acoustic intensity is proportional to the pressure amplitude squared, the TS can be written

$$\text{TS} \;=\; 20 \log_{10} \frac{|p_s|}{|p_i|}\bigg|_{R_{\text{ref}}=1\,\text{m}} \tag{A.2}$$

The reference distance of 1 m is arbitrary and often causes underwater objects to have positive target strength. Positive values should not be interpreted as meaning that the sound returned by the object is greater than that incident upon it; rather it should be regarded as a consequence of an arbitrary reference distance—for example, if a reference distance of 1 km were used, all customary targets would possess negative target strength (due to spherical spreading of he outgoing acoustic wave). If the sonic wavelength inside the scatterer is less than or on the order of the size of the target, resonances can occur, possibly resulting in elevated target strengths.

In Figure A.1, the geometry for a scattering measurement from an arbitrary target is shown. Here, H is the point at which the pressure amplitude of the scattered wave is imagined to be measured and O is the acoustic center of the target. Note that O may lie inside or outside the target itself and is the point from which the returned sound appears to originate on the basis of measurements made at some large distance from the target.

As an illustration, consider the target strength of a perfectly reflecting sphere for large ka. The sphere (radius a) is considered large and rigid and
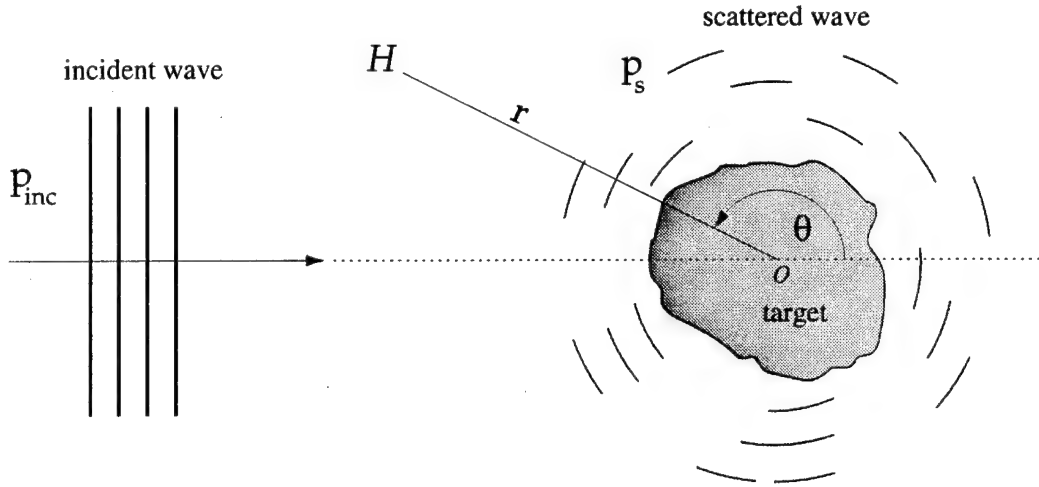
Figure A.1: Geometry of a target strength measurement from an arbitrary scatterer. A plane wave (p_{inc}) is incident on the target from the left. A detector located at point H records the scattered signal (p_s) at a distance r and angle θ from the forward scattering direction. Here, the origin of the scattered signal is the center of the target.

is insonified by plane waves of intensity I_i. The acoustic power intercepted by the sphere is $\mathbb{P}_i = \pi a^2 I_i$. Sound is scattered in all directions uniformly and hence the total scattered power is $\mathbb{P}_s = 4\pi r^2 I_s$. Since rigid targets do not absorb energy, the scattered energy must be equal to that incident on the target. Hence, the scattered acoustic intensity is given by the relation

$$I_s = \frac{\pi a^2 I_i}{4\pi r^2} = I_i \frac{a^2}{4},$$ (A.3)

and thus the target strength for a perfectly reflecting sphere is

$$\text{TS} = 20 \log \frac{a}{2}.$$ (A.4)

Evidently then, for a 2 m–radius perfectly reflecting sphere the TS is 0 dB.

Note that for this example, the reference distance $R_{ref} = 1\,m$ is inside the sphere.

A prerequisite knowledge of the size, shape, and composition of the scatterer are not necessary to perform target strength measurements (only the range and magnitudes of the incident and scattered pressure fields are needed). The preceding statement does not apply when one wishes to compare a TS measurement with a theoretical model—in which case, the size, shape, and composition of the scatterer must be taken into account.

A.2 TS measurements — Steady state

Scattering experiments are usually conducted using directional transmitters and pulses of sound rather than continuous plane waves. This is done primarily to avoid unwanted reverberation from boundaries (tank walls, surfaces, etc.) and the difficulty of measuring a scattered signal in the presence of the cw incident wave. The most common experimental scattering arrangement is the monostatic (pulse–echo) geometry in which the source and receiver are located at the same or closely spaced points. If the transmitter and receiver are separated by a wide distance, then the configuration is known as bistatic.

Consider Figure A.2 in which the geometry for a bistatic (or in this case, *quasi*–monostatic) backscattering target strength measurement is illustrated. A pulsed directional source (S) is aimed at the target (T). Both the incident and scattered waveforms are measured at some point between the target and the source using the receiving hydrophone (H). The separation distances be-

tween each of these objects are known accurately. Furthermore, the distances R_{SH}, R_{ST}, and R_{TH} are large enough that the incident field is sufficiently planar, and the scattered field appears to originate from a point.
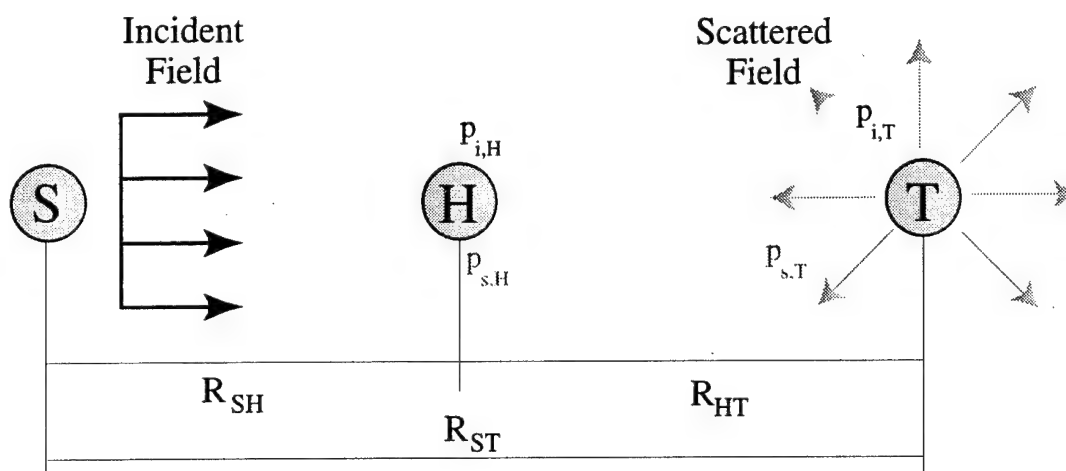
Figure A.2: Geometry for quasi–monostatic scattering measurement. A directional source (S) is aimed at the target (T). Both the incident and scattered waveforms are measured at the receiver (H). The distances between the components are known accurately. The incident pressure amplitude measured at the receiver H is $p_{\mathrm{i,H}}$. Incidentally, the source and receiver are separated by a large distance so that the incoming waves appear planar. Similarly, the scattered pressure evaluated at unit distance from the target T is $p_{\mathrm{s,T}}$. H is small enough that it does not interfere with the incident field.

At time $t_o = 0$, the source sends out a pulse of sound of duration τ and nearly constant angular frequency $\omega = 2\pi f$. The ratio of τ to the period $1/f$ should be much larger than 1 in order for the pulse waveform to reach a steady state amplitude. However, the pulse length τ must be less than $2R_{\mathrm{TH}}/c$ so that the incident and scattered pulses measured at detector H do not overlap at the detector location (c is the sound speed of the surrounding fluid). At time $t_1 = R_{\mathrm{SH}}/c$, the incident waveform is received at detector H,

and the steady state voltage amplitude of this main bang pulse is measured (MBV); the pressure amplitude of the incident pulse measured at the receiver is $p_{i,H}$.

The incident pressure wave continues to propagate toward the target, intercepting it at time $t_2 = R_{ST}/c$ at which point its amplitude is $p_{i,T}$. The target responds to the incident pressure disturbance by absorbing and scattering sound. The portion of the scattered wave propagating in the backward direction is received by detector H at time $t_3 = (R_{ST} + R_{TH})/c$. The echo voltage amplitude recorded is EV; the backscattered pressure amplitude measured is $p_{s,H}$.

The target strength of the scatter is given by Eq. (A.2), and thus we are left to determine the scattered and incident pressure amplitudes evaluated at a distance of 1 m from the target origin. These absolute quantities directly relate to the measured voltages after making corrections for receiving amplifier gain, hydrophone calibration coefficients, and transmission losses due to $1/R$ spherical spreading of the pulses.

The amplitude of the scattered pulse at receiver H is related to the measured voltage amplitude EV as follows:

$$20 \log \frac{p_{s,H}}{p_{ref}} = 20 \log \frac{EV}{V_{ref}} + C - G_{echo}. \qquad (A.5)$$

where $p_{ref} = 1\mu \, Pa$ and $V_{ref} = 1$ volt by convention. The additive term C is the decibel calibration coefficient of the receiver, and G_{echo} is the amplifier gain (in dB) employed to enhance the echo signal.

206

The echo pressure amplitude evaluated at unit distance from the target $(p_{s,T})$ is related the measured scattered pressure amplitude at receiver H by

$$
\begin{aligned}
20\log\frac{p_{s,T}}{p_{ref}} &= 20\log\frac{p_{s,H}}{p_{ref}} + 20\log\frac{R_{TH}}{R_{ref}}, \\
&= 20\log\frac{EV}{V_{ref}} + C - G_{echo} + 20\log\frac{R_{TH}}{R_{ref}}, \quad (A.6)
\end{aligned}
$$

where the quantity $20\log(R_{SH}/R_{ref})$ is known as the transmission loss due to spherical spreading.

Similarly, the measured incident main bang voltage (MBV) is related to the main bang pressure amplitude $(p_{i,H})$ at the receiver by

$$
20\log\frac{p_{i,H}}{p_{ref}} = 20\log\frac{MBV}{V_{ref}} + C - G_{mb}, \quad (A.7)
$$

where G_{mb} is the amplifier gain factor in dB used to enhance the incident signal measurement. Thus, the source level at the S is related to MBV by

$$
\begin{aligned}
SL_0 &= 20\log\frac{p_{i,H}}{p_{ref}} + 20\log\frac{R_{SH}}{R_{ref}}, \\
&= 20\log\frac{MBV}{V_{ref}} + C - G_{mb} + 20\log\frac{R_{SH}}{R_{ref}}, \quad (A.8)
\end{aligned}
$$

after correcting for spherical spreading losses. Using Eq. (A.8), the main bang pressure amplitude evaluated at a unit distance from the target $(p_{i,T})$ is given in the following expression:

$$
20\log\frac{p_{i,T}}{p_{ref}} = SL_0 - 20\log\frac{R_{ST}}{R_{ref}}, \quad (A.9)
$$

207

where R_{ST} is the distance between the source and the target.

Now, the target strength can be evaluated using Eq. (A.2) by substituting Eq. (A.6), (A.8), and (A.9). Hence,

$$TS = 20 \log \left| \frac{p_{\mathrm{s,T}}}{p_{\mathrm{i,T}}} \right|_{r=1\,\mathrm{m}},$$

$$= 20 \log \frac{EV}{MBV} - 20 \log \frac{R_{\mathrm{SH}}}{R_{\mathrm{ST}} R_{\mathrm{TH}}} - (G_{\mathrm{echo}} - G_{\mathrm{mb}}), \qquad (A.10)$$

Notice that all of the relative quantities (*i.e.*, V_{ref}, R_{ref}, p_{ref}) have been eliminated. Furthermore, Eq. (A.10) is independent of the transmitter source level (SL_0) and the receiver calibration coefficient (C). Thus for a bistatic backscattering measurement, only the separation distances between the components, the difference in amplifier gain factors, and the voltage amplitudes of the main bang and echo pulses need to be measured in order to accurately determine the target strength of a scatterer at a given source driving frequency.

Shown in Figure A.3 is an example of a steady state TS measurement. The incident and scattered pulse waveforms were measured from a single hydrophone. The source driving frequency is 1400 Hz, and the incident pulse length is 12 ms. The incident signal was amplified by 20 dB. To increase the resolution of the scattered pulse, the echo signal was amplified by 43 dB. The darker region in each plot corresponds to an 8 ms window over which the steady state rms voltage amplitude measurements were conducted. In this case, the rms voltages are MBV $= 0.6\,\mathrm{V_{rms}}$, EV $= 0.46\,\mathrm{V_{rms}}$. The total transmission loss factor, $20 \log R_{\mathrm{SH}}/(R_{\mathrm{ST}} R_{\mathrm{TH}})$, is -22.38 dB. For the settings listed above, the

208

measured target strength as given by Eq. (A.10) is TS = −2.9 dB.
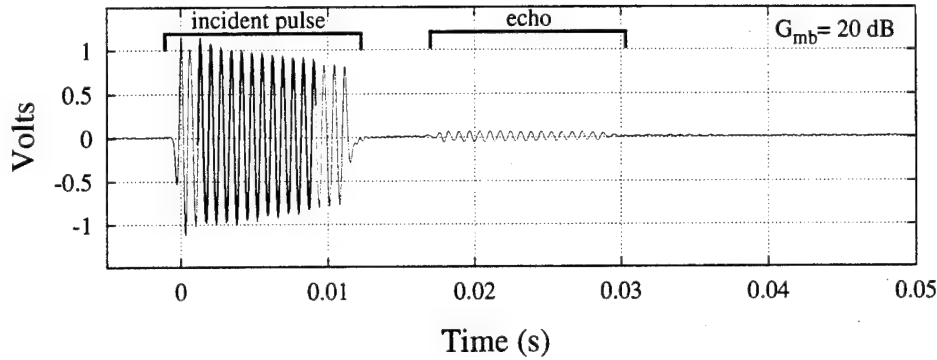
(a) Incident waveform
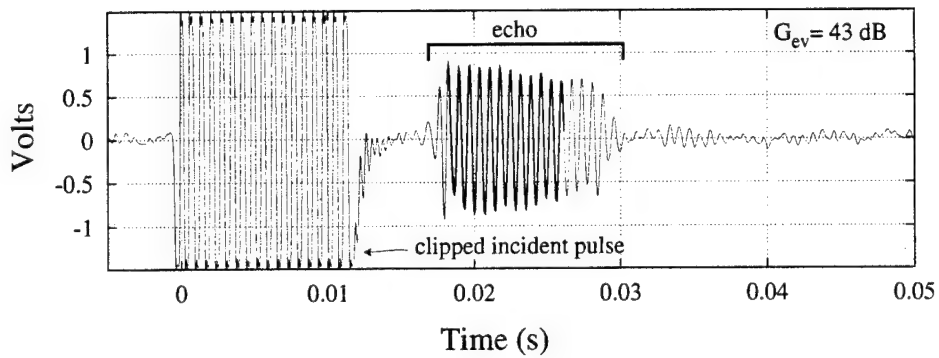
(b) Backscattered waveform

Figure A.3: (a) Incident and scattered signal and (b) same as (a), except added gain to enhance the echo waveform. The signals were acquired from a single hydrophone. The source driving frequency is 1400 Hz, and the incident pulse length is 12 ms. The darker region in each plot corresponds to an 8 ms window over which the steady state rms voltage amplitude measurements were made. In this case, the rms voltages are MBV = 0.6 V_{rms}, EV = 0.46 V_{rms}. The total transmission loss factor is −22.38 dB. Thus, the measured target strength as given by Eq. (A.10) is -2.9 dB.

A.3 TS measurements — transient pulses

In the previous section, the experimental method for determining the backscatter target strength of an arbitrary scatterer versus frequency was outlined. This method requires the use of an incident acoustic pulse at a well defined single frequency, and pulses that are long enough so that a steady state reflected pulse is achieved. In order to determine the target strength over range of frequencies, numerous steady state amplitude measurements must be conducted, one at each frequency of interest.

However, no sound of finite duration produces a pure single frequency note since such a sound theoretically lasts an infinite amount of time. Thus a sound pulse contains frequency components other than the desired frequency which ultimately contribute to the scattered field. In general, the relation between any time–dependent signal ($p_{\text{inc}}(t)$) and the frequency spectrum of the signal is given by Fourier's Integral theorem. That is, the signal can be written in the form

$$p_{\text{inc}}(t) = \int_{-\infty}^{\infty} \tilde{p}_{\text{inc}}(\omega) \, e^{i\omega t} \, d\omega, \tag{A.11}$$

where $\tilde{p}_{\text{inc}}(\omega)$ is the frequency spectrum of the signal and ω is the angular frequency. Likewise, the frequency spectrum can be written as

$$\tilde{p}_{\text{inc}}(\omega) = \frac{1}{2\pi} \int_{-\infty}^{\infty} p_{\text{inc}}(t) \, e^{-i\omega t} \, dt. \tag{A.12}$$

Eq. (A.11) and (A.12), are just generalizations of the corresponding equations

applicable to Fourier series of periodic functions. The time series and frequency spectrum, $p_{inc}(t)$ and $\tilde{p}_{inc}(\omega)$, are generally complex.

Recall from Chapter 3 that the amplitude of the wave scattered from a sphere can be written in terms of a scattering form function ($\mathcal{F}$) and the incident pressure amplitude (p_o) as follows:

$$p_s = \frac{a}{2r} p_o \, |\mathcal{F}(ka)| \,, \qquad (A.13)$$

where a is the sphere radius, r is the distance from its center to the point of reception, and ω is the angular frequency. The amplitude of the incident acoustic pressure measured at the center of the sphere, in its absence, may be regarded as a function of time and is given by

$$p_{inc}(t) = p_o \, e^{i\omega_o t}. \qquad (A.14)$$

Rewriting Eq. (A.13) in terms of the time dependence of Eq. (A.14), the scattered acoustic pressure becomes a function of time:

$$p_s(t) = \frac{a}{2r} \, |\mathcal{F}(\omega_o)| \, p_o \, e^{i\omega_o t}. \qquad (A.15)$$

From Eq. (A.11) and (A.12), it is clear that a time–dependent incident pressure pulse, $p_i(t)$ containing frequencies expressed in ω space has a frequency spectrum $\tilde{p}_i(\omega)$. Similar expressions exist for the time–dependent scattered acoustic pulse and its frequency spectrum. From Eq. (A.15), the scattered acoustic pressure amplitude at a single frequency, it can be shown

211

that the relationship between the scattering form function and time–dependent incident and scattered pulses is given by

$$\int_{-\infty}^{\infty} p_s(t) \, e^{-i\omega't} \, dt \;\; = \;\; \frac{a}{2r} \mathcal{F}(\omega) \int_{-\infty}^{\infty} p_{\mathrm{inc}}(t) \, e^{-i\omega't} \, dt,$$

$$\tilde{p}_s(\omega) \;\; = \;\; \frac{a}{2r} \mathcal{F}(\omega) \tilde{p}_{\mathrm{inc}}(\omega) \tag{A.16}$$

or further,

$$|\mathcal{F}(\omega)| = \frac{2r}{a} \frac{|\tilde{p}_s(\omega)|}{|\tilde{p}_{\mathrm{inc}}(\omega)|}. \tag{A.17}$$

This analysis yields a spectrum of measurements equivalent to the bandwidth of the incident pulse, rather than a single point as in the steady state analysis. That is, using Fourier techniques, one can determine the frequency response over a range of frequencies from a single scattering measurement. This is because the bandwidth of a 'mono–frequency' pulse of center frequency f_o and pulse length τ is approximately $1/\tau$. Thus for short pulse lengths (*i.e.*, large bandwidths), a broad spectrum of information can be obtained by comparing the frequency content of the incident and scattered waveforms.

To perform this analysis using experimentally acquired data, the incident and scattered waveforms are digitized and the Fourier transforms calculated using the well known Fast Fourier Transform (FFT) algorithms. Consider the previous example shown in Figure A.3. Peak normalized frequency spectrums of the incident and scattered pulses are shown in Figure A.4. Although the spectrums appear very similar, it is clear that the peak frequency of the

scattered pulse is shifted to a slightly lower value than center frequency of the incident pulse. Also, for frequencies beyond the center frequency, the amplitude of the scattered pulse frequency spectrum falls off more quickly than the incident wave.
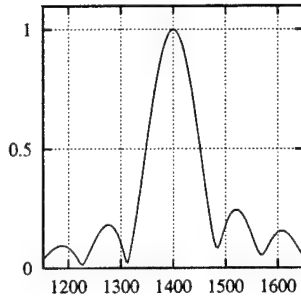
(a) Incident pulse FFT.
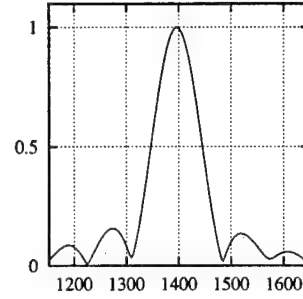
(b) Scattered pulse FFT

Figure A.4: Fourier transform of incident and scattered waveforms shown in Figure A.3. The driving frequency is 1.4 kHz, and the pulse length is 12 ms. In these figures transform amplitudes are normalized to the peak value at the center frequency.

The target strength can be determined from:

$$\text{TS} = 20 \log \left| \frac{\tilde{p}_{\text{s,T}}(\omega)}{\tilde{p}_{\text{i,T}}(\omega)} \right|_{r=1\,\text{m}},$$

$$= 20 \log \frac{\tilde{\text{EV}}(\omega)}{\tilde{\text{MBV}}(\omega)} - 20 \log \frac{R_{\text{SH}}}{R_{\text{ST}} R_{\text{TH}}} - (G_{\text{echo}} - G_{\text{mb}}). \qquad (A.18)$$

Here, the gain, transmission loss, and coefficients (SH, ST, TH) have the same meaning as described in the previous section. Generally, Eq. (A.18) is evaluated only over those frequencies within 3 dB of the of the peak incident signal

level. For the frequency spectrums in Figure A.4, the bandwidth of the pulses is 83 Hz, and the resulting target strength decreases nearly linearly with frequency resulting in target strengths between -0.3 and -2.5 dB, very close the to the steady state measurement of -2.9 dB. The most attractive advantage of using Fourier analysis, compared to the steady state measurement techniques, is that a wider spectrum of data is obtained from a single measurement. Therefore, fewer measurements are required to obtain the same spectrum. In addition, this technique offers improved frequency resolution and is thus better equipped to resolve sharp resonance peaks in the measured form function.

Appendix B

Seneca–2 test schedule and recording parameters

Table B.1: Seneca-2 Data Runs and Recording Parameters.

Data Run FQ	Cloud	log pg	Spd	Tape Desc Count	Filters HP	LP	Ch 1	Ch 2	Ch 3	Ch 4
6400	MB1	43	38	1:330.0—340.0	100	7000	41 dB, H1	41 dB, H2	41 dB, H3	41 dB, H4
	A1			1:355.0—360.0			61 dB, H1	61 dB, H2	61 dB, H3	61 dB, H4
	A2			1:370.0—385.0						
	A3			1:385.0—401.0						
	A4			1:401.0—416.0						
	A5			1:416.0—431.0						
4800	MB	45	38	1:522.0—537.0	100	6000	41 dB, H1	41 dB, H2	41 dB, H3	41 dB, H4
	A1			1:537.0—552.0			61 dB, H1	61 dB, H2	61 dB, H3	61 dB, H4
	A2			1:552.0—567.0						
	A3			1:567.0—582.0						
	A4			1:582.0—598.0						
3200	MB	46	38	2:020.0—035.0	100	4400	41 dB, H1	41 dB, H2	41 dB, H3	41 dB, H4
	A1			2:035.0—050.4			61 dB, H1	61 dB, H2	61 dB, H3	61 dB, H4
	A2			2:050.4—065.6						
	A3			2:065.0—080.8						
	A4			2:080.8—095.9						
	A5			2:111.1—126.3						
2400	MB	48	38	2:217.0—229.0	100	3000	38 dB, H1	38 dB, H2	38 dB, H3	38 dB, H4
	A1			2:232.0—247.0			61 dB, H1	61 dB, H2	61 dB, H3	61 dB, H4
	A2			2:247.0—268.0						
	A3			2:268.0—285.0						
	A4			2:285.0—304.0						
2000	MB1	50	38	2:399.0—418.0	100	2600	38 dB, H1	38 dB, H2	38 dB, H3	38 dB, H4
	A1			2:437.0—456.0	100	2600	61 dB, H1	61 dB, H2	61 dB, H3	61 dB, H4
	A2			2:456.0—475.0						
	A3			2:475.0—494.0						
	A4			2:494.0—513.0						
1600	A1	51	38	2:646.0—665.0	100	2200	61 dB, H1	61 dB, H2	61 dB, H3	61 dB, H4
	A2			2:665.0—684.0			61 dB, H1	61 dB, H2	61 dB, H3	61 dB, H4
	A3			2:684.0—700.0						
	A4			3:010.2—029.2						
	A5			3:029.2—048.1						
	A6			3:048.1—067.1						
Hz #		#	cm/s		Hz	Hz	Gain, Receiver			

Table B.1: *(continued)* .

Data Run		log	Tape Desc		Filters		Recording Channel Description			
FQ	Cloud	pg	Spd	Count	HP	LP	Ch 1	Ch 2	Ch 3	Ch 4
4000	MB	55	38	4:020.0—038.9	100	1800	43 dB, H1	33 dB, H2	43 dB, H3	33 dB, H4
	A1			4:057.9—076.8			61 dB, H1	61 dB, H2	61 dB, H3	61 dB, H4
	A2			4:076.8—95.0						
	A3			4:095.0—114.0						
	A4			4:114.0—133.0						
	A5			4:133.0—153.0						
	A6			4:153.0—171.0						
1200	MB	53	38	3:218.0—237.0	100	1800	43 dB, H1	43 dB, H2	43 dB, H3	43 dB, H4
	A1			3:256.0—275.0			61 dB, H1	61 dB, H2	61 dB, H3	61 dB, H4
	A2			3:275.0—294.0						
	A4			3:313.0—332.0						
	A5			3:332.0—351.0						
7500	MB1	53	38	3:285.0—304.0	100	8200	41 dB, H1	41 dB, H2	41 dB, H3	41 dB, H4
	A1			3:304.0—323.0			61 dB, H1	61 dB, H2	61 dB, H3	61 dB, H4
	A2			3:323.0—341.0						
	A3			3:342.0—361.0						
	A4			3:361.0—380.0						
800	MB	53	38	3:427.0—446.0	100	1000	46 dB, H1	46 dB, H2	46 dB, H3	46 dB, H4
	A1			3:465.0—484.0			61 dB, H1	61 dB, H2	61 dB, H3	61 dB, H4
	A2			3:484.0—503.0						
	A3			3:503.0—522.0						
	A4			3:522.0—535.0						
11k	MB	58	38	4:494.0—513.0	100	1300	33 dB, H1	33 dB, H2	33 dB, H3	33 dB, H4
	A1			4:513.0—532.0			61 dB, H1	61 dB, H2	61 dB, H3	61 dB, H4
	A2			4:532.0—551.0						
	A3			4:551.0—569.0						
	A4			4:569.0—588.0						
9000	PSc MB	61	38	5:594.0—617.0	100	12k	−4 dB, H1	−4 dB, H2	−4 dB, H3	−4 dB, H4
	PSc A1			5:617.0—640.0			21 dB, H1	21 dB, H2	21 dB, H3	21 dB, H4
	PSc A2			5:640.0—662.0						
	PSc A3			5:662.0—686.0						
	PSc A4			5:686.0—710.0						
	PSc A6			6:087.0—109.0						
Hz	#	#	cm/s		Hz	Hz	Gain, Receiver			

217

Data Run		log	Tape Desc		Filters		Recording Channel Description			
FQ	Cloud	pg	Spd	Count	HP	LP	Ch 1	Ch 2	Ch 3	Ch 4
10k	PSc MB	61	38	6:223.0—246.0	100	13k	3 dB, H1	3 dB, H2	3 dB, H3	3 dB, H4
	PSc A1			6:246.0—269.0			21 dB, H1	21 dB, H2	21 dB, H3	21 dB, H4
	PSc A2			6:269.0—292.0						
	PSc A3			6:292.0—314.0						
	PSc A4			6:314.0—337.0						
3000	PSc MB	65	38	6:497.0—519.0	100	4500	44 dB, H1	44 dB, H2	44 dB, H3	44 dB, H4
	PSc A1			6:519.0—542.0			61 dB, H1	61 dB, H2	61 dB, H3	61 dB, H4
	PSc A2			6:542.0—565.0						
	PSc A3			6:565.0—587.0						
	PSc A4			6:587.0—610.0						
xxx	MB	65	xx	6:632.0—655.0	100	4500	41 dB, H1	41 dB, H2	41 dB, H3	41 dB, H4
	A1			6:655.0—678.0			61 dB, H1	61 dB, H2	61 dB, H3	61 dB, H4
	A2			6:678.0—700.0						
14k	PSc MB	65	76	7:045.9—091.5	100	16k	−8 dB, H1	−10 dB, H2	−8 dB, H3	−8 dB, H4
	PSc A1			7:091.5—136.6			11 dB, H1	11 dB, H2	11 dB, H3	11 dB, H4
	PSc A2			7:136.6—181.9						
	PSc A3			7:181.9—227.0						
	PSc A4			7:227.0—273.0						
	PSc A5			7:273.0—319.0						
	PSc A6			7:319.0—364.0						
1000	A1	69	38	7:430.0—452.0	100	2000	63 dB, H1	63 dB,H2	63 dB, H3	63 dB, H4
	A2			7:475.0—498.0			63 dB, H1	63 dB, H2	63 dB, H3	63 dB, H4
	A3			7:498.0—521.0						
	A4			7:521.0—536.0						
1200	MB	69	76	7:627.0—631.0	100	1800	40 dB, H1	40 dB, H2	40 dB, H3	40 dB, H4
	A1			7:631.0—646.0			63 dB, H1	63 dB, H2	63 dB, H3	63 dB, H4
	A2			7:646.0—661.0						
	A3			7:661.0—675.0						
	A4			8:020.0—035.0						
	A5			8:035.0—050.0						
	A6			8:065.0—080.0						
1300	MB	70	38	8:141.0—160.0	100	2000	40 dB, H1	40 dB, H2	40 dB, H3	40 dB, H4
	A1			8:144.0—160.0			63 dB, H1	63 dB, H2	63 dB, H3	63 dB, H4
	A2			8:160.0—175.0						
	A3			8:175.0—190.0						
	A4			8:190.0—206.0						
Hz	#	#	cm/s		Hz	Hz	Gain, Receiver			

Table B.1: *(continued)* .

Data Run		log	Tape Desc		Filters		Recording Channel Description			
FQ	Cloud	pg	Spd	Count	HP	LP	Ch 1	Ch 2	Ch 3	Ch 4
1100	MB	71	38	8:250.0—253.0	100	1800	41 dB, H1	41 dB, H2	41 dB, H3	41 dB, H4
	A1			8:253.0—269.0			63 dB, H1	63 dB, H2	63 dB, H3	63 dB, H4
	A2			8:269.0—284.0						
	A3			8:284.0—299.0						
	A4			8:299.0—314.0						
	A5			8:314.0—329.0						
8250	MB	71	38	8:374.0—378.0	100	9500	41 dB, H1	41 dB, H2	41 dB, H3	41 dB, H4
	A1			8:378.0—393.0			61 dB, H1	61 dB, H2	61 dB, H3	61 dB, H4
	A2			8:393.0—409.0						
	A3			8:409.0—424.0						
	A4			8:424.0—439.0						
	A5			8:439.0—454.0						
7500	MB	72	38	8:469.0—473.0	100	9500	43 dB, H1	43 dB, H2	43 dB, H3	43 dB, H4
	A1			8:473.0—488.0			66 dB, H1	66 dB, H2	66 dB, H3	66 dB, H4
	A2			8:488.0—503.0						
	A3			8:503.0—518.0						
	A4			8:518.0—552.0						
1000	CS1 A2	76	38	10:306.0—315.0	100	1300	41 dB, H1	41 dB, H2	51 dB, H3	42 dB, H4
500	CS1 A1	76	38	10:020.0—044.0	100	1300	50 dB, H1	45 dB, H2	60 dB, H3	46 dB, H4
	CS1 A2			10:044.0—057.0						
550	CS1 A1	76	38	10: 57.0—74.0	100	1300	50 dB, H1	45 dB, H2	60 dB, H3	46 dB, H4
	CS1 A2			10:057.0—074.0						
600	CS1 A1	76	38	10: 74.0—90.0	100	1300	50 dB, H1	45 dB, H2	60 dB, H3	46 dB, H4
	CS1 A2			10:105.0—116.0						
650	CS1 A1	76	38	10:116.0—130.0	100	1300	41 dB, H1	41 dB, H2	51 dB, H3	42 dB, H4
	CS1 A2			10:130.0—145.0						
Hz	#	#	cm/s		Hz	Hz	Gain, Receiver			

219

Appendix C

Seneca–3 test schedule and recording parameters

Table C.1: Seneca–3 Data Runs and Recording Parameters.

| Data Run | | Tape Desc | | Filters | | Recording Channel Description | | | |
FQ	Cloud	Spd	Count	HP	LP	Ch 1	Ch 2	Ch 3	Ch 4
1500	A1 A2 A3 A4	19	7:156.0—165.0 7:165.0—171.0 7:171.0—178.0 7:178.0—184.0	0	2500	20 dB, H1 MB	46 dB, H1 EV	20 dB, H2 MB	46 dB, H2 EV
1300	A1 A2 A3 A4	19	7:204.8—214.0 7:214.0—221.0 7:221.0—232.0 7:232.0—239.0	0	2500	20 dB, H1 MB	46 dB, H1 EV	20 dB, H2 MB	46 dB, H2 EV
1100	A1 A2 A3 A4	19	7:239.0—248.0 7:248.0—252.0 7:257.0—263.0 7:263.0—271.0	0	2500	20 dB, H1 MB	43 dB, H1 EV	20 dB, H2 MB	46 dB, H2 EV
1000	A1 A2 A3 A4	19	7:271.0—279.0 7:279.0—286.0 7:286.0—294.0 7:294.0—301.0	0	2500	20 dB, H1 MB	43 dB, H1 EV	20 dB, H2 MB	46 dB, H2 EV
900	A1 A2 A3 A4	19	7:301.0—310.0 7:310.0—317.0 7:317.0—325.0 7:325.—332.6	0	2500	20 dB, H1 MB	43 dB, H1 EV	23 dB, H2 MB	46 dB, H2 EV
1200	A1 A2 A3 A4	19	7:333.0—341.0 7:341.0—348.0 7:348.0—356.0 7:356.0—362.0	0	2500	20 dB, H1 MB	43 dB, H1 EV	20 dB, H2 MB	46 dB, H2 EV
800	A1 A2 A3 A4	19	7:362.0—371.0 7:371.0—378.0 7:378.0—385.2 7:385.3—392.4	0	2500	23 dB, H1 MB	46 dB, H1 EV	23 dB, H2 MB	50 dB, H2 EV
700	A1 A2 A3 A4	19	7:392.1—401.0 7:401.0—409.8 7:409.8—417.8 7:417.8—426.1	0	2500	23 dB, H1 MB	50 dB, H1 EV	23 dB, H2 MB	53 dB, H2 EV
600	A1 A2 A3 A4	19	7:426.1—435.7 7:435.7—442.8 7:442.8—452.8 7:452.8—459.0	0	2500	23 dB, H1 MB	50 dB, H1 EV	23 dB, H2 MB	53 dB, H2 EV
Hz	#	cm/s		Hz	Hz	Gain, Receiver			

Table C.1: (continued)

Data Run		Tape Desc		Filters		Recording Channel Description			
FQ	Cloud	Spd	Count	HP	LP	Ch 1	Ch 2	Ch 3	Ch 4
550	A1 A2 A3 A4	19	7:459.0—468.1 7:468.0—476.1 7:476.1—484.6 7:484.6—491.5	0	2500	23 dB, H1 MB	50 dB, H1 EV	23 dB, H2 MB	53 dB, H2 EV
500	A1 A2 A3 A4	19	7:491.5—499.5 7:499.0—507.1 7:507.1—515.6 7:515.6—522.4	0	2500	26 dB, H1 MB	50 dB, H1 EV	26 dB, H2 MB	53 dB, H2 EV
450	A1 A2 A3 A4	19	7:522.4—531.8 7:531.8—539.6 7:539.6—548.0 7:548.0—555.1	0	2500	30 dB, H1 MB	50 dB, H1 EV	30 dB, H2 MB	53 dB, H2 EV
400	A1 A2 A3 A4	19	7:555.1—565.0 7:565.0—573.1 7:573.1—580.0 7:580.0—587.4	0	2500	30 dB, H1 MB	50 dB, H1 EV	30 dB, H2 MB	53 dB, H2 EV
350	A1 A2 A3 A4	19	7:593.8—602.8 7:602.8—609.2 7:609.2—616.7 7:616.7—623.0	0	2500	30 dB, H1 MB	50 dB, H1 EV	30 dB, H2 MB	53 dB, H2 EV
300	A1 A2 A3 A4	19	7:623.0—631.7 7:631.7—639.8 7:639.8—647.2 7:647.2—654.9	0	2500	30 dB, H1 MB	50 dB, H1 EV	30 dB, H2 MB	53 dB, H2 EV
250	A1 A2 A3 A4	19	7:654.9—664.0 7:664.0—673.7 7:673.7—680.7 7:680.7—688.0	0	2500	30 dB, H1 MB	50 dB, H1 EV	30 dB, H2 MB	53 dB, H2 EV
1400	A1 A2 A3 A4	19	8: 10.0— 19.2 8:019.2—027.2 8:027.2—035.5 8:035.5—042.6	0	2500	20 dB, H1 MB	43 dB, H1 EV	20 dB, H2 MB	43 dB, H2 EV
Hz	#	cm/s		Hz	Hz	Gain, Receiver			

222

Table C.1: *(continued)*

Data Run		Tape Desc		Filters		Recording Channel Description			
FQ	Cloud	Spd	Count	HP	LP	Ch 1	Ch 2	Ch 3	Ch 4
3000	A1 A2 A3 A4	19	8:042.6—050.9 8:050.9—057.8 8:057.8—064.8 8:064.8—071.4	0	4000	20 dB, H1 MB	43 dB, H1 EV	20 dB, H2 MB	43 dB, H2 EV
3500	A1 A2 A3 A4	19	8:071.4—079.1 8:09.1—086.2 8:086.2—093.5 8:093.5—101.0	0	5000	20 dB, H1 MB	43 dB, H1 EV	20 dB, H2 MB	43 dB, H2 EV
2500	A1 A2 A3 A4	19	8:101.0—108.4 8:108.4—115.7 8:115.7—123.4 8:123.4—129.9	0	4000	20 dB, H1 MB	43 dB, H1 EV	20 dB, H2 MB	43 dB, H2 EV
2000	A1 A2 A3 A4	19	8:129.9—140.2 8:140.2—147.0 8:147.0—155.0 8:155.0—161.7	0	3500	20 dB, H1 MB	43 dB, H1 EV	20 dB, H2 MB	43 dB, H2 EV
Hz	#	cm/s		Hz	Hz	Gain, Receiver			.

223

Appendix D

Error analysis methods

A simple and straightforward error–analysis was performed in order to quantify the accuracy and precision of the measured data and calculated results. A brief description of the fundamental measurements performed, quantifiable errors in these measurements, and the propagation of these errors is described in this section.

D.1 Directly measured quantities

Several direct measurements were performed during the course of this experiment, including, but not limited to: the mass volume of air injected into each bubble cloud released into Lake Seneca, the bubble radius distribution released from a single needle tip, the radius–height profile of a rising bubble cloud, and the incident main bang and backscattered voltages measured from the receiver outputs. In such cases where the number of measurements performed was large (such as the measurement of the total gas volume and of the bubble radius dis-

tribution), the accepted experimental value and uncertainty were determined statistically from the mean and standard deviation of the measurements. For example, the measurement of the total gas volume of a single bubble cloud was described in Chapter 4.3.6. In this case, a large number of measurements were performed with a precisely calibrated instrument (the electronic mass flow meter). Over the course of the experiment, the mean total gas volume injected into the bubble cloud is $\overline{V_{\text{gas}} = 1.22\,l}$, and the standard deviation of these measurements is $dV_{\text{gas}} = .014\,l$. Therefore, the accepted experimental value for the total gas volume is $1.22 \pm .014\,l$.

In other cases where the sample size was relatively small (< 10 samples), the experimental error was estimated from some systematic uncertainty (*i.e.*, limited by the resolution of the measurement device) or, where appropriate, a "best–guess" error estimate (*e.g.*, the radial profile of the bubble cloud is not clearly defined, as described in Chapter 4.3.4). In this case, the error introduced by the non–distinct cloud boundary ($\approx \pm 1 c_e$) exceeded the systematic error of the measuring device (a mm scaled ruler).

D.2 Derived quantities

In addition to the basic measurements described above, there are a host of derived quantities which are dependent on the directly measured values. These include, but are not limited to, derived quantities such as the mixture sound speed, the volume of the scatterer, the resonance frequency of the bubble cloud, the target strength, etc. All of these quantities are derived from the

equations specified in the text. The uncertainties in the basic measurements are propagated through the equations using a Taylor series expansion to first order in the perturbed quantities. For example, the uncertainty in the void fraction is determined by the combined uncertainty in the total gas volume measurement (directly measured), and the uncertainty in the net cloud volume (a derived quantity) as follows:

$$\beta \pm d\beta = \frac{V_{\text{gas}}}{V_{\text{cloud}}} \pm \left| \frac{V_{\text{gas}}}{V_{\text{cloud}}} dV_{\text{gas}} \right| \pm \left| \frac{V_{\text{gas}}}{V_{\text{cloud}}^2} dV_{\text{cloud}} \right|. \tag{D.1}$$

Here, the quantities preceded by d denote the deviation or uncertainty of the (directly or indirectly) measured values. The absolute value of each term was taken to effectively yield an upper bound on net error. The mean and uncertainty in the void fraction are calculated from

$$\beta = \frac{V_{\text{gas}}}{V_{\text{cloud}}} \tag{D.2}$$

$$d\beta = \left| \frac{V_{\text{gas}}}{V_{\text{cloud}}} dV_{\text{gas}} \right| + \left| \frac{V_{\text{gas}}}{V_{\text{cloud}}^2} dV_{\text{cloud}} \right|. \tag{D.3}$$

This technique for propagating the experimental error was carried out for all derived quantities described in the text in a manner analogous to the one described above.

D.3 Experimental Uncertainties

For the most part, the measurements processes are described in Chapter 4. The accepted experimental values and projected errors obtained from these mea-

surements using the error propagation technique described above are summarized in Table 4.5. Listed below is a summary of how the uncertainties (errors) assigned to the various non-derived quantities, measured and otherwise, were determined.

- V_{gas}(Gas volume) Chapter 4.3.6: The error in the total gas volume measurement was taken from the standard deviation of of 112 independent measurements as described in Chapter 4.3.6

- L (Cloud length) Chapter 4.3.3: The error in the cloud length was based on the error in the cloud velocity measurements and the error in the accuracy of the measured height of the camera deployed above the bubble maker.

- Bubble Size distribution Chapter 4.3.7: The error in the bubble size distribution measurements was determined from the standard deviation of the measured values.

- f (Acoustic driving frequency): The center frequency was determined from the readout of the "up/down" shifter for the NUWC parametric source. No uncertainty was assigned to it's measured value.

- MB (Main bang voltage) Chapter 5: For a given driving frequency the mean main bang voltage was determined by multiple measurements taken for repeated cloud releases as described. The uncertainty represents the spread in the maximum and minimum measured values observed at a given frequency.

- EV (Echo voltage) Chapter 5: For a given driving frequency the mean echo voltage was determined by multiple measurements taken for repeated cloud releases as described. The uncertainty represents the spread in the maximum and minimum measured values observed at a given frequency.

- d (depth) Chapters 4 and 5: The deployment depths for the hydrophones, sources, and the bubble maker was determined using a cable meter. The possible error in this measurement was not quantified.

- Po (hydrostatic pressure): The hydrostatic pressure was determined from the deployment depth. The possible error in this measurement was not quantified.

- c (liquid sound speed): The liquid sound speed versus depth profile was provided by NUSC daily. The possible error in this measurement was not quantified.

- c_g (sound speed of air): The ambient pressure dependent gaseous sound speed was determined from the well known relationships provided in texts (Kinsler et $al.$, 1982). No uncertainty was specified.

- ρ (liquid density): The hydrostatic pressure dependent liquid density was determined from the well known relationships provided in texts (Kinsler et $al.$, 1982). No uncertainty was specified.

- ρ_g (density of air): The hydrostatic pressure dependent density of air was determined from the well known relationships provided in texts (Kinsler

et al., 1982). No uncertainty was specified.

- κ (polytropic exponent): The polytropic exponent for air was calculated from equations specified in the text. No uncertainty was specified.

Appendix E

Rise–time dependent target strength measurements

Shown here are the time–elapsed backscattering data runs used to compose Figure 5.16. The target strength measurements were conducted during the Seneca–3 experiment using receiver H1, the closest to the target. The average target strength for these three runs is indicated by by the dashed line. It is clear that there is a significant deviation in the measured TS in the first few seconds after cloud release and again after 20 s. This variability is likely due to the low signal to noise present when the cloud is just entering and exiting the beam, as well as non–uniformities in the shape or localized distribution of the bubbles within the three clouds, as well as the possibility that the clouds did not rise along the same path. However, in bins 5–15, the measured TS for the three clouds is highly repeatable.
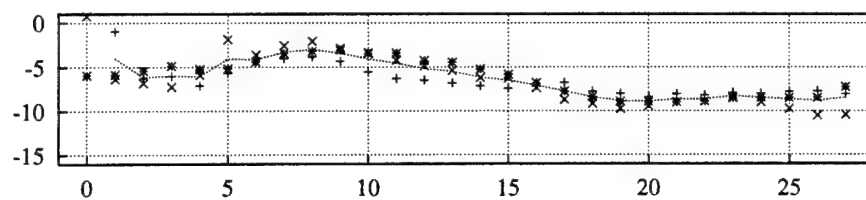
(a) 250 Hz
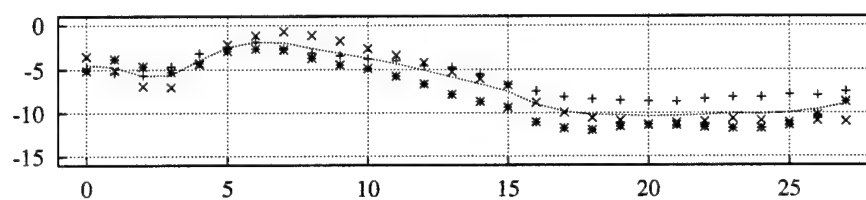
(b) 300 Hz
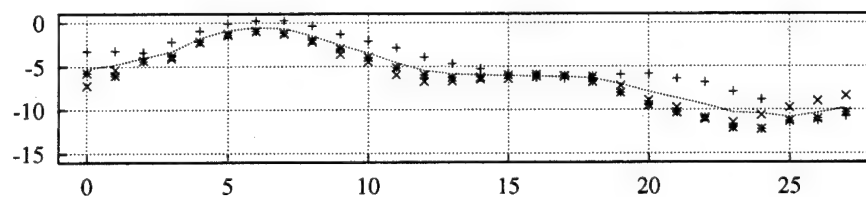
(c) 350 Hz
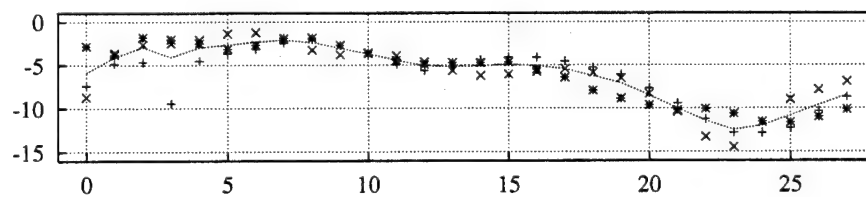
(d) 400 Hz

Figure E.1: Time elapsed TS (dB) versus rise time (s).
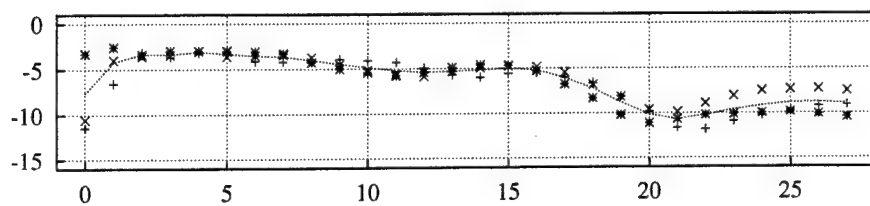
(a) 450 Hz
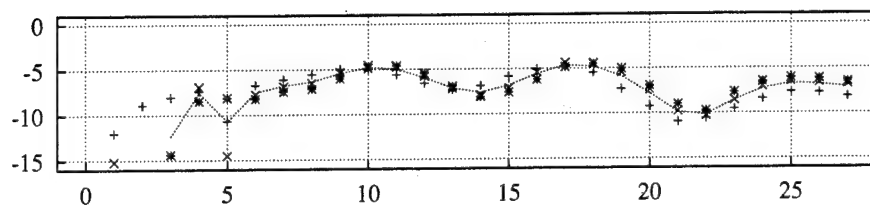
(b) 500 Hz
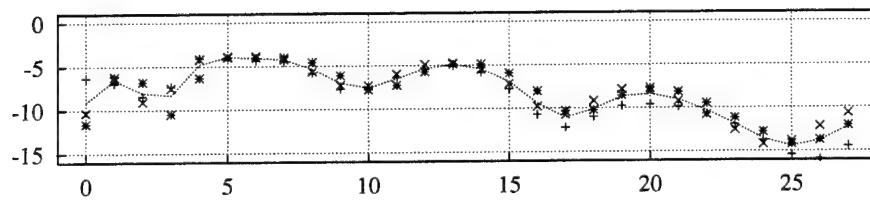
(c) 550 Hz
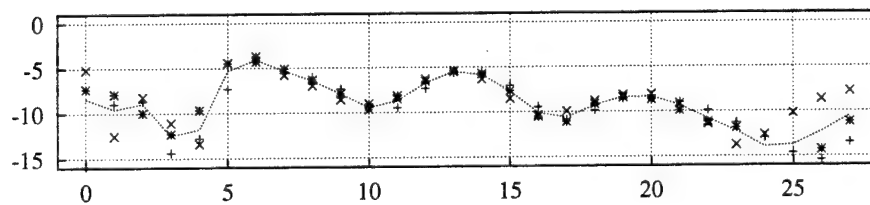
(d) 600 Hz

Figure E.2: Time elapsed TS (dB) versus rise time (s).
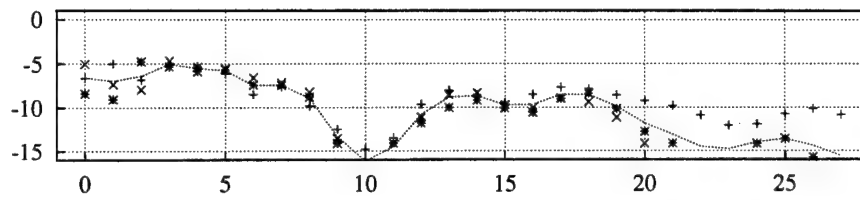
(a) 700 Hz
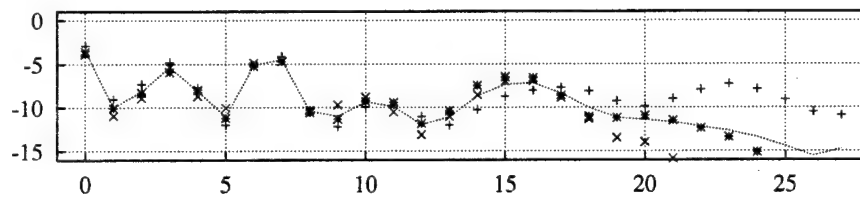
(b) 800 Hz
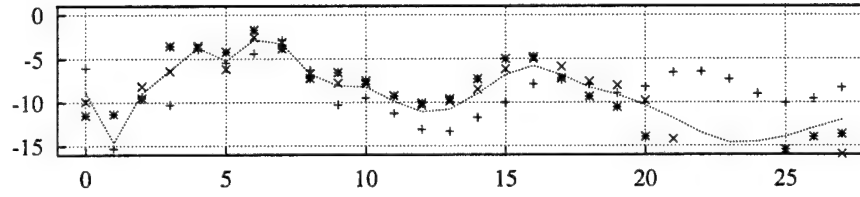
(c) 900 Hz
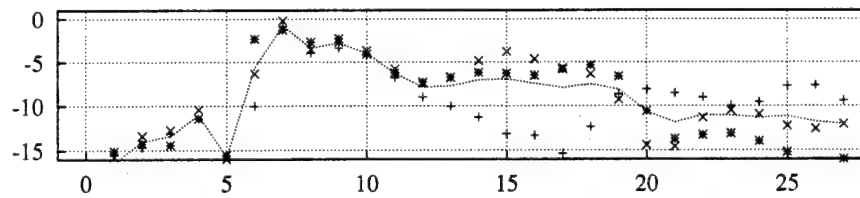
(d) 1000 Hz

Figure E.3: Time elapsed TS (dB) versus rise time (s).
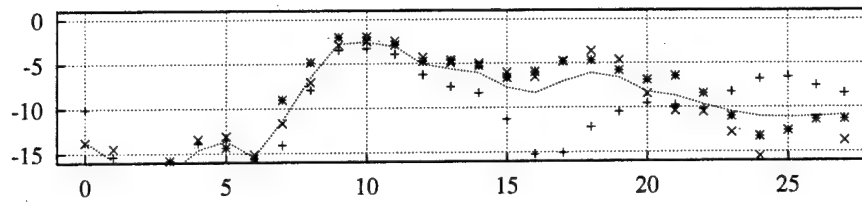
(a) 1100 Hz
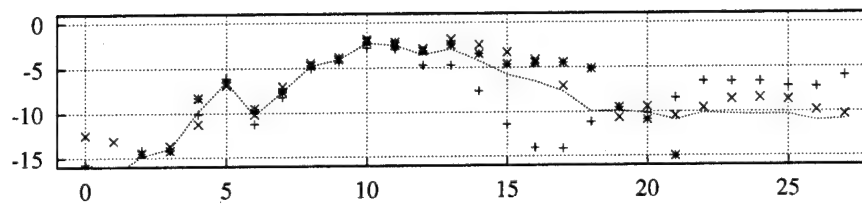
(b) 1200 Hz
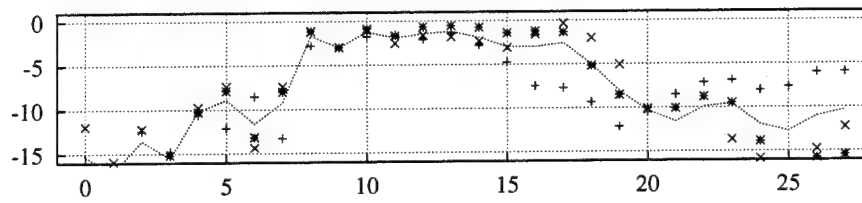
(c) 1300 Hz
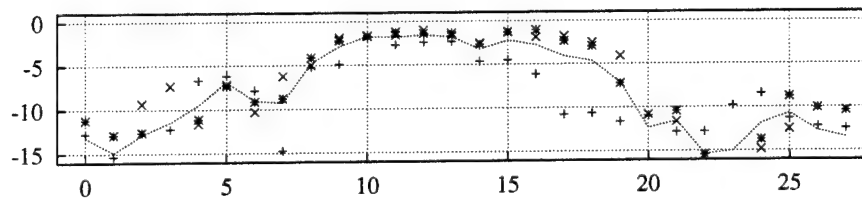
(d) 1400 Hz

Figure E.4: Time elapsed TS (dB) versus rise time (s).
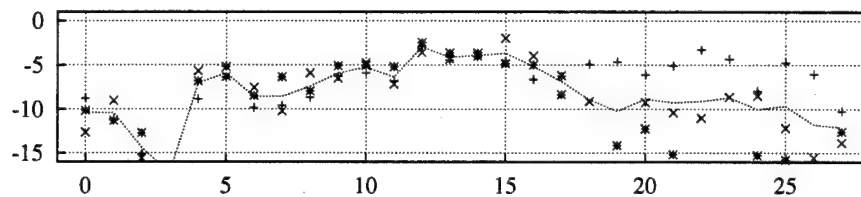
(a) 1500 Hz
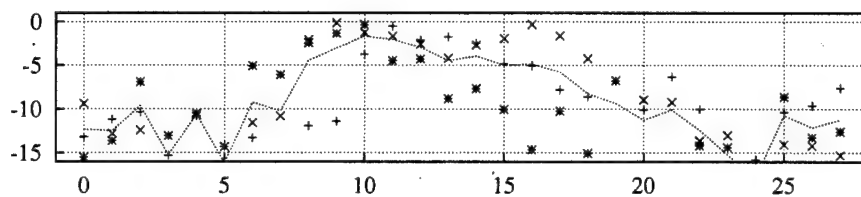
(b) 2000 Hz
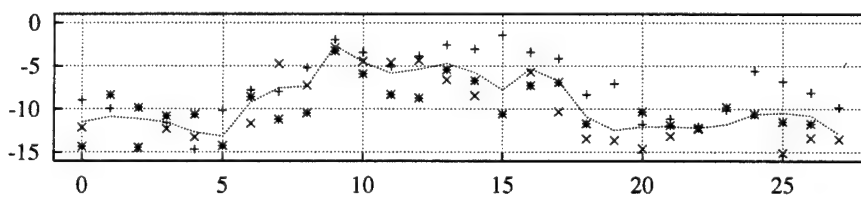
(c) 2500 Hz

Figure E.5: Time elapsed TS (dB) versus rise time (s).

235

Appendix F

Source Codes

```
// nscsp3.1.cxx

// Jeff Schindall    last revision  2DEC93
//
//
// *******************************************************
// ** nscsp3.1 (Near-Surface Cloud Scattering Program) **
// *******************************************************
//
// v3.1  Now uses a separate file for phase speed calcs
//         to reduce redundancy--PhaseSpeed3.1.cxx now
//         calculates complex sound speed using continous
//         gausian or discrete bubble dist.
//
// v3.0  Now compiles under Symmantec C++ and gnuC++
//
// v2.2  Cleaned up program and Fixed Errors
//         Can now run with or w/o bubble damping
//         compile on anchor, run on harel--or UV system.
//
// v2.1  included bubble damping   Commander/Prosperetti
//         and converted to C++ code.
// v2.0  converted to MathLink 2.1   20 mar 93
// v1.0  First version for MathLink1.2 c-source code
//
//
#include "nscsp3.1.h"
#include "nscspglob.h"

FLT_TYPE r;

extern "C"
char* INFO_NSCSP()
{return "\n\nNSCSP 3.1---02 DEC 1993   Jeff schindall\n\n";};

/* ********************************************* */

extern "C"
char* WhitecapCoverage( INT_TYPE coverage)
{
  char *answer;

  if(coverage==0)
  {
    WhitecapCoverageSwitch = 0;
    answer = "Whitecap Coverage OFF";
  }
  else
  {
    WhitecapCoverageSwitch = 1;
    answer = "Whitecap Coverage ON";
  };

  return(answer);
}
/* ********************************************* */
extern "C"
FLT_TYPE putdf(FLT_TYPE deltaf)
{
  dt=deltaf;
  return(dt);
}
/* ********************************************* */
extern "C"
FLT_TYPE
putminmaxf(FLT_TYPE minf, FLT_TYPE maxf)
{
  if (minf < maxf)
  {
    fMIN = minf;
    fMAX = maxf;
  }
  else
  {
    fMIN = maxf;
    fMAX=minf;
  };
  return(0.);
}
// *********************************************
extern "C"
FLT_TYPE puta(FLT_TYPE A)
{
  a=A;
  return(a);
}
// *********************************************
extern "C"
INT_TYPE putM(INT_TYPE m)
{
  M=m;

  return(M);
}
// *********************************************
extern "C"
FLT_TYPE putU(FLT_TYPE UU)
{
  if (UU>0.)
    U=UU;
  else
    U=0.;
  return(U);
}
// *********************************************
extern "C"
FLT_TYPE putz0(FLT_TYPE Z0)
{
  z0 = Z0;
  return(z0);
}
// *********************************************
extern "C"
FLT_TYPE puttheta(FLT_TYPE THETA)
{
  theta=THETA;
  return(theta);
}
// *********************************************
extern "C"
FLT_TYPE putmu(FLT_TYPE MU)
{
  mu=MU;
  return(mu);
}
// *********************************************
extern "C"
FLT_TYPE putphi(FLT_TYPE PHI)
{
  phi=PHI;return(phi);
}
```

```
// **********************************************

FLI_TYPE depth(FLI_TYPE Press)

{
  return( (Press-1.e5)/(rhol() *9.81) );
}

// **********************************************

FLI_TYPE WhitecapCoverageIndex()
{
  FLI_TYPE returnval;

  if (UI=0.)
    returnval = WhitecapCoverageSwitch*10.
      *log10(3.86*.000001*exp(3.4*log(U) ) );

  else
    returnval=0;

  return(returnval);

}

/* ******************************************** */
extern "C"
FLI_TYPE fo(FLI_TYPE f)
{
  return( getcm(f)/(2 * PI * a) * sqrt(3 * rhom()/rhol()));
}

// **********************************************
extern "C"
FLI_TYPE TS(INT_TYPE method)

{
  FLI_TYPE
    w,
    k,
    g,
    z,
    kz,
    answer,
    h1,
    hr;
```

```
  complex
    h;

  g = rhom()/rhol();

  z=depth(Po);
  w = 2*PI*f;
  k = w/c1;
  h = cm(w)/c1;

  answer = -9999.99;
  switch(method)
  {
    case 1:

      answer=(TSassym(k,h,g,a)
        +SurfaceRoughness(k,mu,z,phi)
        );

      break;
    case 2:

      answer=(TSanderson(k,h,g,a,theta,M)
        +SurfaceRoughness(k,mu,z,phi)
        );

      break;

    case 3:  // Calculate Roughness

      kz    = k*sin(phi);
      mu    = mu_approx( U, kz );
      putmu(mu);
      answer=(TSassym(k,h,g,a)
        +SurfaceRoughness(k,mu,z,phi)
        );

      break;

    case 4:  // Calculate Roughness using Assymptotic TS

      kz    = k*sin(phi);
      mu    = mu_approx( U, kz );
      putmu(mu);
      answer=(TSassym(k,h,g,a)
        +SurfaceRoughness(k,mu,z,phi)
        );

      break;

    default:

      answer=-9999.;
      break;

  };
```

```
  return(answer);

}

// **********************************************

extern "C"
FLI_TYPE
TSif(INT_TYPE method)

{

  FLI_TYPE oldmu, oldphi,tmpTS;
  oldmu=mu;
  oldphi=phi;
  putmu(0.);
  putphi(0.);
  tmpTS=TS(method);

  putmu(oldmu);
  putphi(oldphi);
  return(tmpTS);

}

// **********************************************
extern "C"
FLI_TYPE resfq(INT_TYPE method)

{

  FLI_TYPE ans[2];
  if (fres == 0)
    TSatResfq(method,ans);

  return(ans[1]);

}

/* ******************************************** */

extern "C"
void TSatResfq(INT_TYPE method, FLI_TYPE ans[2])

/* this subroutine shall return the maximum TS below the monopole
   resonance frequency as given by the Minneart Expression.

*/
// Suggested changes to make program quicker:
//
// Calculate Cm at 256pts(or 128 pts) btwn fMIN and fMAX
// Extrapolate Cm at each fq based on array of Cm(i).
//
// Include adjustable z==0 plane so that I can look at the bubbler
```

```c
// as a possible reflecting plane.
//
//
{
INT_TYPE
    DF;
FLT_TYPE
    fmpres,
    fmin,
    maxTS,
    tstmp,
    maxf,
    answer[2],
    fq;
fmpres = fo(1.);
maxf = fMAX;
if (fMAX > fmpres)  maxf = 1.1*fmpres;
fres = fmpres;
if ((depth(Po)==0.)||(phi==0.))
    fmin = .8*fmpres;
else
    fmin=(0.9*.25 *c1/(depth(Po)*sin(phi)));
if (fmin <0)
    fmin-- fmin;
if (fmpres < fmin)
    fmin = .8*fmpres;
/* fmin =fMIN; */
DF=1024;
df = (maxf - fmin)/DF;
fqrputf(fmin);
maxTS = TS(method);
while (fq<maxf)
{
    fqrputf(fq+df);
    tstmp = TS(method);
    if (tstmp > maxTS)
    {
    fres = fq;
    maxTS=tstmp;
    };
ans[0] = maxTS;
ans[1] = fres;
}

/* *************************************** */
FLT_TYPE
SCC(FLT_TYPE ka,FLT_TYPE g, complex h, FLT_TYPE theta, int M)
{
FLT_TYPE
    minusitom,
    ans,
    xx,
    m2p1,
    LPm,
    LPmm1,
    LPmm2,
    jm,
    jmp1,
    jmm1,
    nm,
    nmm1,
    nmp1,
    jpm,
    npm;
INT_TYPE   m,NUMBESS;
complex
    r,
    c,
    cdamcom,
    gh,
    jpem_jpm_jem,
    kah,
    jem,
    jmp1,
    jemm1,
    jpm;
r=complex(0.,0.);
// Basis for Spherical Bessel and Neumann functions
gh = hwg;

kah = ka/h;
jmm1=cos(ka)/ka;
jm=sin(ka)/ka;
nmm1=sin(ka)/ka;
nm= -cos(ka)/ka;
jemm1=cos(kah)/kah;
jem=sin(kah)/kah;
// Basis for Legendre Polynomials
xx=cos(PI-theta);
LPmm1=1;
LPm = 1;
NUMBESS=M;
for(m=0;m<=NUMBESS;++m)
{

m2p1=2.0*m+1.0;

// Calculate Legendre Polynomial of order m, argument
// xx=cos(PI-theta)
if (m>0)
    LPm = ((2.*m-1.)*xx*LPmm1-(m-1.)*LPmm2)/m;
// Calculate Bessel and Neumann function of order m+1,
// argument ka, kah.

jmp1 = (m2p1)/(ka)*jm-jmm1;
nmp1 = (m2p1)/(ka)*nm-nmm1;

jemp1 = (m2p1)/(kah)*jem-jemm1;

// Calculate Derivative of Bessel and Neumann function of order m,
// argument ka, kah.

npm=(m* jmm1 - (m+1.) * jmp1)/m2p1;
npm=(m* nmm1 - (m+1.) * nmp1)/m2p1 ;
jpem=(m* jemm1 - (m+1.) * jemp1)/m2p1 ;

jpem_jpm_jem=jpem/jpm/jem;

c= (jpem_jpm_jem*nm - npm/jpm*gh)
    /(jpem_jpm_jem - gb);

switch (mkt)
```

239

```c
xx=cos(PI-theta);
LPmm1=1;
LPm = 1.;
NUMBESS=M;
for(m=0;m<=NUMBESS;++m)
{

    m2p1=2.0*m+1.0;

    // Calculate Legendre Polynomial of order m, argument
    // xx=cos(PI-theta)

    if (m>0)
        LPm = ((2.*m-1.)*xx*LPmm1-(m-1.)*LPmm2)/m;

    // Calculate Bessel and Neumann function of order m+1.
    // argument ka, kah.

    hmp1 = (m2p1)/(kr)*hm-hmm1;

    jmp1 = (m2p1)/(ka)*jm-jmm1;
    nmp1 = (m2p1)/(ka)*nm-nmm1;

    jemp1 = (m2p1)/(kah)*jem-jemm1;

    // Calculate Derivative of Bessel and Neumann function of order m.
    // argument ka, kah.

    jpam=(m* jmm1 - (m+1.) * jmp1)/m2p1;
    npm=(m* nmm1 - (m+1.) * nmp1)/m2p1 ;
    jpem=(m* jemm1 - (m+1.) * jemp1)/m2p1 ;

    jpem_jpm_jem=jpem/jpm/jem;

    c= (jpem_jpm_jemtnm - npm/jpmtgh)
       /(jpem_jpm_jemtjm - gh);

    switch (mk1)
    {
        case 1:
            minusitom=-1.;
            break;
        case 0:
            minusitom=1.;
            break;
    };

    switch (mk3 )
    {
        case 1:
            minusitom=-1.;
            break;
        case 0:
            minusitom=1.;
            break;
    };

    if(c != complex(0.,1.))
        r += minusitom*m2p1/(1+I*c)*LPm ;

    if (M>0)
    {
        jmm1=jm;
        nmm1=nm;
        jemm1=jem;

        jm=jmp1;
        nm=nmp1;
        jem=jemp1;

        LPmm2=LPmm1;
        LPmm1= LPm;
    };

};

ans = (abs(2*r/ka));
if (ans <= 0.)
    return( -9999.99);
else
    return( (ans) );

}

/* ********************************************* */

FLT_TYPE
SCCnf(FLT_TYPE k,FLT_TYPE a,FLT_TYPE R,FLT_TYPE g, complex h,
      FLT_TYPE theta, int M)
{

FLT_TYPE
    minusitom,
    ans,
    xx,
    m2p1,
    LPm,
    LPmm1,
    LPmm2,
    jm,
    jmp1,
    jmm1,
    nm,
    nmm1,
    nmp1,
    jpm,
    npm,
    ka,
    kr;

INT_TYPE   m,NUMBESS;

complex
    r,
    c,
    I2m,
    cdenom,
    gh,
    jpem_jpm_jem,
    kah,
    jem,
    jemp1,
    jemm1,
    jpem,
    hm,
    hmp1,
    hmm1;

r=complex(0.,0.);

// Basis for Spherical Bessel and Neumann functions

gh = h*g;

ka = k*a;
kr = k*R;

kah = ka/h;

hmm1 = cos(kr)/kr + I * sin(kr)/kr;
hm   = sin(kr)/kr - I * cos(kr)/kr;

jmm1=cos(ka)/ka;
jm=sin(ka)/ka;

nmm1=sin(ka)/ka;
nm= -cos(ka)/ka;

jemm1=cos(kah)/kah;
jem=sin(kah)/kah;

// Basis for Legendre Polynomials
```

240

```c
FLT_TYPE
SCCr(FLT_TYPE ka,FLT_TYPE g, FLT_TYPE h, FLT_TYPE theta, int M)
{
FLT_TYPE
    minus1tom,
    ans,
    xx,
    m2p1,
    LPm,

        LPmm1,
        LPmm2,
        jm,
        jmp1,
        jmm1,

        nm,
        nmm1,
        nmp1,

        jpm,
        npm,
        gh,
        jpm_jpm_jsm,
        kah,

        jsm,
        jmp1,
        jsmm1,
        jpmm1;

    INT_TYPE  m,mm1,mp1,NUMBESS;
    complex
        r,
        c,
        cdenom;

//  void sjn(INT_TYPE, FLT_TYPE, FLT_TYPE, *FLT_TYPE);
//  void syn(INT_TYPE, FLT_TYPE, FLT_TYPE, *FLT_TYPE);

    NUMBESS=M;
    r=complex(0.,0.);
//  Basis for Spherical Bessel and Neumann functions

    gh = h*g;

    kah = ka/h;

    jmm1=cos(ka)/ka;
    jm=sin(ka)/ka;

    nmm1=sin(ka)/ka;
    nm= -cos(ka)/ka;

    jsmm1=cos(kah)/kah;
    jsm=sin(kah)/kah;

//  Basis for Legendre Polynomials

    xx=cos(PI-theta);
    LPmm1=1;
    LPm = 1;
    for(m=0;m<=NUMBESS;++m)
    {

        m2p1=2.0*m+1.0;

//  Calculate Legendre Polynomial of order m, argument
//      xx=cos(PI-theta)

        if (m>0)
        {
            LPm = ((2.*m-1.)*xx*LPmm1-(m-1.)*LPmm2)/m;
//  Calculate Bessel and Neumann function of order m+1,
//      argument ka, kah.

            jmp1 = (m2p1)/(ka)*jm-jmm1;
            nmp1 = (m2p1)/(ka)*nm-nmm1;

            jpm1 = (m2p1)/(kah)*jpm-jpmm1;

//  Calculate Derivative of Bessel and Neumann function of order m,
//      argument ka, kah.

            jpm=(m* jmm1 - (m+1.) * jmp1)/m2p1;
            npm=(m* nmm1 - (m+1.) * nmp1)/m2p1 ;
            jpmm=(m* jpmm1 - (m+1.) * jpmp1)/m2p1 ;

            jpm_jpm_jsm=jpm/jpm/jsm;

            c= (jpm_jpm_jsm*nm - npm/jsm*gh)
                    /(jpm_jpm_jsm*jm - gh);

            switch (m&1)
            {
            case 1:
                minus1tom=-1.;
                break;
            case 0:
                minus1tom=1.;
                break;
            };

            if(c != complex(0.,1.))
            r += minus1tom*m2p1/((1+I*c)*LPm ;

            if (M>0)
            {
            case 0:
                I2m=1.;
            break;
            case 1:
                I2m=I;
            break;
            case 2:
                I2m=-1.;
            break;
            case 3:
                I2m=-I;
            break;
            };

            if(c != complex(0.,1.))
            r += minus1tom*m2p1/((1+I*c)*LPm *I2m* hm ;

            if (M>0)
            {
                hmm1=hm;
                jmm1=jm;
                nmm1=nm;
                jsmm1=jsm;

                hm=hmp1;
                jm=jmp1;
                nm=nmp1;
                jsm=jsmp1;

                LPmm2=LPmm1;
                LPmm1= LPm;
            };

            ans = (abs( 2*r/ka * kr ));
            if (ans <= 0.)
                return( -9999.99);
            else
                return( (ans) );

}
```

```c
FLT_TYPE
SCCmodes(FLT_TYPE ka,FLT_TYPE g, FLT_TYPE h, FLT_TYPE theta, int M)
{

FLT_TYPE
    minus1tom,
    ans,
    xx,
    m2p1,
    LPm,
    LPmm1,
    LPmm2,
    jm,
    jmp1,
    jmm1,
    nm,
    nmm1,
    nmp1,
    jpm,
    npm,
    gh,
    jpem,jpm,jem,
    kah,
    jem,
    jemp1,
    jemm1,
    jpem,
    *sj=NULL,
    *sn=NULL,
    *sje=NULL;

INT_TYPE   m,mm1,mp1,NUMBESS;
complex
    r,
    c,
    cdenom;

// void sjn(INT_TYPE, FLT_TYPE, *FLT_TYPE);
// void syn(INT_TYPE, FLT_TYPE, *FLT_TYPE);

NUMBESS=M;
r=complex(0.,0.);
// Basis for Spherical Bessel and Neumann functions

gh = h*g;

kah = ka/h;

jmm1=cos(ka)/ka;
jm=sin(ka)/ka;

nmm1=sin(ka)/ka;
nm= -cos(ka)/ka;

jemm1=cos(kah)/kah;
jem=sin(kah)/kah;

// Basis for Legendre Polynomials

xx=cos(PI-theta);
LPmm1=1;
LPm = 1;
for(m=0;m<=M;++m)
{

m2p1=2.0*m+1.0;

// Calculate Legendre Polynomial of order m, argument
// xx=cos(PI-theta)

if (m>0)
    LPm = ((2.*m-1.)*xx*xt*LPmm1-(m-1.)*LPmm2)/m;

jmp1 = (m2p1)/(ka)*jm-jmm1;
nmp1 = (m2p1)/(ka)*nm-nmm1;

jemp1 = (m2p1)/(kah)*jem-jemm1;

// Calculate Derivative of Bessel and Neumann function of order m,
// argument ka, kah.

mm1=m-1;
mp1=m+1;

if (m==0)
{
    jpam=( - (mp1) * sj[mp1])/m2p1;
    npam=( - (mp1) * sn[mp1])/m2p1 ;
    jpem=( - (mp1) * sje[mp1])/m2p1;
}
else
{
    jpam=(m* sj[mm1] - (mp1) * sj[mp1])/m2p1;
    npam=(m* sn[mm1] - (mp1) * sn[mp1])/m2p1 ;
    jpem=(m* sje[mm1] - (mp1) * sje[mp1])/m2p1;
};

jpem_jpm_jem=jpem/jpm/sje[m];

c= (jpem_jpm_jem*nm - npm/jpm*gh)
   /(jpem_jpm_jem*sj[m] - gh);

minus1tom= (((mk1)==0) ? 1:-1 );

if(c != complex(0.,1.))
    r = minus1tom*m2p1/((1+1*c)*LPm ;

if (M>0)
{
    jmm1=jm;
    nmm1=nm;
    jemm1=jem;

    jm=jmp1;
    nm=nmp1;
    jem=jemp1;

    LPmm2=LPmm1;
    LPmm1= LPm;
};

/* free(sn);
free(sj);

ans = (abs(2*r/ka));
if (ans <= 0.)
    return( -9999.99);
else
    return( (ans) );
}
```

```
free(ejk);
*/

  ans = (abs(2*r/ka));
  if (ans <= 0.)
    return( -9999.99);
  else
    return( (ans) );
}
/* ************************************************** */
FLT_TYPE SurfaceRoughness(FLT_TYPE k,FLT_TYPE mu,FLT_TYPE z,FLT_TYPE phi) //
{
  FLT_TYPE rghness,sinkdphi;
  sinkdphi=sin( k = (z-z0) * sin( phi));

  rghness=  ( 1.+ mu + mu + 2.* mu
            -4. * mu * sinkdphi*sinkdphi
            );

  rghness += rghness;
  if (rghness==0)
    return( -9999.9);
  else
    return( 10*log10(rghness));
}
// *************************************************

FLT_TYPE
TSanderson(FLT_TYPE k,complex h, FLT_TYPE g, FLT_TYPE a,FLT_TYPE theta, int M)
{
  FLT_TYPE
    ka,
    ans;

  ka = k*a;

  ans = SCC( ka,g,h,theta,M)/2*a;
  if (ans <= 0.)
    return( -9999.99);
  else
    return( 20*log10(ans) );
}
// *************************************************

      v,
      k,
      g,
// *************************************************
```

```
FLT_TYPE
TSnf(FLT_TYPE k,complex h, FLT_TYPE g, FLT_TYPE a,FLT_TYPE theta,
     int M, FLT_TYPE r)
{
  FLT_TYPE
    ka,kr,
    ans;

  ka = k*a;
  kr = k*r;

  ans = SCCnf( k,a,r,g,h,theta,M)/2*a;
  if (ans <= 0.)
    return(-9999.99);
  else
    return( 20*log10(ans) );
}
// *************************************************

FLT_TYPE
TSasym(FLT_TYPE k,complex h,FLT_TYPE g, FLT_TYPE a)
// NOTE:  Assymptotic expansion of m=0 term in TSanderson.
//        See Morse and Ingard or Rahevkin for details.
//
{
  complex z,tmp;
  z=1/(g*h*h);
  tmp = (z+z*z*T*k*k/3+k/3*(1 - z)/(1 -z*z+z*k*k/3 -z*z*z*z*T*k*k*k/3));

  return(10.*log10(norm(tmp)));
}
// *************************************************

extern "C"
void TSFQlist(INT_TYPE method, FLT_TYPE *freqs, FLT_TYPE *TSlist, long num)
//TSlist assumed predefined...
{
  int ind,jj;
  FLT_TYPE dummy;
  FLT_TYPE
```

```
      z,
      kz,
      answer,
      hi,
      hr;
  complex
      h;

  CalcClCm();  //calculates cicmlist if need be...

  g = rhom()/rho1();

  z=depth(Po);

  for (jj=0;jj<NUMFQS;jj++)  {

    w = 2*PI*fqlist[jj];
    k = w/c1;
    h = 1/cicmlist[jj]; //cm(w)/c1;

    answer = -9999.99;
    switch(method)
    {

      case 1:
        answer=(TSasym(k,h,g,a)
               +SurfaceRoughness(k,mu,z,phi)
               );
        break;
      case 2:
        answer=(TSanderson(k,h,g,a,theta,M)
               +SurfaceRoughness(k,mu,z,phi)
               );
        break;

      case 3:    // Calculates Roughness

        kz   = k*sin(phi);
        mu   = mu_approx( U, kz );
        putmu(mu);
        answer=(TSanderson(k,h,g,a,theta,M)
               +SurfaceRoughness(k,mu,z,phi)
               );

        break;

      case 4:   // Calculate Roughness using Assymptotic TS
```

243

```
kz      = k*sin(phi);
mu      = mu_approx( U, kz );
putmu(mu);
answer=(TSessym(k,h,g,s)
        +SurfaceRoughness(k,mu,z,phi)
        );

break;

case  5:  // Calculate Near Field TS
answer=(TSnf(k,h,g,a,theta,M,r)
        );

break;

default:
answer=-9999.;
break;

};
TSlist[j]=answer;

};

}
extern "C"
void SCCKAlist(FLT_TYPE *KAs, long num, FLT_TYPE h,
               FLT_TYPE theta0, long MM)
{
int ind;
FLT_TYPE dummy;
/* replace each frequency with its Scattering Cross Section */
//printf('theta0 %f\tg %f\th %f\tH %f\n',theta0, g,h,MM);
for (ind=0;ind<num;ind++)
{
dummy= SCCr(KAs[ind],g,h,theta0,MM);
KAs[ind]=dummy;
};

}

extern "C"
void SCCthetalist(FLT_TYPE *KAs, FLT_TYPE g,FLT_TYPE h, FLT_TYPE *theta0,
                  long num, long MM)
{
int ind;
FLT_TYPE dummy;
/* replace each frequency with its Scattering Cross Section */
//printf('theta0 %f\tg %f\tth %f\tH %f\n',theta0, g,h,MM);
for (ind=0;ind<num;ind++)
{
dummy= SCCr(KAs,g,h,theta0[ind],MM);
theta0[ind]=dummy;
};

}

extern "C"
void SCCKAmodellist(FLT_TYPE *KAs, long num, FLT_TYPE g,FLT_TYPE h,
                    FLT_TYPE theta0, long MM)
{
int ind;
FLT_TYPE dummy;
/* replace each frequency with its Scattering Cross Section */
//printf('theta0 %f\tg %f\tth %f\tH %f\n',theta0, g,h,MM);
for (ind=0;ind<num;ind++)
{
dummy= SCCrmodles(KAs[ind],g,h,theta0,MM);
KAs[ind]=dummy;
};

}
extern "C"
char * init_seneca()
{
FLT_TYPE
mybetas[6];

putZ(87.6);
putZ0(87.6);
putmu(0.);
putcl(1421.5);
putrhol(1024);
putrhog(1.);
puta(0.376);

mybetas[0]=0.0054;
mybetas[1]=1.00;
mybetas[2]=0.0015;

mybetas[3]=0.00;
mybetas[4]=0.00;
mybetas[5]=0.00;

putBetaList(mybetas,6);

puttheta(PI);

return "\n\nInitialized for Lake Seneca Calc\n\n";

}
extern "C"
char * init_marine()
{
FLT_TYPE
mybetas[6];

putZ(0.);

putZ0(0.);

putmu(0.);

putcl(1500.);

putrhol(1024);

putrhog(1.);

puta(0.25);

puttheta(PI);

mybetas[0]=0.0055;
mybetas[1]=1.00;
mybetas[2]=0.0011;
mybetas[3]=0.00;
mybetas[4]=0.00;
mybetas[5]=0.00;

putBetaList(mybetas,6);
return "\n\nInitialized for Marine Calc\n\n";

}

extern "C"
void initNSCSP()
{

FLT_TYPE
```

```
xxx,
aaa[2],          //dummy variables
KAe[3];

char
                 ccc;

INT_TYPE
         iii,num;

complex
                 zzz;

r = 10.19;

xxx=1.E30;

z0=0.;

U=1.;
WhitecapCoverageSwitch=0;      // By default turn off Windspeed
                               // turn off the whitecap coverage

xxx= putrhog(1.);              // Set Density of gas in bubble
xxx= putrhol(1000.);           // Set Density of host liquid

iii= putM(20);                 // Number of Iterations in Solution

xxx= puttheta(PI);             // Scattering Direction PI=BackScatter
xxx= putphi(0.);               // Surface Grazing Angle
xxx= putmu(0.);                // Surface reflection coefficient
xxx=puta(0.1 );                // set initial cloud radius

xxx=putf(300);                 // set the initial frequency

xxx= putminmaxf(1.,fo(100.));  // Max and Minimum frequency range.
xxx=putdf(100.);               // set the delta frequency

zzz=complex(0.8,0);

xxx=putmu(-0.9);
xxx=putZ(89.);
xxx=14./0.376;
xxx=TSanderson(xxx,zzz,1.,0.376,PI,0);
```

```
xxx=20.* log10( SCCr(14.,1.,0.8,PI,0)/2.*0.376);
xxx=14./0.376;
xxx=SenecaTS(xxx,0.376,1.,zzz,89.,0);

KAe[0]=1.;
KAe[1]=2.;
KAe[2]=3.;
num=3;

SCCKAlist(KAe, num,  0.5,  0.5,   PI,  10);
putmu(0.);

init_seneca();

KAe[0]=300;

// TSFQlist(5,KAe,KAe ,50)

}
```

nscspMain3.1.c

nscspglob.cxx

```
//glob.cxx

#include "nscsp3.1.h"
#include "nscspglob.h"

FLT_TYPE
         free,          // Calculated resonance fq of spherical cloud
                        // Wavenumber in host fluid == 2 PI fq/C1
         theta,         // Scattering angle
         a,             // Cloud Radius
         mu,            // Surface reflection coefficient -i< mu < 0
         phi,           // Surface Grazing angle
         fMIN,          // Minimum fq used to calculate peak in TS(fq)
         fMAX,          // Maximum fq used to calculate peak in TS(fq)
         df,            // Change in fq used to calculate peak in TS(fq)
         z0,            // Set z==0 plane
         U;             // Wind speed in m/s.
```

SenecaCorrections.cxx

```
INT_TYPE
         WhitecapCoverageSwitch, //   Turns whitecap coverage on/off---see TS
         M;                      // Number of iterations used to calc TS

#include "nscsp3.1.h"
#include "nscspglob.h"

FLT_TYPE
SenecaTS(FLT_TYPE k,FLT_TYPE a,FLT_TYPE g,complex h,FLT_TYPE Yt,FLT_TYPE K)

{

FLT_TYPE

         km,
         Ya,
         Yr,
         Yb,
         Yl,
         Yt,
         Xa,
         Xr,
         Xt,
         Xl,
         Xb,
         Xa,
         Rst,
         Rrb,
         Rrt,
         Rrl,
         Rar,
         Raa,
         Rra,
         Rab,
         Theta_st,
         Theta_aa,
         Theta_ar,
         Theta_rt,
         Theta_rl,
         Theta_rb,
         Theta_ab,
```

```c
Theta_s1,
kzSinThetarb,
kzSinThetart,
kzSinThetari,
SCCrt,
SCCri,
mup,
BeamWidth,
C_Beam,
BSF_arg,
freq,
Cbeam,
BSF,
DP_corr,
TSff,
TS,
rsqm1, isqm1, rm1, im1, irm1;

complex m1,sqm1;

ks=kts;

m1=complex(-1.e0,0.);
rm1=real(m1);
im1=imag(m1);

irm1=im1/rm1;

sqm1= sqrt(m1);
rsqm1=real(sqm1);
isqm1=imag(sqm1);

Ys= 60.96;
Yr=Ys+20.58000;
Yb= Ys+30.48000;
Yi= 2*Yb -Yr;
Ya= Ys+26.52000;

Xs= 0.;
Xr= Xs+28.72000;
Xt=Xi=Xb=Xa= Xs+37.01000;

Rst= sqrt( (Ys-Yt)*(Ys-Yt) + (Xs-Xt)*(Xs-Xt));
Rrb= sqrt( (Yr-Yb)*(Yr-Yb) + (Xr-Xb)*(Xr-Xb));
Rrt= sqrt( (Yr-Yt)*(Yr-Yt) + (Xr-Xt)*(Xr-Xt));
Rri= sqrt( (Yr-Yi)*(Yr-Yi) + (Xr-Xi)*(Xr-Xi));
Rar= sqrt( (Yr-Ya)*(Yr-Ya) + (Xr-Xa)*(Xr-Xa));
Ras= sqrt( (Ya-Ys)*(Ya-Ys) + (Xa-Xs)*(Xa-Xs));
Rrs= sqrt( (Yr-Ys)*(Yr-Ys) + (Xr-Xs)*(Xr-Xs));

Rsb= sqrt( (Ys-Yb)*(Ys-Yb) + (Xs-Xb)*(Xs-Xb));

Theta_st= atan( (Ys-Yt)/ (Xs-Xt));
Theta_sr= atan( (Ys-Yr)/ (Xs-Xr));
Theta_rt= atan( (Yr-Yt)/ (Xr-Xt));
Theta_ri= atan( (Yr-Yi)/ (Xr-Xi));
Theta_rb= atan( (Yr-Yb)/ (Xr-Xb));
Theta_ar= atan( (Ys-Yb)/ (Xs-Xb));
Theta_ai= atan( (Ys-Yi)/ (Xs-Xi));

kzSinThetarb=k*(Yi-Yt)*sin(Theta_rb);
kzSinThetart=k*(Yt-Yb)*sin(Theta_rt);
kzSinThetari=k*(Yi-Yb)*sin(Theta_ri);

SCCrt= SCC(ks,g,h,PI-Theta_rt,M);
SCCri= SCC(ks,g,h,PI-Theta_ri,M);

mup = mu*SCCri*SCCri/SCCrt/SCCrt;

freq= k*cl/2/PI;

BeamWidth=8.5*PI/180.;

BeamWidth= PI/180.*(14.483 + -2.228*log10(freq));
C_Beam= sqrt((-log10(exp(1.))*BeamWidth*BeamWidth/4.)/log10(0.5));
BSF_arg=((Theta_st-Theta_sa)/C_Beam);

BSF= 20.*log10(Rst/Rsa)
    +10.*log10(exp( BSF_arg*BSF_arg) );

#ifdef FARFIELD_APPROX

// Far-Field Approximations.

Rrt = Rr1  - Rrb;
kzSinThetart= 0.;
kzSinThetari= kzSinThetarb;

#endif

DP_corr = 20.*log10(1./Rra)
            -10.*log10(norm( exp(I* kzSinThetart)/Rrt
            +mup*exp(I*kzSinThetari)/Rri
            )
            );

TSff= 20.*log10(SCCrt/2.*a);

TS = TSff  -DP_corr;

return (TS);
}

// *********************************************

extern "C"

void SenecaTSdepthlist(FLT_TYPE fq, FLT_TYPE cloudrad, FLT_TYPE *depths, long num)
{
    int ind;
    FLT_TYPE v,k,g,z,dummy;

    complex h;

    dummy= puta(cloudrad);
    dummy= putf(fq);
    w = 2*PI*fq;
    k = w/cl;

    /* replace each depth with its TS */

    for (ind=0;ind<num;ind++)
    {
        dummy= putf(depths[ind]);

        z=putZ(87.7824);

        g = rhom()/rhol();
        h = cm(v)/cl;
```

```cpp
PhaseSpeed3.1.2.cxx

// Jeff Schindall    last revision   24OCT93
//
// ******************************************************
// PhaseSpeed (Phase Speed--Collective Oscillations Program) **
// ******************************************************
//
// This code calculates the phase speed of sound in a bubbly
// medium consisting of a single bubble radius and constant
// volume fraction.  Future versions of this code will be modified to
// include many bubble radii and perhaps continuous distributions
// of bubbles.
//
// Based on Commander and Prosperetti--Linear Pressure Waves in bubbly
// liquids:Comparison between theory and experiments.
//
//
//

#include "nscep3.1.h"
#include "PhaseSpeedGlob.h"

#include <stdio.h>
#include <stdlib.h>
#include <math.h>

#define SIGMA  ((1.E-5)/0.01*(75.68-0.138*TMP-3.56e-6*TMP*TMP+4.7e-7*TMP*TMP*TMP))
#define Gamma 1.4
#define EPS 1.E-6

extern "C"
char* INFO_PhaseSpeed()
{
  return "\nPhaseSpeed--24 OCT 1993  Jeff schindall\n\n";
};
```

```cpp
dummy= SenscaTS(k,s,g,h,depths[ind],M);
depths[ind]=dummy;
};

#define ALPHA  8.1e-3
#define BETA   0.74
#define G      9.81
FLT_TYPE mu_approx(FLT_TYPE U,FLT_TYPE kz)
{
// Compute Intensity Reflection Coefficient for rough surface
// based on Pierson-Moskovitz Wave Height Spectrum and the
// Kirchoff Approximation.

FLT_TYPE
hsqrd,
ans;

//Mean-Square Wave Height from Pierson-MOskowitz Spectrum

hsqrd = ALPHA*U*U*U*U/(4.*BETA*G*G) ;

ans  = - exp( - 2.*hsqrd*kz*kz ) ;   //2 for amplitude refl
                                     //4 for intensity refl

return ans;
}

#undef ALPHA
#undef BETA
#undef G

extern "C"
FLT_TYPE get_mu_approx( FLT_TYPE U, FLT_TYPE kz )
{

FLT_TYPE ans;

ans=mu_approx(U,kz);
return ans;
}
```

```cpp
cl=CL;
RECALC=1;
return(cl);
}

// ******************************************************

// ******************************************************

extern "C"
FLT_TYPE putBetaList(FLT_TYPE betalist[], long num)
{

INT_TYPE
index;              // Number of bubble radii in distribution

beta = betalist[0];

Beta_Amp=0.;
NUMDIST = num/6;
for (index=0;index < NUMDIST;++index)
{
  numbub[index]  = betalist[6*index+1];
  bubrad[index]  = betalist[6*index+2];
  bubradsd[index] = betalist[6*index+3];
  bubradmin[index] = betalist[6*index+4];
  bubradmax[index] = betalist[6*index+5];
};

RECALC=1;

return beta;
}

// ******************************************************

extern "C"
FLT_TYPE putcl(FLT_TYPE CL)
```

```
extern "C"
FLT_TYPE putrho1(FLT_TYPE RHO1)
{
    rho1O=RHO1;
    RECALC=1;
    return(rho1O);
}
// ***************************
extern "C"
FLT_TYPE putrhog(FLT_TYPE RHOG)
{
    rhogO=RHOG;
    RECALC=1;
    return(rhogO);
}
// ***************************
FLT_TYPE rhog()
{
    return( rhogO*Po/(1.E5) *273.12/(273.12+TMP));
}
// ***************************
extern "C"
FLT_TYPE rhom()
{
    return( (1.-beta)*rho1() +beta*rhog());
}
/* *************************** */
extern "C"
FLT_TYPE putPo(FLT_TYPE PO)
{
    Po=PO;
    RECALC=1;
    return(Po);
}

extern "C"
FLT_TYPE putZ(FLT_TYPE ZZ)
{
    zz=ZZ;
    Po = 1.e5 + rho1() * 9.81 * zz;
    RECALC=1;
    return(zz);
}
// ***************************
extern "C"
FLT_TYPE putf(FLT_TYPE F)
{
    f=F;
    //K = 2*PI*f/c1;
    return(f);
}
// ***************************
FLT_TYPE rho1()
{
    RECALC=1;
    return( rho1O );
}

/* ***************************** */
FLT_TYPE Sigma(FLT_TYPE tmp)
{
    // Surface tension of bubble
    FLT_TYPE dyne,CM,T2,ans;
    dyne = (1.E-5);
    CM = .01; // centimeter
    T2=tmp*tmp;
    ans=(dyne/CM*(75.68 - 0.138*tmp
        - 3.56e-6*T2 + 4.7e-7*T2*tmp));
    return ans;
}
// ********************************
#define TO  273.15
#define TK  (TMP+TO)
#define TA  245.4
#define TB  27.6
#define KO  2.64529e-2

//Kappa == Thermal Conductivity see Pierce, pg 513, eq 10-1.16b
#define KAPPA KO*TK/TO*sqrt(TK/TO)*(TO+TA/ exp(TB/TO))/(TK+TA/exp(TB/TK))

complex PHI(FLT_TYPE v,FLT_TYPE r,FLT_TYPE Po)
{
    complex
        ans,
        sqrt_I_chi,
        I_chi;
    FLT_TYPE
        chi,
        Dtherm;
```

```
if (Gamma ==1.0)
    ans = 3;
else {
//Dtherm=Kappa/rhog0/Cp == See Prosperetti-Thermal Behavior of oscillating
//                gas bubbles.  JFM '91(222)
//    Same as (1-Gamma)/Gamma*TK/Po

Dtherm=((-1. + Gamma)*(TK)*KAPPA/(Gamma*Po));

chi=( Dtherm/w/r/r);

sqrt_I_chi = sqrt(I/chi);

ans=(3.*Gamma/((1. - 3.*I*(-1. + Gamma)*chi*
    (-1. + sqrt_I_chi*coth(sqrt_I_chi) )) );

};

return (ans);
}

#undef KAPPA
#undef TK
#undef TA
#undef TB
#undef TO

// ******************************************************

FLT_TYPE po(FLT_TYPE r, FLT_TYPE Po)
{
    FLT_TYPE ans;

    ans=( Po + 2*SIGMA/r);   // pressure inside the bubble

    return ans;
}

// ******************************************************

complex b(FLT_TYPE w,FLT_TYPE r,FLT_TYPE Po,FLT_TYPE c1)
{ FLT_TYPE MU;
  complex ans;

  MU = 1.02e (1.E-3);

  ans=( rw=w/(2*c1) + (2*MU/(r*r*rhol())
      +imag(PHI(w,r,Po))*po(r,Po)/(2*r*r*rhol()*w)));

  return ans;
}

// ******************************************************

extern "C"
FLT_TYPE vo(FLT_TYPE r,FLT_TYPE w)
{
    FLT_TYPE ans,pb;

    pb=po(r,Po);

    ans=sqrt( pb/rhol()/r/r*( real(PHI(w,r,Po))- 2*SIGMA/r/pb));

    return ans;
}

// ******************************************************

FLT_TYPE SimpsonInt(FLT_TYPE (*func)(FLT_TYPE), FLT_TYPE a, FLT_TYPE b)
{
    FLT_TYPE sum;
    FLT_TYPE x,dx;
    INT_TYPE i,MAXITER;

    MAXITER=256;
    sum = 0;
    x=a;
    dx = (b-a)/MAXITER;

    if (dx==0)
        sum=func(a);
    else
    {
        for (i=0;i<MAXITER; ++i)
        {
            sum += func(x);
            x += dx;
        };

        sum *= dx;
    };

    return sum;
}

#define REAL_F(x) ( real( (*func)(x) ) )
#define IMAG_F(x) ( imag( (*func)(x) ) )

complex CompSimpsonInt( complex (*func)(FLT_TYPE)(FLT_TYPE),
                        FLT_TYPE a, FLT_TYPE b)
{
    complex sum;
    FLT_TYPE realint,imagint;

    FLT_TYPE resum,imsum;
    FLT_TYPE x,dx;
    INT_TYPE i,MAXITER;

    MAXITER=256;
    sum = 0;
    x=a;
    dx = (b-a)/MAXITER;

    if (dx==0)
        sum=func(a);   // special case for delta fn.
    else
    {
        for (i=0;i<MAXITER; ++i)
        {
            sum += (func(x));
            x += dx;
        };

        sum *= dx;
    };

    resum= real(sum);
    imsum= imag(sum);
```

```cpp
    return sum;
}

#undef REAL_F
#undef IMAG_F

// *********************************************************

complex DispDenom(FLT_TYPE x)
{
    complex ans;
    FLT_TYPE w,reans,imans,W0;

    w = 2*PI*f;

    W0 = wo(x,w);

    ans = ( -w*w +2*PI*w*b(w,x,Po,,ci) + W0*W0);

    reans=real(ans);
    imans=imag(ans);

    return ans;
}

FLT_TYPE BETA(FLT_TYPE x )
{
    FLT_TYPE ans;
    FLT_TYPE arg;
    INT_TYPE i;

    i=BubIndex;

    if (bubrad[i]==0)
        ans = bubrad[i]*bubrad[i]*bubrad[i];
    else
    {
        arg = (x-bubrad[i])/bubrad[i];
        ans = r *r*r  * exp( - arg * arg) ;

        arg = (x-bubrad[i])/bubrad[i];
        ans = r *exp( - arg*arg)/DispDenom(x);

        reans= real(ans);
        imans= imag(ans);
    };

    return 4*PI/3*numbub[i]*ans;
}

FLT_TYPE check_Beta()
{
    int i;
    FLT_TYPE betavalue,a,b;

    betavalue=0;

    for(i=0; i<NUMDIST;++i)
    {
        BubIndex = i;
        a=bubradmin[i];
        b=bubradmax[i];

        betavalue += SimpsonInt(BETA,a,b);
    }

    return betavalue;
}

complex DispIntegrand(FLT_TYPE x)
{
    complex ans;
    FLT_TYPE arg,reans,imans;
    INT_TYPE i;

    i = BubIndex;

    if (bubrad[i]==0)
        ans = bubrad[i]/DispDenom(bubrad[i]);
    else
    {
        arg = (x-bubrad[i])/bubrad[i];
        ans = r *exp( - arg*arg)/DispDenom(x);

        reans= real(ans);
        imans= imag(ans);
    };

    reans= real(ans);
    imans= imag(ans);

    return ans;
};

complex dispersion()
{
    complex denom,tempdisp,W0;
    FLT_TYPE a, b,redisp,imdisp;

    int i;

    if (Beta_Amp==0)
        Beta_Amp = beta/ check_Beta();

    tempdisp = complex(0..0.);

    for (i=0; i<NUMDIST; ++i)
    {
        BubIndex=i;

        a = bubradmin[i];
        b = bubradmax[i];

        if (a < 0.) a=EPS;

        tempdisp += 4*PI*ci*ci*numbub[i]* Beta_Amp *
                    CompSimpsonInt(DispIntegrand,a,b);
    };

    redisp=real(tempdisp);
    imdisp=imag(tempdisp);

    return(tempdisp);
}
```

250

```
// *****************************
complex clcm(FLT_TYPE w)
{
complex tempclcm,sqrtpludispersion,garmma;

sqrtpludispersion=sqrt(1+ dispersion());

if(sqrtpludispersion1=complex(0.,0.))
tempclcm=conj(sqrtpludispersion);

else
tempclcm=CIMF;

RECALC=0;

// garmma=1./3. * real(PHI(f,bubrad[0],Po));

// tempcm=sqrt( Po*garmma/
//          (Po *garmma/c1/c1+beta*(1.-beta) *rho1()));

return( tempclcm);
}

// *****************************

void CalcClCm()
{
int jj;

complex tempclcm,sqrtpludispersion,garmma;
FLT_TYPE w,rclcmlist,iclcmlist;

if (RECALC=1)   {

free(clcmlist);

clcmlist = (complex *) malloc( (size_t) NUMFQS * sizeof(complex));

for (jj=0;jj<NUMFQS;jj++)  {

w=2*PI*putf(frqlist[jj]);


clcmlist[jj]=clcm(w);
rclcmlist=real( clcmlist[jj]);
iclcmlist=imag( clcmlist[jj]);

}
};

rclcmlist=real(((complex * ) clcmlist)[0]);
rclcmlist=real(((complex * ) clcmlist)[3]);

// garmma=1./3. * real(PHI(f,bubrad[0],Po));

// tempcm=sqrt( Po*garmma/
//          (Po *garmma/c1/c1+beta*(1.-beta) *rho1()));

return( tempclcm);
}

// *****************************

complex cm(FLT_TYPE w)
{
complex tempcm;

tempcm=c1/clcm(w);

return( tempcm);
}

// *****************************

extern "C"


FLT_TYPE getcm(FLT_TYPE frq)
{
complex sqrtpludispersion;
FLT_TYPE tempcm,w;

w=2*PI*frq;

tempcm=c1/real(clcm(w));

return(tempcm);

}

// *****************************

extern "C"
FLT_TYPE GETWo(FLT_TYPE rad, FLT_TYPE fq)
{

// returns complex resonance fq of bubble

FLT_TYPE dummyfq,WO;

dummyfq=putf(fq);

WO = wo(rad,2*PIef);

return(WO);

}

// *****************************

extern "C"

void CmFQlist( FLT_TYPE *frage, FLT_TYPE *cmlist, long num)

{
int
ind;

FLT_TYPE
dummy,rclcm;
```

251

```c
/* replace each frequency with its Cm */

CalcClCm();

rclcm=cl/real(clcmlist[0]);
rclcm=cl/real(clcmlist[1]);

for (ind=0;ind<NUMFQS;ind++)
{

dummy= cl/real(clcmlist[ind]);
cmlist[ind]=dummy;
};

dummy= cl/real( clcmlist[3]);
dummy= cl/real(clcmlist[0]);

}

// **********************************************

extern "C"
FLT_TYPE Attenuation(FLT_TYPE freq)
{
FLT_TYPE
       ans,
       w;

w= 2*PI*putf(freq);

ans = 8.68589* w* imag(1./cm(w))/100;

return ans;

}

// **********************************************

extern "C"
void AttenFQlist( FLT_TYPE *freqs, FLT_TYPE *Attenlist, long num)
{
```

```c
int
       ind;
FLT_TYPE
       dummy,w;

/* replace each frequency with its Attenuation */

CalcClCm();

for (ind=0;ind<NUMFQS;ind++)
{

w=2*PI*fqlist[ind];

dummy= 8.68589* w* imag( clcmlist[ind])/cl/100; // Attenuation(freqs[ind])*1;
Attenlist[ind]=dummy;
};

}

// **********************************************

extern "C"
void PolytropicIndex( FLT_TYPE *freqs, long num)
{
int
       ind;
FLT_TYPE
       dummy,
       w;

/* replace each frequency with its Polytropic Index */

for (ind=0;ind<num;ind++)
{
w=putf(freqs[ind]);
dummy= 1./3. * real(PHI(w,bubrad[0],Po));
freqs[ind]=dummy;
};

}

// **********************************************
```

```c
complex jsqrt(const complex z) ;

extern "C"
void initPhaseSpeed()
{
FLT_TYPE
       BETALIST[16],
       xxx;                    // dummy variables

char*
       ccc;

INT_TYPE
       NUMDIST = 0;
       RECALC = 0;
       NUMFQS=0;

complex
       zzz;

BETALIST[0]=.001;
BETALIST[1]=1.;
BETALIST[2]=.0005;
BETALIST[3]=0.;
BETALIST[4]=0.;
BETALIST[5]=0.;

putBetaList(BETALIST,6);

xxx= putcl(1500.);          // Sound speed in surrounding medium
xxx= putrhol(1000.);        // density of surrounding medium
xxx= putrhog(1.);           // density of gas medium

xxx= putZ(0.) ;             // Ambient Surrounding pressure

xxx=putf(0.1);              // set the initial frequency
```

252

PhaseSpeedGlob.cxx

```
#include "nscsp3.1.h"
#include "PhaseSpeedGlob.h"

FLT_TYPE

    c1,
    Po,
    zz,
    rho10,
    f,
    K,

    beta,
    numbub[MAXBUBDIST],
    bubrad[MAXBUBDIST],
    bubradsd[MAXBUBDIST],
    bubradmin[MAXBUBDIST],
    bubradmax[MAXBUBDIST],
    Beta_Amp,
    rhog0 .
    //*cmlist=NULL,
    //*Attenlist=NULL,
    *fqlist=NULL;

                                    RECALC,
                                    NUMFQS;

int

    BubIndex,
    NUMDIST,

complex

                                    *clmlist=NULL;
```

PhaseSpeedMain3.1.c

complex.h

Bibliography

Abramowitz, M., & Stegun, I.A. 1972. *Handbook of mathematical functions.* New York: Dover.

Adair, R., Huster, M., & Miklovic, D. 1992. Backscattering of underwater noise by bubble clouds. *J. Acoust. Soc. of Amer.*, **92**, 2479.

Adair, R.G., & Huster, M.E. 1993. *High resolution surface reverberation imaging during CST7 Phase 2.* Tech. rept. ARS–239–001–TR. Areté Associates, La Jolla, CA.

Allen, W.T.R. 1983. *Wind and Sea.* Canadian Government Publishing Center.

Anderson, Victor C. 1950. Sound Scattering from a fluid sphere. *J. Acoust. Soc. of Amer.*, **22**(4), 426–431.

Bannister, R., Denham, R., Guthrie, K., & Browning, D. 1981. Measurements of the low–frequency wind generated ambient noise in the deep ocean. *J. Acoust. Soc. of Amer.*, **69**, 595.

Bowman, J. J., Senior, T. B. A., & Uslenghi, P. L. E. (eds). 1987. *Electromagnetic and Acoustic Scattering by Simple Shapes.* Revised edn. New York: Hemishphere Publishing.

Brekhovskikh, L. M., & Lysanov, Y. P. 1991. *Fundamentals of Ocean Acoustics.* second edn. Wave Phenomenon. New York: Springer–Verlag.

Brennen, C.E. 1995. *Cavitation and bubble dynamics.* New York: Oxford University Press.

Carey, W. M., & Browning, D. 1988. Low–frequency ocean ambient noise: Measurement and theory. *Pages 361–76 of:* Kerman, B. R. (ed), *Sea Surface Sound: Natural mechanisms of surface generated noise in the ocean.* Boston: Kluwer.

Carey, W. M., & Fitzgerald, J. W. 1993. Low frequency noise from breaking waves. *Pages 277–304 of:* Kerman, B. R. (ed), *Natural Physical Sources of Underwater Sound: Sea Surface Sound,* vol. 2. Boston: Kluwer.

Carey, W. M., & Monahan, E. C. 1990. Guest Editorial. *IEEE J. Ocean Eng.,* **15**(4), 265–267.

Carey, W. M., & Roy, R. A. 1993. Sound scattering from microbubble distributions near the sea surface. *Pages 25–43 of:* Ellis, D., Preston, J. R., & Urban, H. G. (eds), *Ocean Reverberation.* Boston: Kluwer.

Carey, W. M., & Wagstaff, R. A. 1986. Low frequency noise fields. *J. Acoust. Soc. of Amer.,* **80**(5), 1523–1526.

Carey, W. M., Fitzgerald, James W., Monahan, E. C., & Wang, Q. 1993. Measurement of the sound produced by a tipping trough with fresh and salt water. *J. Acoust. Soc. of Amer.,* **93**(6), 3178–3192.

Carey, W.M., & Bradley, M.P. 1985. Low–frequency ocean surface noise sources. *J. Acoust. Soc. of Amer.,* **78**(S1–S2).

Chapman, R. P., & Harris, J. 1962. Surface backscattering strength measured with explosive sound sources. *J. Acoust. Soc. of Amer.,* **34**, 1592–97.

Chapman, R.P., & Scott, H.D. 1964. Surface backscattering strengths measured over an extended range of frequencies and grazing angles. *J. Acoust. Soc. of Amer.,* **36**, 1735–1737.

Cheyne, S.A., Stebbings, C.T., & Roy, R.A. 1995. Phase velocity measurements in bubbly liquids using a fiber optic laser interferometer. *J. Acoust. Soc. of Amer.*, **97**(3), 1621–4.

Clay, C.S., & Medwin, H. 1977. *Acoustical Oceanography: prinicples and applications*. New York: John Wiley & Sons.

Commander, K. W., & Prosperetti, A. 1989. Linear pressure waves in bubbly liquids: Comparison between theory and experiments. *J. Acoust. Soc. of Amer.*, **85**(2), 732–746.

Crighton, D. G., Dowling, A. P., Ffowcs Williams, J. E., Heckl, M., & Leppington, F. G. 1992. *Modern Methods in Analytical Acoustics: Lecture Notes*. New York: Springer–Verlag.

d'Agostino, L., & Brennen, C. E. 1983. On the acoustical dynamics of bubble clouds. *ASME Cavitation and Multiphase Flow Forum*, 72–75.

Donelan, M. A., Hamilton, J., & Hui, W. H. 1985. Directional spectra of wind generated waves. *Philos. Trans. R. Soc. London Ser. A*, **315**, 509–562.

Eckart, Carl. 1953. Sea surface scattering. *J. Acoust. Soc. of Amer.*, **25**, 566–570.

Farmer, D., & Vagle, S. 1989. Waveguide propagation of ambient sound in the ocean–surface bubble layer. *J. Acoust. Soc. of Amer.*, **86**, 1897–1908.

Farmer, D. M. 1992 (March). *FLEX Instrument Survey*. Tech. rept. University of Brittish Columbia.

Flax, L., Gaunaurd, G.C., & Überall, H. 1981. *Physical Acoustics: principles and methods*. Vol. XV. New York: Academic Press. Chap. 3.

Fox, F.E., *et al.* 1955. Phase velocity and absorption measurements in water containing air bubbles. *J. Acoust. Soc. of Amer.*, **27**, 534–539.

Furduev, A.V. 1966. Undersurface cavitation as a source of noise in the ocean. *Atmospheric and Oceanic Physics*, **2**, 523.

Gauss, R.C., Fialkiowski, J.M., & Soukup, R. J. 1993. Low–frequency direct–path surface and volume scattering measured using narrowband and broadband pulses. *Page 235 of:* Ellis, D., *et al.* (eds), *Ocean Reverberation.* Boston: Kluwer.

Gilbert, K. E. 1993. A stochastic model for scattering from the near–surface oceanic bubble layer. *J. Acoust. Soc. of Amer.*, **94**(6), 3325–34.

Gouse, S.W., & Brown, G.A. 1964. *A survey of the velocity of sound in two–phase mixtures.* Tech. rept. Paper 64–WA/FE–35. ASME.

Gragg, R. F., & Wurmser, D. 1993. Low–frequency scattering from intermediate bubble plumes: theory and computational parameter study. *J. Acoust. Soc. of Amer.*, **94**(1), 319–29.

Hasselman, K., Ross, d. B., Müller, P., & Sell, W. 1976. A parametric wave prediction model. *J. Phys. Oceanogr.*, **6**, 200–228.

Henyey, F. S. 1991. Acoustic scattering from ocean microbubble plumes in the 100 Hz to 2 kHz region. *J. Acoust. Soc. of Amer.*, **90**(1), 399–405.

Hollet, R. D. 1994. Observations of underwater sound at frequencies below 1500 Hz from breaking waves at sea. *J. Acoust. Soc. of Amer.*, **95**(6), 165–70.

Hollet, R.D., & Heitmeyer, R.M. 1988. Noise generation by bubbles formed in breaking waves. *Pages 449–461 of:* Kerman, B. R. (ed), *Sea Surface Sound: Natural mechanisms of surface generated noise in the ocean.* Boston: Kluwer.

Karplus, H.B. 1958. *The velocity of sound in a liquid containing gas bubbles.* Tech. rept. COO–248. Illinois Inst. Tech.

Keller, J. B., & Kolodner, I. I. 1956. Damping of underwater explosion bubble oscillations. *J. Appl. Phys.*, **27**, 1152–1161.

Kennedy, R.M., & Goodnow, T.V. 1990. Measuring the vertical directional spectra caused by sea surface sound. *IEEE J. Ocean Eng.*, **15**(4), 299–310.

257

Kerman, B.R. 1984. Underwater sound generation by breaking waves. *J. Acoust. Soc. of Amer.*, **75**, 148.

Kewley, D. J., Browning, D. G., & Carey, W. M. 1990. Low–frequency wind–generated ambient noise source levels. *J. Acoust. Soc. of Amer.*, **88**, 1894–1902.

Kibblewhite, A.C., Shooter, J.A., & Watkins, S.L. 1976. Examination of attenuation at very low frequencies using the deep water ambient noise field. *J. Acoust. Soc. of Amer.*, **60**, 1040.

Kinsler, L. E., Frey, A., Coppens, A. B., & Sanders, J. V. 1982. *Fundamentals of Acoustics*. New York: John Wiley & Sons.

Knudsen, V.O., Alford, R.S., & Emling, J.W. 1948. Underwater Ambient Noise. *J. Mar. Res.*, **7**, 410.

Kolaini, A. R., Roy, R. A., Crum, L. A., & Mao, Yi. 1993. Low–frequency underwater sound generation by impacting transient cylindrical water jets. *J. Acoust. Soc. of Amer.*, **1994**(5), 2809–20.

Kolaini, A.R., Roy, R.A., & Gardner, D.L. 1994. Low–frequency acoustic emissions in fresh and salt water. *J. Acoust. Soc. of Amer.*, **96**(Sep), 1766–72.

Koller, D. P., & Shankar, P. M. 1994. Acoustical emissions from bubble clouds. *Ultrasonics*, **32**(3), 229–33.

Koller, D.P., & Shankar, P.M. 1993. Low–frequency oscillations of bubble plumes. *J. Acoust. Soc. of Amer.*, **93**(3), 1362–1364.

Konrad, W. L., & Geary, J. III. 1991. *Potential application fo a parametriec source for target strength measurements*. Tech. rept. TM 811067. Naval Underwater Systems Center.

Lamarre, E. 1993. *An experimental study of air entrainment by breaking waves*. Ph.D. thesis, Massachusetts institute of Technology & Woods Hole Oceanographic Institution, MA.

Lamarre, E., & Melville, W. K. 1992. Instrumentation for the measurement of void–fraction in breaking waves: laboratory and field results. *IEEE J. Ocean Eng.*, **17**(2), 204–15.

Lamarre, E., & Melville, W. K. 1994. Sound–speed measurements near the ocean surface. *J. Acoust. Soc. of Amer.*, **96**(6), 3605–16.

Lighthill, James (ed). 1975. *Waves in Fluids.* Cambridge University Press.

Longuet-Higgens, M. 1993. Bubble noise mechanisms—a review. *Pages 419–452 of:* Kerman, B. R. (ed), *Natural Physical Sources of Underwater Sound: Sea Surface Sound*, vol. 2. Boston: Kluwer.

Lu, N. Q., Prosperetti, A., & Yoon, S. W. 1990. Underwater noise emissions from bubble clouds. *IEEE J. Ocean Eng.*, **15**, 275–281.

McDaniel, S. T. 1988. High–frequency sea surface scattering: Recent progress. *J. Acoust. Soc. of Amer.*, **84**.

McDaniel, S. T. 1993. Sea surface reverberation: a review. *J. Acoust. Soc. of Amer.*, **94**(4), 1905–22.

McDonald, B. E. 1991. Echoes from vertically striated subresonant bubble clouds: A model for ocean surface reverberation. *J. Acoust. Soc. of Amer.*, **89**, 617–22.

Miklovic, D. W., Huster, M. E., & Moser-Breaker, Michelle. 1995. The spatial variability of surface reverberation under high and low wind speeds. *IEEE J. Ocean Eng.*, October, Accepted for publication. Accepted for publication.

Minneart, M. 1933. On musical air–bubbles and the sounds of running water. *Phil. Mag.*, **16**, 235–248.

Monahan, E. C. 1988. Whitecap coverage as a remotely monitorable indication of the rate of bubble injection into the oceanic mixed layer. *Pages 85–96 of:* Kerman, B. R. (ed), *Sea Surface Sound.* Boston: Kluwer.

Monahan, E. C., & Lu, M. 1990. Acoustically relevant bubble assemblages and their dependence on meteorological parameters. *IEEE J. Ocean Eng.*, **15**(4), 340–9.

Monahan, Edward C., & Niocaill, Gearoid Mac (eds). 1986. *Oceanic whitecaps and their role in air-sea exchange processes*. Kluwer.

Morris, G.B. 1978. Depth dependence of ambient noise in the northeastern Pacific Ocean. *J. Acoust. Soc. of Amer.*, **64**, 581–590.

Morse, P., & Ingard, U. K. 1968. *Theoretical Acoustics*. New York: McGraw–Hill.

Morse, P.M., & Feshbach, H. 1953. *Methods of theoretical physics*. New York: McGraw–Hill.

NDRC. 1946. *The physics of sound in the sea*. Tech. rept. National Defense Research Committee., Washington, DC. United States. Office of Scientific Research and Development.

Nicholas, M., Roy, R. A., Crum, L. A., Oğuz, H., & Prosperetti, A. 1994. Sound emissions by a laboratory bubble cloud. *J. Acoust. Soc. of Amer.*, **95**(6), 3171–82.

Nicholas, M., Roy, R. A., Crum, L. A., Carey, William M., & Schindall, J. to be submitted. Passive Underwater Acoustic Emissions from Artificial Bubble Clouds. *J. Acoust. Soc. of Amer.*

Nützel. 1993. Measurements of acoustic backscattering of the near–surface layer. *In:* Ellis, D., Preston, J. R., & Urban, H. G. (eds), *Ocean Reverberation*. Boston: Kluwer.

Nützel, B., Herwig, H., Koenigs, P. D., & Monti, J. M. 1994. Acoustic backscatter measurements in the North Sea: 3–18 kHz. *J. Acoust. Soc. of Amer.*, **95**(5), 2488–94.

Oğuz, H. N. 1994. A theoretical study of low–frequency oceanic ambient noise. *J. Acoust. Soc. of Amer.*, **95**(4), 1895–1912.

Oğuz, H.N., Prosperetti, A., & Kolaini, A.R. 1995. Air entrapment by a falling water mass. *Journal of Fluid Mechanics.*, **294. pp. 181-207. 10 July 1995.** boundary-integral-equations. bubbles. flow-simulation.

Ogden, P. M., & Erskine, F. T. 1994. Surface scattering measurements using broadband explosive charges in the Critical Sea Test experiments. *J. Acoust. Soc. of Amer.*, **95**(2), 746–61.

Pierce, Allan D. 1989. *Acoustics: An introduction to its physical principles and applications.* Woodbury, NY: Acoustical Society of America.

Pierson, W. J., & Moskowitz, L. 1964. A proposed spectral form of fully developed wind seas based on the similarity theory of S. A. Kitaigorodskii. *J. Geophys. Res.*, **18**, 5181–5190.

Prosperetti, A., Crum, L.A., & Commander, K.W. 1988. Nonlinear bubble dynamics. *J. Acoust. Soc. of Amer.*, **83**, 502–513.

Prosperetti, A., Lu, N. Q., & Kim, H. S. 1993. Active and passive acoustic behavior of bubble clouds at the oceans surface. *J. Acoust. Soc. of Amer.*, **93**(6), 3117–3127.

Prosperetti, A. P. 1988a. Bubble Dynamics in ocean ambient noise. *Pages 151–71 of:* Kerman, B. R. (ed), *Sea Surface Sound.* Boston: Kluwer.

Prosperetti, Andrea. 1988b. Bubble–related ambient noise in the ocean. *J. Acoust. Soc. of Amer.*, **84**(3), 1042–54.

Prosperetti, Andrea. 1991. The thermal behavior of oscillating gas bubbles. *J. Fluid Mech.*, **222**, 587–616.

Prosperetti, A.P. 1985. Bubble related ambient noise in the ocean. *J. Acoust. Soc. of Amer.*, **78**(S1).

Prosperetti, A.P., & Lu, N.Q. 1988. Cavitation and bubble bursting as sources of oceanic ambient noise. *J. Acoust. Soc. of Amer.*, **84**, 1037–1041.

Pumphrey, H.C., & Ffowcs-Williams, J.E. 1990. Bubbles as sources of ambient noise. *IEEE J. Ocean Eng.*, **15**, 268–74.

Rayleigh, Lord (Strutt, J.W.). 1877. *The theory of sound.* London: MacMillan and Co.

Roy, R. A., Carey, W. M., Nicholas, M., Schindall, J., & Crum, L. A. 1992. Low–frequency scattering from submerged bubble clouds. *J. Acoust. Soc. of Amer.*, **92**(5), 2993–6.

Roy, R. A., Schindall, J., Carey, W. M., & Crum, L. A. in press. Can near–surface bubble clouds and plumes lead to anomalous perturbations in low–frequency sea–surface scattering?

Roy, R.A., Nicholas, M., Markiewicz, K., & Crum, L.A. 1991. Collective oscillations in fresh and salt water bubble clouds. *J. Acoust. Soc. of Amer.*, 2318.

Rschevkin, S. N. 1963. *The Theory of Sound.* New York: Pergamon Press.

Ruggles, A.E. 1987. *The propagation of pressure perturbations in bubbly air/water flows.* Ph.D. thesis, Rensselaer Polytechnic Institute, NY.

Sarkar, K., & Prosperetti, A. 1993. Backscattering of underwater noise by bubble clouds. *J. Acoust. Soc. of Amer.*, **93**(6), 3128–38.

Silberman. 1957. Sound velocity and attenuation in bubbly mixtures measured in standig wave tubes. *J. Acoust. Soc. of Amer.*, **29**, 925–933.

Spitzer, L. Jr. 1943. *NDRC Report No. 6.* Tech. rept. 1–sr20–918. National Defense Research Committee., Washington, DC. United States. Office of Scientific Research and Development.

Thorpe, S. A. 1982. On the clouds of bubbles formed by breaking wind–waves in deep water, and their role in air–sea gas transfer. *Phil. Trans. Roy. Soc.*, **304**, 155–185.

Thorpe, S.A. 1984. The effect of Langmuir circulation on the distribution of submerged bubbles caused by breaking waves. *J. Fluid Mech.*, **142**, 151–70.

Thorsos, Eric I. 1990. Acoustic scattering from a "Pierson–Moskowitz" sea surface. *J. Acoust. Soc. of Amer.*, **88**(1), 335–349.

Urick, R. J. 1967. *Principles of Underwater Sound for Engineers*. New York: McGraw–Hill.

Urick, R. J. 1984. *Ambient noise in the sea*. Washington, D.C.: Department of the Navy.

Urick, R.J., & Hoover, R.M. 1956. Backscattering of sound from the sea surface: Its measurement, causes, and application to the prediction of reverberation levels. *J. Acoust. Soc. of Amer.*, **28**, 1038–1042.

Vagle, S., & Farmer, D. M. 1992. The measurement of bubble–size distributions by acoustical backscatter. *Journal of Atmospheric and Oceanic Technology*, **9**(5), 630–44.

Wenz, G.M. 1962. Acoustic Ambient Noise in the Ocean: Spectra and Sources. *J. Acoust. Soc. of Amer.*, **34**, 1936.

Whittenborn, A. 1976. *Ambient Noise and Associated propagations factors as a function of depth and wind speed in the deep ocean*. Tech. rept. ADC006902. DTIC, Cameron Station.

Wilson, J.H. 1980. Low–frequency wind–generated noise produced by the impact of spray with the ocean surface. *J. Acoust. Soc. of Amer.*, **68**, 952.

Wood, A. B. 1941. *A Text Book of Sound*. New York, Macmillan.

Wu, J. 1981. Bubble populations and spectra in near–surface ocean: summary and review of field measurements. *J. Geog. Res.*, **86**, 457–463.

Yoon, S. W., Crum, L, A., Prosperetti, A., & Lu, N. Q. 1991. An investigation of the collective oscillations of a bubble cloud. *J. Acoust. Soc. of Amer.*, **89**(2), 700–6.

REPORT DOCUMENTATION PAGE

Public reporting burden for this collection of information is estimated to average 1 hour per response, including the time for reviewing instructions, searching existing data sources, gathering and maintaining the data needed, and reviewing the collection of information. Send comments regarding this burden estimate or any other aspect of this collection of information, including suggestions for reducing this burden, to Washington Headquarters Services, Directorate for Information Operations and Reports, 1215 Jefferson Davis Highway, Suite 1204, Arlington, VA 22202-4302, and to the Office of Information and Regulatory Affairs, Office of Management and Budget, Washington, DC 20503.

1. AGENCY USE ONLY (Leave blank)	2. REPORT DATE	3. REPORT TYPE AND DATES COVERED
	June 1996	Final Technical Report

4. TITLE AND SUBTITLE

Acoustic Scattering From Compact Bubble Clouds

5. FUNDING NUMBERS

6. AUTHOR(S)

Ronald A. Roy and Jeffrey A. Schindall

7. PERFORMING ORGANIZATION NAME(S) AND ADDRESS(ES)

Applied Physics Laboratory
University of Washington
1013 NE 40th Street
Seattle, WA 98105-6698

8. PERFORMING ORGANIZATION REPORT NUMBER

9. SPONSORING / MONITORING AGENCY NAME(S) AND ADDRESS(ES)

Office of Naval Research
Ballston Centre Tower One
800 North Quincy Street
Arlington, VA 22217-5660

10. SPONSORING / MONITORING AGENCY REPORT NUMBER

11. SUPPLEMENTARY NOTES

12a. DISTRIBUTION / AVAILABILITY STATEMENT

Proposed: Approved for public release.

12b. DISTRIBUTION CODE

13. ABSTRACT (Maximum 200 words)

In this study, a simple model describing the low-frequency scattering properties of high void fraction bubble clouds in both the free field and near the ocean surface is developed. This model, which is based on an effective medium approximation and acoustically compact scatterers, successfully predicts the results of the bubble cloud scattering experiment carried out at Lake Seneca NY for frequencies consistent with the model assumptions (Roy et al., 1992). The introduction of the surface is facilitated by the method of images is subject to the same constraint of low acoustic frequency imposed by the compact scatterer assumption. This model is not intended to serve as an exact replicate of oceanic bubble cloud scattering. The model herein was kept simple by design, for only then can the complex physical behavior be expressed in analytical form. Simple, analytic theories facilitate the exploration of parameter space, and more importantly serve to illuminate the underlying physics.

14. SUBJECT TERMS

Bubbles, Bubble Clouds, Resonance Scattering, Ambient Noise, Lake Seneca Bubble Cloud Scattering Experiment, Parametric Source, Collective Oscillations, Low-Frequency Sea Surface Scattering

15. NUMBER OF PAGES

280

16. PRICE CODE

17. SECURITY CLASSIFICATION OF REPORT	18. SECURITY CLASSIFICATION OF THIS PAGE	19. SECURITY CLASSIFICATION OF ABSTRACT	20. LIMITATION OF ABSTRACT
Unclassified	Unclassified	Unclassified	SAR